Investigation and Optimization of Corrosion-resistant Electroless Ni-P Coating in Steam-assisted Gravity Drainage System

by

Jiankuan Li

A thesis submitted in partial fulfillment of the requirements for the degree of

Doctor of Philosophy

in

Materials Engineering

Department of Chemical and Materials Engineering
University of Alberta

Abstract

The boosting energy demand has propelled the increasing utilization of oil and gas resources, but severe corrosion occurs on traditional carbon steel materials. Driven by the harsh service conditions in steam-assisted gravity drainage system (SAGD) operations, a promising corrosion-resistant coating, electroless Ni-P coating, has attracted growing attentions due to its good balance between satisfactory performance and reasonable cost. Therefore, in this thesis, the corrosion behavior and mechanism of Ni-P coating in SAGD-related environments were elucidated, and further coating optimization approaches were made to meet diverse requirements under service conditions.

First, the electrochemical corrosion behavior of Ni-P coating in $CO_2/H_2S/Cl^-$ brine was investigated. The added H_2S enhances the corrosion of Ni-P coating by affecting both anodic and cathodic processes. The well-accepted $H_2PO_2^-$ adsorbed layer only exists in the early stage of corrosion and barely improves the anti-corrosion performance. The formation of NiO and Ni_3S_2 renders temporary protection during immersion, but the addition of H_2S accelerates the diffusion process at the electrolyte/coating interface and promotes the electrolyte penetration through the coating, causing severe localized corrosion and coating disbondment. A corrosion model was proposed to illustrate the corrosion and degradation process of Ni-P coated steel in the $CO_2/H_2S/Cl^-$ environment.

Secondly, the effects of Ca^{2+} on the corrosion behavior and film characteristics of N80 carbon steel and electroless Ni-P coating at high temperature and high pressure were studied. The corrosion of N80 steel is significantly influenced by Ca^{2+} concentrations, which not only alters the corrosion film microstructure, but also changes the water

chemistry of the aqueous phase. Meanwhile, Ni-P coating exhibits exceptional corrosion resistance regardless of Ca^{2+} concentration, owing to the protection of the formed $NiO/Ni(OH)_2$ film and the absence of scale formation.

The optimization methods of Ni-P coating were then developed to acquire better anti-corrosion properties. The electroless Ni-Mo-P/Ni-P composite coating was successfully applied on N80 carbon steel, and the effects of Mo addition and heat treatment on the corrosion resistance enhancement in $CO_2/H_2S/Cl^-$ brine were studied. The Mo addition in the as-deposited Ni-P coating causes the microstructural transformation from amorphous to crystalline due to the reduced P content, thereby suffering severe corrosion. Nonetheless, the heat-treated Ni-Mo-P/Ni-P coating exhibits desirable corrosion resistance. Heat treatment facilitates the formation of Ni_4Mo phase and the growth of an oxide film consisting of nickel and molybdenum oxides with better passivation properties, which accounts for the remarkable corrosion resistance improvement.

In addition, a smart electroless Ni-P composite coating incorporated with pH-responsive benzotriazole-loaded nanocapsules was successfully fabricated and applied on N80 carbon steel, and the improved corrosion resistance was evaluated. The coating incorporated with the functionalized nanocapsules exhibits excellent anti-corrosion performance. It is primarily originated from the filling of nanocapsules into intrinsic micropores of the coating that impairs the electrolyte penetration, and the release of BTA when triggered by the local acidification of the micropores due to penetration of aggressive medium. The incorporated nanocapsules endow the smart coating with good anti-corrosion stability, showing a maximum inhibition efficiency of nearly 80%, as well as a well-protected coating surface with much less corrosion pits and the absence of lateral coating disbondment at the coating/substrate interface.

Preface

This thesis is an original work by Jiankuan Li under the co-supervision of Prof. Jing-Li Luo and Prof. Hongbo Zeng.

Chapter 1 is the introduction that contains the fundamentals of electroless Ni-P coating and corrosion issues in SAGD operations.

Chapter 2 covers the literature survey of the corrosion behavior of electroless Ni-P coating in various corrosive environments and current coating optimization approaches to mitigate corrosion.

Chapter 3 presents the employed methodologies, including coating fabrication, corrosion measurements and characterizations.

Chapter 4 has been published as **J. Li**, C. Sun, M. Roostaei, M. Mahmoudi, V. Fattahpour, H. Zeng, J.-L. Luo. Insights into the electrochemical corrosion behavior and mechanism of electroless Ni-P coating in the $CO_2/H_2S/Cl^-$ environment. ***Corrosion***, 76 (2020) 578–590.

Chapter 5 has been submitted to ***Materials Chemistry and Physics*** for publication as **J. Li**, C. Sun, M. Roostaei, M. Mahmoudi, V. Fattahpour, H. Zeng, J.-L. Luo. Role of Ca^{2+} in the CO_2 corrosion behavior and film characteristics of N80 steel and electroless Ni-P coating at high temperature and high pressure.

Chapter 6 has been published as **J. Li**, C. Sun, M. Roostaei, M. Mahmoudi, V. Fattahpour, H. Zeng, J.-L. Luo. Characterization and corrosion behavior of electroless Ni-Mo-P/Ni-P composite coating in $CO_2/H_2S/Cl^-$ brine: effects of Mo addition and heat treatment. ***Surface and Coatings Technology***, 403 (2020) 126416.

Chapter 7 has been submitted to ***Chemical Engineering Journal*** for publication as **J. Li**, H. Zeng, J.-L. Luo. Probing the corrosion resistance of a smart electroless Ni-P composite coating embedded with pH-responsive corrosion inhibitor-loaded nanocapsules.

Chapter 8 includes the summary of the thesis and briefly presents some future prospects.

Appendix has been published as **J. Li**, C. Sun, S. Shuang, M. Roostaei, V. Fattahpour, M. Mahmoudi, H. Zeng, J.-L. Luo. Investigation on the flow-induced corrosion and degradation behavior of underground J55 pipe in a water production well in the Athabasca oil sands reservoir. ***Journal of Petroleum Science and Engineering***, 182 (2019) 106325.

I was responsible for designing and conducting all the experiments, data collection and analysis and manuscript writing. For Chapter 5, Dr. Chong Sun assisted on the software and calculation of water chemistry. For all the work above, Dr. Chong Sun, Prof. Jing-Li Luo and Prof. Hongbo Zeng provided valuable comments and suggestions and made revisions for the manuscripts.

Acknowledgements

First and foremost, I would like to express my most sincere thanks to my supervisor, Dr. Jing-Li Luo, who has provided incredible academic and financial support in the last four years. She shared her knowledge of how to better conduct scientific research and think creatively, which were invaluable for my future career. My deep appreciation also goes to my co-supervisor, Dr. Hongbo Zeng for all his great help and guidance in my research.

I also would like to thank my supervisor committee member, Dr. Qi Liu for his thoughtful suggestions and assistance during my research progress.

This work has also benefited from the assistance of many individuals in my group. My special thanks goes to Dr. Chong Sun, who offers great help in my experimental design and paper writing. I am truly grateful to Dr. Subiao Liu, Mr. Shuo Shuang, Miss. Jing Xiao, Miss. Yuanyuan Hong, Mr. Minrui Gao, Mr. Pengfei Sui, Mr. Shaoqing Liu, Miss. Mengnan Zhu, Mr. Bowen Zhang, for their help and collaboration during my research in the lab. Besides, I would like to thank Dr. Shihong Xu, Dr. Nancy Zhang and Dr. Anqiang He in Nanofab, University of Alberta, for their support and suggestions in material characterizations.

This research was funded by Natural Sciences and Engineering Research Council of Canada/RGL (RGL Reservoir Management Inc.) Collaborative Research and Development Grants (No. CRDPJ 488361) and the Natural Sciences and Engineering Research Council of Canada-Discovery Grant (No. GRPIN–2016–05494). It would not have been possible without their financial support.

Finally, my deepest thanks and love go to my family, especially my better half, Minna Yang, who always support and encourage me to go through this tough but meaningful journey.

Table of Contents

List of Figures

List of Tables

List of Symbols

SAGD	Steam-assisted gravity drainage
CRA	Corrosion-resistance alloy
TOC	Total organic carbon
DNP	Dispersed diamond particles
CNT	Carbon nanotubes
PTFE	Polytetrafluoroethylene
rGO	Reduced graphene oxide
MSN	Mesoporous silica nanoparticles
TEOS	Tetraethoxysilane
CTAB	Cetyltrimethylammonium bromide
BTA	Benzotriazole
SCE	Saturated calomel electrode
WE	Working electrode
CE	Counter electrode
RE	Reference electrode
OCP	Open circuit potential
LPR	Linear polarization resistance
EIS	Electrochemical impedance spectroscopy

CPE	Constant phase element
EEC	Equivalent electric circuit
EN	Electrochemical noise
PSD	Power spectral density
ZRA	Zero resistance ammeter
EPN	Electrochemical potential noise
ECN	Electrochemical current noise
FFT	Fast Fourier transform
HTHP	High temperature high pressure
CR	Corrosion rate
SEM	Scanning electron microscopy
EDS	Energy-dispersive X-ray spectroscopy
XRD	X-ray diffraction
FESEM	Field emission scanning electron microscopy
TEM	Transmission electron microscopy
XPS	X-ray photoelectron spectroscopy
OSM	Optical stereo microscopy
NMR	Nuclear magnetic resonance

List of Abbreviations

E_{corr}	Corrosion potential
i_{corr}	Corrosion current density
η	Corrosion inhibition efficiency
R_{s}	Solution resistance
R_{ct}	Charge transfer resistance
R_{c}	Coating resistance
R_{f}	Film resistance
R_{p}	Polarization resistance
Q_{dl}	Double-layer capacitance
Q_{c}	Coating capacitance
Q_{f}	Film capacitance
W	Warburg impedance
j	Imaginary number
ω	Angular frequency
n	Empirical exponent
χ^2	Quality of fit
$\beta_{\mathrm{a}}/\beta_{\mathrm{c}}$	Anodic/cathodic Tafel constant
B	Stern-Geary coefficient

EW	Equivalent weight
K_{sp}	Solubility product
R_{n}	Noise resistance
$\sigma_{\mathrm{V}}/\sigma_{\mathrm{i}}$	Standard deviations of potential noise and current noise
A	Noise intensity
S	Roll-off slope

1 Introduction

1.1 Introduction of SAGD

The energy demand has become an increasingly significant issue with the globalization and economic development in recent decades. It was reported that Canada has the largest amount of heavy oil and bitumen reserves (Figure 1.1), and Alberta's oil sands account for a large proportion of the total deposits. Among the several existing oil recovery methods that deal with the relatively deep resources with large gravity and viscosity, steam assisted gravity drainage (SAGD) is widely considered as one of the most promising and efficient methods.

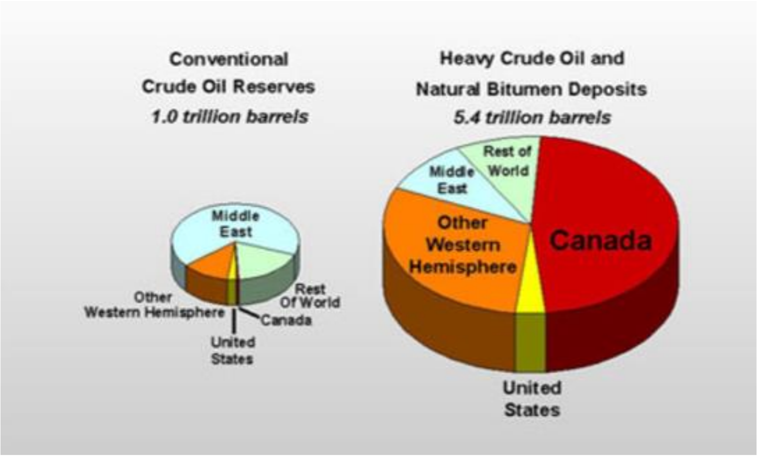

Figure 1.1 Worldwide distributions of conventional oil and heavy crude oil reserves [1].

SAGD process was firstly introduced and developed by Dr. Butler and his colleagues in the late 1970s [2]. A typical SAGD configuration involves the drilling of two parallel horizontal wells for each well pair. Steam is injected through the upper well to heat the bitumen and sands in the reservoir, and the bottom well, which is placed a few meters below the injection well, is used as the production well. The injected steam heats up the sands and bitumen in the reservoir, which decreases the bitumen viscosity so that it can be easily pumped to the surface for further treatment and utilization. The schematic illustration of SAGD configuration are shown in Figure 1.2.

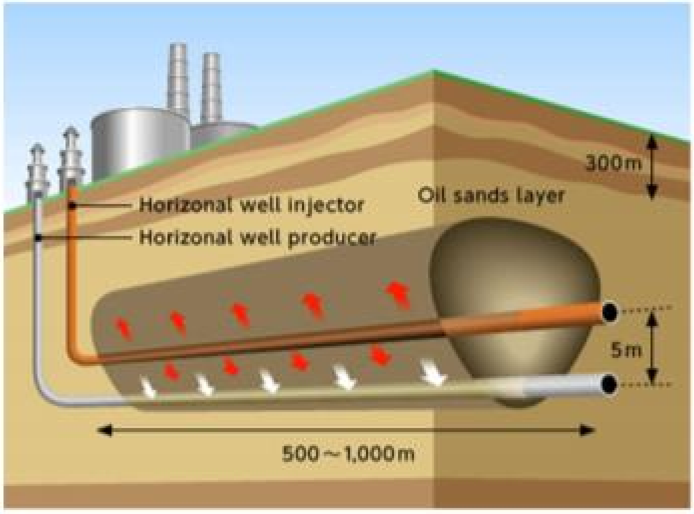

Figure 1.2 Schematic diagram of SAGD configuration [3].

1.1 Corrosion concerns in SAGD operations

During the SAGD operation, the aquathermolysis process takes place and gives rise to the formation of acidic gases (e.g., CO_2 and H_2S) [4,5], which causes severe corrosion damage of downhole completions and tubular materials when dissolved in water. In addition, the elevated temperatures (>200 °C) and high pressures (>3 MPa) in SAGD operations greatly intensify the corrosivity. Take Athabasca reservoirs as an example, it was reported that up to 75 L of H_2S and 10000 L of CO_2 per m^3 of the bitumen were produced at 240 °C [6]. More essentially, growing corrosion concerns emerge in long-term SAGD operations due to the high susceptibility to CO_2/H_2S corrosion of carbon steel materials in HTHP corrosive environments.

CO_2 corrosion (sweet corrosion) and H_2S corrosion (sour corrosion) are the most common corrosion forms in oil-related environments. Theoretically, in CO_2 and H_2S corrosion of steels, species such as H^+, CO_3^{2-}, HCO_3^-, H_2CO_3, S^{2-}, HS^-, and H_2S are involved in the electrochemical reactions, which makes the corrosion mechanism complicated. The cathodic process mainly includes the following reactions [7]:

$$2H_2CO_3 + 2e^- \rightarrow 2HCO_3{}^- + H_2 \qquad \text{(Eq. 1.1)}$$

$$2HCO_3{}^- + 2e^- \rightarrow 2CO_3{}^{2-} + H_2 \qquad \text{(Eq. 1.2)}$$

$$2H_2S + 2e^- \rightarrow 2HS^- + H_2 \qquad \text{(Eq. 1.3)}$$

$$2HS^- + 2e^- \rightarrow 2S^{2-} + H_2 \qquad \text{(Eq. 1.4)}$$

$$2H^+ + 2e^- \rightarrow H_2 \qquad \text{(Eq. 1.5)}$$

The anodic process is primarily the steel dissolution and corrosion product formation, which can be represented by the following reactions [7]:

$$Fe \rightarrow Fe^{2+} + 2e^- \qquad \text{(Eq. 1.6)}$$

$$Fe + H_2CO_3 \rightarrow FeCO_3 + 2H^+ + 2e^- \qquad \text{(Eq. 1.7)}$$

$$Fe + H_2S \rightarrow FeS + 2H^+ + 2e^- \qquad \text{(Eq. 1.8)}$$

CO_2/H_2S corrosion highly depends on several factors, such as pH, temperature, partial pressure, and the properties of the formed corrosion film. The variation of pH indicates the H^+ concentration and directly alters the acidity of the corrosion medium, thereby affecting corrosion. The cathodic reaction is controlled by the reduction of H^+ at lower pH ($pH<4$) and lower partial pressures, while at higher pH ($pH>5$) and higher partial pressures, the direct reduction of H_2CO_3 and H_2S dominates the cathodic reaction [8,9]. The effect of temperature mainly depends on the formation of corrosion films. Corrosion rates increase with temperature when protective films are not formed, but decline as temperature rises in the presence of corrosion film because the accelerated precipitation rate favors the formation of corrosion film with better protection [10].

The corrosion behavior in the co-existence of CO_2 and H_2S is much more complicated than that in the sole presence of either one due to their synergy, and it is generally believed that the domination of CO_2 corrosion or H_2S corrosion relies on the ratio of CO_2 pressure to H_2S pressure, p_{CO_2}/p_{H_2S}, as shown in Figure 1.3 [11]. Besides, the formed corrosion product film plays a vital role in the corrosion rate and corrosion form (general or localized corrosion), which can be attributed to the precipitation rate, stability, compactness, and the adhesion with steel substrate.

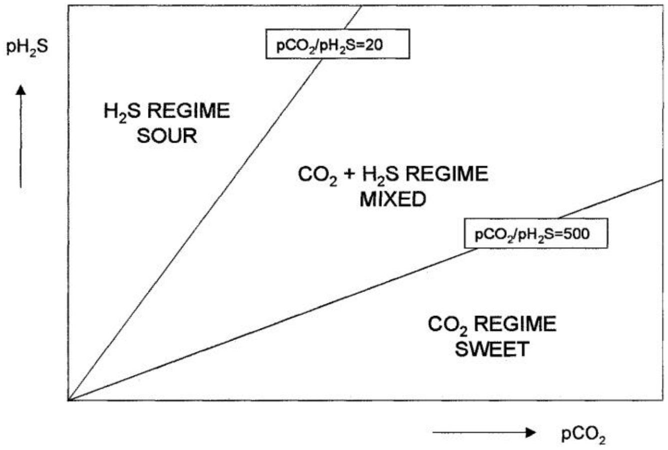

Figure 1.3 Corrosion regimes in CO_2/H_2S corrosion [11].

In addition, diverse distributions of species are found in the produced fluid and gas from a SAGD well, as shown in Tables 1.1 and 1.2 [12,13]. The high salinity of the produced water and the enrichment of certain ions (such as Ca^{2+} and Cl^-, etc.) impacts the corrosion behavior notably due to the complicated interactions between these ions and the materials.

Such corrosion concerns lead to the huge economic loss and impair the production efficiency. According to a NACE study [14], the total annual cost of corrosion in the oil and gas production industry is estimated to be \$1.372 billion, \$463 million of which is the downhole tubing expense. In this regard, new approaches should be made to prevent the tubular materials from being attacked, especially in highly corrosive SAGD operations. To date, several mainstream methods have received growing attentions, such as cathodic protection, corrosion inhibitors, corrosion resistant alloys (CRAs) and anti-corrosion coatings. CRAs, such as stainless steels and Ni-based alloys, usually exhibit great corrosion resistance, but their applications are considerably limited because of the high cost and the potential risk of suffering severe localized corrosion. The efficiency of corrosion inhibitors in SAGD operations is relatively low, and the caused contamination of oil productions is also a critical concern. For anti-corrosion coatings that efficiently provide a physical barrier to isolate the metal substrate from direct contact with corrosive medium, most of organic coatings cannot survive in HTHP environments of SAGD. Therefore, among all the candidate methods, a type of metallic coating, electroless Ni-P coating, outcompetes other methods owing to its excellent corrosion resistance, good mechanical properties and low cost, and extensive investigations have been conducted related to its corrosion performance and properties.

Table 1.1 Typical concentration range of species in the produced water in SAGD operations [12].

Species	Concentration range (ppm)
Calcium (Ca^{2+})	1–52
Magnesium (Mg^{2+})	1.6–14
Sodium (Na^{+})	130–3000

Chloride (Cl^-)	48–4800
Potassium (K^+)	14–240
Ammonia (NH_3)	11–64
Silica (SiO_2)	11–260
Alkalinity (as $CaCO_3$)	140–1400
Total organic carbon (TOC)	170–430

Table 1.2 Average produced gas compositions from a typical SAGD well in Athabasca [13].

Compound	Concentration (mol fraction %)
CH_4	40–70
CO_2	35–55
H_2S	1–15
N_2	<1.5
H_2	<1

1.2 Fundamentals of electroless Ni-P coating

Electroless Ni-P coating (hereinafter referred to as “Ni-P coating”) is an electrochemical method to deposit metallic nickel onto metal surfaces without electric current supply. It was first initiated by Wurtz in 1844, who discovered that nickel ions could be reduced to produce porous metallic nickel. A century later, Ni-P coating was first prepared successfully in laboratory by Brenner and Riddell [15].

As compared to iron, nickel displays a slower oxidation rate in the corrosive environment, which makes it more resistant to corrosion. However, since the volatile price of nickel in the global market significantly limits the massive applicability of Ni-based alloys, Ni-P coating, as a comparable alternative, has been widely used as protective coatings in many industrial fields because of its excellent corrosion resistance and mechanical properties and relatively low cost.

The mechanism of Ni-P coating formation has been studied systematically by many researchers. It is defined as a spontaneous reaction in which nickel ions are reduced and deposited on the metal surface with the assistance of the reducing agent. For Ni-P coating systems, hypophosphite bath is one of the most commonly used baths, and the overall reactions for Ni-P coating formation in the hypophosphite bath can be expressed as below [16]:

$$H_2PO_2{}^- + H_2O + Ni^{2+} \rightarrow H_2PO_3{}^- + 2H^+ + Ni \qquad \text{(Eq. 1.9)}$$

$$3H_2PO_2{}^- + 2H^+ \rightarrow H_2PO_3{}^- + 3H_2O + 2P \qquad \text{(Eq. 1.10)}$$

where Eq. 1.9 represents the reduction of nickel and Eq. 1.10 corresponds to the phosphorus reduction. Several reaction mechanisms have been proposed to elucidate the Ni-P coating deposition, such as atomic hydrogen mechanism [17], hydride transfer mechanism [18], electrochemical mechanism [15] and hydroxyl ion coordination mechanism [19], among which the atomic hydrogen mechanism is the most accepted one. It is believed that the actual nickel reductant in the plating bath is the atomic hydrogen which is produced by the reactions of the hypophosphite ion with water. According to this mechanism, the overall reactions can be divided into several separate reactions as follows:

$$H_2PO_2{}^- + H_2O \rightarrow H_2PO_3{}^- + 2H_{ads} \qquad \text{(Eq. 1.11)}$$

$$Ni^{2+} + 2H_{ads} \rightarrow Ni + 2H^+ \qquad \text{(Eq. 1.12)}$$

$$H_2PO_2{}^- + H_{ads} \rightarrow H_2O + OH^- + P \qquad \text{(Eq. 1.13)}$$

$$Ni^{2+} + HPO_3{}^{2-} \rightarrow NiHPO_3 \qquad \text{(Eq. 1.14)}$$

$$H_2PO_2^{-} + H_2O \rightarrow H^{+} + HPO_3^{2-} + H_2 \qquad \text{(Eq. 1.15)}$$

According to the schematic illustration in Figure 1.4 [20], Eqs. (1.11–1.13) correspond to the deposition process, where the adsorbed hydrogen atoms generate and reduce Ni^{2+} and $H_2PO_2^-$ to the elemental Ni and P. Besides, some side reactions also occur, leading to a lowered deposition efficiency and coating property. In Eq. 1.14, the formation of nickel orthophosphate results in the impoverishment of Ni^{2+} in the bath and a rougher coating surface [20]. Eq. 1.15 indicates the formation of hydrogen gas molecules instead of atomic hydrogen, which decreases the concentration of the reducing agent and more importantly, the presence of hydrogen gas "bubbles" in the coating leads to the formation of pinholes (named as "micropores") in the coating and greatly impairs the corrosion resistance.

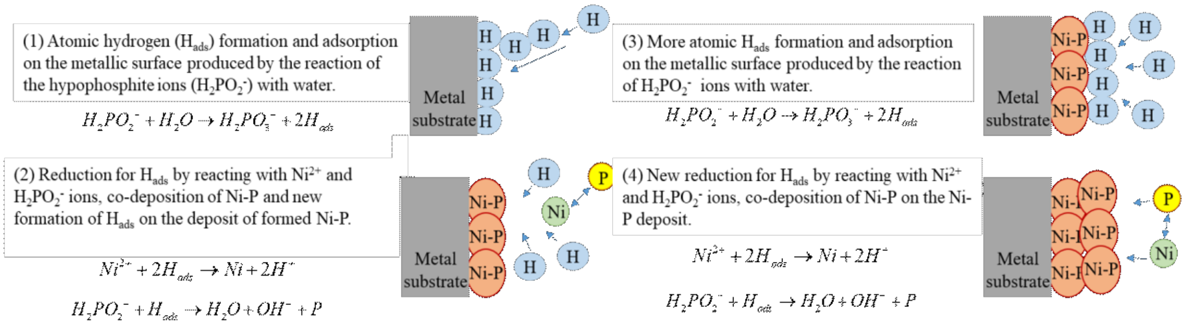
(1) Atomic hydrogen (H_{ads}) formation and adsorption on the metallic surface produced by the reaction of the hypophosphite ions ($H_2PO_2^-$) with water.

$H_2PO_2^- + H_2O \rightarrow H_2PO_3^- + 2H_{ads}$

(3) More atomic H_{ads} formation and adsorption on the metallic surface produced by the reaction of $H_2PO_2^-$ ions with water.

$H_2PO_2^- + H_2O \rightarrow H_2PO_3^- + 2H_{ads}$

(2) Reduction for H_{ads} by reacting with Ni^{2+} and $H_2PO_2^-$ ions, co-deposition of Ni-P and new formation of H_{ads} on the deposit of formed Ni-P.

$Ni^{2+} + 2H_{ads} \rightarrow Ni + 2H^+$

$H_2PO_2^- + H_{ads} \rightarrow H_2O + OH^- + P$

(4) New reduction for H_{ads} by reacting with Ni^{2+} and $H_2PO_2^-$ ions, co-deposition of Ni-P on the Ni-P deposit.

$Ni^{2+} + 2H_{ads} \rightarrow Ni + 2H^+$

$H_2PO_2^- + H_{ads} \rightarrow H_2O + OH^- + P$

Figure 1.4 Schematic illustration of electroless Ni-P coating deposition process [20].

Several key parameters, such as bath temperature, pH, bath composition and loading capacity, etc., affect the deposition rate and the elemental compositions in the coating, which directly reflect on the coating microstructure and properties. Generally, Ni-P coating can be classified into three categories based on the P content: low-P coating (1–4 wt.%) with crystalline microstructure, medium-P coating (5–8 wt.%) with mixed microstructure and high-P coating (9–12 wt.%) with amorphous microstructure [21]. High-P coating exhibits better resistance to corrosion attack in acidic environments because of less active sites of the amorphous microstructure in the absence of grain boundaries, while a multi-layered protective passive layer is formed on top of low-P and medium-P coatings in alkaline solutions and accounts for good corrosion protection [22].

1.3 Content of the thesis

There are totally 8 chapters in this thesis. Chapter 1 begins with a brief introduction of SAGD and corrosion problems in SAGD, and then presents the fundamentals of Ni-P coating. Chapter 2 reviews the previous literatures on the corrosion studies of Ni-P coating and the existing optimization methods for corrosion resistance enhancement. Chapter 3 introduces the employed experimental methodologies. Chapter 4 discusses the corrosion behavior and corrosion mechanism of Ni-P coating in $CO_2/H_2S/Cl^-$ environment. Chapter 5 reports the effect of Ca^{2+} on the HTHP corrosion behavior and corrosion film characteristics of N80 carbon steel and Ni-P coating in sweet brines. Chapter 6 describes the effects of Mo addition and heat treatment on the characterization and corrosion behavior of Ni-Mo-P/Ni-P coating in $CO_2/H_2S/Cl^-$ brine. Chapter 7 develops a smart Ni-P composite coating embedded with pH-responsive corrosion inhibitor-loaded nanocapsules and evaluates its improved corrosion resistance. Finally, the main conclusions and future prospects are summarized in Chapter 8.

To get a clearer image of the corrosion issues in SAGD environments, a failure analysis of underground carbon steel pipes in a water production well in Athabasca oil sands reservoir is conducted and presented in Appendix I.

1.4 References

[1] E.H. Herron, Heavy Oil: A solution to dwindling domestic oil supplies, Petroleum Equities Reports, 2000.

[2] R.M. Butler, G.S. McNab, H.Y. Lo, Theoretical studies on the gravity drainage of heavy oil during in-situ steam heating, Can. J. Chem. Eng. 59 (1981) 455–460.

[3] Oil sand development by the SAGD method,
https://www.japex.co.jp/english/business/ep_o/canada_oilsands.html

[4] R.A. Marriott, P. Pirzadeh, J.J. Marrugo-Hernandez, S. Raval, Hydrogen sulfide formation in oil and gas, Can. J. Chem. 94 (2016) 406–413.

[5] J.D.M. Belgrave, R.G. Moore, M.G. Ursenbach, Comprehensive kinetic models for the aquathermolysis of heavy oils, J. Can. Petrol. Technol. 36 (1997).

[6] H.F. Thimm, Dependence of some SAGD operations characteristics on steam zone pressure. In SPE/CIM Eighth One-Day Conference on Horizontal Well Technology, Society of Petroleum Engineers, 2001.

[7] J. Sun, C. Sun, G. Zhang, X. Li, W. Zhao, T. Jiang, H. Liu, X. Cheng, Y. Wang, Effect of O_2 and H_2S impurities on the corrosion behavior of X65 steel in water-saturated supercritical CO_2 system, Corros. Sci. 107 (2016) 31–40.

[8] S. Nesic, J. Postlethwaite, S. Olsen, An electrochemical model for prediction of corrosion of mild steel in aqueous carbon dioxide solutions, Corrosion 52 (1996) 280–294.

[9] Y. Zheng, J. Ning, B. Brown, S. Nešić, Electrochemical model of mild steel corrosion in a mixed H_2S/CO_2 aqueous environment in the absence of protective corrosion product layers, Corrosion 71 (2015) 316–325.

[10] S. Nesic, K.L.J. Lee, V. Ruzic, A mechanistic model of iron carbonate film growth and the effect on CO_2 corrosion of mild steel. In CORROSION 2002.

[11] B.F. Pots, S.D. Kapusta, R.C. John, M.J.J. Thomas, I.J. Rippon, T.S. Whitham, M. Girgis, Improvements on de Waard-Milliams corrosion prediction and applications to corrosion management. In CORROSION 2002.

[12] W.H. Goodman, M.R. Godfrey, T.M. Miller, N. Comany, Scale and deposit formation in steam assisted gravity drainage (SAGD) facilities. In International Water Conference 2010.

[13] T. Pehlke, Studies of aqueous hydrogen sulfide corrosion in producing SAGD wells. SPE Thermal Well Integrity and Design Symposium, 2017.

[14] M.R. Simons, Report of offshore technology conference (OTC) presentation. NACE International Oil and Gas Production, 2008.

[15] A. Brenner, Nickel plating on steel by chemical reduction, J. Res. NBS 37 (1946) 31–34.

[16] W. Riedel, Electroless nickel plating, ASM International, 1991.

[17] F.B. Mainier, M.M. Araujo, On the effect of the electroless nickel-phosphorus coating defects on the performance of this type of coating in oilfield environments, SPE Advanced Technology Series, 2(1994) 63–67.

[18] R.M. Lukes, The mechanism for the autocatalytic reduction of nickel by hypophosphite ion, Plating 51 (1964) 969.

[19] P. Cavallotti, G. Salvago, Studies on chemical reduction of nickel and cobalt by hypophosphite. Pt. 2. Characteristics of the process, Electrochim Metallorum 3 (1968) 239–266.

[20] F.B. Mainier, M.P.C. Fonseca, S.S. Tavares, J.M. Pardal, Quality of electroless Ni-P (nickel-phosphorus) coatings applied in oil production equipment with salinity, J. Mater. Sci. Chem. Eng. 1 (2013) 1–8.

[21] R. N. Duncan, The metallurgical structure of electroless nickel deposits: effect on coating properties, Plating Surf. Finish. 83 (1996) 65–69.

[22] A.A. Wronkowska, In situ and ex situ characterization of passive layers on $Ni_{1-x}P_x$ in alkaline solution, J. Electrochem. Soc. 140 (1993) 995.

2 Literature review on corrosion studies of electroless Ni-P coating

2.1 Corrosion behavior and mechanism of Ni-P coating in acidic environments

2.1.1 Effect of P content

The anti-corrosion properties of Ni-P coating have attracted much attention in the past few decades since it was successfully prepared, and extensive investigations suggest that the coating displays a better corrosion resistance than the carbon steel substrate, offering good protection by isolating the substrate from corrosive environments [1–10]. In general, elemental Ni in the coating reacts preferentially in acidic media, leading to the enrichment of P on the coating surface. As mentioned above, amorphous Ni-P coating with higher P content shows better corrosion resistance in acidic environments due to the absence of grain boundaries.

To date, a few anti-corrosion mechanisms have been proposed to explain the satisfactory corrosion resistance of Ni-P coating in acidic environments. First, the enriched P due to the preferential dissolution of nickel reacts with H_2O to form a layer of adsorbed $H_2PO_2^-$, which inhibits the further hydration of Ni by blocking the electrolyte transfer. This "chemical passivity" model was initiated by Diegle et al. [11], and their findings reported the enrichment of elemental P and the presence of $H_2PO_2^-$ ions from XPS results of Ni-P coating after anodic polarization in 0.2 N HCl solution. Authors claimed that elemental P may contribute to corrosion inhibition at lower anodic overpotentials, but the primary passivation role was ascribed to $H_2PO_2^-$ ions because of the beneficial effect on passivity by adding NaH_2PO_2 to the electrolyte. Similarly, the second model suggests the formation of P-rich film at the coating/solution, and the dissolution of Ni is controlled via the diffusion through this P-rich layer. The existence of the P-rich layer was confirmed by the Elsener group [12,13] and a current decay following a square root law with time was observed, indicating a diffusion-limited electrochemical process controlled by the P-rich layer. The third model states that the dissolution of amorphous alloys depends on the alloy constituent having a lower dissolution rate, therefore the anti-corrosion properties of Ni-P coating are attributed to the lower dissolution rate constant of P [14]. Fourth, the cathodic reaction rate is influenced by the P content because P has a much smaller exchange current density for hydrogen combination reaction than Ni. Therefore, the P-rich layer suppresses the cathodic reaction kinetics and slows down the anodic reaction. This mechanism was proposed by Zeller III and his colleagues [15]. Among these mechanisms, the "chemical passivity" model has gained the most popularity in recent years.

2.1.2 Effect of coating porosity

Except for the notable effect of P content on the corrosion performance of Ni-P coating, the coating porosity also plays an influential role. As mentioned above in Chapter 1, micropores are present inside Ni-P coating due to the hydrogen formation in the coating deposition process, which is inevitable for electroless plating. Once the micropores are formed, they allow the electrolyte penetration and form corrosion pathways, which causes coating degradation and loses protection for the substrate underneath. Research has shown that coatings with larger porosity exhibited higher corrosion current densities than those with smaller porosity [16,17]. Therefore, better control of coating porosity is beneficial to the corrosion resistance of Ni-P coating.

Based on the previous studies, the porosity of Ni-P coating can be adjusted by the following methods. First, an appropriate deposition rate can be maintained by adding stabilizers, which moderate the deposition process, to avoid the excess formation of micropores due to the fast reactions. Pb^{2+} and thiourea have been proved to be the effective stabilizers, and the coating obtained in the Pb^{2+}-containing bath showed a smoother surface with lower porosity and better corrosion resistance than that obtained in the bath containing thiourea [18]. Second, H^+ concentration can be controlled via the buffering agent in the coating bath to regulate the hydrogen gas formation and reduce the porosity of the coating. Ying et al. [19] investigated the effects of NH_4F as buffering agents on the porosity and corrosion resistance of Ni-P coating, and it was shown that the variation of pH value of the plating bath with NH_4F after 1 h coating was much lower than that without NH_4F, indicating a good buffering effect. This further led to a more uniform and homogenous coating surface and better corrosion performance. Similar buffering effects of $(NH_4)_2SO_4$ [20] and CH_3COONa [21] were also reported. Third, nanoparticles can be co-deposited with Ni-P coating and fill in the micropores to form less porous coatings. Figure 2.1 shows the schematic illustration of corrosion paths in Ni-P coatings before and after adding dispersed diamond particles (DNP) [22]. Nanoparticles fill the vacancies of the coating and block the corrosion paths, thereby effectively hindering the electrolyte penetration. As compared to the first two methods that modify coating bath recipes, the incorporation of nanoparticles gains most popularity due to its simpler applicability and multiple functions brought by the introduced nanoparticles. More systematic explanations and previous studies will be included in Chapter 2.2.

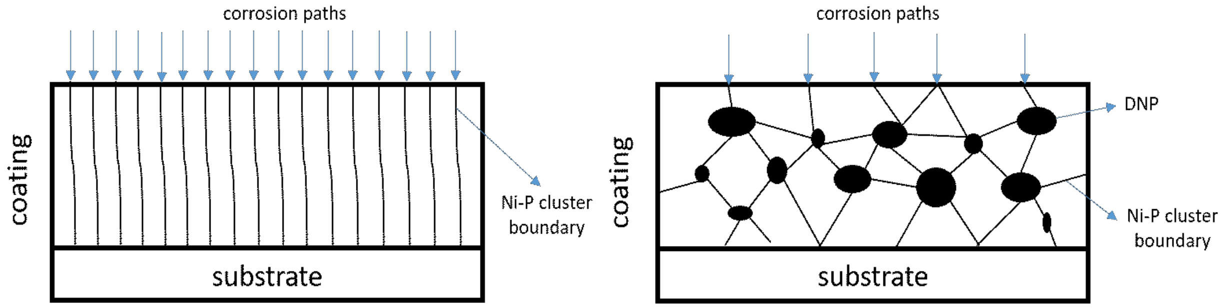

Figure 2.1 Schematic of corrosion paths in Ni-P coating and Ni-P-DNP coating (Figure reproduced from ref [22]).

2.1.3 Effect of environmental factors

The corrosion of Ni-P coating also highly relies on the environmental factors, such as corrosion medium and service time, etc., the variation of which may lead to huge difference in corrosion rates and mechanism. Although extensive studies suggest the good corrosion resistance of Ni-P coating in common acids (e.g., HCl and H_2SO_4 solutions) [7,8,23,24], limited research has been conducted in CO_2/H_2S-containing environments. Xu et al. [25] studied the corrosion behavior of Ni-P coated 20# carbon steel in H_2S (1 psi)/Cl^- environment at 0.07 MPa and 80 °C, and demonstrated that its corrosion resistance outcompeted 316L stainless steel without further explaining the reason for the improved corrosion resistance. The corrosion and degradation of Ni-P coating in CO_2-saturated NaCl solution were investigated, and authors claimed that corrosion occurred at the micropores and extended towards the inside of coating after 6 d of immersion, but coating disbondment was not observed [26]. Recently, Sun et al. [27] reported the effects of CO_2 and/or H_2S on the corrosion behavior of Ni-P coating at HTHP, and proposed that the coexistence of two dissolved gases caused a CO_2-enhanced H_2S corrosion effect, synergistically accelerating corrosion and changing the corrosion film characteristics.

The anti-corrosion performance of Ni-P coating weakens after long-term service because of the gradual penetration of corrosive electrolyte through the micropores. Wang et al. [28] demonstrated that corrosion pits formed on the Ni-P coating surface after immersion in NaCl solution for 1 month, while severe coating disbondment was observed after 10 d exposure in CO_2/H_2S-saturated NaCl solution [29]. A case study showing the failure of Ni-P coated slotted liner in a SAGD production well can interpret the long-term coating stability in $CO_2/H_2S/Cl^-$ environment clearly. As shown in Figure 2.2, a thick layer of corrosion product composed by Ni and S is formed above the damaged coating after 18 months of service. Besides, the presence of a double-layered corrosion product (Ni-Fe-S layer close to coating and Fe-O layer near the substrate) between coating and carbon steel substrate indicates the full penetration of aggressive medium and the substrate degradation accordingly.

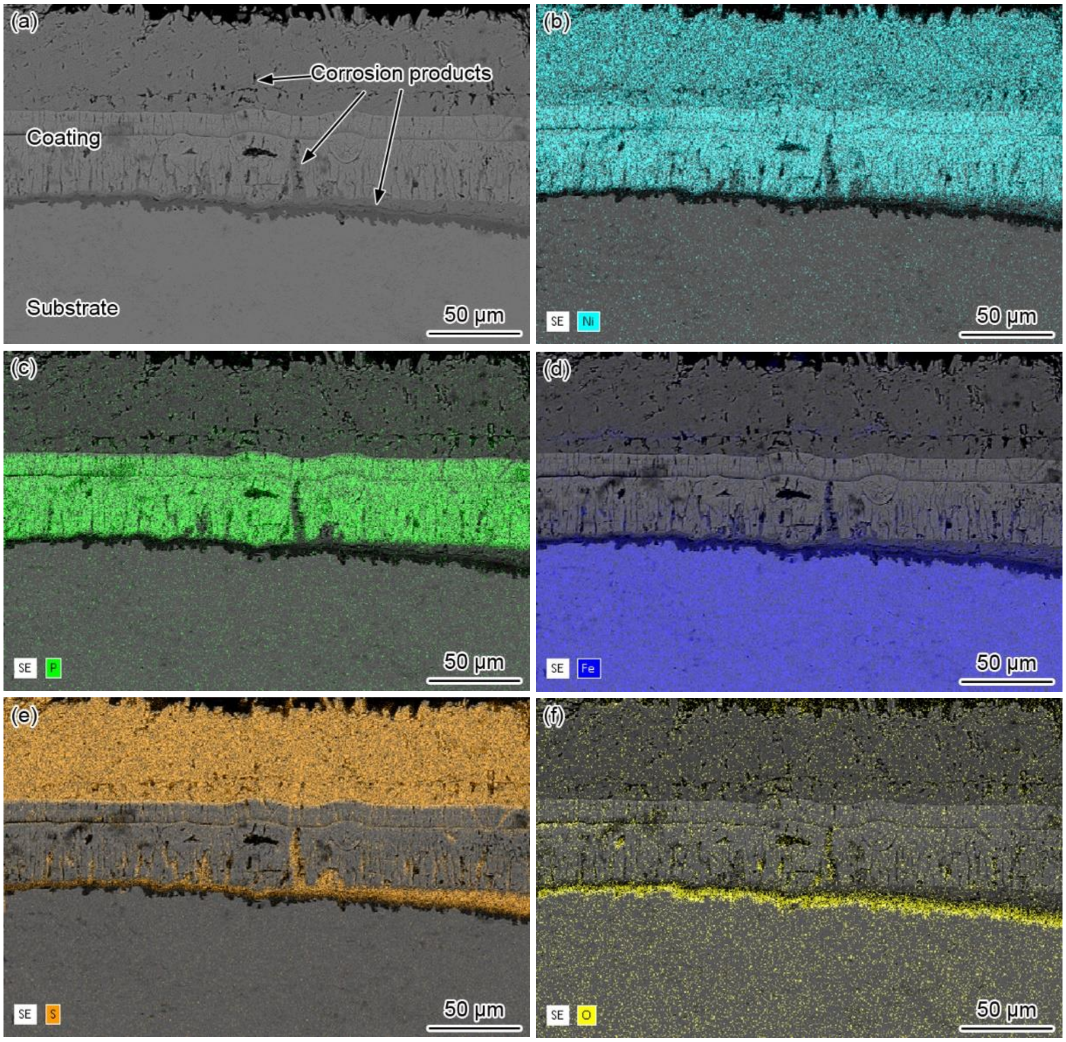

Figure 2.2 (a) SEM cross-sectional backscattered electron image and (b–f) the corresponding elemental distributions of (b) Ni, (c) P, (d) Fe, (e) S and (f) O of the slotted liner with Ni-P coating after 18 months of service in the production well of SAGD system containing CO_2, H_2S and Cl^- [29].

2.2 Optimization methods of Ni-P coating for corrosion resistance enhancement

From the abovementioned literatures and case study, even though Ni-P coating shows excellent corrosion resistance, it still suffers severe corrosion in some harsh environments. Therefore, it is highly desirable to optimize Ni-P coating and acquire better anti-corrosion performance. Three mainstream methods are introduced in this chapter: heat treatment, co-deposition with alloying elements and nanoparticle incorporation.

2.2.1 Heat treatment

It is generally known that the mechanical properties of Ni-P coating, such as microhardness and wear resistance, can be improved by heat treatment, which is attributed to the formation of fine Ni crystallites and hard intermetallic Ni_3P phase precipitated during the crystallization of the amorphous phase above 300 °C [30]. Meanwhile, the enhanced corrosion resistance caused by heat treatment was reported as well. Ashassi-Sorkhabi et al. [1] reported that the heat treatment at 400 °C for 1 h significantly decreased the i_{corr} values of high-P coating in aerated 3.5% NaCl solution, while medium-P coating experienced intergranular corrosion. Rabizadeh et al. [31] accredited the enhanced corrosion resistance of heat-treated low-P Ni-P coating to the reduced grain boundaries because of the grain growth of crystalline Ni. In addition, NiO tends to form on the coating surface upon annealing at elevated temperatures and acts as a passivation layer to inhibit corrosion [32,33].

2.2.2 Co-deposition with alloying elements

Considerable amount of work has been conducted in the development of Ni-P coating by co-depositing one or more alloying elements to further enhance the coating properties. Metals, such as cobalt [34], molybdenum [35,36], tungsten [37,38], copper [38,39], zinc [40], tin [41], can be deposited in Ni-P matrix. The findings of Gao et al. [34] indicated that the enhancement of corrosion resistance of Ni-P deposit reached the maximum when Co content was 8.3 wt.%, above which the structure of Ni-P deposits changed from amorphous to mix-crystal. Lu et al. [42] compared the corrosion resistance of ternary Ni-P based coatings by the addition of Mo and W, and suggested that added W slightly improved the corrosion resistance, whereas the Mo addition had no obvious beneficial effect on the anti-corrosion performance. However, opposite conclusions were made by Song et al. [43], who claimed that Ni-Mo-P displayed better corrosion resistance due to its compact surface and low porosity. Cu element led to the enrichment of P and hindered the further dissolution and diffusion of Ni^{2+}, thereby enhancing the corrosion resistance of Ni-Cu-P coating [44]. Moreover, some quaternary Ni-P composite coatings were also developed [38, 45]. These results demonstrate the great potential of alloying elements as the promising approaches to enhance the coating properties, despite controversies in the contributions of alloying elements on the corrosion resistance improvement and limited explanations of the anti-corrosion mechanism.

2.2.3 The incorporation of nano-scale components

As stated above, the anti-corrosion ability of Ni-P coating diminishes after long-term service because of the gradual penetration of corrosive electrolyte through the micropores in the amorphous coating. Such imperfection can be mitigated to some extent by the addition of inorganic nanoparticles by filling in the micropores and blocking the electrolyte penetration. Ni-P-TiO_2 nanocomposite coating had superior corrosion resistance in 3.5 wt.% NaCl solution as compared to Ni-P coating due to the co-deposition of TiO_2 nanoparticles [46]. The anticorrosion property and passivity were improved in the CeO_2-containing coating due to its less liability to undergo local-cell corrosion at the nodule boundaries than its CeO_2-free counterpart. During the co-deposition process, Ce^{n+} (n=3, 4) ions may be adsorbed to the metal/solution interface, hindering the crystal-typed deposition of Ni and promoting P deposition [47]. In a recent study, the ZrO_2-containing Ni-W-P composite coating showed excellent resistance to CO_2/H_2S corrosion [48]. Some other nanoparticles, such as WC [49], SiC [50], WS_2 [51], Fe_3O_4 [52], Al_2O_3 [53], TiC [54], etc., were also reported as the promising materials to be incorporated into Ni-P composite coating.

In addition, some organic components, such as carbon nanotubes (CNT) [55], polytetrafluoroethylene (PTFE) [56], reduced graphene oxide (rGO) [57], etc., also exhibit good compatibility with Ni-P coating, and their incorporation promotes the mechanical and tribological properties and corrosion resistance. The good compatibility between organic components and Ni-P coating offers the possibilities for various functional additives to be incorporated to endow with specific functionality. From this perspective, nano-scale capsules loaded with corrosion inhibitors can be considered as an encouraging material that is suitable to be incorporated into Ni-P coating to achieve an enhanced anti-corrosion performance for longer lifespans.

The method of nano-/micro-encapsulation refers to the techniques that allow the entrapment of active species (core material) inside the nanocapsules (shell material), and has attracted growing interests recently due to the isolation of core materials from the surroundings and the controllable release upon meeting certain triggering criteria, such as pH value, temperature, mechanical damage, ion concentration, etc. [58–61]. The core materials can be self-healing agents, lubricants and corrosion inhibitors, etc. A schematic example of self-healing effect of microcapsules-contained coatings is shown in Figure 2.3 [62]. The healing agent is trapped in the microcapsules without external stimulus and can be released from the ruptured microcapsules when triggered, thereby healing the cracks automatically with or without chemical reactions.

So far, most research on the incorporation of nanocapsules has focused on organic coatings with micro-scale thicknesses by direct mixing, while very limited findings have been reported for metallic coatings, especially thin electroless Ni-P coating. Stankiewicz et al. [63] developed an electroless Ni-P/alginate microgels coating, and it was proven that the reduction of Ni^{2+} ions released from the microgels occurred on the steel and Ni-P coating surface, which displayed a self-healing effect of the composite coating. Xie et al. [64] reported the synthesis of NaF-loaded mesoporous silica nanocontainers (MSNs) and its incorporation into Ni-P coating. The release of F^- ions from the nanocontainers facilitated the formation of a protective MgF_2 film and enhanced the corrosion resistance of Ni-P coated Mg alloys.

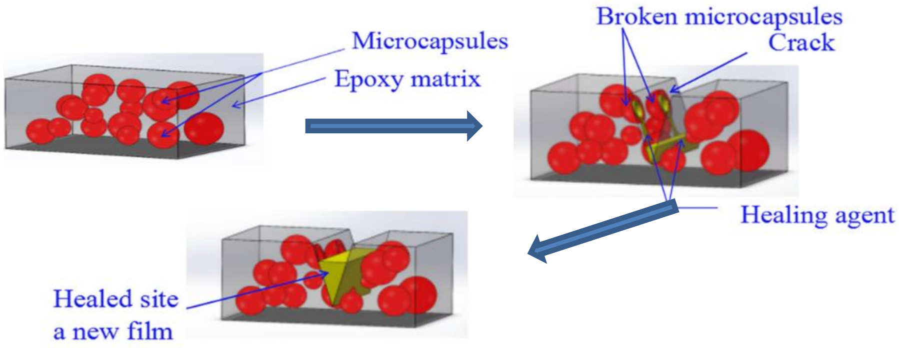

Figure 2.3 Schematic diagram of self-healing mechanism (Figure reproduced from ref [62]).

2.3 Current status and remaining challenges

Despite extensive studies on the corrosion behavior of Ni-P coating, there are still some controversies about the anti-corrosion mechanism under debate. The well-accepted "chemical passivity" model only discussed the enhanced corrosion protection in a very short time period (less than 1 h), therefore the stability of the adsorbed $H_2PO_2^-$ layer needs to be investigated. Furthermore, this model claimed that the "oxide passivity" observed on pure nickel could be ruled out due to the non-existence of nickel oxide. However, the formation of nickel oxide and nickel hydroxide was clearly detected as corrosion time proceeded according to our studies, and the ratio of two components significantly impacted the anti-corrosion performance [27,29]. Therefore, the true anti-corrosion mechanism of Ni-P coating and the effect of corrosion film on the enhanced corrosion resistance need to be elucidated. In addition, unlike common acids, H_2S serves as the cathodic depolarizer and shows a high chemical affinity to Ni, thereby accelerating corrosion [65,66]. However, limited research has paid attention to the synergy of CO_2 and H_2S in the corrosion of Ni-P coating. Furthermore, even though Ni-P coating has started to serve as downhole tubing materials in some reservoirs, corrosion studies of Ni-P coating under HTHP conditions are still lacking. In addition, the effect of Ca^{2+}, as a scaling-promoting element, on the corrosion of carbon steels has been still in debate, and no research has been reported in regards to the role of Ca^{2+} in the corrosion behavior and corrosion film characteristics of Ni-P coating in HTHP environments. Therefore, related studies will provide technical guidance to substantiate the applicability of Ni-P coating in Ca^{2+}-containing SAGD operations.

For the optimization of Ni-P coating in terms of corrosion protection, most of the published findings have reported the good corrosion resistance without further elaborating the origin of the enhanced performance, and none of these developments is specifically focused on the corrosion resistance improvement in the presence of H_2S. From this perspective, efficient optimization approaches should be made to enhance the anti-H_2S corrosion performance of Ni-P coating and the anti-corrosion mechanism needs further exploration. In this work, Mo was selected as the alloying element because it has been well-accepted to show good anti-H_2S corrosion performance in stainless steels and Ni-based alloys, but none of similar studies has been reported to Ni-P coating.

Moreover, inspired by the various properties brought by the incorporated functionalized nanocontainers in organic coating systems, the development of new smart Ni-P coatings with adjustable functionalities needs to be further pursued due to the growing applications of Ni-P coating under more complicated service conditions. However, there have been very limited published reports on the controllable anti-corrosion performance of Ni-P coating so far.

2.4 Research objectives

Based on the current status and remaining challenges of this topic, the research objectives of the thesis are as follows:

1) To elucidate the corrosion behavior and mechanism of Ni-P coating in brines containing CO_2/H_2S and study the promotion effect of H_2S on the CO_2 corrosion of Ni-P coating.
2) To demonstrate the effect of Ca^{2+} ions on the corrosion behavior and corrosion film characteristics of N80 carbon steel and Ni-P coating under HTHP conditions.
3) To optimize Ni-P coating by Mo addition and heat treatment and to investigate their roles in the corrosion resistance improvement of Ni-P composite coating in H_2S-containing aqueous environment.
4) To develop a smart Ni-P composite coating incorporated with corrosion inhibitor-loaded nanocapsules that exhibits superior and controllable corrosion resistance.

2.5 References

[1] H. Ashassi-Sorkhabi, S.H. Rafizadeh, Effect of coating time and heat treatment on structures and corrosion characteristics of electroless Ni–P alloy deposits, Surf. Coat. Technol. 176 (2004) 318–326.

[2] S.Q. Guo, L.F. Hou, C.L. Guo, Y.H. Wei, Characteristics and corrosion behavior of nickel-phosphorus coatings deposited by a simplified bath, Mater. Corros. 68 (2017) 468–475.

[3] T.S. Narayanan, I. Baskaran, K. Krishnaveni, S. Parthiban, Deposition of electroless Ni–P graded coatings and evaluation of their corrosion resistance, Surf. Coat. Technol. 200 (2006) 3438–3445.

[4] J. Balaraju, T.S. Narayanan, S. Seshadri, Evaluation of the corrosion resistance of electroless Ni-P and Ni-P composite coatings by electrochemical impedance spectroscopy, J. Solid State Electrochem. 5 (2001) 334–338.

[5] C. Gu, J. Lian, G. Li, L. Niu, Z. Jiang, High corrosion-resistant Ni–P/Ni/Ni–P multilayer coatings on steel. Surf. Coat. Technol. 197 (2005) 61–67.

[6] H. Luo, X. Wang, S. Gao, C. Dong, X. Li, Synthesis of a duplex Ni-P-YSZ/Ni-P nano composite coating and investigation of its performance, Surf. Coat. Technol. 311 (2017) 70–79.

[7] F.B. Mainier, M.P.C. Fonseca, S.S. Tavares, J.M. Pardal, Quality of electroless Ni-P (nickel-phosphorus) coatings applied in oil production equipment with salinity, J. Mater. Sci. Chem. Eng. 1 (2013) 1–8.

[8] F.B. Mainier, M.M. Araujo, On the effect of the electroless nickel-phosphorus coating defects on the performance of this type of coating in oilfield environments, SPE Advanced Technology Series, 2 (1994) 63–67.

[9] N. El Mahallawy, A. Bakkar, M. Shoeib, H. Palkowski, V. Neubert, Electroless Ni–P coating of different magnesium alloys, Surf. Coat. Technol. 202 (2008) 5151–5157.

[10] Y.W. Song, D.Y. Shan, E.H. Han, Corrosion behaviors of electroless plating Ni–P coatings deposited on magnesium alloys in artificial sweat solution, Electrochim. Acta 53 (2007) 2009–2015.

[11] R.B. Diegle, N.R. Sorensen, C.R. Clayton, M.A. Helfand, Y.C. Yu, An XPS investigation into the passivity of an amorphous Ni-20P alloy, J. Electrochem. Soc. 135 (1988) 1085.

[12] B. Elsener, M. Crobu, M.A. Scorciapino, A. Rossi, Electroless deposited Ni–P alloys: corrosion resistance mechanism, J. of Appl. Electrochem. 38 (2008) 1053.

[13] M. Crobu, A. Scorciapino, B. Elsener, A. Rossi, The corrosion resistance of electroless deposited nano-crystalline Ni–P alloys, Electrochim. Acta 53 (2008) 3364–3370.

[14] H. Habazaki, S.Q. Ding, A. Kawashima, K. Asami, K. Hashimoto, A. Inoue, T. Masumoto, The anodic behavior of amorphous Ni-19P alloys in different amorphous states, Corros. Sci. 29 (1989) 1319–1328.

[15] R.L. Zeller III, Electrochemical corrosion testing of high phosphorus electroless nickel in 5% NaCl, Corrosion 47 (1991) 692–702.

[16] F.C. Walsh, C.P. de León, C. Kerr, S. Court, B.D. Barker, Electrochemical characterisation of the porosity and corrosion resistance of electrochemically deposited metal coatings, Surf. Coat. Technol. 202 (2008) 5092–5102.

[17] Y. Xu, Y. Zhou, T. Luan, Electrochemical characterization and evaluation of electroless coating porosity, J. Funct. Mater. 44 (2013) 902–910.

[18] A.R. Rahimi, H. Modarres, M. Abdouss, Study on morphology and corrosion resistance of electroless Ni–P coatings, Surf. Eng. 25 (2009) 367–371.

[19] H.G. Ying, M. Yan, T.Y. Ma, J.M. Wu, L.Q. Yu, Effects of NH_4F on the deposition rate and buffering capability of electroless Ni–P plating solution, Surf. Coat. Technol. 202 (2007) 217–221.

[20] Z. Xie, G. Yu, B. Hu, X. Lei, T. Li, J. Zhang, Effects of $(NH_4)_2SO_4$ on the characteristics of the deposits and properties of an electroless Ni–P plating solution, Appl. Surf. Sci. 257 (2011) 5025–5031.

[21] Y. Jin, H. Yu, D. Yang, D. Sun, Effects of complexing agents on acidic electroless nickel deposition, Rare Met. 29 (2010) 401–406.

[22] H. Ashassi-Sorkhabi, M. Es'haghi, Corrosion resistance enhancement of electroless Ni–P coating by incorporation of ultrasonically dispersed diamond nanoparticles, Corros. Sci. 77 (2013) 185–193.

[23] S.R. Allahkaram, M.H. Nazari, S. Mamaghani, A. Zarebidaki, Characterization and corrosion behavior of electroless Ni–P/nano-SiC coating inside the CO_2 containing media in the presence of acetic acid, Mater. Des. 32 (2011) 750–755.

[24] B. Zhou, L. Kong, L. Niu, J. Lian, G. Li, Effects of passivation on the properties of Ni-P alloy coating deposited on CFs reinforced PEEK. Surf. Coat. Technol. 232 (2013) 269–274.

[25] X. Xiu-qing, M. Jian, B. Zhen-quan, F. Yao-rong, M. Qiu-rong, Z. Wen-zhen, The corrosion behavior of electroless Ni–P coating in Cl^{-}/H_2S environment. Appl. Surf. Sci. 258 (2012) 8802–8806.

[26] C. Sun, J. Li, S. Shuang, H. Zeng, J.L. Luo, Effect of defect on corrosion behavior of electroless Ni-P coating in CO_2-saturated NaCl solution, Corros. Sci. 134 (2018) 23–37.

[27] C. Sun, H. Zeng, J.L. Luo, Unraveling the effects of CO_2 and H_2S on the corrosion behavior of electroless Ni-P coating in $CO_2/H_2S/Cl^{-}$ environments at high temperature and high pressure, Corros. Sci. 148 (2019) 317–330.

[28] L.L. Wang, H.L. Chen, L. Hao, A. Lin, F.X. Gan, Electrochemical corrosion behavior of electroless Ni-P coating in NaCl and H_2SO_4 solutions, Mater. Corros. 62 (2011) 1003–1007.

[29] J. Li, C. Sun, H. Zeng, J.L. Luo, Insights into the electrochemical corrosion behavior and mechanism of electroless Ni-P coating in the $CO_2/H_2S/Cl^{-}$ environment, Corrosion 76 (2020) 578–590.

[30] M. Yan, H.G. Ying, T.Y. Ma, Improved microhardness and wear resistance of the as-deposited electroless Ni–P coating, Surf. Coat. Technol. 202 (2008) 5909–5913.

[31] T. Rabizadeh, S.R. Allahkaram, A. Zarebidaki, An investigation on effects of heat treatment on corrosion properties of Ni–P electroless nano-coatings, Mater. Des. 31 (2010) 3174–3179.

[32] M. Sribalaji, P. Arunkumar, K.S. Babu, A.K. Keshri, Crystallization mechanism and corrosion property of electroless nickel phosphorus coating during intermediate temperature oxidation, Appl. Surf. Sci. 355 (2015) 112–120.

[33] M.A. Shoeib, M.M. Kamel, S.M. Rashwan, O.M. Hafez, Corrosion behavior of electroless Ni–P/TiO_2 nanocomposite coatings, Surf. Interface Anal. 47 (2015) 672–680.

[34] Y. Gao, L. Huang, Z.J. Zheng, H. Li, M. Zhu, The influence of cobalt on the corrosion resistance and electromagnetic shielding of electroless Ni–Co–P deposits on Al substrate, Appl. Surf. Sci. 253 (2007) 9470–9475.

[35] H. Liu, Z. Liu, Evaluation of microstructures and properties of laser-annealed electroless Ni–P/Ni–Mo–P duplex coatings, Surf. Coat. Technol. 330 (2017) 270–276.

[36] A.E. Fetohi, R.A. Hameed, K.M. El-Khatib, Ni–P and Ni–Mo–P modified aluminium alloy 6061 as bipolar plate material for proton exchange membrane fuel cells, J. Power Sources 240 (2013) 589–597.

[37] H. Liu, R.-X. Guo, Y. Zong, B.-Q. He, Z. Liu, Comparative study of microstructure and corrosion resistance of electroless Ni-W-P coatings treated by laser and furnace-annealing, Trans. Nonferrous Met. Soc. China 20 (2012) 1024–1031.

[38] J.N. Balaraju, K.S. Rajam, Electroless deposition of Ni–Cu–P, Ni–W–P and Ni–W–Cu–P alloys, Surf. Coat. Technol. 195 (2005) 154–161.

[39] Y. Liu, Q. Zhao, Study of electroless Ni–Cu–P coatings and their anti-corrosion properties, Appl. Surf. Sci. 228 (2004) 57–62.

[40] S. Ranganatha, T.V. Venkatesha, K. Vathsala, Development of electroless Ni–Zn–P/nano-TiO_2 composite coatings and their properties, Appl. Surf. Sci. 256 (2010) 7377–7383.

[41] W.X. Zhang, Z.H. Jiang, G.Y. Li, Q. Jiang, J.S. Lian, Electroless Ni–Sn–P coating on AZ91D magnesium alloy and its corrosion resistance, Surf. Coat. Technol. 202 (2008) 2570–2576.

[42] G. Lu, G. Zangari, Corrosion resistance of ternary Ni–P based alloys in sulfuric acid solutions, Electrochim. Acta 47 (2002) 2969–2979.

[43] G.S. Song, S. Sun, Z.C. Wang, C.Z. Luo, C.X. Pan, Synthesis and characterization of electroless Ni–P/Ni–Mo–P duplex coating with different thickness combinations, Acta Metall. Sin. (Engl. Lett.) 30 (2017) 1008–1016.

[44] G. Liu, L. Yang, L. Wang, S. Wang, L. Chongyang, J. Wang, Corrosion behavior of electroless deposited Ni–Cu–P coating in flue gas condensate, Surf. Coat. Technol. 204 (2010) 3382–3386.

[45] J.N. Balaraju, V.E. Selvi, V.K.W. Grips, K.S. Rajam, Electrochemical studies on electroless ternary and quaternary Ni–P based alloys, Electrochim. Acta 52 (2006) 1064–1074.

[46] M. Momenzadeh, S. Sanjabi, The effect of TiO_2 nanoparticle codeposition on microstructure and corrosion resistance of electroless Ni–P coating, Mater. Corros. 63 (2012) 614–619.

[47] H. Jin, S. Jiang, L. Zhang, Structural characterization and corrosive property of Ni-P/CeO_2 composite coating, J. Rare Earths 27 (2009) 109–113.

[48] H. Luo, M. Leitch, H. Zeng, J.-L. Luo, Characterization of microstructure and properties of electroless duplex Ni-W-P/Ni-P nano-ZrO_2 composite coating, Mater. Today Phys. 4 (2018) 36–42.

[49] H. Luo, M. Leitch, Y. Behnamian, Y. Ma, H. Zeng, J.L. Luo, Development of electroless Ni–P/nano-WC composite coatings and investigation on its properties, Surf. Coat. Technol. 277 (2015) 99–106.

[50] S. Zhang, K. Han, L. Cheng, The effect of SiC particles added in electroless Ni–P plating solution on the properties of composite coatings, Surf. Coat. Technol. 202 (2008) 2807–2812.

[51] S. Ranganatha, T.V. Venkatesha, K. Vathsala, Electroless Ni–W–P coating and its nano-WS_2 composite: preparation and properties, Ind. Eng. Chem. Res. 51 (2012) 7932–7940.

[52] A.A. Zuleta, O.A. Galvis, J.G. Castaño, F.Echeverría, F.J. Bolivar, M.P.Hierro, F.J. Pérez-Trujillo, Preparation and characterization of electroless Ni–P–Fe_3O_4 composite coatings and evaluation of its high temperature oxidation behaviour, Surf. Coat. Technol. 203 (2009) 3569–3578.

[53] J.N. Balaraju, Kalavati, K.S. Rajam, Influence of particle size on the microstructure, hardness and corrosion resistance of electroless Ni–P–Al_2O_3 composite coatings, Surf. Coat. Technol. 200 (2006) 3933–3941.

[54] S. Afroukhteh, C. Dehghanian, M. Emamy, Preparation of the Ni–P composite coating co-deposited by nano TiC particles and evaluation of it's corrosion property, Appl. Surf. Sci. 258 (2012) 2597–2601.

[55] M. Alishahi, S.M. Monirvaghefi, A. Saatchi, S.M. Hosseini, The effect of carbon nanotubes on the corrosion and tribological behavior of electroless Ni–P–CNT composite coating, Appl. Surf. Sci. 258 (2012) 2439–2446.

[56] I.R. Mafi, C. Dehghanian, Comparison of the coating properties and corrosion rates in electroless Ni–P/PTFE composites prepared by different types of surfactants, Appl. Surf. Sci. 257 (2011) 8653–8658.

[57] T.R. Tamilarasan, U. Sanjith, M.S. Shankar, G. Rajagopal, Effect of reduced graphene oxide (rGO) on corrosion and erosion-corrosion behaviour of electroless Ni-P coatings, Wear 390 (2017) 385–391.

[58] F. Maia, K.A. Yasakau, J. Carneiro, S. Kallip, J. Tedim, T. Henriques, A. Cabral, J. Venâncio, M.L. Zheludkevich, M.G.S. Ferreira, Corrosion protection of AA2024 by sol–gel coatings modified with MBT-loaded polyurea microcapsules, Chem. Eng. J. 283 (2016) 1108–1117.

[59] Z. Zheng, M. Schenderlein, X. Huang, N.J. Brownbill, F. Blanc, D. Shchukin, Influence of functionalization of nanocontainers on self-healing anticorrosive coatings, ACS Appl. Mater. Interfaces 7 (2015) 22756–22766.

[60] C. Kim, A.I. Karayan, J. Milla, M. Hassan, H. Castaneda, Smart Coating Embedded with pH-Responsive Nanocapsules Containing a Corrosion Inhibiting Agent, ACS Appl. Mater. Interfaces 12 (2020) 6451–6459.

[61] J. Fu, T. Chen, M. Wang, N. Yang, S. Li, Y. Wang, X.Liu, Acid and alkaline dual stimuli-responsive mechanized hollow mesoporous silica nanoparticles as smart nanocontainers for intelligent anticorrosion coatings, ACS Nano 7 (2013) 11397–11408.

[62] H. Li, Y. Cui, H. Wang, Y. Zhu, B. Wang, Preparation and application of polysulfone microcapsules containing tung oil in self-healing and self-lubricating epoxy coating, Colloids Surf. A Physicochem. Eng. Asp. 518 (2017) 181–187.

[63] A. Stankiewicz, Z. Kefallinou, G. Mordarski, Z. Jagoda, B. Spencer, Surface functionalisation by the introduction of self-healing properties into electroless Ni-P coatings, Electrochim. Acta 297 (2019) 427–434.

[64] Z.H. Xie, D. Li, Z. Skeete, A. Sharma, C.J. Zhong, Nanocontainer-enhanced self-healing for corrosion-resistant Ni coating on Mg alloy, ACS Appl. Mater. Interfaces 9 (2017) 36247–36260.

[65] Z.F. Yin, W.Z. Zhao, W.Y. Lai, X.H. Zhao, Electrochemical behaviour of Ni-base alloys exposed under oil/gas field environments, Corros. Sci. 51 (2009) 1702–1706.

[66] J.M. Hernandez, D.H. Lim, H.V.P. Nguyen, S.P. Yoon, J. Han, S.W. Nam, C.W. Yoon, S.K. Kim, H.C. Ham, Decomposition of hydrogen sulfide (H_2S) on Ni (100) and Ni_3Al (100) surfaces from first-principles, Int. J. Hydrog. Energy 39 (2014) 12251–12258.

3 Methodologies

3.1 Coating fabrication and material synthesis

3.1.1 Fabrication of as-deposited electroless Ni-P coating

In this work, tubing steels, such as L80 steel and N80 steel, with the size of 1 cm × 1 cm × 1 cm, were used as the substrate for electroless Ni-P coating. The chemical compositions of these two steels are listed in Table 3.1. The substrates were first ground sequentially to 1200 grit with SiC sandpapers, cleaned with deionized water and alcohol, and then dried in flowing air. Prior to electroless plating, the samples were degreased in the solution consisting of 3 wt.% sodium carbonate (Na_2CO_3) + 3 wt.% sodium hydroxide (NaOH) for 20 min at 60 °C and then pickled in 10 wt.% hydrochloric acid (HCl) solution for 50 s for surface activation. After the treatment, the samples were dipped in the plating bath at (85±1) °C and at a stirring rate of 200 rpm. The chemical composition of the plating bath is listed in Table 3.2. A loading capacity of 1 dm^2/L was maintained, and the pH value of the coating bath was adjusted to 5.5–6 by adding NaOH. The total plating time is 2 h. After the coating process, all coated samples were cleaned with alcohol by ultrasonic dispersion and dried in flowing air for further testing.

Table 3.1 Chemical compositions (wt.%) of L80 carbon steel and N80 carbon steel.

Material	C	Mn	Si	Cr	Cu	Ni	P	S	Fe
L80 steel	0.32	0.80	0.25	-	0.12	0.016	0.006	0.028	98.46
N80 steel	0.29	1.38	0.25	0.037	0.009	0.002	0.002	0.002	98.028

Table 3.2 Chemical compositions of electroless Ni-P plating bath.

Reagent	Concentration
Nickel sulphate ($NiSO_4 \cdot 6H_2O$)	25 g/L
Sodium hypophosphite ($NaH_2PO_2 \cdot H_2O$)	30 g/L
Lactic acid ($C_3H_6O_3$)	20 mL/L
Citric acid ($C_6H_8O_7$)	19 g/L
Succinic acid ($C_4H_6O_4$)	14 g/L
Saccharin Sodium ($C_6H_4SO_2NNaCO \cdot 2H_2O$)	0.06-0.08 g/L
Sodium dodecyl sulfate (SDS, $C_{12}H_{25}SO_4Na$)	0.04 g/L
Lead nitrate ($Pb(NO_3)_2$)	1 mg/L

3.1.2 Fabrication of as-deposited and heat-treated electroless Ni-Mo-P/Ni-P coating

The fabrication procedure of the as-deposited Ni-Mo-P/Ni-P coating contains two steps: 1 h of Ni-P coating and 1 h of Ni-Mo-P coating. The chemical compositions of Ni-P and Ni-Mo-P coating bath are listed in Tables 3.2 and 3.3, respectively. The entire procedure follows the one described in 3.1.1. Then, the coated samples were heated in a furnace under air flow condition at 400 °C for 2 h at a heating rate of 5 °C/min, followed by furnace cooling under air flow condition.

Table 3.3 Chemical compositions of electroless Ni-Mo-P plating bath.

Reagent	Concentration
Nickel sulphate ($NiSO_4 \cdot 6H_2O$)	20 g/L
Sodium hypophosphite ($NaH_2PO_2 \cdot H_2O$)	40 g/L
Sodium molybdate ($Na_2MoO_4 \cdot 2H_2O$)	5 g/L
Citric acid ($C_6H_8O_7$)	10 g/L

Sodium citrate ($Na_3C_6H_5O_7$)	20 g/L
Ammonium chloride (NH_4Cl)	15 g/L
Sodium dodecyl sulfate (SDS, $C_{12}H_{25}SO_4Na$)	0.01 g/L
Sodium fluoride (NaF)	0.004 g/L
Sodium hydroxide (NaOH)	15 g/L

3.1.3 Synthesis of corrosion inhibitor-loaded nanocapsules and fabrication of nanocapsule-embedded Ni-P coating

The reagents used for nanocapsule fabrication are tetraethoxysilane [TEOS, $Si(OC_2H_5)_4$], cetyltrimethylammonium bromide [CTAB, $(C_{16}H_{33})N(CH_3)_3Br$] and 1H-benzotriazole (1H-BTA, $C_6H_5N_3$). First, 0.2 g of CTAB was added slowly into 200 mL of 0.5 g/L NaOH solution at 80 °C under vigorous magnetic stirring, followed by the addition of 0.3 g of BTA. Then, 2 mL of TEOS was added dropwise to the mixed solution. The reaction was maintained at 80 °C under vigorous stirring for 2 h. The mixture was centrifuged, washed twice with deionized water, and dried in furnace at 90 °C for 6 h. The product was then ground to fine powder for the subsequent coating procedure. As for the coating process, the substrates were first dipped in the plating bath (Table 3.1), and in the meanwhile, the prepared nanocapsule powder was mixed with a little amount of plating bath solution (approximately 30 mL) ultrasonically for 1 min to avoid the agglomeration, and then the mixed solution was transferred into the heated plating bath in which the concentration of nanocapsules was fixed at 0.1 g/L. All coated samples were cleaned with alcohol by ultrasonic dispersion and dried in flowing air for corrosion testing.

3.2 Corrosion testing methods

3.2.1 Electrochemical measurements at room temperature and atmospheric pressure

The electrochemical measurements at room temperature and atmospheric pressure were carried out in a three-electrode cell by using a Gamry Interface 1000E Electrochemical Workstation, with a carbon rod as the counter electrode (CE), the epoxy-sealed sample as the working electrode (WE) and a saturated calomel electrode (SCE) as the reference electrode (RE). An area of 1 cm × 1 cm was exposed for electrochemical tests. Initially, the solution was deoxygenated by purging nitrogen gas for 3 h. Then specific gases (CO_2 and/or H_2S) were purged into the solution for 2 h to ensure saturation. During the test, CO_2 and/or H_2S were continuously purged in the solution with a flow rate of 10 mL/min to maintain saturation. First, the open circuit potential (OCP) was recorded for 1 hour to reach the steady-state potential. The linear polarization resistance (LPR) was then measured in the potential range of ±10 mV vs. OCP with a scan rate of 0.125 mV/s. Then the electrochemical impedance spectroscopy (EIS) measurements were conducted with an alternating current signal amplitude of 10 mV applied in the frequency range from 100 kHz to 10 mHz at OCP. ZSimpWin software was used to fit the measured data by using appropriate equivalent circuits. The potentiodynamic polarization curves were recorded from -0.3 V to 1.2 V vs. OCP at a scanning rate of 0.167 mV/s. At least three parallel tests were performed for all the electrochemical tests under each test condition to ensure reproducibility.

The electrochemical noise (EN) measurements were also performed at OCP via ESA 410 software of Gamry Interface 1000E Electrochemical Workstation. Zero resistance ammeter

(ZRA) mode was used in this work for data acquisition, with two identical samples as the WE and SCE as the RE. A sampling interval of 0.2 s was selected over 2048 consecutive data points after different periods. The frequency domain based on the sampling conditions was between 2.5 Hz ($f_{\max}$) and 2.4 mHz ($f_{\min}$) from $f_{max} = \frac{1}{2\Delta t}$ and $f_{min} = \frac{1}{N\Delta t}$, where Δt is the sampling interval and N is the total number of data points. The power spectral densities (PSDs) of the signals were calculated by the program *psd-detrend_ECG-COMON.exe* (free download on www.ecg-comon.org) based on the fast Fourier transform (FFT) and the linear detrending of raw electrochemical potential noise (EPN) and electrochemical current noise (ECN) data to avoid the effect of corrosion potential drift on signal fluctuations during the tests [1].

3.2.2 Immersion tests

The immersion tests were carried out in a 1 L vessel saturated with specific gases for certain test periods. The deoxygenating and purging procedure followed that in the electrochemical tests. After immersion, the samples were taken out from the vessel, cleaned with deionized water and alcohol, and dried in flowing air for further characterizations.

3.2.3 HTHP autoclave tests

3.2.3.1 Weight loss tests

The weight loss tests were performed in a 1.5 L autoclave under specific conditions. The samples were hung in the autoclave to avoid any possible galvanic effects during the immersion. Four parallel samples were tested under each condition, three of which were weighed via an electronic balance (0.1 mg precision) prior to the test. Highly purified N_2

gas was purged into the autoclave to deoxygenate for 2 h, followed by adding N_2/CO_2 mixed gas to reach the required partial pressure. The experiment started at the time point when the required operating temperature was reached. After immersion, the samples were cleaned with deionized water and alcohol and dried in air. Three of the four samples were descaled in the pickling solution. The descaled samples were weighed again, and the corrosion rate (CR, mm/y) was calculated by the equation given below:

$$CR = \frac{8.76\times10^4(W_0-W_1)}{S\rho t} \qquad \text{(Eq. 3.1)}$$

where W_0 and W_1 are the masses of the samples before the test and after descaling, respectively, g; S is the total exposed area, cm^2; ρ is the density of the material, g/cm^3; t is the immersion time, h.

3.2.3.2 In-situ electrochemical measurements at HTHP

In-situ electrochemical tests were performed under HTHP conditions in the autoclave by using a Gamry Interface 1000E Electrochemical Workstation, with the specimens as the WE, a carbon rod as the CE and an Ag/AgCl electrode as the RE. The exposed area of each sample is 1 cm^2, and the deoxygenating and purging process and test solution followed the same procedure for the weight loss tests. The samples were first immersed for 24 h to achieve the pre-filmed surface and a steady-state OCP. The EIS test procedure follows the one in Chapter 3.2.1.

3.3 Material characterizations

The material characterization methods used in this work are summarized as follows:

(1) Scanning electron microscopy (SEM) equipped with energy-dispersive X-ray spectroscopy (EDS): The surface and cross-sectional morphologies of studied specimens before and after corrosion tests were observed by using Tescan Vega-3 SEM, and the elemental distribution was examined by EDS. The morphology of nanocapsules were observed by a Zeiss Sigma 300 VP field emission-SEM (FE-SEM).

(2) Transmission electron microscopy (TEM): The morphologies of nanocapsules were observed by using a JEOL JEM-2100 TEM.

(3) Optical stereo microscopy (OSM): The corrosion morphologies and the depth profiles of surfaces were observed by OSM.

(4) X-ray diffraction (XRD): XRD (Rigaku Ultima IV) was employed to identify the phase compositions. XRD was performed with a Cu K_α X-ray source operated at 40 kV and 44 mA, and the patterns were recorded from 20° to 80° at a scanning rate of 4°/min.

(5) X-ray photoelectron spectroscopy (XPS): The chemical valence was examined by XPS (Kratos AXIS Ultra). The C 1s peak at the binding energy of 284.6 eV was used to calibrate the shifted XPS data.

(6) Nuclear magnetic resonance (NMR): ^{1}H NMR spectra was obtained by using an Agilent Inova 400 MHz spectrometer to verify the release of corrosion inhibitors from the nanocapsules.

3.4 References

[1] F. Mansfeld, Z. Sun, C.H. Hsu, A. Nagiub, Concerning trend removal in electrochemical noise measurements, Corros. Sci. 43 (2001) 341–352.

4 Insights into the electrochemical corrosion behavior and mechanism of electroless Ni-P coating in the $CO_2/H_2S/Cl^-$ environment

ABSTRACT: The electrochemical corrosion behavior of Ni-P coating in 3.5 wt.% NaCl solution-containing CO_2 and H_2S was investigated using electrochemical methods and surface characterization techniques. The results show that the presence of H_2S can enhance the CO_2 corrosion of Ni-P coated carbon steel by affecting both anodic and cathodic processes. The $H_2PO_2^-$ adsorbed layer only exists in the very early stage of corrosion and barely improves the anticorrosion performance of the coating. The formation of corrosion products (NiO and Ni_3S_2) renders temporary protection during immersion, but the addition of H_2S accelerates the diffusion process at the electrolyte/coating interface and promotes the electrolyte penetration through the coating, causing severe localized corrosion and coating disbondment. A corrosion model is proposed to illustrate the corrosion and degradation process of Ni-P coated steel in the $CO_2/H_2S/Cl^-$ environment.

4.1 Introduction

Carbon steel has been widely utilized in the oil and gas industries in the past decades due to its good mechanical and chemical properties and relatively low cost. However, corrosion of carbon steel becomes a non-negligible problem, especially in some harsh environments containing acidic gases such as CO_2 and H_2S, which deteriorates the materials and thus causes failure in the oil and gas applications. Therefore, several anticorrosion methods have been applied under service conditions to mitigate the corrosion of carbon steel.[1-4] Among these methods, coating is regarded as an efficient way to improve the physical and chemical properties of carbon steel substrate. The electroless Ni-P coating, due to its satisfactory corrosion resistance, good mechanical properties, and reasonable cost, has been considered as a promising approach in the oil and gas applications and thus received widespread attention.[5-9]

The anticorrosion performance of electroless Ni-P coating has been studied in recent years, and the findings indicate that the coating steel performs much better than uncoated in the acidic environments.[6,10-12] It is generally believed that the formation of an adsorbed layer of $H_2PO_2^-$ would retard the further hydration of nickel and the corrosive medium transport.[13,14] However, localized corrosion of Ni-P coating has been reported by some researchers. Crobu et al.[15] observed the localized corrosion features on the Ni-P alloys after prolonged polarization in chloride and sulfate solutions. Wang et al.[10] reported the localized corrosion behavior of Ni-P coating in the Cl-containing solution after immersion for 1 month. Recently, Sun et al.[16] investigated the effect of coating defects on the corrosion behavior of Ni-P coating in the CO_2-saturated solution and found that the localized corrosion of the coating occurred after the corrosion was accelerated by cathodic polarization.

Based on the research on CO_2/H_2S corrosion of carbon steel and stainless steel, it is widely acknowledged that H_2S plays a notable role in affecting the corrosion process. As reported, H_2S can either promote CO_2 corrosion by controlling the electrochemical reaction process or inhibit the corrosion by the formation of sulfur-containing corrosion products on the surface.[17-20] However, limited research has focused on the effect of CO_2/H_2S on the corrosion behavior of Ni-based coatings. Yin et al. investigated the CO_2/H_2S corrosion of Ni-based alloys at 80 °C, showing that H_2S served as the cathodic depolarizer and accelerated the corrosion.[21] Moreover, Zhao et al. found that the presence of H_2S could cause the change in chemical composition of the corrosion film and result in the localized corrosion of Ni-based alloys.[22] Recently, Sun et al. reported the synergistic effect of CO_2 and H_2S on Ni-P coating at high temperature and high pressure and proposed that the co-existence of two gases led to a CO_2-enhanced H_2S corrosion mode.[23] However, to date, the role that CO_2 and/or H_2S plays in the electrochemical behavior and mechanism of Ni-P coating is still unclear, and the effect of H_2S on the CO_2 corrosion of Ni-P coated steel in the aqueous environment at room temperature has not yet been fully investigated.

Hence, in this study, the electrochemical corrosion behavior of Ni-P coating on L80 carbon steel in $CO_2/H_2S/Cl^-$ environment was investigated and the effect of H_2S on CO_2 corrosion was clarified by electrochemical techniques. The surface morphology and corrosion product were observed and characterized by using surface analysis techniques such as scanning electron microscope (SEM), energy dispersive X-ray spectroscopy (EDS) and X-ray photoelectron spectroscopy (XPS). Furthermore, a corrosion model was proposed to illustrate the corrosion and disbonding process of Ni-P coating under the specific conditions.

4.2 Experimental

4.2.1 Coating fabrication

L80 steel, with the chemical composition (wt.%) of 0.32 C, 0.80 Mn, 0.016 Ni, 0.12 Cu, 0.25 Si, 0.006 P, 0.028 S, and balance Fe, was used as the substrate for the electroless Ni-P coating. The samples were first cut into 10 mm × 10 mm × 5 mm, ground to 1200 grit, degreased with acetone and alcohol, and rinsed with deionized water. Prior to the coating process, the samples were cleaned in 3 wt.% sodium carbonate (Na_2CO_3) and 3 wt.% sodium hydroxide (NaOH) solution for 20 min at 60°C and then etched in 10 wt.% hydrochloric acid (HCl) solution for 50 s for surface activation. After the treatment, the samples were dipped in the plating bath with a stirring rate of 200 rpm at 85±1°C for 120 min. The chemical compositions of the plating bath are listed in Table 4.1. After the coating process, the coated samples were cleaned with alcohol by ultrasonic dispersion for 10 min for plating solution removal.

Table 4.1 Chemical compositions of electroless Ni-P plating bath.

Reagent	Concentration
Nickel sulphate ($NiSO_4 \cdot 6H_2O$)	25 g/L
Sodium hypophosphite ($NaH_2PO_2 \cdot H_2O$)	30 g/L
Lactic acid ($C_3H_6O_3$)	20 mL/L
Citric acid ($C_6H_8O_7$)	19 g/L
Succinic acid ($C_4H_6O_4$)	14 g/L
Saccharin Sodium ($C_6H_4SO_2NNaCO \cdot 2H_2O$)	0.06-0.08 g/L
Sodium dodecyl sulfate (SDS, $C_{12}H_{25}SO_4Na$)	0.04 g/L
Lead nitrate ($Pb(NO_3)_2$)	1 mg/L

4.2.2 Solution preparation and test conditions

The test solution used in this study was 3.5 wt.% sodium chloride (NaCl) solution. Initially, the solution was deoxygenated for 3 hours by purging nitrogen gas. Then CO_2 and/or H_2S were purged into the solution for 2 hours to ensure saturation. The combined pressure is 0.1 MPa. During the test, CO_2 and/or H_2S were continuously purged in the solution with a flow rate of 10 mL/min to maintain saturation. The pH values of CO_2-

saturated and CO_2/H_2S-saturated NaCl solution were 4.01 and 4.10, respectively. The bulk solution, which only contained 3.5 wt.% NaCl, was chosen as the control group for electrochemical tests. For the control group, nitrogen gas was purged continuously before and during the electrochemical tests. The pH value of all four kinds of solution was adjusted to 4 by adding HCl.

4.2.3 Electrochemical measurements

The electrochemical measurements were conducted at room temperature by using the Gamry Interface 1000E electrochemical workstation in the three-electrode cell with the epoxy-sealed sample as working electrode (WE), a carbon rod as counter electrode, and saturated calomel electrode (SCE) as reference electrode. The exposed area of WE for electrochemical tests was 1 cm^2. The open-circuit potential (OCP) measurements were first performed for 1 h to monitor the corrosion potential and make sure that a steady-state potential has been reached. The linear polarization resistance (LPR) was then measured in the potential range of ±10 mV vs. OCP with a scan rate of 0.125 mV/s. The corrosion current density (i_{corr}, $\mu A/cm^2$) and the corrosion rate (*LPR-CR*, μm/year) were calculated according to Eqs. 4.1 and 4.2:[24,25]

$$i_{corr} = \frac{B}{R_p} = \frac{\beta_a \beta_c}{2.3 R_p (\beta_a + \beta_c)} \qquad \text{(Eq. 4.1)}$$

$$LPR - CR = \frac{3.27 i_{corr} EW}{\rho} \qquad \text{(Eq. 4.2)}$$

where B is the Stern-Geary coefficient, mV; β_a and β_c are anodic and cathodic Tafel constants, respectively, mV/decade; R_p is the polarization resistance, $k\Omega \cdot cm^2$; EW is the equivalent weight, g and ρ is the density, g/cm^3.

4.2.4 Immersion tests and surface characterizations

To further evaluate the stability of Ni-P coating, immersion tests were performed in a 1 L vessel in CO_2 and CO_2/H_2S environments for 5 d and 10 d. The deoxygenating and purging process followed the electrochemical tests. After immersion, the samples were cleaned with deionized water and alcohol and dried in air. The surface morphology before and after immersion test was observed by SEM and the composition of the corrosion film was examined by EDS and XRD. The XRD analysis was carried out with Cu K_α radiation and the patterns were recorded from 10° to 80° at a scanning step of 0.02° and a scanning rate of 4°/min. XPS was then employed to analyze the chemical valence of corrosion product after immersion test. The C 1s peak at the binding energy of 284.6 eV was used to calibrate the shifted spectra.

4.3 Results

4.3.1 Structure and morphology of electroless Ni-P coating

Figure 4.1a shows the SEM surface morphology of electroless Ni-P coating, and it displays the nodule-like microstructure. The coating is uniformly deposited and closely attached on the carbon steel surface, and the thickness is around 20 μm (Figure 4.1b). The EDS line scan results in Figure 4.1c indicate the uniform distributions of Ni and P elements. The XRD pattern in Figure 4.1d displays a broad diffraction peak of nickel around the 2θ position of 45°, which demonstrates the amorphous phase structure.

4.3.2 Corrosion rates from LPR tests

The LPR corrosion rates of Ni-P coating under different test conditions are shown in Figure 4.2. β_a and β_c are maintained at 40 mV/decade based on the polarization sweep results. The corrosion rate is only 6.0 μm/year in the bulk solution, and it increases to 11.1 μm/year with the addition of saturated CO_2. The corrosion rate of Ni-P coating further increases to 16.8 μm/year with the coexistence of CO_2 and H_2S. This indicates that the added CO_2 increases the corrosion rate of the coating as compared to the bulk solution, and the co-presence of the two gases further promotes the electrochemical reaction process.

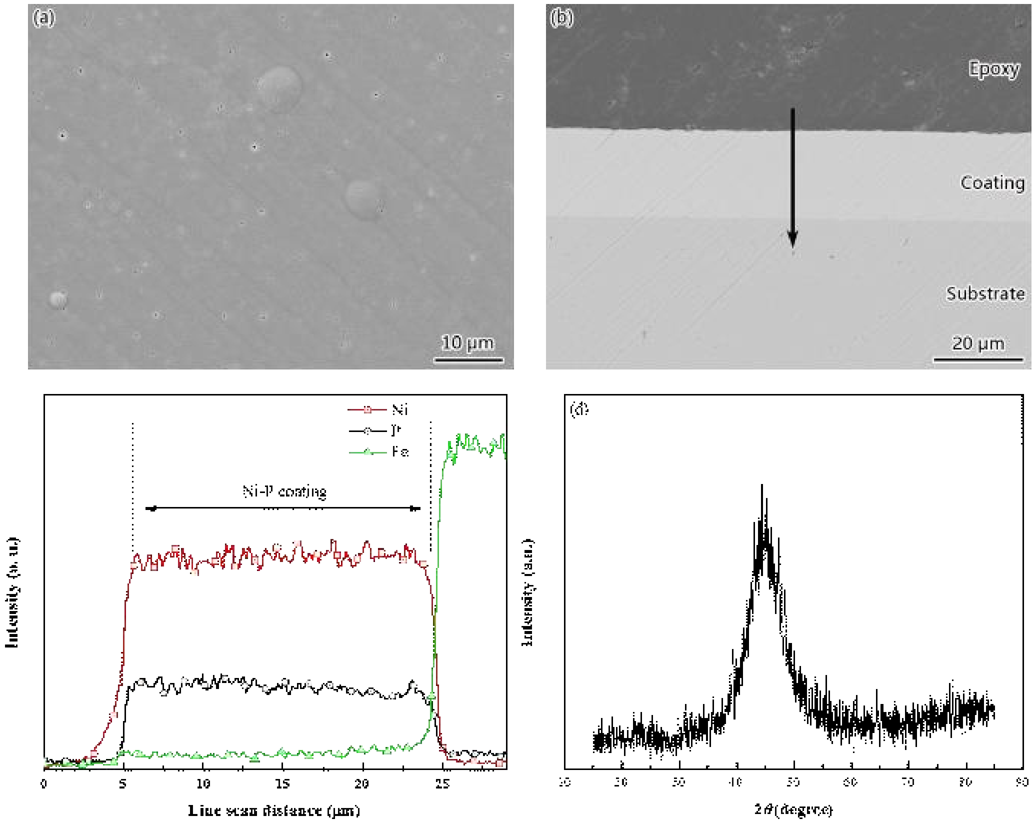

Figure 4.1 Characterization results of as-deposited electroless Ni-P coating: (a) surface morphology; (b) cross-sectional morphology; (c) elemental distribution; (d) XRD patterns.

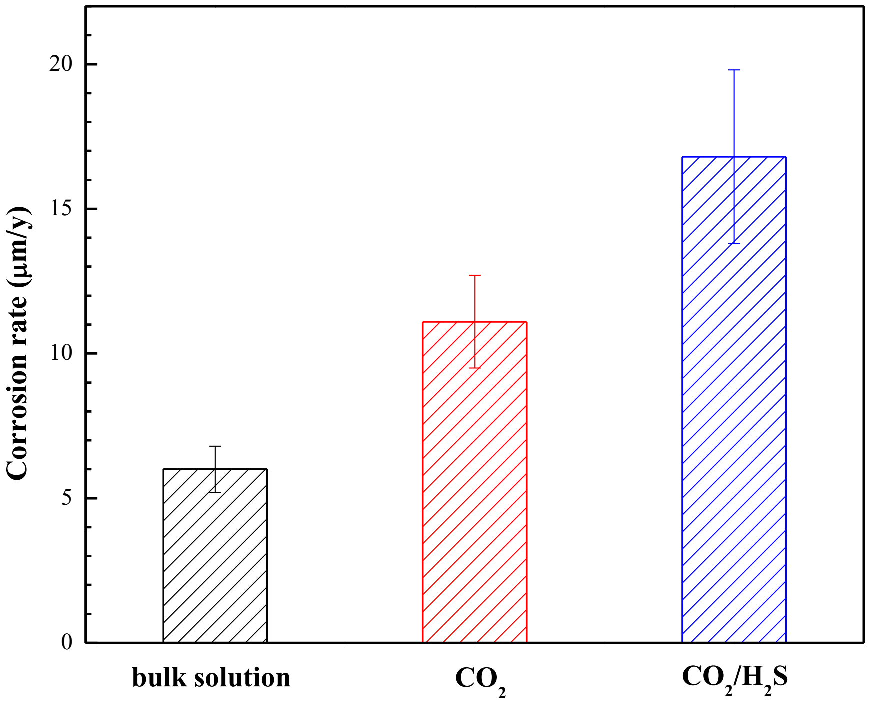

Figure 4.2 LPR corrosion rates of Ni-P coating under different test conditions.

4.3.3 Polarization curves

Figure 4.3 depicts the potentiodynamic polarization curves of Ni-P coating at different environments. Different potential regions are divided to clearly illustrate the electrochemical behaviors. Direct H_2O reduction occurs in Region 1 (lower than -1.0 V_{SCE}). When the potential range increases to around -0.5~-1.0 V_{SCE} (Region 2), the cathodic current density notably increases in CO_2 environment and reaches the maximum with the co-existence of CO_2 and H_2S as compared to the bulk solution, revealing that the added acidic gases significantly facilitate the cathodic reactions because of the extra reactions of direct H_2CO_3 and H_2S reduction. Nevertheless, HCO_3^- and HS^- may also contribute to the cathodic current increase.[23,26,27]

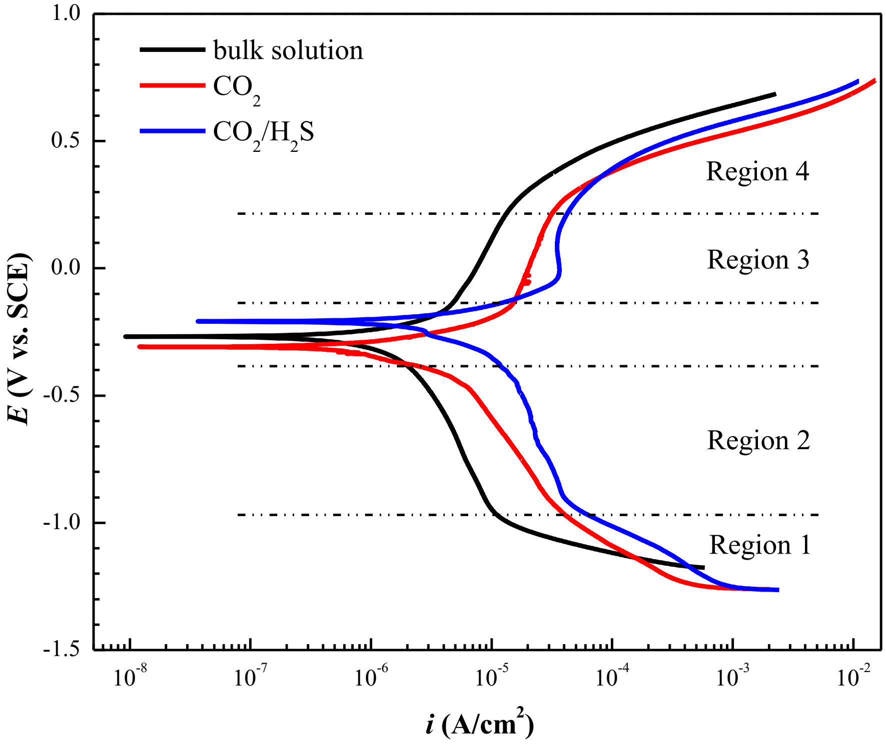

Figure 4.3 Potentiodynamic polarization curves of Ni-P coating under different test conditions.

As for the anodic branches in the potential range from -0.1 V_{SCE} to 0.2 V_{SCE} (Region 3), the current densities increase slowly and, therefore, this region can be regarded as a pseudo-passivation region. This mixed controlled electrochemical process can be attributed to the formation of a thin protective P-rich layer on the coating surface and the microstructure and P content of Ni-P coating[27,28]. Compared to the bulk solution and CO_2-saturated solution, the anodic branches display a more obvious current plateau region in the solutions containing H_2S. The same phenomenon was also found on Ni-based alloys in CO_2/H_2S-containing environment[22]. The high affinity of sulfide species to Ni facilitates the formation of the nickel sulfide film, and thereby gives rise to an enhanced "pseudo-passivation" property. In Region 4 (higher than +0.2 V_{SCE}), all the samples undergo the rapid anodic dissolution, and the anodic current density in CO_2/H_2S environment is close to that in CO_2 environment, both of which exceed that in the bulk solution. In this potential range, nickel undergoes rapid dissolution as the equation below:

$$Ni \rightarrow Ni^{2+} + 2e^- \qquad \text{(Eq. 4.3)}$$

Meanwhile, the P species also participate in the electrochemical reactions and are oxidized to $H_2PO_2^-$ and H_3PO_3:[27,29,30]

$$P + 2H_2O \rightarrow 2H^+ + e^- + H_2PO_2{}^- \qquad \text{(Eq. 4.4)}$$

$$H_2PO_2{}^- + H_2O \rightarrow H_3PO_3 + H^+ + 2e^- \qquad \text{(Eq. 4.5)}$$

4.3.4 EIS analysis for immersion tests

Figure 4.4 depicts Nyquist and Bode plots of Ni-P coating exposed to CO_2 and CO_2/H_2S environments for different time durations, respectively. Only one time constant is found in the CO_2 environment, while both Bode plots and Nyquist plots show two time constants in the CO_2/H_2S environment, demonstrating a changed corrosion mechanism after introducing H_2S. As the immersion time proceeds, the shape of the semicircles at both conditions does not change, revealing that the corrosion mechanism remains the same in the test duration. The radii of the semicircles first increase and then decrease with time under both conditions, demonstrating that the corrosion resistance of the coating reaches its peak value after immersion for a specific period.

The equivalent electrical circuits used for fitting the EIS data are shown in Figure 4.5a and 4.5b, representing the CO_2 and CO_2/H_2S environments, respectively, where R_s is the solution resistance, Q_{dl} and R_{ct} are the double layer capacitance and charge-transfer resistance, Q_f and R_f are the capacitance and resistance of the formed sulfide film on the coating surface. In this electrochemical system, constant phase elements (CPE) designated as Q_{dl} and Q_f are used in the fitting instead of pure capacitance, and the impedance of CPE is given by the following equation:[31]

$$Z = \frac{1}{Y_0}(j\omega)^{-n} \qquad \text{(Eq. 4.6)}$$

where Z is the impedance; Y_0 is the admittance constant; j is the imaginary number; ω is the angular frequency; n is the empirical exponent. The fitted data of main electrochemical parameters in CO_2 and CO_2/H_2S environments are listed in Table 4.2 and Table 4.3, respectively. The quality of fit is indicated by χ^2 values obtained via ZSimpWin software, which represent the discrepancies between the measured data and the fitted data. All χ^2 values in Tables 4.2 and 4.3 are no larger than 3×10^{-3}, suggesting that the fitted data fit well with the measured ones.

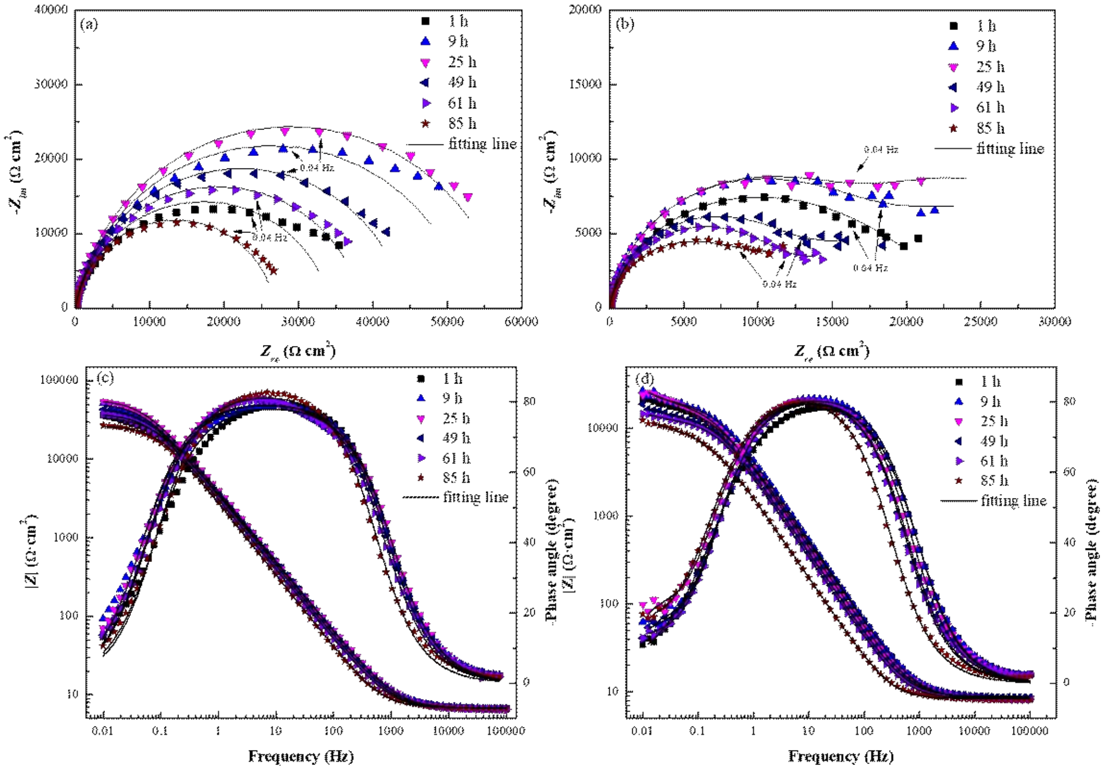

Figure 4.4 Nyquist plots of Ni-P coating in (a) CO_2 and (b) CO_2/H_2S environment and Bode plots of Ni-P coating in (c) CO_2 and (d) CO_2/H_2S environment at different immersion times.

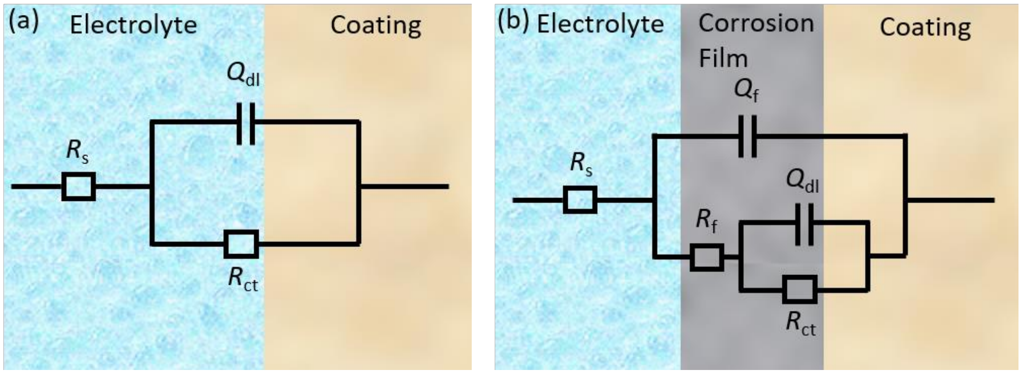

Figure 4.5 Equivalent electrical circuit models used for EIS data fitting: (a) CO_2 environment in Figure 4.4a and 4.4c; (b) CO_2/H_2S environment in Figure 4.4b and 4.4d.

According to the fitted data, the R_p values ($R_p = R_{ct} + R_f$) under CO_2/H_2S condition after the same immersion time are smaller than those under CO_2 condition ($R_p = R_{ct}$), suggesting a decline of corrosion resistance with the addition of H_2S. In the CO_2 environment, R_{ct} first increases and then decreases and reaches the maximum at 25 h, implying an enhanced resistance to the mass transport at this stage. Meanwhile, $Y_0(Q_{dl})$ keeps almost stable in the early stage and starts to increase with time after 49 h, indicative of a promoted electrochemical reaction process as immersion time prolongs. In the CO_2/H_2S environment, R_f-Q_f corresponds to the corrosion product in high frequency (HF), and R_{ct}-Q_{dl} represents the contribution of charge transfer process at the corrosion film/coating interface in low frequency (LF). The R_{ct} values in the CO_2/H_2S environment are about one third of those in the CO_2 environment, suggesting the acceleration effect of H_2S. R_f increases in the first 25 h and then decreases, revealing a rapid film formation in the early stage and the opposite tendency of Q_f suggests the following decline of film thickness during immersion. Moreover, R_{ct} in the CO_2/H_2S case displays a similar variation to that in the CO_2 case, and $Y_0(Q_{dl})$ increases with immersion time, suggesting the increased exposed surface area, and thus corrosion of the coating is promoted during immersion.

Table 4.2 Main electrochemical parameters fitted from EIS data in Figure 4.4a and 4.4c.

Time (h)	R_s (Ω cm^2)	$Y_0(Q_{dl})$ (Ω^{-1} cm^{-2} s^n)	n	R_{ct} (Ω cm^2)	Quality of fit
1	6.670	5.326×10^{-5}	0.8836	3.443×10^{4}	2.532×10^{-3}
9	6.702	5.412×10^{-5}	0.8808	5.276×10^{4}	1.522×10^{-3}
25	6.698	4.931×10^{-5}	0.8922	5.790×10^{4}	0.947×10^{-3}
49	6.701	5.593×10^{-5}	0.8928	4.447×10^{4}	1.125×10^{-3}
61	6.705	6.149×10^{-5}	0.8955	3.856×10^{4}	1.159×10^{-3}
85	6.832	6.567×10^{-5}	0.9216	2.683×10^{4}	1.530×10^{-4}

Table 4.3 Main electrochemical parameters fitted from EIS data in Figure 4.4b and 4.4d.

Time (h)	R_s (Ω cm^2)	$Y_0(Q_{dl})$ (Ω^{-1} cm^{-2} s^n)	R_{ct} (Ω cm^2)	$Y_0(Q_f)$ (Ω^{-1} cm^{-2} s^n)	R_f (Ω cm^2)	Quality of fit
1	8.490	7.498×10^{-4}	1.170×10^{4}	4.794×10^{-5}	1.270×10^{4}	3.595×10^{-4}
9	8.699	5.639×10^{-4}	1.703×10^{4}	4.134×10^{-5}	1.874×10^{4}	6.808×10^{-4}
25	8.782	6.443×10^{-4}	1.517×10^{4}	5.146×10^{-5}	1.937×10^{4}	1.219×10^{-3}
49	8.923	1.202×10^{-3}	8.456×10^{3}	5.938×10^{-5}	1.376×10^{4}	1.117×10^{-3}
61	8.488	1.286×10^{-3}	9.421×10^{3}	6.464×10^{-5}	1.202×10^{4}	7.804×10^{-4}
85	8.339	5.506×10^{-4}	1.223×10^{4}	1.093×10^{-4}	8.128×10^{3}	5.252×10^{-4}

4.3.5 Morphologies and chemical compositions of corrosion products

4.3.5.1 SEM morphologies and EDS analysis

Figure 4.6 shows the surface morphologies and EDS results of as-deposited Ni-P coating and the Ni-P coating immersed in the solution saturated with CO_2. A small number of "dots" in nano-scale, namely the "micropores" (due to the coating process), are observed on the as-deposited Ni-P coating surface as shown in Figure 4.6a. After immersion in the CO_2-saturated solution for 5 d (Figure 4.6b), more pits appear on the surface, especially at the nodule boundaries, indicating that the corrosive medium has started to penetrate from some active sites of the coating. However, no noticeable corrosion product is found on the surface. After 10 d of immersion (Figure 4.6c), the top layer of coating is damaged along the nodule boundaries where corrosion pits aggregate, and even more corrosion pits are found under the damaged coating, implying that the corrosion process continues downwards through some corrosion pathways inside the coating. Moreover, the corrosion product is detected on the coating surface and consists of Ni, P, Fe, C and O elements from the EDS results in Figure 4.6d. Since the detection depth of the electron beam is no larger than 3 µm, much smaller than the coating thickness (approximately 20 µm), the existence of Fe is an evidence that the corrosion electrolyte has penetrated to the coating/substrate interface and caused the corrosion of carbon steel substrate. Fe ions then diffuse outwards through the corrosion pathways, forming the corrosion products on the coating surface.

The coating degradation in the CO_2/H_2S case is much more intense. As seen in Figure 4.7a, the corrosion of coating occurs obviously and the formed corrosion product film peels off along the nodule boundaries only after 5 d of immersion, which further facilitates the electrolyte penetration and initiates localized corrosion. Moreover, small amount of corrosion product is observed in some severely corroded regions. After 10 d of immersion (Figure 4.7b), the coating damage and peeling continue to take place downwards, leading to the formation of more corrosion products on the surface. The EDS results show higher contents of Fe and O than that in the CO_2 case, demonstrating an accelerated corrosion process on the substrate with the addition of H_2S in the corrosive medium.

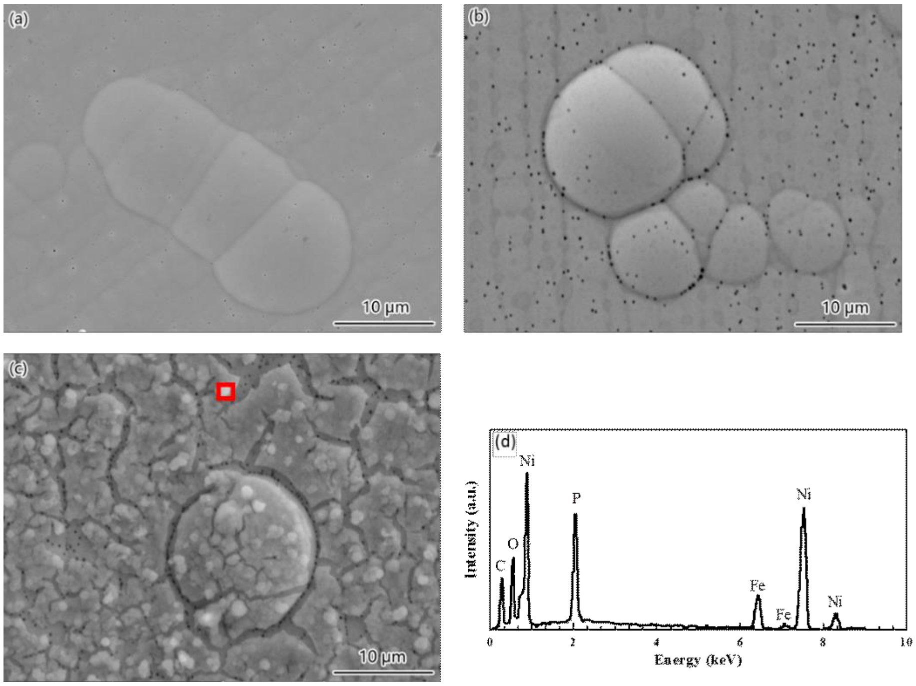

Figure 4.6 SEM surface morphologies of (a) as-deposited Ni-P coating; (b–c) Ni-P coating in CO_2 environment for 5 d and 10 d, respectively; (d) EDS analysis of corrosion product denoted by red box in (c).

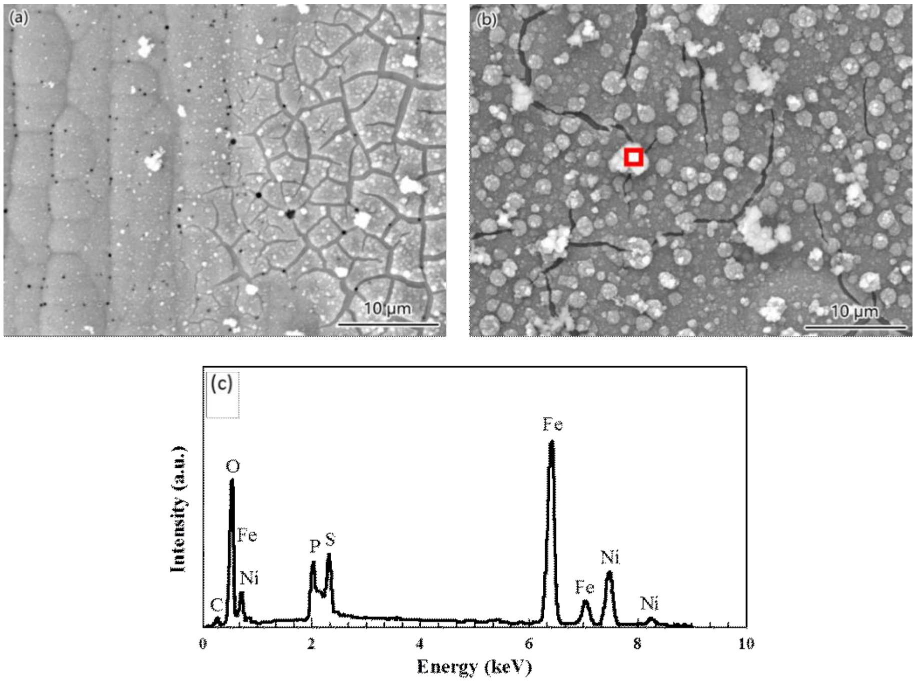

Figure 4.7 SEM surface morphologies of Ni-P coating in CO_2/H_2S environment for (a) 5 d and (b) 10 d, respectively; (c) EDS analysis of corrosion products denoted by the red box in (b).

Figure 4.8 depicts the cross-sectional images of Ni-P coated steel after the different times of immersion that better illustrate the electrolyte penetration process through the coating. In the CO_2 case, as shown in Figure 4.8a, some minor corrosion pathways are formed inside the coating after 5 d of immersion, suggesting that the corrosive medium starts to penetrate downwards. However, the average length of these visible corrosion pathways is only around 2 μm to 3 μm. Therefore, the substrate is still free from corrosion attack, which can also be proved by the good adhesion of the coating and substrate. Moreover, the flat coating surface indicates a relatively slight corrosion at this condition. After immersion for 10 d, the average length of the visible corrosion pathways increases, meaning that the electrolyte continues to penetrate downwards. Also, the presence of the gap between the coating and the substrate is an implication that the corrosion medium has reached the interface and resulted in the corrosion of steel substrate. The EDS line scan analysis (Figure 4.8e) shows that the corrosion product contains trace amount of O and Cl elements in this gap, confirming the occurrence of localized corrosion at the interface.

The cross-sectional images of Ni-P coated steel after immersion in the CO_2/H_2S-saturated solution for 5 d and 10 d are depicted in Figure 4.8c and 4.8d, respectively. From Figure 4.8c, the corrosion pathways can be obviously found, and the average length of these pathways is larger than that in the CO_2 case (shown in Figure 4.8a). Furthermore, slight localized corrosion is also observed at the coating/substrate interface, initiating the coating disbondment after about 5 d of immersion. Since the corrosion of coating itself is insignificant during the entire period and the galvanic corrosion leads to the severe corrosion of substrate, the coating thickness hardly changes, as shown in the cross-sectional images. As prolonging the immersion time to 10 d, the propagation of corrosion pathways allows more electrolyte to diffuse, and a large localized corrosion region is observed under the coating. Meanwhile, the disbondment propagates laterally along the interface, confirmed by the shape of the localized corrosion region at the edge. The elemental composition of corrosion product in this region is obtained from EDS line scan results. Besides Fe and O, the presence of Cl element indicates that these anions have penetrated and reached the interface.

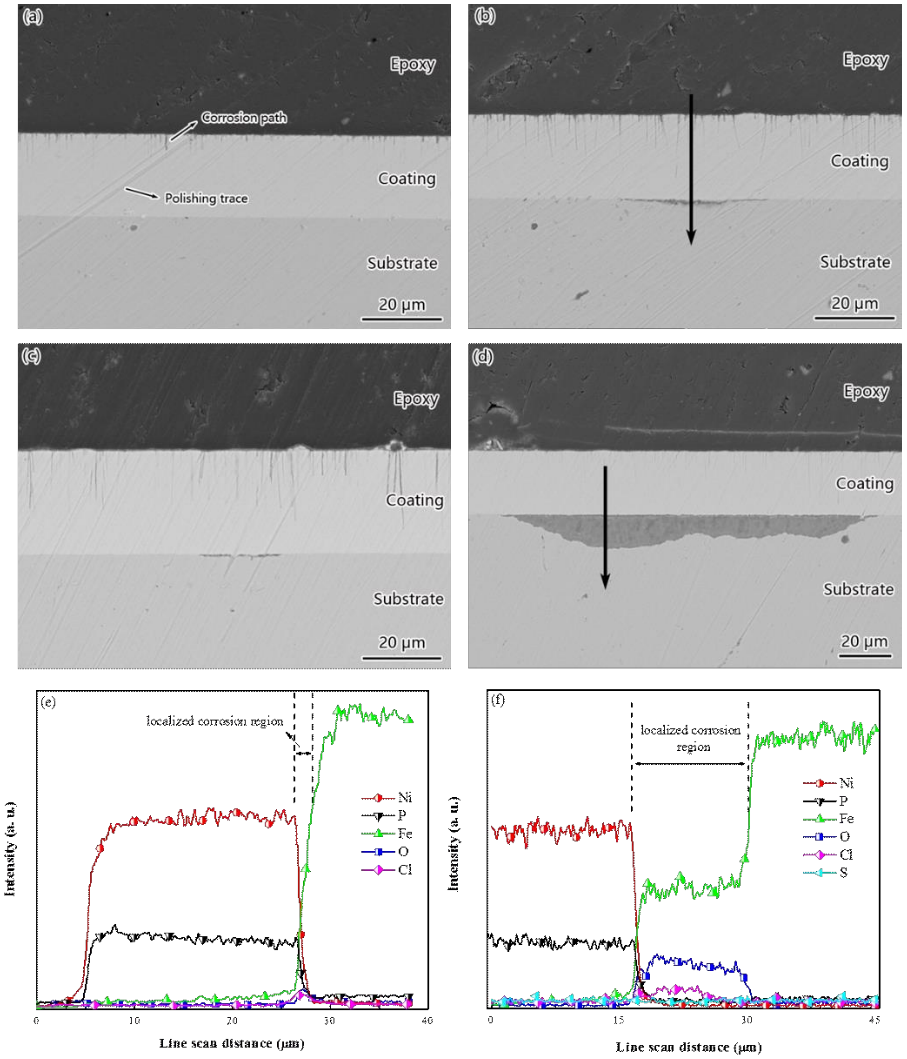

Figure 4.8 (a–d) SEM cross-sectional images of Ni-P coating and (e–f) EDS line scan analysis: Ni-P coating (a) (b) in CO_2 environment for 5 d and 10 d, respectively, and (c) (d) in CO_2/H_2S environment for 5 d and 10 d, respectively; (e) (f) elemental distributions denoted by the black arrow line in (b) and (d), respectively.

4.3.5.2 XPS analysis

Figure 4.9 shows the high-resolution XPS spectra of corrosion products on Ni-P coating in CO_2/H_2S environment for various time lengths of immersion. Four time lengths (1 h, 24 h, 48 h and 10 d) were chosen to represent the corresponding corrosion stages: 1 h represents the initial stage of immersion, 24 h the occurrence of the highest corrosion resistance, 48 h the stage that the coating gradually loses the protection, and 10 d the maximum length of immersion in this study. The fitted binding energies and the corresponding species are summarized in Table 4.4.

Ni^0 and Ni^{2+} from the native oxide film are detected on the surface of the as-deposited sample. After 1 h of immersion, the signal of Ni^0 decreases and Ni species converts to Ni^{2+} and Ni^{3+} due to the electrochemical reactions on the coating surface[32]. Ni^0 signal disappears after 24 h, indicating that the entire surface has participated in the electrochemical process. With immersion time prolonging to 48 h, the Ni^{3+}/Ni^{2+} ratio remains quite stable. However, the intensity of Ni^{3+} signal dramatically weakens after 10 days of immersion, implying that Ni^{3+} species transform to Ni^{2+}.[33]

The P 2p spectrum of the as-deposited sample is composed of two P^0 peaks and a peak of oxidized P. The spectrum almost keeps unchanged after 1 h. However, from 24 h to 10 days of immersion, no obvious P peaks can be discerned, revealing that all P species on the coating surface are involved in the electrochemical reactions and dissolved in the solution. It is worth noting that the absence of P peaks after 24 h means that the P-rich layer has been completely consumed at this stage, i.e., the corrosion resistance is not rendered by this layer.

From the O 1s and S 2p spectra, it is concluded that the corrosion product is mainly composed of NiO, $Ni(OH)_2$, NiS, Ni_3S_2 and FeS. The ratios of NiO to $Ni(OH)_2$ and NiS to Ni_3S_2 vary as the immersion time proceeds, and the intensity of NiO and Ni_3S_2 reach the maximum at 24 h, implying that NiO and Ni_3S_2 might be responsible for the corrosion resistance increase. The NiO peak disappears after 10 days of immersion, leaving $Ni(OH)_2$ as the main corrosion product. As for S species, the presence of FeS after 10 days reveals that corrosion has occurred at the coating/substrate interface, causing Fe ions to diffuse outwards to the electrolyte.[39,40]

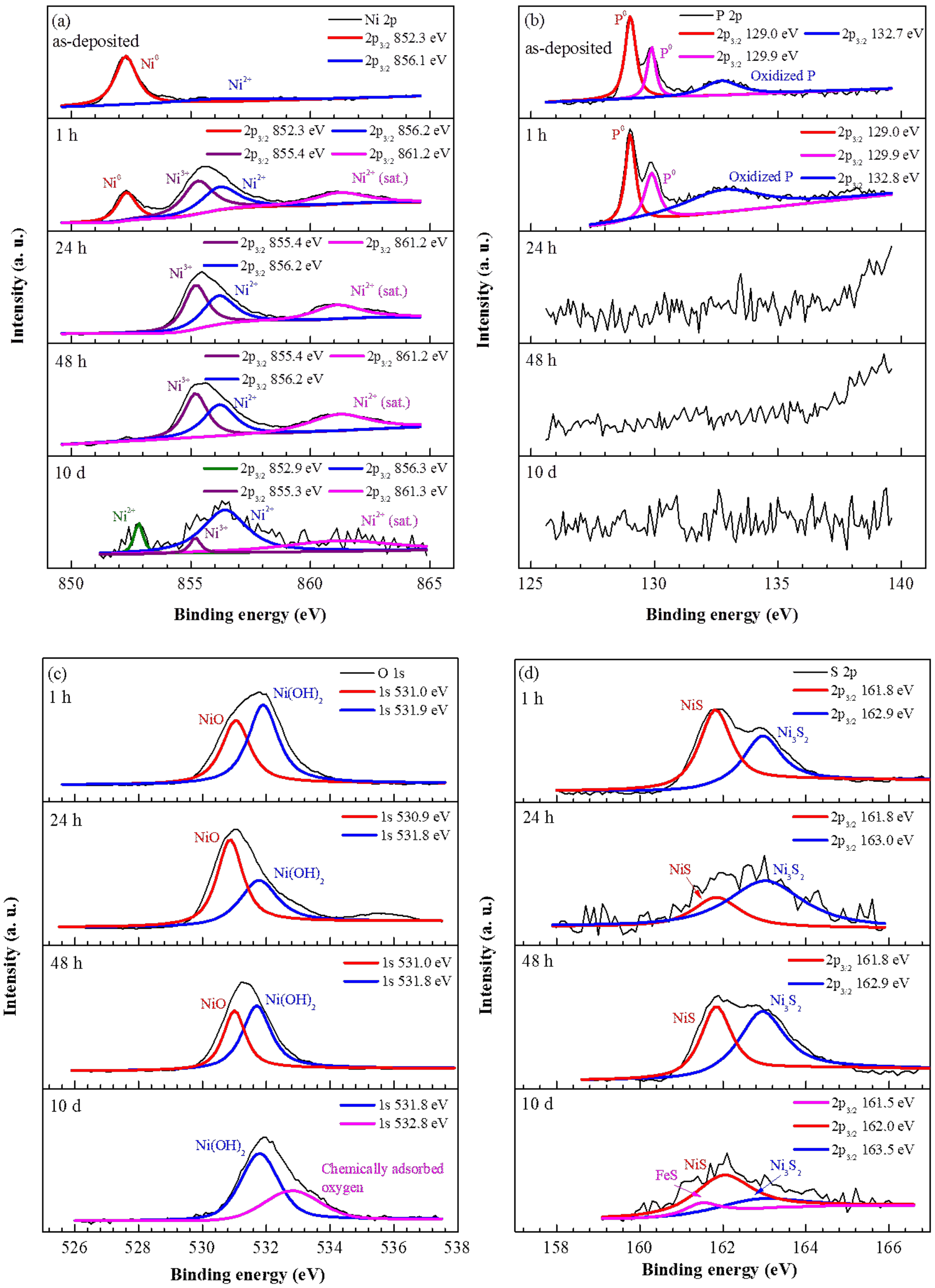

Figure 4.9 XPS spectra of corrosion product on the Ni-P coating surface after immersion in CO_2/H_2S environment for different times: (a) Ni 2p; (b) P 2p; (c) O 1s and (d) S 2p.

Table 4.4 Summary of fitted binding energies of the spectra in Figure 4.9 and the corresponding species of corrosion products.

Element	Binding energy (eV)	Fitted species
Ni $2p_{3/2}$	852.3	Ni^0 [16]
	856.1, 852.9	Ni^{2+} [16, 33]
	855.4	Ni^{3+} [32]
P 2p	129.0, 129.9	P^0 [34]
	132.7	Oxidized P[35]
O 1s	531.0	NiO[36]
	531.9	$Ni(OH)_2$[37]
	532.8	Chemically adsorbed O[38]
S 2p	161.8	NiS[39]
	162.9	Ni_3S_2[39]
	161.5	FeS[40]

4.4 Discussion

4.4.1 Effect of H_2S in the corrosion of Ni-P coating in the $CO_2/H_2S/Cl^-$ environment

In the CO_2/H_2S aqueous environment, both acidic species will dissolve in water to form acids which partially dissociate in several steps to provide H^+ ions. For CO_2, it is widely acknowledged that carbonic acid will be ionized to form HCO_3^- and CO_3^{2-}.[41,42] When H_2S is introduced in the CO_2-saturated solution, aqueous H_2S will also form anions such as HS^- and S^{2-}.[43]

The addition of H_2S can affect both anodic and cathodic processes. For the cathodic process, H_2S can provide an additional cathodic reaction (direct reduction of H_2S) and thus promote corrosion, which was also reported by some previous results.[44] According to the findings of Dickinson et al., nickel exhibits a passivation behavior in the acidic environment, and the main chemical compositions of the passive layer are NiO and $Ni(OH)_2$, which implies that the dissolution of nickel is ascribed to OH^- concentration on the metal surface.[45] Since sulfide species have strong chemisorption ability on nickel,[46] they will substitute OH^- and form the nickel sulfide thin film on the surface. Although this film acts as a temporary physical layer to achieve a passivation feature, its formation process accelerates the dissolution of Ni.

To further confirm the promoting effect of H_2S in the corrosion process and the protectiveness of sulfides, 500 ppm of H_2S (N_2 balance) was twice purged in the CO_2-saturated solution for a very short time (10 min). The EIS data were recorded at different immersion times, and Figure 4.10 shows the fitted R_p variation with the addition of H_2S. Figure 4.5a and 4.5b are chosen as the equivalent circuit before (1 h–4 h) and after purging (4 h–96 h), respectively. The corrosion resistance increases at first 4 h, implying the formation of corrosion products. However, the resistance dramatically drops after first H_2S purge at 4 h, which indicates that the added H_2S accelerates the electrochemical process on the coating surface significantly. After the first purge, the corrosion resistance first increases, and then rapidly decreases until the second purge. This increase is attributed to the continuous formation of nickel sulfides and oxides/hydroxides, and the further dissolution of nickel and the electrolyte penetration leads to the resistance decline. H_2S was purged again at 48 h when the electrolyte penetration becomes more influential. It is evident that the corrosion resistance increases obviously after the second purge, further confirming the protectiveness of the newly formed sulfide. As corrosion proceeds, the electrolyte penetration continues to be dominant, thus the resistance gradually declines after immersion for 80 h.

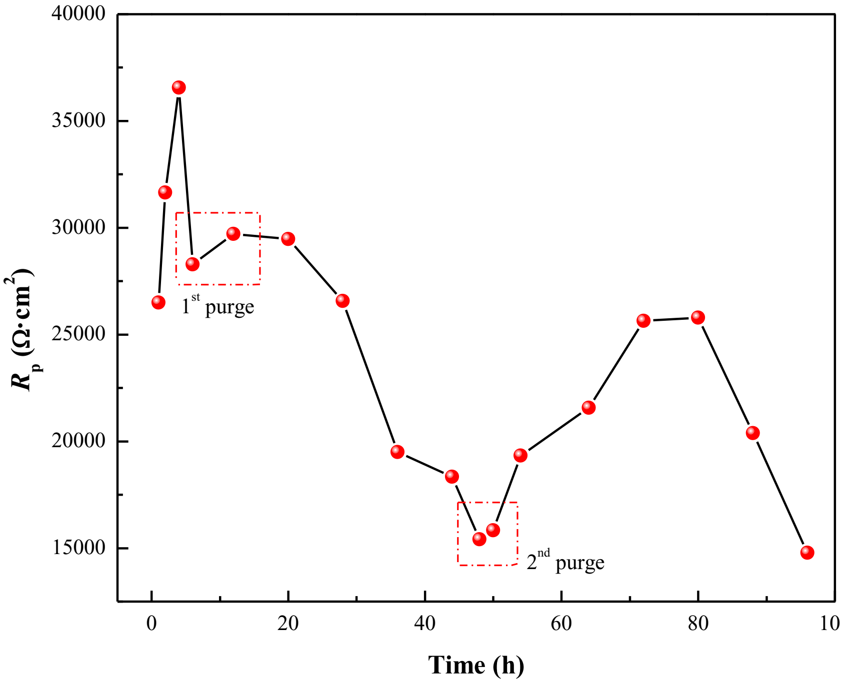

Figure 4.10 R_p variation of Ni-P coating in CO_2 environment with the addition of H_2S.

4.4.2 Corrosion model of Ni-P coated steel in the environment containing $CO_2/H_2S/Cl^-$

Based on all the results, a corrosion model is established to illustrate the corrosion process of Ni-P coated steel in CO_2/H_2S environment, as depicted in Figure 4.11. It can be divided into five stages. In the early stage (Figure 4.11a), the dissolved ions (such as H^+, HS^-, S^{2-}, HCO_3^-, CO_3^{2-}, Cl^-, etc.) diffuse and adsorb at the coating/electrolyte interface, initiating corrosion of nickel. Therefore, the P-rich layer forms due to the dissolution of nickel and attenuate the further corrosion. However, this layer oxidizes and loses the protection capability very quickly, and thus the corrosive electrolyte, especially some anions with higher chemisorption ability such as Cl^-, starts to penetrate inwards through the micropores at the nodule boundaries, which leaves corrosion pathways in the coating and gives rise to localized corrosion, as exhibited in Figure 4.11b. It was reported that both H_2S (Eqs. 4.7–4.9) and Cl^- (Eqs. 4.10–4.12) can induce the hydration of Ni and thus accelerate the anodic dissolution:[16,47]

$$Ni + H_2S + H_2O \rightarrow NiHS_{ads} + H_3O^+ + e^- \qquad \text{(Eq. 4.7)}$$

$$NiHS_{ads} \rightarrow NiHS^+ + e^- \qquad \text{(Eq. 4.8)}$$

$$NiHS^+ + H_3O^+ \rightarrow Ni^{2+} + H_2S + H_2O \qquad \text{(Eq. 4.9)}$$

$$Ni + Cl^- + H_2O \rightarrow [NiCl(OH)]_{ads} + H^+ + e^- \qquad \text{(Eq. 4.10)}$$

$$[NiCl(OH)]_{ads} \rightarrow NiClOH + e^- \qquad \text{(Eq. 4.11)}$$

$$NiClOH + H^+ \rightarrow Ni^{2+} + Cl^- + H_2O \qquad \text{(Eq. 4.12)}$$

Subsequently, excessive Ni ions generated by the dissolution of Ni can react with S species, forming NiS and Ni-rich Ni_3S_2.[48] In the meantime, nickel oxide and nickel hydroxide are also formed on the coating surface.[26,49] Therefore, the corrosion film composed of sulfides, oxide and hydroxide renders extra corrosion inhibition, and it exhibits the best performance as the proportions of Ni_3S_2 and NiO reach the maximum at around 24 h. In Stage 3 (48–72 h) (Figure 4.11c), more sulfur species participate in the reactions, thereby leading to the transformation from Ni_3S_2 to NiS by releasing the Ni^{2+} ions.[50]

Concurrently, NiO serves as nucleation sites and adsorb H_2O molecules to form $Ni(OH)_2$.[51] The electrolyte penetration continues through the corrosion pathways. As immersion time extends to about 5 d (Figure 4.11d), the further penetration of corrosive medium with the aid of Cl^- ions reaches the coating/substrate interface and gives rise to the initial localized corrosion. The cracking of the formed corrosion film can be observed on the coating surface, which is more likely due to the dehydration after the sample is taken out of the solution for the SEM preparation.

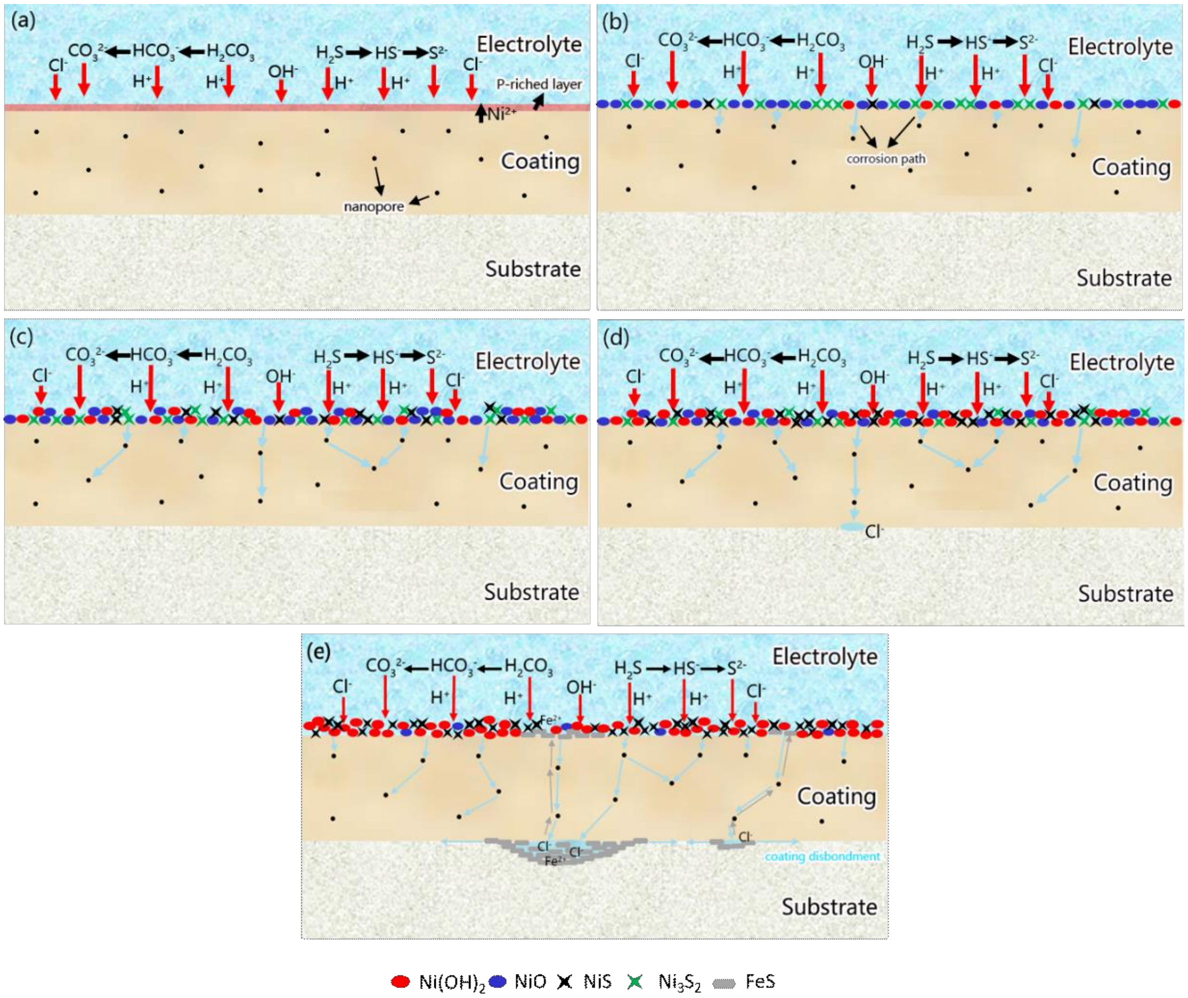

Figure 4.11 Schematic diagram of the corrosion process and coating disbonding mechanism of Ni-P coated steel in $CO_2/H_2S/Cl^-$ environment: (a) diffusion and adsorption of ions; (b) localized corrosion initiation; (c) corrosion product transformation; (d) further electrolyte penetration and (e) lateral coating disbondment and substrate consumption.

In the later stage (10 d or longer) (Figure 4.11e), more electrolyte reaches the coating/substrate interface, and thus creates more corrosion pathways and intensifies the localized corrosion. The corrosion process is governed by the rapid dissolution of the substrate due to the galvanic effect between Ni-P coating and Fe substrate, and the lateral penetration of electrolyte at the interface gives rise to the coating disbondment. Meanwhile, dissolved Fe ions diffuse outwards through the corrosion pathways and form FeS on the coating surface. Since the corrosion of coating itself is insignificant during the entire period and the galvanic corrosion leads to the severe corrosion of substrate, the coating thickness hardly changes, as shown in the previous SEM cross-sectional image (Figure 4.8d).

4.5 Conclusions

The corrosion rate of electroless Ni-P coating in CO_2/H_2S environment is higher than that in CO_2 environment because H_2S can promote corrosion by affecting both anodic and cathodic processes. The adsorbed $H_2PO_2^-$ layer only exists in the very early stage of corrosion and hardly contributes to the corrosion resistance of Ni-P coating. The corrosion resistance of Ni-P coating first increases and then decreases under both conditions and reaches the maximum values at around 24 h, and the temporary corrosion resistance improvement is ascribed to the formation of corrosion products (NiO and Ni_3S_2) formed on the coating surface. The presence of H_2S facilitates the electrolyte uptake of the coating, and dramatically reduces the stability of Ni-P coating, resulting in faster coating consumption, faster propagation of corrosion pathways and electrolyte penetration, and more severe localized corrosion and coating disbondment at the coating/steel interface. A corrosion model is proposed to interpret the corrosion and degradation process of the coating. The electrolyte penetration leaves corrosion pathways in the coating and initiates the localized corrosion. As corrosion proceeds, the formed NiO and Ni_3S_2 provide extra corrosion resistance, which declines with the transformation to other species. The corrosion process is then governed by the governed by the rapid dissolution of the substrate as the corrosive medium penetrates to the coating/substrate interface, and the lateral coating disbondment occurs afterwards.

4.6 References

1. M. Ueda, *Corrosion* 62, 10 (2006): p. 856.

2. M. F. Montemor, *Surf. Coat. Technol.* 258 (2014): p. 17.

3. M. Finšgar, J. Jackson, *Corros. Sci.* 86 (2014): p. 17.

4. M. Fenker, M. Balzer, H. Kappl, *Surf. Coat. Technol.* 257 (2014): p. 182.

5. M. Czagány, P. Baumli, G. Kaptay, *Appl. Surf. Sci.* 423 (2017): p. 160.

6. E. Georgiza, J. Novakovic, P. Vassiliou, *Surf. Coat. Technol.* 232 (2013): p. 432.

7. A. Akyol, A. Algul, M. Uysal, H. Akbulut, A. Alp, *Appl. Surf. Sci.* 453 (2018): p. 482.

8. H. Luo, M. Leitch, Y. Behnamian, Y. Ma, H. Zeng, J. L. Luo, *Surf. Coat. Technol.* 277 (2015): p. 99.

9. Z. Rajabalizadeh, D. Seifzadeh, *Appl. Surf. Sci.* 422 (2017): p. 696.

10. L. L. Wang, H. J. Chen, L. Hao, A. Lin, F. X. Gan, *Mater. Corros.* 62, 11 (2011): p. 1003.

11. H. Ashassi-Sorkhabi, M. Es'haghi, *Corros. Sci.* 77 (2013): p. 185.

12. S. Q. Guo, L. F. Hou, C. L. Guo, Y. H. Wei, *Mater. Corros.* 68, 4 (2017): p. 468.

13. B. Elsener, M. Crobu, M. A. Scorciapino, A. Rossi, *J. Appl. Electrochem.* 38, 7 (2008): p. 1053.

14. S. R. Allahkaram, M. H. Nazari, S. Mamaghani, A. Zarebidaki, *Mater. Design* 32,2 (2011): p. 750.

15. M. Crobu, A. Scorciapino, B. Elsener, A. Rossi, *Electrochim. Acta* 53, 8 (2008): p. 3364.

16. C. Sun, J. Li, S. Shuang, H. Zeng, J. L. Luo, *Corros. Sci.* 134 (2018): p. 23.

17. D. P. Li, L. Zhang, J. W. Yang, M. X. Lu, J. H. Ding, M. L. Liu, *Int. J. Min. Met. Mater.* 21,4 (2014): p. 388.

18. W. He, O. Ø. Knudsen, S. Diplas, *Corros. Sci.* 51 (2009): p. 2811.

19. Y. S. Choi, S. Nesic, S. Ling, *Electrochim. Acta* 56, 4 (2011): p. 1752.

20. J. Banaś, U. Lelek-Borkowska, B. Mazurkiewicz, W. Solarski, *Electrochim. Acta* 52, 18 (2007): p. 5704.

21. Z. F. Yin, W. Z. Zhao, W. Y. Lai, X. H. Zhao, *Corros. Sci.* 51 (2009): p. 1702.

22. X. H. Zhao, Y. Han, Z. Q. Bai, B. Wei, *Electrochim. Acta* 56, 22 (2011): p. 7725.

23. C. Sun, H. Zeng, J. L. Luo, *Corros. Sci.* 148 (2019): p. 317.

24. M. Stern, A. L. Geary, *J. Electrochem. Soc.* 104, 1 (1957): p. 56.

25. ASTM G59-97, "Standard test method for conducting potentiodynamic polarization resistance measurements" (West Conshohocken, PA: ASTM, 2014), p. 237.

26. L. Wei, X. L. Pang, K. W. Gao, *Corros. Sci.* 111 (2016): p. 637.

27. R. B. Diegle, N. R. Sorensen, C. R. Clayton, M. A. Helfand, Y. C. Yu, J. *Electrochem. Soc.* 135, 5 (1988): p. 1085.

28. A. Krolikowski, P. Butkiewicz, *Electrochim. Acta* 38 (1993): p. 1979.

29. R. B. Diegle, N. R. Sorensen, G. C. Nelson, *J. Electrochem. Soc.* 133, 9 (1986): p. 1769.

30. H. Habazaki, S. Q. Ding, A. Kawashima, K. Asami, K. Hashimoto, A. Inoue, T. Masumoto, *Corros. Sci.* 29, 11–12 (1989): p. 1319.

31. Q. Y. Wang, Y. Behnamian, H. Luo, X. Z. Wang, M. Leitch, H. Zeng, J. L. Luo, *Appl. Surf. Sci.* 419 (2017): p. 197.

32. T. A. Ho, C. Bae, H. Nam, E. Kim, S. Y. Lee, J. H. Park, H. Shin, *ACS Appl. Mater. Interfaces* 10, 15 (2018): p. 12807.

33. H. W. Nesbitt, D. Legrand, G. M. Bancroft, *Phys. Chem. Miner.* 27, 5 (2000): p. 357.

34. B. Elsener, M. Crobu, M. A. Scorciapino, A. Rossi, *J. Appl. Electrochem.* 38 (2008): p. 1053.

35. M. Hao, M. Xiao, Y. Yan, Y. Miao, *Adv. Powder. Technol.* 28, 11 (2017): p. 3095.

36. A. M. Venezia, R. Bertoncello, G. Deganello, *Surf. Interface Anal.* 23, 4 (1995): p. 239.

37. C. C. Wu, C. F. Yang, *Nanoscale Res. Lett.* 8 (2013): p. 33.

38. L. Q. Wu, Y. C. Li, S. Q. Li, Z. Z. Li, G. D. Tang, W. H. Qi, L. C. Xue, X. S. Ge, L. L. Ding, *AIP Adv.* 5, 9 (2015): p. 097210.

39. M. Matoba, S. Anzai, A. Fujimori, *J. Phys. Soc. Jpn.* 60 (1991): p. 4230.

40. X. Wang, Q. Xiang, B. Liu, L. Wang, T. Luo, D. Chen, G. Shen, *Sci. Rep.* 3 (2013): p. 2007.

41. J. Sun, C. Sun, G. Zhang, X. Li, W. Zhao, T. Jiang, H. Liu, X. Cheng, Y. Wang, *Corros. Sci.* 107 (2016): p. 31.

42. G. A. Zhang, Y. F. Cheng, *Corros. Sci.* 52 (2010): p. 2716.

43. E. Abelev, T. A. Ramanarayanan, S. L. Bernasek, *J. Electrochem. Soc.* 156, 9 (2009): p. C331.

44. S. Nesic, J. Postlethwaite, S. Olsen, *Corrosion* 52, 4 (1996): p. 280.

45. T. Dickinson, A. F. Povey, P. M. A. Sherwood, *J. Chem. Soc., Faraday Trans. 1* 73 (1977): p. 327.

46. J. M. Hernandez, D. H. Lim, H. V. P. Nguyen, S. P. Yoon, J. Han, S. W. Nam, C. W. Yoon, S. K. Kim, H. C. Ham, *Int. J. Hydrog. Energy*, 39, 23 (2014): p. 12251.

47. X. Cheng, H. Ma, S. Chen, X. Chen, Z. Yao, *Corros. Sci.* 42 (2000): p. 299.

48. A. Okuwaki, O. Kanome, T. Okabe, *Metall. Mater. B.* 15, 4 (1984): p. 609.

49. T. S. De Gromoboy, L. L. Shreir, *Electrochim. Acta* 11, 7 (1966): p. 895.

50. A. N. Buckley, R. Woods, *J. Appl. Electrochem.* 21, 7 (1991): p. 575.

51. B. I. Onyeachu, E. E. Oguzie, I. C. Ukaga, D. I. Njoku, X. Peng, *Port. Electrochim. Acta* 35, 3 (2017): p. 127.

5 Role of Ca^{2+} in the corrosion behavior and film characteristics of N80 steel and electroless Ni-P coating at high temperature and high pressure

ABSTRACT: The effects of Ca^{2+} on the corrosion behavior and film characteristics of N80 carbon steel and electroless Ni-P coating at high temperature and high pressure were investigated by immersion tests, *in-situ* electrochemical measurements, surface characterization techniques and water chemistry analysis. The results demonstrate that the corrosion of N80 steel is significantly influenced by Ca^{2+} concentrations, which not only alters the corrosion film microstructure, but also changes the water chemistry of the aqueous phase. Meanwhile, Ni-P coating exhibits exceptional corrosion resistance regardless of Ca^{2+} concentration, owing to the protection of the formed $NiO/Ni(OH)_2$ film and the absence of scale formation.

5.1 Introduction

Calcium (Ca^{2+}) ions are commonly present in the formation brines in oil and gas fields. As the fundamental element of scale formation, the presence of Ca poses a significant risk to the metal constructions applied in oil and gas industries owing to the close relation between scaling and corrosion [1–5]. A recent case study reported the failures of slotted liners in the production wells of a steam-assisted gravity drainage (SAGD) system in Northern Alberta, Canada, and it was validated that slots suffered plugging and corrosion after exposed in the Ca-containing brine environment, which notably decreased the production efficiency [6]. Hence, it necessitates the need to elaborate the role of Ca^{2+} in the corrosion behavior and scale formation of oil country tubular goods (OCTG) in oil and gas industry.

In recent decades, the effects of Ca^{2+} on the corrosion of carbon steel has drawn growing attentions [7–13], and some controversies also arise due to the discrepancies in the test conditions and studied materials, which remains as an obstacle in understanding the actual corrosion mechanism in light of the influence of Ca^{2+} and providing guidance for corrosion prevention in the SAGD system. Some researchers believed that the added Ca^{2+} promoted corrosion [7,12], while others stated that corrosion rates were reduced by the introduction of Ca^{2+} [9,10,13]. Nonetheless, it has been well-accepted that the effect of Ca^{2+} is primarily accredited to the corrosion product film on carbon steel surface, therefore the corrosion film characteristics play a decisive role in the corrosion behavior of carbon steels. Researchers have proposed that Ca^{2+} concentration can affect the chemical composition of the corrosion film, where a protective $FeCO_3$ and/or $Fe_xCa_yCO_3$ layer is formed when Ca^{2+} concentrations is lower, whereas high Ca^{2+} concentrations lead to the formation of non-protective $CaCO_3$ [8]. However, most of the research correlated the corrosion resistance with the corrosion film properties without further explanation, and few efforts have been devoted to the change of the corrosion film microstructure (e.g., crystallinity, porosity, etc.) caused by Ca^{2+} concentrations. From this perspective, it is highly desirable to explore the microstructural variations of the corrosion product film in the presence of Ca^{2+}. In addition, the precipitation of corrosion product greatly relies on the water chemistry factors, such as pH, saturation degree and ion concentration, etc. Hence, the influence of water chemistry should also be taken into consideration. Moreover, SAGD systems are typically operated under high temperature/high pressure (HT/HP) conditions, however, most of Ca-related researches only focus on the corrosion behavior below the boiling temperature and the results cannot be extrapolated to predict corrosion in HT/HP oil-related environments. Besides, vast majority of studies have evaluated the corrosion rates by using weight loss method, which only provides a general tendency of corrosion, but cannot precisely reflect the electrochemical process at the corrosion product film. In this regard, it necessitates the need to perform *in-situ* electrochemical measurements of carbon steels under HT/HP conditions to correlate the corrosion rate with the electrochemical process and further reveal the effect of Ca^{2+} on the corrosion behavior of carbon steel from an electrochemical point of view.

To mitigate corrosion in oil/gas related environments as mentioned above, to date, effective approaches such as corrosion-resistant alloys (CRAs) and protective coatings, have been proposed to mitigate the corrosion in oil/gas related environments [12–14]. CRAs are normally considered as a good option because of their outstanding corrosion resistance, but the likelihood of undergoing localized corrosion and the high cost limit its broader applications. Protective coatings have gained much popularity due to the efficient protectiveness and increasing applications. In this regard, electroless Ni-P coating, recognized as one of the most promising metallic coatings, has been utilized in oilfields on account of the satisfactory anti-corrosion and mechanical properties, reasonable cost, and simplified fabrication process [15–18]. Related research indicates that Ni-P coating exhibits good corrosion resistance in brines in the presence of CO_2 and Cl^- both at room temperature [19,20] and elevated temperatures [21]. It is generally believed that the satisfactory corrosion performance is credited to the formation of the adsorbed $H_2PO_2^-$ layer which serves as a physical barrier and retards the diffusion of corrosive electrolyte into the inside of coating [22,23], but recent reports have pointed out that the formed nickel-rich corrosion film contributes to the excellent corrosion resistance [24]. In light of the abundant presence of Ca element in oilfield environments, the influence of Ca on the coating properties is one of factors that determines its extensive applications in the future. Nevertheless, as of this writing, studies addressing the corrosion behavior of Ni-P coating in Ca^{2+}-containing environments under HT/HP conditions have not been reported yet. Therefore, an in-depth understanding of Ca^{2+}-dependent corrosion behavior of Ni-P coating is highly necessitated, and the interaction between Ca^{2+} ions and the formed nickel-rich corrosion film needs to be explored, to validate the applications of Ni-P coating in Ca^{2+}-rich oil-related environments.

Hence, in this study, the corrosion behavior and film characteristics of N80 carbon steel and electroless Ni-P coating in Ca^{2+}-containing CO_2-saturated HT/HP environments were investigated by means of immersion tests, *in-situ* electrochemical measurements and surface analysis techniques. The role of Ca^{2+} in the film forming process, together with its impact on the corrosion protection performance, was discussed in detail with water chemistry taken into consideration. This study is anticipated to provide new insights into the Ca-induced corrosion behavior of carbon steel and further address the feasibility of Ni-P coating in oil and gas applications in the existence of Ca^{2+}.

5.2 Experimental

5.2.1 Material preparation

N80 tubing steel, with the composition (wt. %) of 0.29 C, 0.25 Si, 1.38 Mn, 0.002 P, 0.002 S, 0.037 Cr, 0.002 Ni, 0.009 Cu and Fe balance, was used in this study. The samples were machined to the dimension of 35 mm × 10 mm × 3 mm. Prior to tests, all the surfaces were ground sequentially to 1,200 grit, degreased with acetone and alcohol and cleaned with deionized water. Electroless Ni-P coating was coated on the cleaned N80 steel samples. The coating procedure, including degreasing, surface activation and electroless plating, is illustrated in Figure 5.1 (See details in Supporting Information), and Table 5.1 lists the chemical composition of the coating bath and plating conditions.

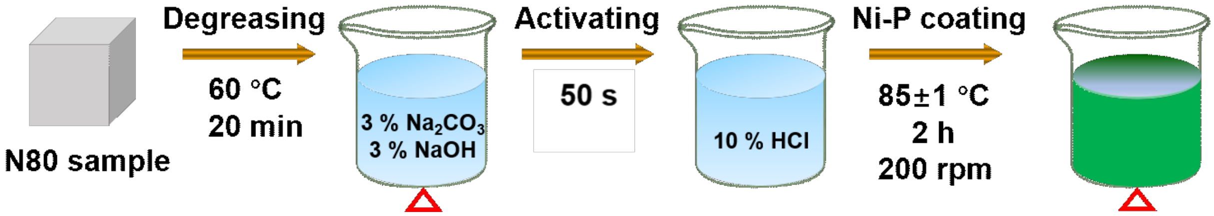

Figure 5.1 Schematic of electroless Ni-P coating procedure.

Table 5.1 Chemical composition of electroless Ni-P coating bath and plating condition.

Reagent	Concentration	Plating condition
Nickel sulphate ($NiSO_4 \cdot 6H_2O$)	25 g/L	Temperature: (85±1) °C
Sodium hypophosphite ($NaH_2PO_2 \cdot H_2O$)	30 g/L	Plating time: 120 min
Lactic acid ($C_3H_6O_3$)	20 mL/L	Stirring rate: 200 rpm
Citric acid ($C_6H_8O_7$)	19 g/L	pH: 5.5–6.0
Succinic acid ($C_4H_6O_4$)	14 g/L	Loading capacity: 1 dm^2/L
Saccharin ($C_6H_4SO_2NNaCO \cdot 2H_2O$)	0.06-0.08 g/L	
Sodium dodecyl sulfate ($C_{12}H_{25}SO_4Na$)	0.04 g/L	
Lead nitrate ($Pb(NO_3)_2$)	1 mg/L	
Sodium hydroxide (NaOH)	28 g/L	

5.2.2 Weight loss tests

The immersion tests were performed in a 1.5 L autoclave under the test conditions listed in the test matrix (Table 5.2). The test solution is NaCl/$CaCl_2$ solution with a fixed Cl^- concentration of 22,009 ppm to avoid Cl^- impact. The samples were hung in the autoclave to avoid any possible galvanic effects during the immersion. Four parallel samples were tested under each condition, three of which were weighed via an electronic balance (0.1 mg precision) prior to the test. Highly purified N_2 gas was purged into the autoclave to deoxygenate for 2 h, followed by adding N_2/CO_2 mixed gas to reach the required partial pressure. The experiment started at the time point when the required operating temperature was reached. After the immersion tests, the samples were cleaned with deionized water and alcohol and dried in air. Three of the four samples were descaled in the pickling solution. A solution of 500 mL hydrochloric acid, 500 mL deionized water and 5 g hexamethylenetetramine was used for N80 steel, and the Ni-P coated samples were descaled in the solution consisting of 150 mL hydrochloric acid and 850 mL deionized water. The descaled samples were weighed again, and the corrosion rate (CR, mm/y) was calculated by the equation given below:

$$CR = \frac{8.76\times10^4(W_0-W_1)}{S\rho t} \qquad \text{(Eq. 5.1)}$$

where W_0 and W_1 are the masses of the sample before the test and after descaling, respectively, g; S is the total exposed area, cm^2; ρ is the density of the material, g/cm^3; t is the immersion time, h.

Table 5.2 Immersion test matrix.

Solution	Ca^{2+} concentration (ppm)	Temperature (°C)	Pressure (MPa)	Time (d)
$NaCl/CaCl_2$	0 100 1000 2000 10000	150	3.8 (2 CO_2+1.8 N_2)	7

5.2.3 *In-situ* electrochemical measurements

In-situ electrochemical tests were performed under HTHP conditions in the autoclave by using a Gamry Interface 1000E Electrochemical Workstation, with the specimens as the working electrode (WE), a carbon rod as the counter electrode (CE) and an Ag/AgCl electrode as the reference electrode (RE). The exposed area of each sample is 1 cm^2, and the deoxygenating and purging process and test solution follow the same procedure for the immersion tests. The samples were first immersed for 24 h to achieve the pre-filmed surface and a steady-state open-circuit potential (OCP). The findings of Shamsa et al. indicated that most of the corrosion products had precipitated in CO_2-saturated Ca^{2+}-containing brines after 24 h at 150 °C due to the extremely fast kinetics [11], therefore the corrosion protection characteristics of the corrosion film can be evaluated by electrochemical impedance spectroscopy (EIS), which was carried out at OCP with an alternating current (AC) amplitude of 10 mV in the frequency range from 100 kHz to 10 mHz. The measured EIS data were then fitted with appropriate electric equivalent circuits

(EEC) by ZSimpWin software. All the electrochemical tests were carried out at least three times to ensure the reproducibility.

5.2.4 Surface characterizations and water chemistry analysis

The surface morphologies of corrosion film and the pitting profile of the substrate were observed by scanning electron spectroscope (SEM) and optical stereo microscope (OSM) after the autoclave tests. The chemical composition, phase structure and chemical valence were characterized by energy-dispersive X-ray spectroscopy (EDS), X-ray diffraction (XRD) and X-ray photoelectron spectroscopy (XPS), respectively. XRD was performed with a Cu K_α X-ray source operated at 40 kV and 44 mA, and the patterns were recorded from 20° to 80° at a scanning rate of 4°/min. The C 1s peak at the binding energy of 284.6 eV was used to calibrate the shifted XPS data. The pH value and ion concentrations under each condition was calculated by using OLI Analyzer software using the "Aqueous (H^+ ions)" thermodynamic model.

5.3 Results

5.3.1 Morphological and chemical characterizations of Ni-P coating

Figure 5.2 shows the morphologies and chemical compositions of the as-deposited Ni-P coating. A nodular structure is observed from Figure 5.2a, and the weight ratio of Ni/P is around 88/12, indicating a high-phosphorus Ni-P coating. As shown in Figure 5.2b, the coating is uniformly and closely attached on the steel substrate with homogenous distributions of Ni and P elements, confirmed by EDS line scan results. Moreover, the coating displays an amorphous structure due to the relatively high P elements, verified by the broad Ni peak at $2\theta \approx 44°$ in Figure 5.2c.

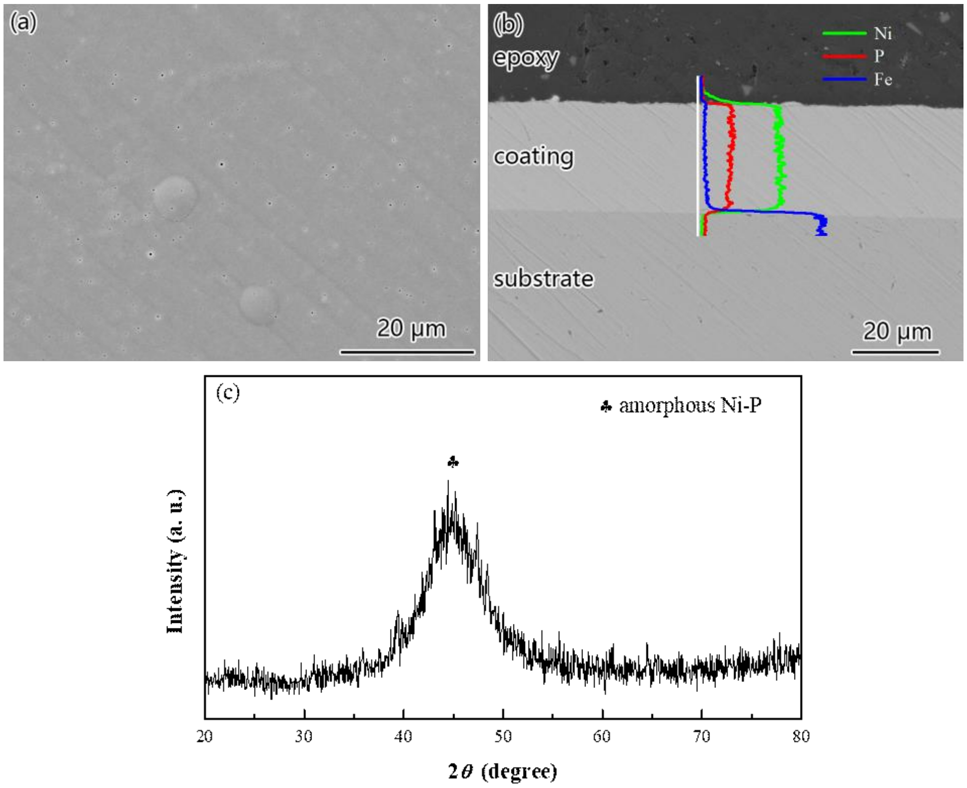

Figure 5.2 (a) SEM surface morphology and corresponding EDS results, (b) SEM cross-sectional morphology and EDS mapping analysis and (c) XRD pattern of as-deposited Ni-P coating.

5.3.2 Corrosion rates of N80 steel and Ni-P coating

Figure 5.3 exhibits the general corrosion rates of N80 steel and Ni-P coating under different test conditions. The corrosion rate of N80 steel is relatively low (0.0180 mm/y) in the solution without Ca^{2+}. The addition of 100 ppm Ca^{2+} leads to an increase by nearly 6 times (0.1059 mm/y), and the corrosion rate greatly increases to 0.2874 mm/y with the addition of 1,000 ppm Ca^{2+}. The maximum corrosion rate appears at 2,000 ppm Ca^{2+} (0.3589 mm/y) and reduces slightly to 0.3070 mm/y as Ca^{2+} concentration rises to 10,000 ppm. Unlike N80 steel, the corrosion rate of Ni-P coating increases with the Ca^{2+} concentration and reaches its maximum of 0.0284 mm/y at 10,000 ppm Ca^{2+}, indicating a significant corrosion inhibition of the coating. The corrosion inhibition efficiency (CIE) is further calculated to evaluate the corrosion resistance performance of Ni-P coating following the given equation:

$$CIE\% = \frac{CR_{N80} - CR_{Ni-P}}{CR_{N80}} \times 100\% \qquad \text{(Eq. 5.2)}$$

where CR_{N80} and $CR_{\mathrm{Ni\text{-}P}}$ are corrosion rates of N80 steel and Ni-P coating, respectively. As presented in Figure 5.3, the CIE values increase from 74.21 without Ca^{2+} to higher than 90 after introducing Ca^{2+}, suggesting that Ni-P coating exhibits even better resistance to corrosion in the presence of Ca^{2+}, and Ca^{2+} concentration barely influences the corrosion protection effectiveness of the coating.

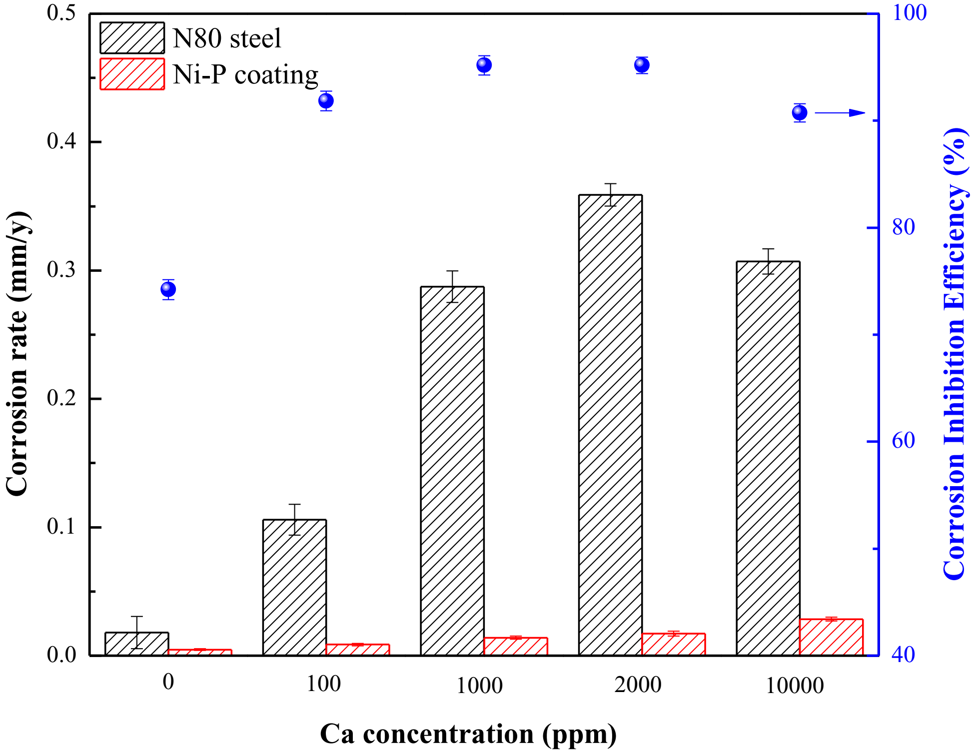

Figure 5.3 Corrosion rates and corrosion inhibition efficiency of N80 steel and Ni-P coating immersed in CO_2-saturated brines with different Ca^{2+} concentrations at 150 °C and 3.8 MPa for 7 d.

5.3.3 Corrosion film characteristics of N80 steel and Ni-P coating

5.3.3.1 XRD and XPS analysis of corrosion products

The XRD patterns of corrosion products for N80 steel were shown in Figure 5.4. The XRD patterns indicate that $FeCO_3$ is the predominant corrosion product at lower Ca^{2+} concentrations, while the corrosion film in the 10,000 ppm Ca^{2+} case is mainly composed by $CaCO_3$ and $FeCO_3$. In fact, Ca atoms tend to incorporate into $FeCO_3$ crystal lattices by substituting Fe atoms, thereby forming $Fe_xCa_{1-x}CO_3$ compound [5,8,9]. The most intense diffraction, with respect to the *hkl* (104) Bragg peak, for $FeCO_3$ and $CaCO_3$ are positioned at 2θ values of 32.07° and 29.42°, respectively. As shown in Figure 5.4(a–d), the addition of Ca^{2+} leads to a gradual shift of $FeCO_3$ peaks towards $CaCO_3$ with the increase of Ca^{2+} concentrations. Furthermore, Fe peak can be found under all conditions, but the intensity increases with Ca^{2+} concentrations, which reveals that the thickness of corrosion film declines so that the X-ray beam reaches the steel substrate. The XRD pattern of Ni-P coating still displays a sole broaden Ni peak (see Figure S5.1), similar to the as-deposited coating, highlighting that trace amount of corrosion product was formed on the coating surface exposed to 10,000 ppm Ca^{2+} for 7 d, which is credited to the superior anti-corrosion and anti-scaling performance of the coating.

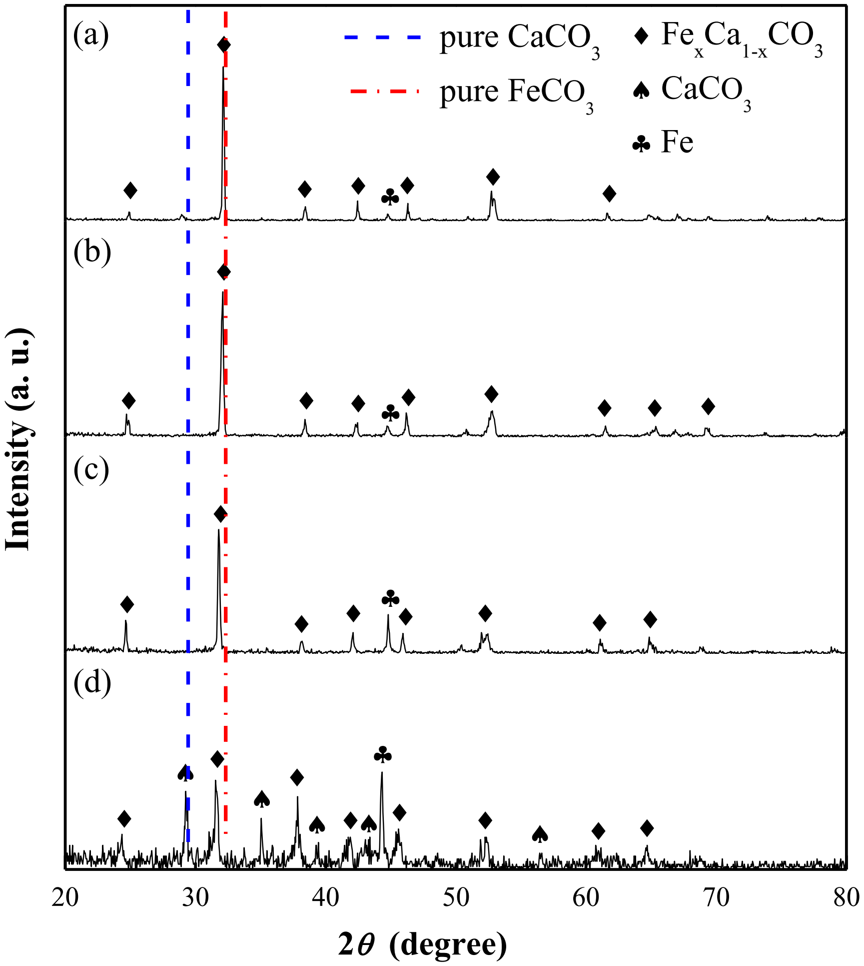

Figure 5.4 XRD patterns of N80 steel exposed to CO_2-saturated brines with different Ca^{2+} concentrations of (a) 0 ppm; (b) 100 ppm; (c) 1,000 ppm and (d) 10,000 ppm at 150 °C and 3.8 MPa for 7 d.

Since XRD pattern of Ni-P coating provides limited information on the thin corrosion film, XPS analysis was performed to elucidate its chemical composition, as seen in Figure 5.5. The peaks at 856.2 eV ($2p_{3/2}$) and 874.0 eV ($2p_{1/2}$) suggest the presence of Ni^{2+} along with their satellite peaks at 861.5 eV and 879.8 eV, respectively [25,26]. The Ca 2p spectra contain $2p_{3/2}$ and $2p_{1/2}$ doublets at the binding energy of 347.1 eV and 350.7 eV, respectively, indicative of Ca^{2+}-containing compounds [27]. The detailed peak deconvolution results of C 1s and O 1s spectra and the corresponding species are summarized in Table 5.3 [28–31], and the results reveal that the corrosion film on the coating surface mainly consists of NiO and $Ni(OH)_2$ with trace amounts of carbonates. The weak signal of Fe^{2+} peaks implies that the electrolyte penetration through the coating to the steel substrate is limited after 7 d of immersion, and the absence of P peaks is ascribed to the complete dissolution of P species in the coating [21,24].

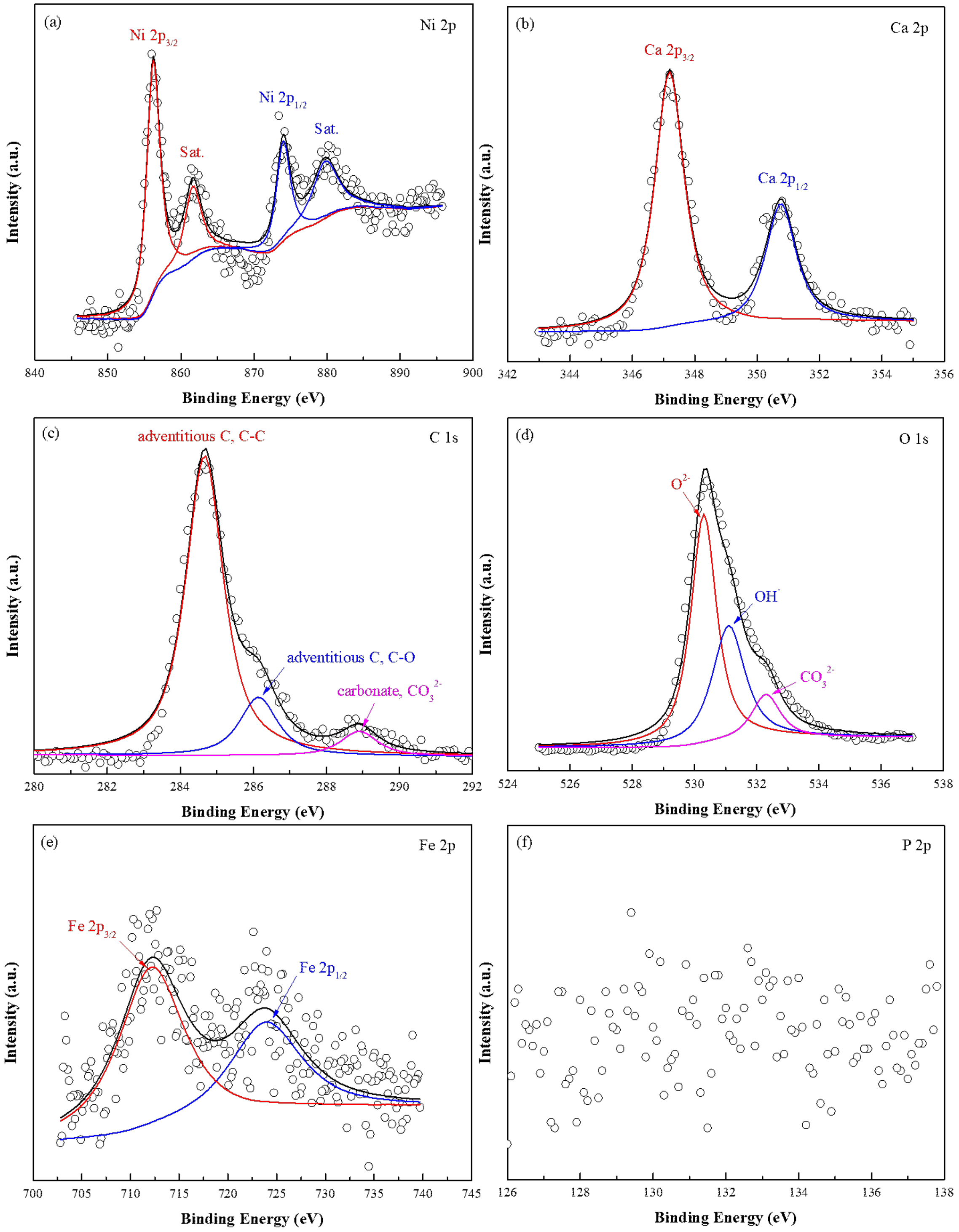

Figure 5.5 XPS patterns of corrosion product on the surface of Ni-P coating after 7 d of immersion in CO$_2$-saturated brines with 10,000 ppm Ca^{2+} at 150 °C and 3.8 MPa: (a) Ni 2p; (b) Fe 2p; (c) Ca 2p; (d) C 1s; (e) O 1s; (f) P 2p.

Table 5.3 Summary of fitted binding energies and the corresponding species of the XPS spectra in Figure 5.5.

Element	Binding energy (eV)	Fitted species
C 1s	284.6	Adventitious C, C-C
	286.2	Adventitious C, C-O [30]
	289.0	CO_3^{2-} [31]
O 1s	530.3	O^{2-} [32]
	531.1	OH^- [27]
	532.3	CO_3^{2-} [33]

5.3.3.2 Morphological observations and EDS analysis after immersion tests

The SEM surface morphologies of N80 steel after immersion tests with various Ca^{2+} concentrations are shown in Figure 5.6. It can be seen obviously that the morphological structure of corrosion product is greatly influenced by Ca^{2+} concentrations. At lower concentrations (less than 2,000 ppm), $FeCO_3$ crystals are formed on the surface, and the crystal size reduces upon increasing the Ca^{2+} concentration. Besides, increasing number of lamellar structures appears on the $FeCO_3$ crystals as Ca^{2+} concentration rises, and apparent defects on the crystal edges can be observed at 2,000 ppm, as seen in the magnified image in Figure 5.7a. These phenomena are due to the replacement of Ca atoms into the $FeCO_3$ lattice, which gets more intense with the increase of Ca^{2+} concentrations, as revealed from the Ca contents in the corrosion film by EDS in Table 5.4. As Ca^{2+} concentration further increases up to 10,000 ppm, the crystalline structure is no longer observed and transforms amorphously. To further determine the critical Ca^{2+} concentration that causes the microstructure transformation and elucidate the film forming mechanism, additional concentrations (2,500 ppm, 3,000 ppm and 5,000 ppm) were also introduced, as seen in

Figure 5.6(e–g). Morphological change is observed when Ca^{2+} concentration is higher than 2,500 ppm, implying that the critical concentration that triggers this structural variation lies between 2,000 and 2,500 ppm. It is also worth noting that the porosity of corrosion film declines with increasing Ca^{2+} concentration, implying that the substitution of Ca can fill the gap between collapsed $FeCO_3$ crystals, thereby enhancing the protectiveness of the corrosion film. Furthermore, the corrosion film gets more compact at higher Ca^{2+} concentrations, and the local enrichment of Ca is detected at 10,000 ppm Ca^{2+} from the EDS results in Figure 5.7b.

Table 5.4 Elemental compositions (at.%) of corrosion product on N80 steel exposed to CO_2-saturated brines with different Ca^{2+} concentrations at 150 °C and 3.8 MPa for 7 d.

Ca^{2+} concentration (ppm)	Fe	Ca	C	O
0	26.91	-	18.35	54.74
100	30.02	0.94	17.54	51.50
1,000	32.71	4.36	15.99	46.95
2,000	25.27	6.99	13.25	54.49

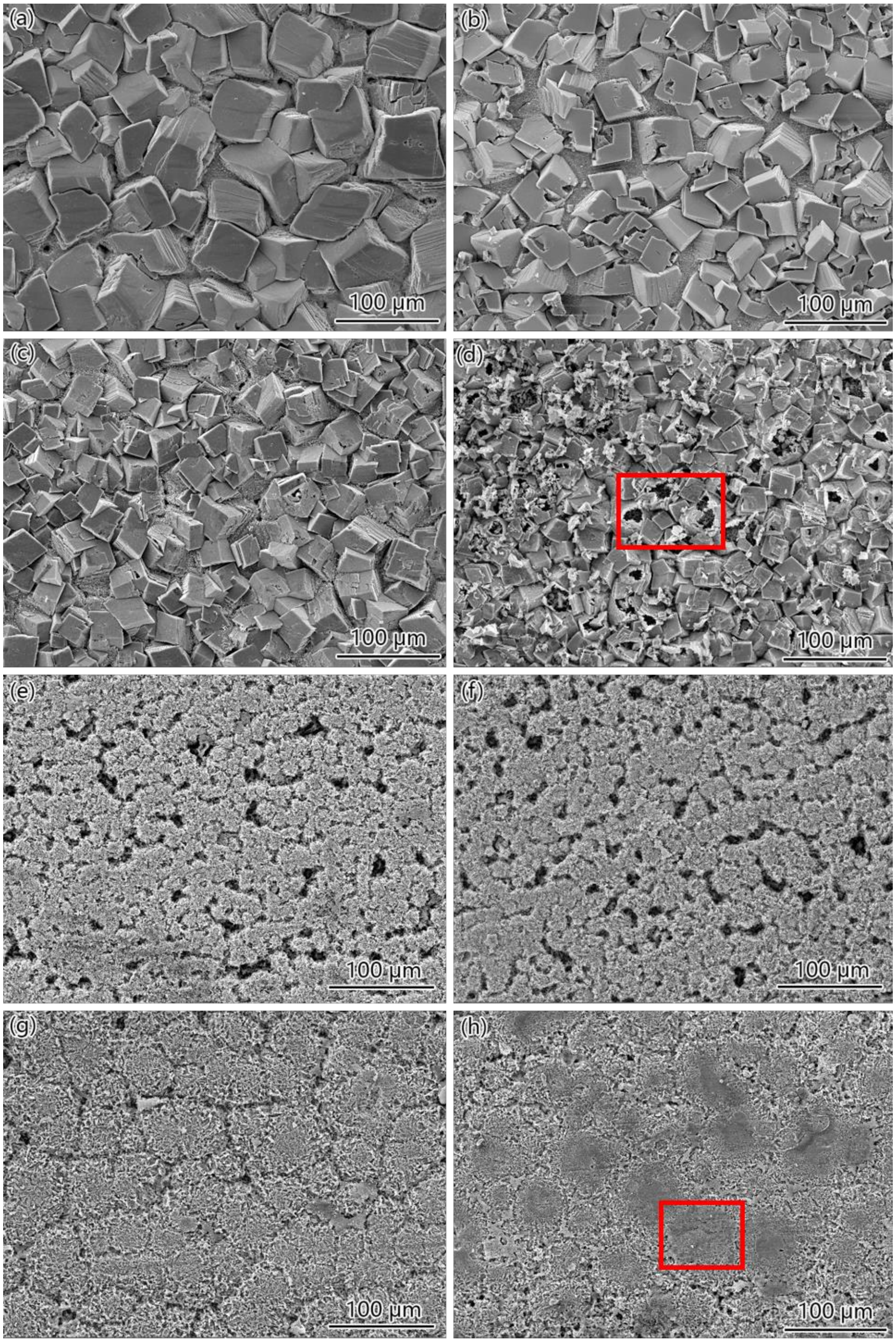

Figure 5.6 SEM surface morphologies of N80 steel after immersed in CO_2-saturated brines with various Ca^{2+} concentrations at 150 °C and 3.8 MPa for 7 d: (a) 0 ppm; (b) 100 ppm; (c) 1,000 ppm; (d) 2,000 ppm; (e) 2,500 ppm; (f) 3,000 ppm; (g) 5,000 ppm; (h) 10,000 ppm.

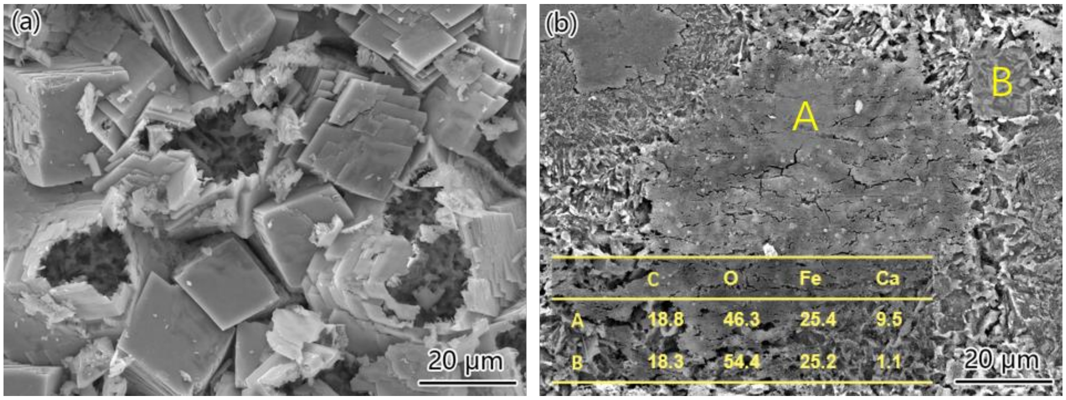

Figure 5.7 Magnified images in the red box in (a) Figure 5.6d and (b) Figure 5.6h.

Figure 5.8 presents the SEM cross-sectional images of N80 steel at various Ca^{2+} concentrations and the corresponding EDS line scan results. A thick layer of $FeCO_3$ corrosion film is formed and well attached to the substrate without Ca^{2+}. When Ca^{2+} concentration increases to 1,000 ppm, the corrosion film becomes thinner and more porous, along with the initiation of localized corrosion. As Ca^{2+} concentration further rises to 10,000 ppm, the corrosion film layer gets denser and more compact due to more involvement of Ca atoms, and a Ca-rich layer can be observed in the outer layer of the corrosion film, which is also validated in a previous study [5]. Moreover, a higher Ca^{2+} concentration also results in more severe localized corrosion of the steel substrate. The depth profiles of corrosion pits on the surfaces of N80 steel after 7 d of immersion were evaluated by OSM as presented in Figure 5.9. Under 1,000 ppm Ca^{2+} condition, many localized active sites emerge on the surface and evolve as shallow corrosion pits. The number of pits notably decreases with the increase of Ca^{2+} concentration, but the pit depth rises significantly, indicative of a higher localized corrosion susceptibility in the Ca^{2+}-richer environment.

SEM surface and cross-sectional morphologies of Ni-P coating and the corresponding EDS analysis are shown in Figures 5.10 and 5.11, respectively. The coating displays an obvious nodular structure with no noticeable corrosion product when the added Ca^{2+} concentration is less than 1,000 ppm. A thin corrosion film layer is formed at 10,000 ppm Ca^{2+}, and some cracks can be found at the nodular boundaries, which may be caused by the dehydration during the SEM preparation process. This layer is also substantiated by the EDS line scan results in Fig. 11b, which contains Ca element besides Fe, C and O elements. Furthermore, the coating is well attached to the substrate and no apparent corrosion pathways or localized corrosion of the substrate is detected, implying that the coating exhibits outstanding corrosion resistance in the CO_2-saturated HT/HP environment abundant with Ca^{2+} as compared to N80 steel.

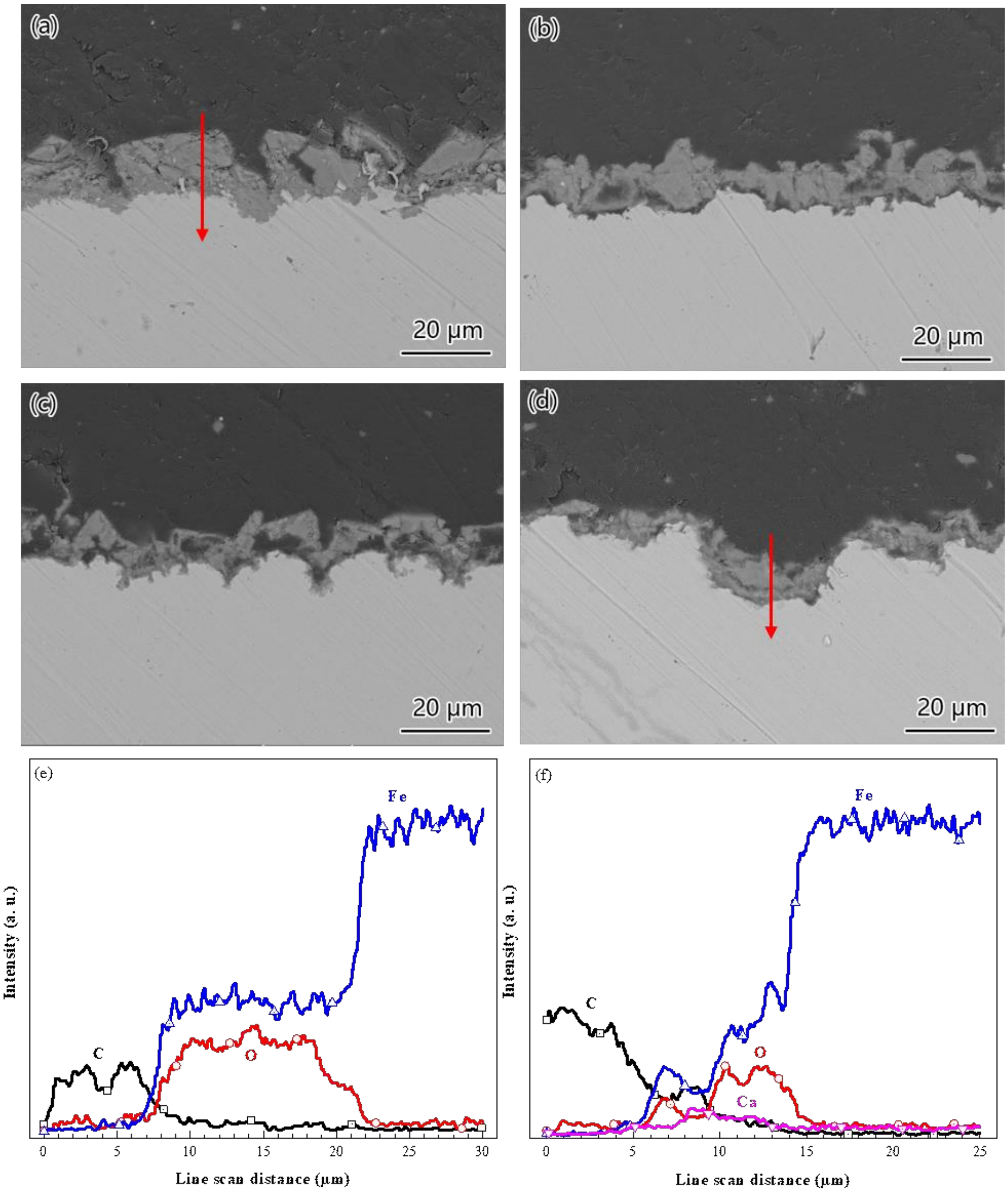

Figure 5.8 SEM cross-sectional morphologies of N80 steel after immersed in CO_2-saturated brines with different Ca^{2+} concentrations at 150 °C and 3.8 MPa for 7 d: (a) 0 ppm; (b) 100 ppm; (c) 1,000 ppm; (d) 10,000 ppm; (e) (f) elemental distributions of the cross-section denoted by the red arrow lines in (a) and (d), respectively.

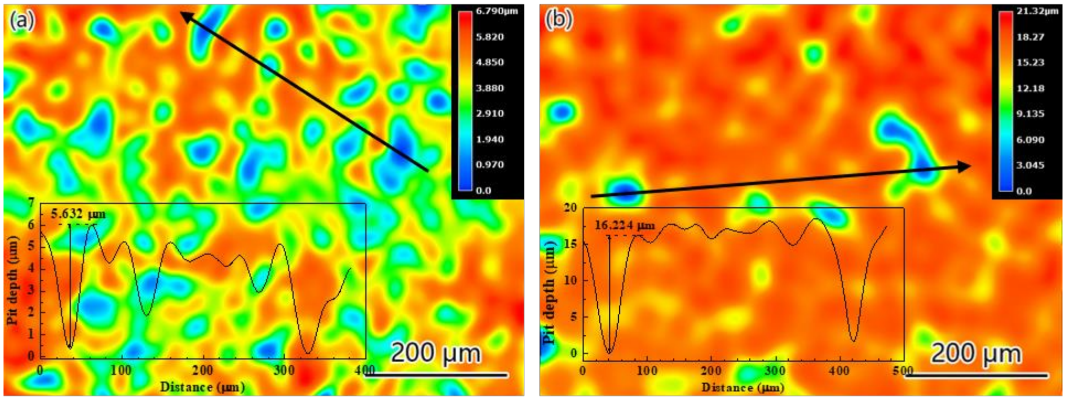

Figure 5.9 OSM morphologies of descaled N80 steel exposed in CO_2-saturated brines with different Ca^{2+} concentrations at 150 °C and 3.8 MPa for 7 d: (a) 1,000 ppm and (b) 10,000 ppm (The insets indicate the depth profiles along the black arrow line in each image).

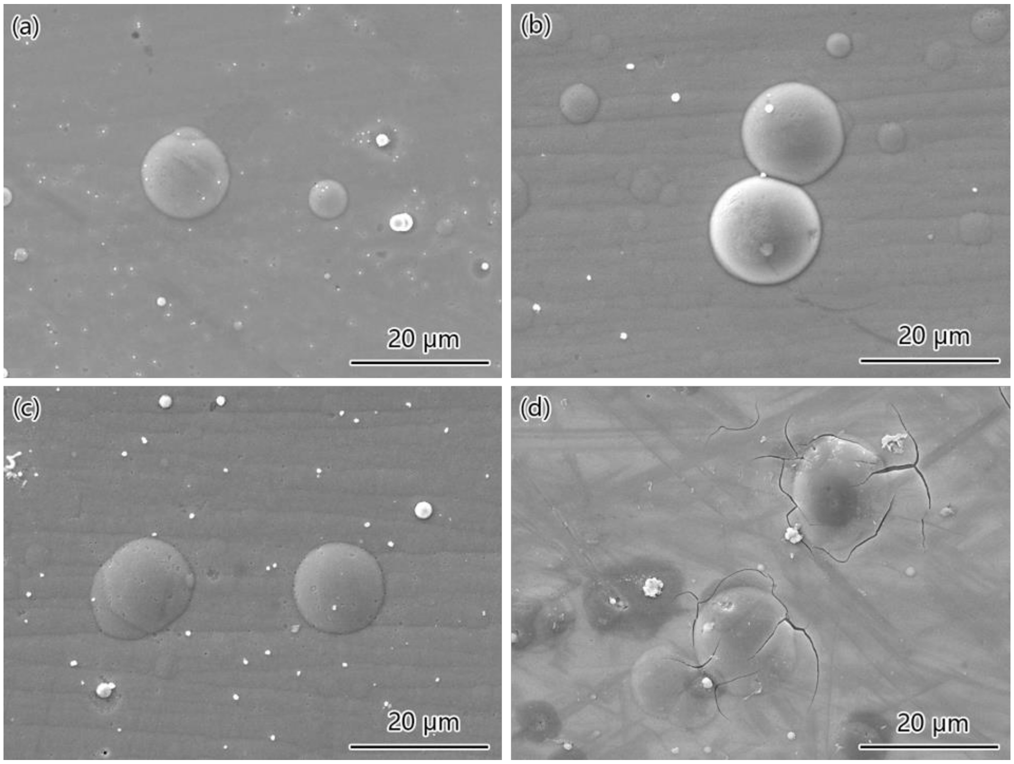

Figure 5.10 SEM surface morphologies of Ni-P coating exposed to CO_2-saturated brines with different Ca^{2+} concentrations at 150 °C and 3.8 MPa for 7 d: (a) 0 ppm; (b) 100 ppm; (c) 1,000 ppm; (d) 10,000 ppm.

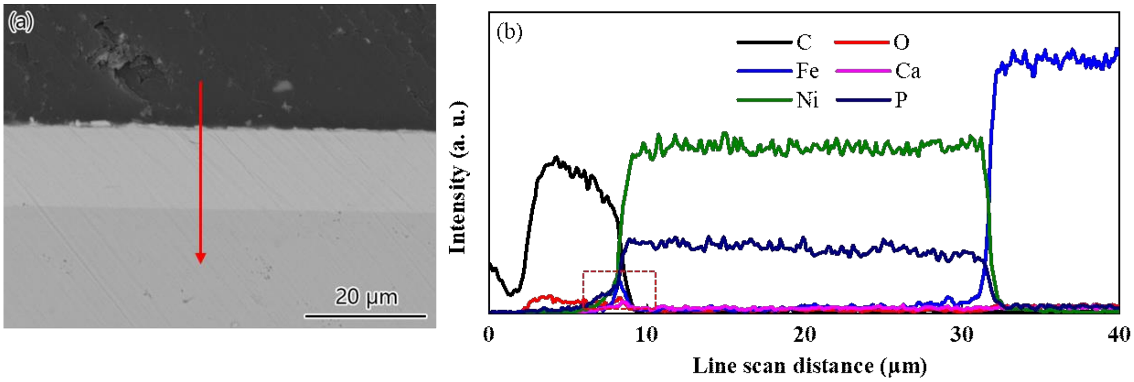

Figure 5.11 (a) SEM cross-sectional morphologies of Ni-P coating immersed in CO_2-saturated brines with 10,000 Ca^{2+} concentrations at 150 °C and 3.8 MPa for 7 d; (b) elemental distribution of the cross-section denoted by the red arrow line in (a).

5.3.4 *In-situ* electrochemical performance of N80 steel and Ni-P coating

Figure 5.12 depicts the Nyquist and Bode plots of uncoated and coated N80 steel with various Ca^{2+} concentrations to reveal its effect on the protectiveness of the formed corrosion film. For N80 steel, one conductive loop is revealed at high-medium frequencies corresponding to the corrosion film and a second incomplete conductive loop is present at low frequencies related to the electric double layer at film/substrate interface. The shape of the curve does not change with Ca^{2+} concentrations, an indication of unchanged corrosion mechanism, but the variation of radius implies the fluctuated protectiveness of the corrosion film. The coating exhibits much higher impedance than N80 steel, and its Nyquist plots can be characterized with a capacitive loop at high frequencies representing the thin $NiO/Ni(OH)_2$ film, and the superposition of a medium-low-frequency capacitive loop, ascribed to the electric double layer at film/coating interface, and the Warburg impedance (W) in low frequencies, indicated by a straight line, suggesting the diffusion-limited corrosion process.

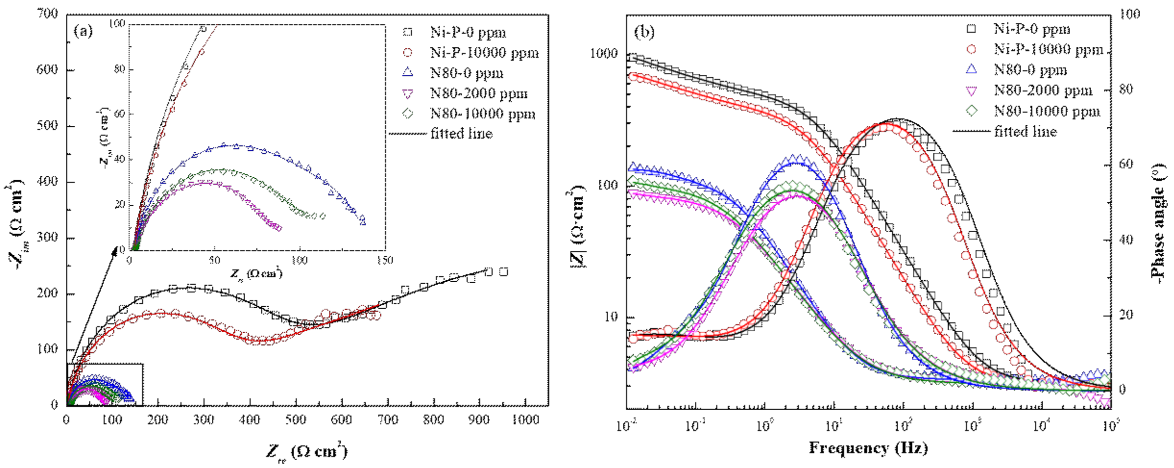

Figure 5.12 (a) Nyquist plot and (b) Bode plot of N80 steel and Ni-P coating exposed to CO_2-saturated brines with various Ca^{2+} concentrations at 150 °C and 3.8 MPa for 24 h.

The EIS data are fitted by using the EECs in Figure 5.13, and the fitted parameters are listed in Table 5.5. In the circuit, R_s is the solution resistance, R_{ct} is the charge transfer resistance, and Q_{dl} is the capacitance of the electric double layer. R_f and Q_f are the resistance and capacitance of the corrosion film on the surface. The constant phase element (CPE) is introduced in the ECCs (designated as Q_{dl} and Q_f) to replace pure capacitance for a better fitting, and its admittance is given as [32]:

$$Y(Q) = Y_0(Q)(j\omega)^n \qquad \text{(Eq. 5.3)}$$

where $Y_0(Q)$ is the admittance constant of CPE; j is the imaginary number; ω is the angular frequency; n is the empirical exponent. Z_w is the Warburg impedance, and its definition is [32]:

$$Z_w = \frac{1}{Y_0(W)}(j\omega)^{-0.5} \qquad \text{(Eq. 5.4)}$$

where $Y_0(W)$ is the admittance constant of W. It is found in Table 5.5 that results obtained in the 2,000 ppm Ca^{2+} test show the lowest R_f and R_{ct} and highest $Y_0(Q_{dl})$, followed by those in 10,000 ppm and 0 ppm, suggesting that the incorporation of Ca from 0 to 2,000 ppm reduces the scale resistance and promotes the electrochemical process, and the resistance increases as the concentration rises to 10,000 ppm, inhibiting corrosion consequently. As compared to N80 steel, the coating is regarded as "substrate" in the EEC and the electric double layer is located at film/coating interface, because the electrolyte penetration cannot reach the coating/steel interface after pre-filming for 24 h before the electrochemical tests. The coating exhibits much higher R_f and lower $Y_0(Q_f)$, implicative of good isolation property of the NiO/$Ni(OH)_2$ film between the corrosive electrolyte and the coating, which results in the retarded electrochemical process, as confirmed by the declined $Y_0(Q_{dl})$ and increased R_{ct} in the coating system. The coating still displays comparative corrosion resistance with the addition of 10,000 ppm Ca^{2+}, despite a slight decrease of R_f and R_{ct}. In addition, an increase of $Y_0(W)$ from 1.80×10^{-3} $\Omega^{-1}\cdot cm^{-2}\cdot s^{0.5}$ to 2.29×10^{-2} $\Omega^{-1}\cdot cm^{-2}\cdot s^{0.5}$ indicates a faster diffusion rate with the existence of 10,000 ppm Ca^{2+}.

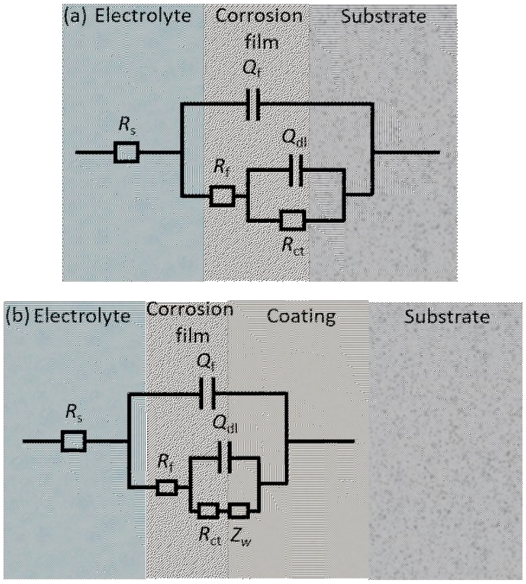

Figure 5.13 Equivalent electrical circuit models for EIS data fitting: (a) N80 steel and (b) Ni-P coating.

Table 5.5 Fitted electrochemical parameters from EIS data in Figure 5.12.

Specimen-[Ca^{2+}] (ppm)	R_s ($\Omega\cdot cm^2$)	$Y_0(Q_f)$ ($\Omega^{-1}\cdot cm^{-2}\cdot s^n$)	R_f ($\Omega\cdot cm^2$)	$Y_0(Q_{dl})$ ($\Omega^{-1}\cdot cm^{-2}\cdot s^n$)	R_{ct} ($\Omega\cdot cm^2$)	$Y_0(W)$ ($\Omega^{-1}\cdot cm^{-2}\cdot s^{0.5}$)	Quality of fit
N80-0 ppm	3.36	4.25×10^{-3}	109.7	0.10	26.9	-	1.29×10^{-3}
N80-2000 ppm	3.13	6.47×10^{-3}	83.31	1.56	8.68	-	3.76×10^{-4}
N80-10000 ppm	3.13	6.60×10^{-3}	99.84	0.77	12.3	-	1.10×10^{-3}
Ni-P-0 ppm	3.18	8.92×10^{-5}	440.6	7.98×10^{-4}	1.47×10^{2}	1.80×10^{-3}	3.45×10^{-3}
Ni-P-10000 ppm	3.16	1.51×10^{-4}	351.3	5.32×10^{-3}	604	2.29×10^{-2}	1.55×10^{-3}

5.4 Discussion

5.4.1 Dependence of Ca^{2+} on the corrosion film formation and the resulting corrosion behavior of N80 steel

$FeCO_3$ is the most observed corrosion product in oil and gas applications containing CO_2 and generally regarded to offer certain protection against corrosion in many cases [33]. It forms and precipitates due to the release of Fe ions during the corrosion process, and the precipitation occurs when the product of iron ions and carbonate ions exceeds the solubility limit (K_{sp}) of $FeCO_3$ [34]. Calcium, as a widely distributed element in oilfield industry, favors the precipitation of $CaCO_3$ in the formation brines. Both iron and calcium carbonate precipitations are significantly dependent on their saturation degrees in the bulk solution with different pH, temperature and ion activities [35,36]. As proposed by Bénézeth et al. [37] and Plummer et al. [38], the K_{sp} of siderite and calcite is given in Eqs. 5.5 and 5.6, respectively:

$$\log K_{sp,FeCO_3} = 175.568 + 0.0139T - \frac{6738.483}{T} - 67.898 \log T \quad \text{(Eq. 5.5)}$$

$$\log K_{sp,CaCO_3} = -171.9065 - 0.077993T + \frac{2839.319}{T} + 71.595 \log T \qquad \text{(Eq. 5.6)}$$

where T is the temperature in Kelvin. $K_{sp,FeCO_3}$ is calculated to be 1.55×10^{-13} at 150 °C, nearly two orders of magnitude lower than $K_{sp,CaCO_3}$ (6.99×10^{-11}), an implication that $FeCO_3$ reaches saturation prior to $CaCO_3$. Furthermore, before calcite precipitation occurs, the presence of Ca^{2+} leads to the formation of mixed carbonates ($Fe_xCa_{1-x}CO_3$) due to the isostructurality of iron and calcium carbonate, which potentially results in morphological and chemical changes.

In this work, Ca^{2+} ions have been identified to remarkably affect the corrosion behavior of N80 steel in the HT/HP CO_2-containing environment, which is manifested by altering the corrosion film protectiveness and affecting the water chemistry of the aqueous phase. Without the presence of Ca^{2+}, the formed $FeCO_3$ corrosion film exhibits relatively good corrosion resistance, confirmed by the lowest corrosion rate among all the conditions of N80 steel. This can also be seen from the thick and well adhered $FeCO_3$ layer in Figure 5.8a, which serves as a barrier layer to inhibit further metal dissolution evidenced by the impedance data. When Ca^{2+} is introduced in the solution, the corrosion rate starts to increase rapidly with the Ca^{2+} concentration, suggesting an accelerating effect on the corrosion process of N80 steel. As seen in Figure 5.6, the incorporation of Ca atoms into $FeCO_3$ lattice gets more intense as Ca^{2+} concentration further increases to 2,000 ppm, leading to the decrease of crystal size, and, more importantly, the crystal fragmentation. Despite the isomorphism of the two types of carbonates, Ca involvement gives rise to larger lattice distortion because of the larger atomic radius of Ca. When the substitution of Fe atoms by Ca atoms exceeds the critical value, the $FeCO_3$ lattice collapses due to the relaxation of the atomic-level stress and a more topologically stabilized and disordered structure is generated instead of the crystalline structure [39], thereby leaving gaps between the damaged crystals. The crystal damage and microstructural transformation can be evidenced by the broadening $FeCO_3$ peaks as Ca^{2+} concentration increases shown in Figure 5.4. These defects on crystal edges facilitate the penetration of corrosive electrolyte through the corrosion film, resulting in the promoted corrosion process. Moreover, the addition of Ca^{2+} considerably increases the solubility of $FeCO_3$, and the effect is aggravated with higher Ca^{2+} concentrations [9,40]. Figure 5.14 presents the concentrations of H^+, HCO_3^- and CO_3^{2-} in the aqueous phase and the corresponding pH calculated by OLI Analyzer software with the addition of various Ca^{2+} concentrations (See the detailed information in Tables S5.1 and S5.2). It is observed that the presence of Ca^{2+} ions causes the augmentation of H^+ ions and the reduction of HCO_3^- and CO_3^{2-} ions consequently, and this tendency is more accentuated at higher Ca^{2+} concentrations. Therefore, the more acidic electrolyte with the depletion of anions postpones the formation of $FeCO_3$ film with the presence of Ca^{2+}, enhancing corrosion process.

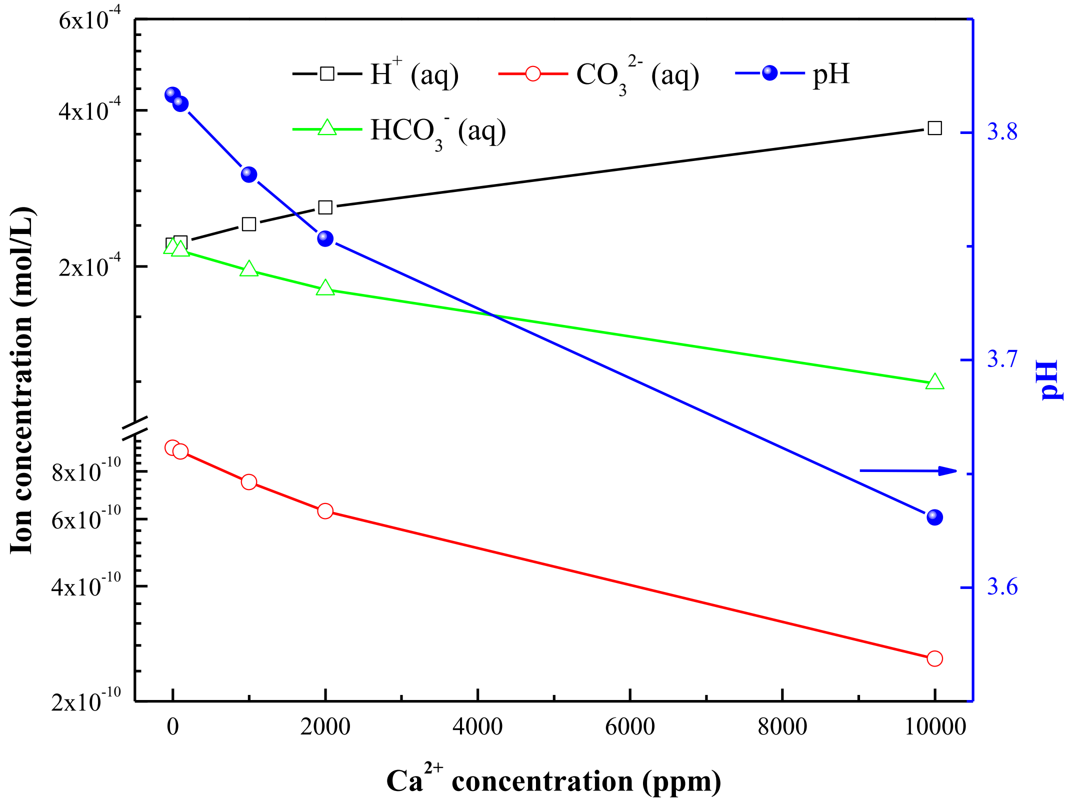

Figure 5.14 Concentrations of H^+, CO_3^{2-} and HCO_3^- and pH values calculated using OLI Analyzer software with the addition of different Ca^{2+} concentrations.

Generally, the protectiveness of corrosion film is notably related to its structure (i.e., microstructure and porosity) and precipitation rate. As Ca^{2+} concentration rises, the corrosion rate of N80 steel starts to decrease, also verified by the additional mass loss test at 2,500 ppm Ca^{2+}, showing a corrosion rate of 0.3486 mm/y, slightly slower than 2,000 ppm. As some previous research has reported, the Ca-enriched corrosion film results in a better anti-corrosion performance [5,41,42]. In this study, the higher impedance with the addition of 10,000 ppm Ca^{2+} demonstrates that the further incorporation of Ca^{2+} enhanced the protectiveness of the corrosion film. Moreover, the porosity of corrosion film considerably decreases with the increase of Ca^{2+} concentration from 2,500 ppm to 10,000 ppm in such a way that the newly formed Ca-rich corrosion product fills the gaps between collapsed crystals, as presented in Figure 5.6 (e–h). Wang et al. [10] discovered that the precipitation of $Ca_xFe_{1-x}CO_3$ can fill the pores in the corrosion film and improve the "pseudo-passivation" of 3Cr steel by isolating the steel from the corrosive medium. However, the high Ca^{2+} concentration also gives rise to more severe localized corrosion, which can be seen from the severe pit propagation in SEM (Figure 5.8d) and OSM (Figure 5.9b) images. Although the compactness is enhanced by Ca^{2+} incorporation, the corrosion film still exhibits inhomogeneity, as evidenced by Figure 5.7b. Region A with compact corrosion film is more Ca-enriched than Region B with loose scale, and it can be hypothesized that Region A effectively isolates the corrosive medium from the steel, but Region B serves as active sites and allows the electrolyte to penetrate, thereby facilitating the localized corrosion. Similar localized attack caused by carbonate scaling has also been reported earlier in real service cases [43]. Therefore, the corrosion mode is transformed from general corrosion to localized corrosion at higher Ca^{2+} concentration, which nevertheless cannot be reflected from the mass loss test and the impedance data because they only interpret the overall protectiveness of the corrosion film.

In general, Ca^{2+} ions play an influential role and its effect is concentration dependent, which is mainly divided into two ranges. At a lower concentration below 2,000 ppm, the corrosion of N80 steel is dominated by Ca^{2+} altering the crystalline microstructure and postponing the $FeCO_3$ precipitation. After the Ca concentration reaches or goes beyond the critical value that causes the crystal collapse, more involvement of Ca atoms into the corrosion film improves its density and compactness by filling the gaps, inhibiting the uniform corrosion rate form further increasing. However, in the meantime, the scale heterogeneity promotes the occurrence of localized corrosion and eventually intensifies the degradation of the steel.

5.4.2 The origins for the superior resistance to corrosion and scaling of Ni-P coating in Ca^{2+}-containing environments

Electroless Ni-P coating with high P content exhibits superior corrosion resistance in acidic environments benefiting from its amorphous and chemically homogenous microstructure with limited active corrosion sites at nodular boundaries [44–46]. In this study, the excellent performance is again substantiated by the low mass loss and high impedance, and the presence of Ca^{2+} does not pose considerable influence on the corrosion rate of the coating. Generally, the passive film of Ni metal and Ni-based alloys is majorly composed by NiO and $Ni(OH)_2$ [47,48] in the acidic environment, and our previous study [20,49] revealed that the formed protective $NiO/Ni(OH)_2$ film could inhibit corrosion in the CO_2-saturated solution at room temperature and supercritical CO_2 environments. Likewise, in this study, the corrosion film mainly composed of $NiO/Ni(OH)_2$ with little amount of $CaCO_3$ precipitation efficiently blocks the penetration of corrosive medium and consequently retards the corrosion process under the HT/HP condition with saturated CO_2. Moreover, the less distributed Fe element on the coating surface and no sign of coating disbondment from the cross-sectional SEM image and XPS results also demonstrate the outstanding isolating effect of the coating. Our earlier research [24] showed that corrosion paths appear after 5 d of immersion, leading to the electrolyte penetration and lateral coating disbondment after 10 d in the CO_2-saturated solution at room temperature. Comparatively, no noticeable corrosion path is observed for Ni-P coated steel after immersion for 7 d in this study. This discrepancy potentially highlights the enhanced corrosion resistance of $NiO/Ni(OH)_2$ film under HT/HP conditions, which requires further experimental investigation. Nonetheless, the corrosion rate of the coating still moderately rises with Ca^{2+} concentration based on the mass loss results, irrespective of the phenomenal corrosion resistance under all conditions. It implies that the presence of Ca^{2+} advances the formation of nickel-rich corrosion film and weakens the isolation property of the film, as proved by the increased $Y_0(W)$ at 10,000 ppm Ca^{2+}. It can be inferred based on the water chemistry calculations that the addition of Ca^{2+} leads to the accumulation of H^+, which facilitates the hydration of Ni and further consumption of the coating, thereby increasing the corrosion rate consequently.

Moreover, the thin Ca-rich layer (see Figure 5.11b) suggests the limited scale formation on the coating surface even at high Ca^{2+} concentrations, which considerably alleviates the localized corrosion due to the non-uniform deposition of corrosion film for carbon steels. Scale formation results from the precipitation from solution containing sparingly soluble salts on the surface, and occurs in steps of ion pairing, nucleation, crystal growth and eventually scale agglomeration [50]. The deposition process is influenced not only by various environmental factors, such as pH, temperature, hydrodynamic conditions, etc., but also by surface properties, e.g., surface energy and surface roughness. Surfaces with lower surface energy, such as electroless coating, exhibit lower adhesion strength between crystals and the surface, thereby prolonging the induction time for nucleation and resulting in a lower scaling rate [51]. Furthermore, the presence of $NiO/Ni(OH)_2$ passive film drastically reduces active corrosion sites which usually serve as the initiation sites of nucleation. Surface roughness also greatly affects the scale formation process, which is reflected in impairing the heterogeneous nucleation when scale grows on pre-existing surface defects such as rough spots and scratches [52]. Since Ni-P coating owns smoother surfaces than carbon steel due to the intrinsic characteristics of electroless plating that can fill the polishing trace of steel (Figure 5.2a), the rate of heterogeneous nucleation is declined accordingly, which slows down the scale formation rate. Overall, the formed NiO/Ni(OH)$_2$ corrosion film, along with the relatively low surface energy and smaller roughness, endows Ni-P coating with superior anti-corrosion and anti-scaling performance in CO$_2$-saturated HT/HP environments containing Ca^{2+}.

5.5 Conclusions

In summary, the corrosion behavior of N80 steel and electroless Ni-P coating under HT/HP CO$_2$-saturated condition was investigated, and the effect of Ca^{2+} was further explored. The results show that corrosion of N80 steel is remarkably promoted with the addition of Ca^{2+} ions, however Ni-P coating exhibits outstanding corrosion resistance.

The presence of Ca^{2+} leads to the change of corrosion film microstructure of N80 steel and subsequently affects the corrosion behavior. The incorporation of Ca atoms into FeCO$_3$ lattice results in smaller crystal sizes with more defects, which consequently enhances the electrolyte diffusion and promotes the corrosion process. The critical Ca^{2+} concentration above which the microstructural transformation takes place is between 2,000 ppm and 2,500 ppm. The addition of Ca^{2+} at concentrations higher than the critical value strengthens the corrosion film by improving its compactness. However, the localized corrosion of the steel is accelerated at higher Ca^{2+} concentration due to non-uniformity of corrosion film where the region of loose corrosion film allows the electrolyte penetration. Meanwhile, the introduction of Ca^{2+} also impacts the water chemistry of the aqueous phase, resulting in the accumulation of H$^+$ and consequently postpones the precipitation of FeCO$_3$.

The protection effectiveness of Ni-P coating is barely impacted by Ca^{2+} concentrations. The corrosion film, mainly composed by NiO and $Ni(OH)_2$, offers superior corrosion resistance by isolating the electrolyte from coating underneath, which is evidenced by satisfactory impedance results and the absence of corrosion pathways and coating disbondment. Furthermore, the less tendency of scale formation on the coating surface also mitigates the localized corrosion due to the heterogeneous distribution of corrosion film for carbon steels.

5.6 References

[1] H. Mansoori, D. Young, B. Brown, M. Singer, Influence of calcium and magnesium ions on CO_2 corrosion of carbon steel in oil and gas production systems-A review, J. Nat. Gas Sci. Eng. 59 (2018) 287–296.

[2] M.M. Vazirian, T.V. Charpentier, M. de Oliveira Penna, A. Neville, Surface inorganic scale formation in oil and gas industry: As adhesion and deposition processes, J. Petrol. Sci. Eng. 137 (2016) 22–32.

[3] M.S. Kamal, I. Hussein, M. Mahmoud, A.S. Sultan, M.A. Saad, Oilfield scale formation and chemical removal: A review, J. Petrol. Sci. Eng. 171 (2018) 127–139.

[4] J. Li, M. Tang, Z. Ye, L. Chen, Y. Zhou, Scale formation and control in oil and gas fields: A review, J. Disper. Sci. Technol. 38 (2017) 661–670.

[5] A.A. Olajire, A review of oilfield scale management technology for oil and gas production, J. of Petrol. Sci. Eng. 135 (2015) 723–737.

[6] J. Li, C. Sun, S. Shuang, M. Roostaei, V. Fattahpour, M. Mahmoudi, H. Zeng, J.L. Luo, 2019. Investigation on the flow-induced corrosion and degradation behavior of

underground J55 pipe in a water production well in the Athabasca oil sands reservoir. J. Petrol. Sci. Eng. 182, 106325.

[7] C. Ding, K.W. Gao, C.F. Chen, Effect of Ca^{2+} on CO_2 corrosion properties of X65 pipeline steel, Int. J. Min. Met. Mater. 16 (2009) 661–666.

[8] S.N. Esmaeely, D. Young, B. Brown, S. Nešić, Effect of incorporation of calcium into iron carbonate protective layers in CO_2 corrosion of mild steel, Corrosion 73 (2017) 238–246.

[9] Y. Hua, A. Shamsa, R. Barker, A. Neville, Protectiveness, morphology and composition of corrosion products formed on carbon steel in the presence of Cl^-, Ca^{2+} and Mg^{2+} in high pressure CO_2 environments, Appl. Surf. Sci. 455 (2018) 667–682.

[10] B. Wang, L. Xu, G. Liu, M. Lu, Corrosion behavior and mechanism of 3Cr steel in CO_2 environment with various Ca^{2+} concentration, Corros. Sci. 136 (2018) 210–220.

[11] A. Shamsa, R. Barker, Y. Hua, E. Barmatov, T.L. Hughes, A. Neville, The role of Ca^{2+} ions on Ca/Fe carbonate products on X65 carbon steel in CO_2 corrosion environments at 80 and 150 °C, Corros. Sci. 156 (2019) 58–70.

[12] K. Gao, F. Yu, X. Pang, G. Zhang, L. Qiao, W. Chu, M. Lu, Mechanical properties of CO_2 corrosion product scales and their relationship to corrosion rates, Corros. Sci. 50 (2008) 2796–2803.

[13] X. Jiang, Y.G. Zheng, D.R. Qu, W. Ke, Effect of calcium ions on pitting corrosion and inhibition performance in CO_2 corrosion of N80 steel, Corros. Sci. 48 (2006) 3091–3108.

[14] P.R. Rhodes, Environment-assisted cracking of corrosion-resistant alloys in oil and gas production environments: a review, Corrosion 57 (2001) 923–966.

[15] H. Zhang, Y.L. Zhao, Z.D. Jiang, Effects of temperature on the corrosion behavior of 13Cr martensitic stainless steel during exposure to CO_2 and Cl^- environment, Mater. Lett. 59 (2005) 3370–3374.

[16] L.T. Popoola, A.S. Grema, G.K. Latinwo, B. Gutti, A.S. Balogun, Corrosion problems during oil and gas production and its mitigation, Int. J. Ind. Chem. 4 (2013) 35.

[17] H. Ashassi-Sorkhabi, M. Es'haghi, Corrosion resistance enhancement of electroless Ni–P coating by incorporation of ultrasonically dispersed diamond nanoparticles, Corros. Sci. 77 (2013) 185–193.

[18] H. Luo, M. Leitch, Y. Behnamian, Y. Ma, H. Zeng, J.L. Luo, Development of electroless Ni–P/nano-WC composite coatings and investigation on its properties, Surf. Coat. Technol. 277 (2015) 99–106.

[19] N. Ghavidel, S.R. Allahkaram, R. Naderi, M. Barzegar, H. Bakhshandeh, 2020. Corrosion and wear behavior of an electroless Ni-P/nano-SiC coating on AZ31 Mg alloy obtained through environmentally-friendly conversion coating. Surf. Coat. Technol. 382, 125156.

[20] L.L. Wang, H.J. Chen, L. Hao, A. Lin, F.X. Gan, Electrochemical corrosion behavior of electroless Ni–P coating in NaCl and H_2SO_4 solutions, Mater. Corros. 62 (2011) 1003–1007.

[21] S.R. Allahkaram, M.H. Nazari, S. Mamaghani, A. Zarebidaki, Characterization and corrosion behavior of electroless Ni–P/nano-SiC coating inside the CO_2 containing media in the presence of acetic acid, Mater. Des. 32 (2011) 750–755.

[22] C. Sun, J. Li, S. Shuang, H. Zeng, J.L. Luo, Effect of defect on corrosion behavior of electroless Ni-P coating in CO_2-saturated NaCl solution, Corros. Sci. 134 (2018) 23–37.

[23] C. Sun, H. Zeng, J.L. Luo, Unraveling the effects of CO_2 and H_2S on the corrosion behavior of electroless Ni-P coating in $CO_2/H_2S/Cl^-$ environments at high temperature and high pressure, Corros. Sci. 148 (2019) 317–330.

[24] H. Habazaki, S.Q. Ding, A. Kawashima, K. Asami, K. Hashimoto, A. Inoue, T. Masumoto, The anodic behavior of amorphous Ni-19P alloys in different amorphous states, Corros. Sci. 29 (1989) 1319–1328.

[25] J.N. Balaraju, V.E. Selvi, V.W. Grips, K.S. Rajam, Electrochemical studies on electroless ternary and quaternary Ni–P based alloys, Electrochim. Acta 52 (2006) 1064–1074.

[26] J. Li, C. Sun, H. Zeng, J.L. Luo, Insights into the electrochemical corrosion behavior and mechanism of electroless Ni-P coating in the $CO_2/H_2S/Cl^-$ environment, Corrosion 76 (2020) 578–590.

[27] Z. Yan, C. Guo, F. Yang, C. Zhang, Y. Mao, S. Cui, Y. Wei, L. Hou, L. Xu, Cliff-like NiO/Ni_3S_2 directly grown on Ni foam for battery-type electrode with high area capacity and long cycle stability, Electrochim. Acta 251 (2017) 235–243.

[28] J. Li, S. Wang, T. Xiao, X. Tan, P. Xiang, L. Jiang, C. Deng, W. Li, M. Li, Controllable preparation of nanoporous Ni_3S_2 films by sulfuration of nickel foam as promising asymmetric supercapacitor electrodes, Appl. Surf. Sci. 420 (2017) 919–926.

[29] X. Zhao, T. Hu, H. Li, M. Chen, S. Cao, L. Zhang, X. Hou, Electrochemically assisted co-deposition of calcium phosphate/collagen coatings on carbon/carbon composites, Appl. Surf. Sci. 257 (2011) 3612–3619.

[30] K. Jiang, Y. Wang, X. Gao, C. Cai, H. Lin, Facile, quick, and gram-scale synthesis of ultralong-lifetime room-temperature-phosphorescent carbon dots by microwave irradiation, Angew. Chem. Int. Ed. 57 (2018) 6216–6220.

[31] K. Song, Y.N. Jang, W. Kim, M.G. Lee, D. Shin, J.H. Bang, C.W. Jeon, S.C. Chae, Precipitation of calcium carbonate during direct aqueous carbonation of flue gas desulfurization gypsum, Chem. Eng. J. 213 (2012) 251–258.

[32] S.V. Green, A. Kuzmin, J. Purans, C.G. Granqvist, G.A. Niklasson, Structure and composition of sputter-deposited nickel-tungsten oxide films, Thin Solid Films 519 (2011) 2062–2066.

[33] W.J. Lee, K. Prasanna, Y.N. Jo, K.J. Kim, H.S. Kim, C.W. Lee, Depth profile studies on nickel rich cathode material surfaces after cycling with an electrolyte containing vinylene carbonate at elevated temperature, Phys. Chem. Chem. Phys. 16 (2014) 17062–17071.

[34] C.N. Cao, J.Q. Zhang, An introduction to electrochemical impedance spectroscopy, Science, Beijing, 2002.

[35] S. Nešić, Key issues related to modelling of internal corrosion of oil and gas pipelines–A review, Corros. Sci. 49 (2007) 4308–4338.

[36] W. Sun, S. Nešić, R.C. Woollam, The effect of temperature and ionic strength on iron carbonate ($FeCO_3$) solubility limit, Corros. Sci. 51 (2009) 1273–1276.

[37] Y. Zhang, H. Shaw, R. Farquhar, R. Dawe, The kinetics of carbonate scaling—application for the prediction of downhole carbonate scaling, J. Petrol. Sci. Eng. 29 (2001) 85–95.

[38] R. Rizzo, S. Gupta, M. Rogowska, R. Ambat, 2020. Corrosion of carbon steel under CO_2 conditions: Effect of $CaCO_3$ precipitation on the stability of the $FeCO_3$ protective layer. Corros. Sci. 162, 108214.

[39] P. Bénézeth, J.L. Dandurand, J.C. Harrichoury, Solubility product of siderite ($FeCO_3$) as a function of temperature (25–250 C), Chem. Geol. 265 (2009) 3–12.

[40] L.N. Plummer, E. Busenberg, The solubilities of calcite, aragonite and vaterite in CO_2-H_2O solutions between 0 and 90 °C, and an evaluation of the aqueous model for the system $CaCO_3$-CO_2-H_2O, Geochim. Cosmochim. Acta 46 (1982) 1011–1040.

[41] Q. Wang, J.H. Li, J.B. Liu, B.X. Liu, Atomistic design of favored compositions for synthesizing the Al-Ni-Y metallic glasses, Sci. Rep. 5 (2015) 16218.

[42] H.A. Alsaiari, A. Kan, M. Tomson, Effect of calcium and iron (II) ions on the precipitation of calcium carbonate and ferrous carbonate, SPE J. 15 (2010) 294–300.

[43] S. Navabzadeh Esmaeely, Y.S. Choi, D. Young, S. Nešić, Effect of calcium on the formation and protectiveness of iron carbonate layer in CO_2 corrosion, Corrosion 69 (2013) 912–920.

[44] L.M. Tavares, E.M. da Costa, J.J. de Oliveira Andrade, R. Hubler, B. Huet, Effect of calcium carbonate on low carbon steel corrosion behavior in saline CO_2 high pressure environments, Appl. Surf. Sci. 359 (2015) 143–152.

[45] H. Mansoori, R. Mirzaee, F. Esmaeilzadeh, A. Vojood, A.S. Dowrani, Pitting corrosion failure analysis of a wet gas pipeline, Eng. Fail. Anal. 82 (2017) 16–25.

[46] X. Xiu-qing, M. Jian, B. Zhen-quan, F. Yao-rong, M. Qiu-rong, Z. Wen-zhen, The corrosion behavior of electroless Ni–P coating in Cl^-/H_2S environment, Appl. Surf. Sci. 258 (2012) 8802–8806.

[47] M. Crobu, A. Scorciapino, B. Elsener, A. Rossi, The corrosion resistance of electroless deposited nano-crystalline Ni–P alloys, Electrochim. Acta 53 (2008) 3364–3370.

[48] K.G. Keong, W. Sha, S. Malinov, Crystallization and phase transformation behaviour of electroless nickel-phosphorus deposits with low and medium phosphorus contents under continuous heating, J. Mater. Sci. 37 (2002) 4445–4450.

[49] C.A. Melendres, M. Pankuch, On the composition of the passive film on nickel: a surface-enhanced Raman spectroelectrochemical study, J. Electroanal. Chem. 333 (1992) 103–113.

[50] M.D.C. Belo, N.E. Hakiki, M.G.S. Ferreira, Semiconducting properties of passive films formed on nickel–base alloys type Alloy 600: influence of the alloying elements, Electrochim. Acta 44 (1999) 2473–2481.

[51] C. Sun, S. Liu, J. Li, H. Zeng, J.L. Luo, Insights into the interfacial process in electroless Ni–P coating on supercritical CO_2 transport pipeline as relevant to carbon capture and storage, ACS appl. Mater. Inter. 11 (2019) 16243–16251.

[52] T.A. Hoang, Mechanisms of scale formation and inhibition, in: Z. Amjad, K.D. Demadis (Eds.), Mineral Scales and Deposits, Elsevier, 2015, pp. 47–83.

[53] Q. Yang, J. Ding, Z. Shen, Investigation of calcium carbonate scaling on ELP surface, J. Chem. Eng. Japan 33 (2000) 591–596.

[54] J.W. Mullin, Crystallization, Elsevier, 2001.

5.7 Supporting information

5.7.1 Details of electroless coating procedure

The samples were first degreased in 3 wt.% sodium carbonate (Na_2CO_3) and sodium hydroxide (NaOH) at 60 °C for 20 min, followed by etched in 10 wt.% hydrochloric acid (HCl) for 50 s to activate the surface. Subsequently, the samples were dipped in the plating bath with a stirring rate of 200 rpm at (85±1) °C for 2 h. The coated samples were then ultrasonically cleaned in alcohol for 10 min and dried in flowing air for future use.

5.7.2 XRD analysis of Ni-P coating after immersion

Figure S5.1 shows the XRD pattern of Ni-P coating after 7 d of immersion with the presence of 10000 ppm Ca^{2+}. A sole broaden peak, indicating amorphous Ni, is observed from the pattern, an implication that tiny amount of corrosion product is formed on the surface. This further confirms the superior anti-corrosion and anti-scaling properties of the coating.

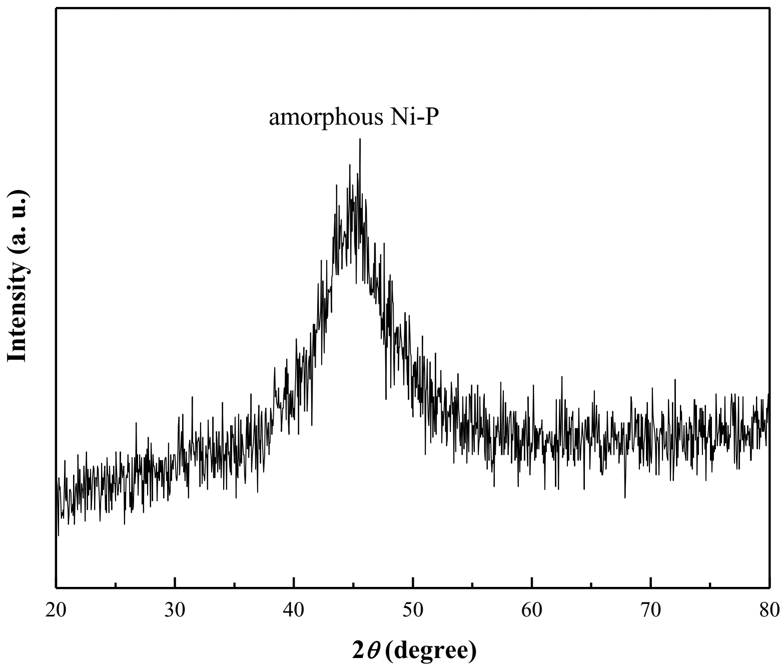

Figure S5.15 XRD pattern of Ni-P coating exposed to CO_2-saturated brines with 10000 ppm Ca^{2+} at 150 °C and 3.8 MPa for 7 d.

5.7.3 Water chemistry analysis

Table S5.1 Compositions of the fluids in the autoclave calculated based on Table 5.2 for water chemistry analysis.

Conditions	H_2O (g)	$CaCl_2 \cdot 2H_2O$ (g)	NaCl (g)	CO_2 (g)*	N_2 (g)*
0 ppm Ca^{2+}	1000	0	36.268	12.71	7.27
100 ppm Ca^{2+}	1000	0.368	35.976	12.71	7.27
1000 ppm Ca^{2+}	1000	3.675	33.343	12.71	7.27
2000 ppm Ca^{2+}	1000	7.35	30.418	12.71	7.27
10000 ppm Ca^{2+}	1000	36.75	7.018	12.71	7.27

* The calculated densities of CO_2 and N_2 at 150 °C and their partial pressures based on the thermodynamic model proposed by Bakker et al. [1,2] are 25.41 kg/m^3 and 14.53 kg/m^3, respectively.

Table S5.2 Concentrations of species in the aqueous phase and pH values calculated using OLI Analyzer software with the addition of different Ca^{2+} concentrations.

Species (mol/L)	0 ppm Ca^{2+}	100 ppm Ca^{2+}	1000 ppm Ca^{2+}	2000 ppm Ca^{2+}	10000 ppm Ca^{2+}
$CO_{2\ (aq)}$	0.10	0.10	0.10	0.10	0.10
$N_{2\ (aq)}$	9.15×10^{-3}	9.15×10^{-3}	9.14×10^{-3}	9.13×10^{-3}	9.04×10^{-3}
$HCl_{(aq)}$	9.97×10^{-9}	1.01×10^{-8}	1.08×10^{-8}	1.15×10^{-8}	1.51×10^{-8}
H^+	2.20×10^{-4}	2.22×10^{-4}	2.41×10^{-4}	2.60×10^{-4}	3.69×10^{-4}
HCO_3^-	2.17×10^{-4}	2.14×10^{-4}	1.96×10^{-4}	1.81×10^{-4}	1.19×10^{-4}
CO_3^{2-}	9.21×10^{-10}	9.00×10^{-10}	7.49×10^{-10}	6.29×10^{-10}	2.58×10^{-10}
OH^-	4.54×10^{-11}	4.50×10^{-11}	4.15×10^{-11}	3.85×10^{-11}	2.71×10^{-11}
Na^+	0.59	0.58	0.54	0.49	0.11
Cl^-	0.59	0.59	0.59	0.59	0.58
Ca^{2+}	0	2.34×10^{-3}	0.02	0.05	0.23
pH	3.82	3.81	3.78	3.75	3.63

5.7.4 References

[1] R.J. Bakker, Package FLUIDS. Part 3: correlations between equations of state, thermodynamics and fluid inclusions, Geofluids 9 (2009) 63–74.

[2] R.J. Bakker, Thermodynamic properties and applications of modified van-der-Waals equations of state, in: Ricardo Morales-Rodriguez (Ed.), Thermodynamics - Fundamentals and Its Application in Science, InTech, 2012, pp. 163–190.

6 Characterization and corrosion behavior of electroless Ni-Mo-P/Ni-P composite coating in $CO_2/H_2S/Cl^-$ brine: effects of Mo addition and heat treatment

ABSTRACT: The electroless Ni-Mo-P/Ni-P composite coating was applied on N80 carbon steel, and the effects of Mo addition and heat treatment on the corrosion resistance enhancement in $CO_2/H_2S/Cl^-$ brine were studied by electrochemical measurements and surface analysis techniques. The Mo addition in the as-deposited Ni-P coating causes the microstructural transformation from amorphous to crystalline due to the reduced P content, thereby suffering severe corrosion. The impaired corrosion performance of as-deposited Mo-incorporated coating is also originated from the absence of the oxide film on the coating surface. Nonetheless, the heat-treated Ni-Mo-P/Ni-P coating exhibits desirable corrosion resistance, which is reflected by the outstanding corrosion inhibition efficiency (η=96.1%). Heat treatment facilitates the formation of Ni_4Mo phase and more importantly, the growth of an oxide film consisting of nickel and molybdenum oxides (H_2S-immuned MoO_3) with better passivation properties, which accounts for the remarkable corrosion resistance improvement, as compared to as-deposited coatings.

6.1 Introduction

Growing energy consumption worldwide and dwindling light oil resources have prompted the recovery of heavy oil, and thus caused severe corrosion problems of carbon steels due to the extremely harsh environment containing acidic gases (e.g., CO_2 and H_2S). Electroless Ni-P coating, as an advantageous metallic coating with good mechanical properties, low cost and extraordinary corrosion resistance, has been adopted as a promising candidate for carbon steels in oil and gas industries [1–4]. Although decent corrosion performance in CO_2-containing environments or other acidic media has been reported by researchers [5–7], H_2S still severely impedes the further application of Ni-P coating due to the high chemical affinity of S species to Ni, causing the acceleration of corrosion and electrolyte penetration [8,9]. Therefore, it is desirable to develop a Ni-P composite coating that displays superb anti-H_2S corrosion performance.

To date, several methods have been identified to improve the corrosion performance of Ni-P coating, for instance, introducing alloying elements [10–13] and incorporating functional nanoparticles [3,14–17]. The primary contribution of nanoparticles in the corrosion resistance enhancement is to fill in the intrinsic micropores formed due to the hydrogen evolution reaction during the coating deposition process, thereby hindering the penetration of corrosive electrolyte. Luo et al. [3] reported the increased microhardness and improved corrosion resistance of Ni-P/nano-WC composite coating in 3.5 wt.% sodium chloride (NaCl) solution. The study on the incorporation of carbon nanotubes (CNTs) into Ni-P coating showed that added CNTs led to the formation of a denser and more homogeneous coating by filling in coating defects and accelerated the chemical passivity of the coating due to their high chemical stability [14]. However, very limited research has been devoted to the corrosion resistance improvement by nanoparticle incorporation in CO_2/H_2S environments. Recently, ZrO_2 nanoparticles were added into Ni-W-P/Ni-P coating and proved to reduce the corrosion rate in $CO_2/H_2S/Cl^-$ brine [18], however the inhibition efficiency is relatively low. In this regard, the co-deposition of Ni-P coating and suitable alloying elements owing good anti-H_2S properties would be a better option.

Among all the alloying elements that are compatible with electroless Ni-P coating, molybdenum (Mo) element is believed to exhibit satisfactory anti-H_2S corrosion performance, which has been substantiated in corrosion-resistant alloys and stainless steels with alloyed Mo [19–21]. Several theories have been proposed on the roles of Mo in enhancing the corrosion resistance: (1) formation of insoluble Mo-containing compounds, e.g., molybdates, molybdenum oxides and molybdenum sulfide [22–24], (2) inhibition effect of molybdate ions [25,26], (3) cation selectivity of molybdenum sulfide, specifically in sour environments [19]. Pardo et al. [22] discovered the presence of molybdenum trioxide in the outer layer of the passive film of 304 and 316 stainless steel with alloyed Mo, proposing that the decreased dissolution rate was ascribed to this Mo-rich oxide film which acted as a barrier against the diffusion of dissolution species. Similar findings about molybdates and molybdenum sulfide were also reported [23,24]. Denpo et al. [25] studied the effect of MoO_4^{2-} ions on the passivity of Ni-Cr-Mo-Fe and reported that the formation of MoO_4^{2-} on the surface of passive films improved the passivity in H_2S/Cl^- environments. Moreover, MoO_4^{2-} ions facilitate the formation of a bipolar film together with CrO_4^{2-} ions, which provides ion selectivity and repels Cl^- ions penetrating through the film [26]. The cation selectivity of molybdenum sulfide was proposed by Tomio et al. [19], who claimed that the cation-selective stable molybdenum sulfide promoted the protectiveness of inner chromium-rich oxide film by retarding the dissolution reaction caused by Cl^- ions and attenuating the activity of dissolved H_2S. Therefore, Mo addition in the electroless Ni-P coating is expected to exhibit more desirable corrosion performance in $CO_2/H_2S/Cl^-$ brine. Recently, ternary Ni-Mo-P coating has received growing attention in terms of its good mechanical properties and corrosion resistance in neutral solutions [27–29], but the effect of Mo has not yet been elucidated in H_2S-containing environments.

Moreover, heat treatment has been widely regarded as a favorable approach to improve the mechanical properties and corrosion resistance of Ni-P coating [30–33]. The precipitation of Ni3P and Ni crystals because of heat treatment contributes to the enhanced mechanical properties [30,34], and the corrosion resistance of crystalline Ni-P coating can be improved via heat treatment by reducing grain boundaries because of the grain growth of crystalline Ni [33]. Furthermore, NiO tends to form on the coating surface upon air annealing at elevated temperatures and acts as a passivation layer to inhibit corrosion [34,35]. Moreover, as stated above, the superb protection by Mo element is mainly accredited to the formation of Mo-containing compounds or ions, which may be obtained by proper heat treatment procedures. In addition, since most underground oil and gas applications are operated at elevated temperatures, it is desirable to study the effect of heat treatment on as-deposited coatings in sweat/sour brines. However, limited studies have focused on the phase transformation and microstructural changes of heat-treated Ni-Mo-P coating and the corresponding variations in terms of corrosion resistance.

Herein, we fabricated a duplex outer Ni-Mo-P/inner Ni-P electroless coating in this work, evaluated the corrosion resistance by various electrochemical measurements, and characterized the chemical compositions of corrosion product via surface analysis techniques. This study aims at optimizing electroless Ni-P composite coating to achieve the outstanding anti-H_2S corrosion performance and elucidating the role of Mo addition and heat treatment in the corrosion resistance advancement.

6.2 Experimental methods

6.2.1 Electroless coating preparation

N80 carbon steel substrates with a size of 10 mm × 10 mm × 10 mm were used for electroless coatings, and the chemical composition of N80 steel is as follows (wt.%): 0.29 C, 1.38 Mn, 0.25 Si, 0.037 Cr, 0.009 Cu, 0.002 Ni, 0.002 P, 0.002 S and Fe balance. The substrates were first sequentially ground up to 1200 grit, cleaned with deionized water and ethanol, and dried with flowing air. The electroless composite coating process contains two steps: 1 hour of Ni-P coating and 1 hour of Ni-Mo-P coating. The chemical compositions of both coating baths are listed in Table 6.1. Prior to coating deposition, the substrates were degreased in the solution consisting of 3 wt.% sodium carbonate (Na_2CO_3) and 3 wt.% sodium hydroxide (NaOH) at 60 °C for 20 min, and then pickled in 10 wt.% hydrochloric acid solution for 1 min for surface activation. The inner Ni-P coating and the outer Ni-Mo-P coating were then sequentially fabricated in water bath (85±1 °C) at the stirring rate of 200 rpm. Finally, the as-deposited coating (denoted as "Ni-Mo-P/Ni-P coating") was cleaned ultrasonically with ethanol to remove coating bath residue. For comparison, single-layered Ni-P coating (denoted as "Ni-P coating") was also prepared using the same plating parameters for 2 h to maintain a comparable coating thickness as the double-layered Ni-Mo-P/Ni-P coating. For heat-treated coatings, the coated samples were heated in a furnace under air flow condition at 400 °C for 2 h at a heating rate of 5 °C/min, followed by furnace cooling under air flow condition.

Table 6.1 Chemical composition of Ni-P coating and Ni-Mo-P coating baths.

Reagent	Concentration	
	Ni-P coating	Ni-Mo-P coating
Nickel sulphate ($NiSO_4 \cdot 6H_2O$)	25 g/L	20 g/L
Sodium hypophosphite ($NaH_2PO_2 \cdot H_2O$)	30 g/L	40 g/L
Sodium molybdate ($Na_2MoO_4 \cdot 2H_2O$)	-	5 g/L
Lactic acid ($C_3H_6O_3$)	20 mL/L	-
Citric acid ($C_6H_8O_7$)	20 g/L	10 g/L
Succinic acid ($C_4H_6O_4$)	14 g/L	-
Sodium citrate ($Na_3C_6H_5O_7$)	-	20 g/L
Ammonium chloride (NH_4Cl)	-	15 g/L
Saccharin ($C_6H_4SO_2NNaCO \cdot 2H_2O$)	0.06-0.08 g/L	-
Sodium dodecyl sulfate ($C_{12}H_{25}SO_4Na$)	0.04 g/L	0.01 g/L
Lead nitrate ($Pb(NO_3)_2$)	1 mg/L	-
Sodium fluoride (NaF)	-	0.004 g/L
Sodium hydroxide ($NaOH$)	28 g/L	15 g/L

6.2.2 Electrochemical measurements and immersion tests

The test solution for both electrochemical tests and immersion tests is 3.5 wt.% NaCl solution saturated with CO_2 and H_2S. Prior to the tests, nitrogen gas was initially purged into the test solution for 2 h for deoxygenation, followed by purging CO_2 and H_2S till saturation. The two gases were continuously supplemented into the solution to maintain the saturation during the tests. The electrochemical measurements were carried out in the three-electrode cell by using a Gamry Interface 1000E Electrochemical Workstation, with a carbon rod as the counter electrode, the epoxy-sealed sample as the working electrode and a saturated calomel electrode (SCE) as the reference electrode. An area of 1 cm × 1 cm was exposed for electrochemical tests. First, the open circuit potential (OCP) was recorded for 1 h to reach the steady-state potential. Then the electrochemical impedance spectroscopy (EIS) measurements were conducted with an alternating current signal amplitude of 10 mV applied in the frequency range from 100 kHz to 10 mHz at OCP. ZSimpWin software was used to fit the measured data by using appropriate equivalent circuits. The potentiodynamic polarization curves were recorded from -0.3 V to 1.2 V vs. OCP at a scanning rate of 0.167 mV/s.

The electrochemical noise (EN) measurements were also performed at OCP via ESA 410 software of Gamry Interface 1000E Electrochemical Workstation. Zero resistance ammeter (ZRA) mode was used in this work for data acquisition, with two identical samples as the working electrodes and SCE as the reference electrode. A sampling interval of 0.2 s was selected over 2048 consecutive data points after different periods. The total test time is 24 h. The frequency domain based on the sampling conditions was between 2.5 Hz ($f_{\max}$) and 2.4 mHz ($f_{\min}$) from $f_{max} = \frac{1}{2\Delta t}$ and $f_{min} = \frac{1}{N\Delta t}$, where Δt is the sampling interval and N is the total number of data points. The power spectral densities (PSDs) of the signals were calculated by the program *psd-detrend_ECG-COMON.exe* (free download on www.ecg-comon.org) based on the fast Fourier transform (FFT) and the linear detrending of raw electrochemical potential noise (EPN) and electrochemical current noise (ECN) data to avoid the effect of corrosion potential drift on signal fluctuations during the tests [36]. All the electrochemical tests were performed at least three times to ensure the reproducibility, and the representative results were presented. Immersion tests were performed for a period of 7 d under the same test condition as the electrochemical tests, and the tested samples were cleaned with deionized water and alcohol, and dried with flowing air prior to the post-immersion surface characterizations.

6.2.3 Surface characterizations

The surface morphologies and chemical compositions of each coating were examined via scanning electron microscopy (SEM, Tescan Vega-3) and energy-dispersive X-ray spectroscopy (EDS, Oxford INCA X-art), and the phase compositions and chemical valence were identified by X-ray diffraction (XRD, Rigaku Ultima IV) and X-ray photoelectron spectroscopy (XPS, Kratos AXIS Ultra), respectively. XRD was performed with a Cu K_α X-ray source operated at 40 kV and 44 mA, and the patterns were recorded from 20° to 80° at a scanning rate of 4°/min. XPS analysis was conducted with monochromatized Al K_α ($h\upsilon = 1486.71$ eV) at 5×10^{-10} Torr. The C 1s peak at the binding energy of 284.6 eV was used to calibrate the shifted XPS data. The XPS data were then fitted using XPSPEAK 41 software with a Shirley background subtraction and a Gaussian-Lorentzian combination function.

6.3 Results and discussion

6.3.1 Characterizations of as-deposited and heat-treated coatings prior to tests

Figure 6.1 shows the surface characterization results of as-deposited coatings. As seen in Figure 6.1a, the as-deposited Ni-P coating exhibits typical a nodular microstructure with apparent micropores observed on the coating surface. However, a crystalline microstructure with a much smaller crystal size is identified on the as-deposited Ni-Mo-P/Ni-P coating (Figure 6.1c), as evidenced by the XRD pattern showing a sharp Ni (111) peak (Figure 6.1h), as compared to the broad Ni peak of amorphous Ni-P coating (Figure 6.1g). In addition, micropores are barely detected on the surface of the Mo-incorporated coating because of the crystalline microstructure. Both coatings are deposited homogeneously and well adhered on the substrate without any noticeable defects (Figure 6.1b and 6.1d), indicative of good compatibility between layers. The thicknesses of the inner Ni-P coating and outer Ni-Mo-P coating are about 12 μm, revealing that the Mo incorporation does not affect the deposition rate.

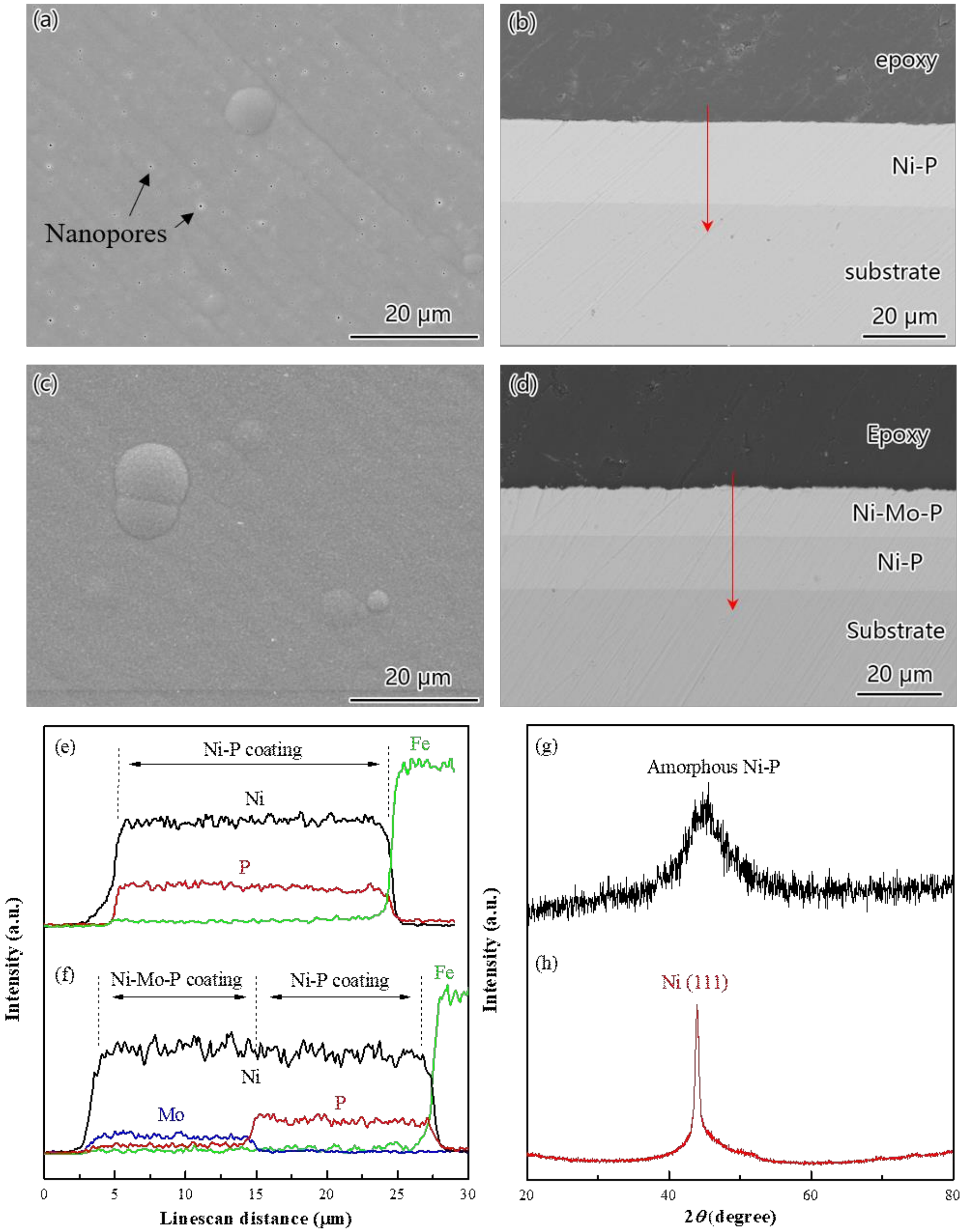

Figure 6.1 Characterizations of as-deposited coatings: (a) surface and (b) cross-sectional SEM images of Ni-P coating; (c) surface and (d) cross-sectional SEM images of Ni-Mo-P/Ni-P coating; (e)(f) EDS line scan results of the red lines denoted in (b) and (d), respectively; XRD patterns of (g) Ni-P coating and (h) Ni-Mo-P/Ni-P coating.

The primary overall reactions of the Ni-Mo-P electroless plating process in the alkaline bath are listed as below [37,38]:

$$Ni^{2+} + 2H_2PO_2{}^- + 2OH^- \rightarrow 2H_2PO_3{}^- + H_2 + Ni \qquad \text{(Eq. 6.1)}$$

$$3H_2PO_2{}^- \rightarrow H_2PO_3{}^- + H_2O + 2OH^- + 2P \qquad \text{(Eq. 6.2)}$$

$$MoO_4{}^{2-} + 6H_2PO_2{}^- + 4H_2O \rightarrow 6H_2PO_3{}^- + 3H_2 + 2OH^- + Mo \qquad \text{(Eq. 6.3)}$$

The microstructure and properties of Ni-P coatings are greatly dependent on the P content. It is generally accepted that high-phosphorus Ni-P coating (P content > 9 wt. %) exhibits amorphous structure, while crystalline structure appears in low-phosphorus Ni-P coating (P content < 5 wt. %) [39]. As Mo element is incorporated into the coating, the increase of metal-to-hypophosphite ratio in the coating bath results in the decline of P co-deposition from 11 wt.% to 2 wt. % (see Table 2), thereby altering the microstructure and properties accordingly.

The surface morphologies of heat-treated Ni-P coating and Ni-Mo-P/Ni-P coating and their corresponding XRD patterns are presented in Figure 6.2. The microstructure of Ni-P coating transforms from amorphous to crystalline after the heat treatment, confirmed by the absence of nodular structure and the appearance of grain boundaries (Figure 6.2a). Comparatively, the fine crystals on the as-deposited Ni-Mo-P/Ni-P coating are not clearly seen after the heat treatment, which may be ascribed to the formation of the oxide film on the coating surface. The X-ray diffraction patterns (Figure 6.2c) reveal that the heat treatment at 400 °C gives rise to the precipitation of Ni_3P phase and residual Ni phase for Ni-P coating, while Ni_4Mo is the major phase of heat-treated Ni-Mo-P/Ni-P coating, along with trace amount of Ni_3P. As shown from the EDS results in Table 6.2, the presence of O element indicates the formation of oxides due to the heat treatment, the composition of which needs to be verified via XPS analysis results.

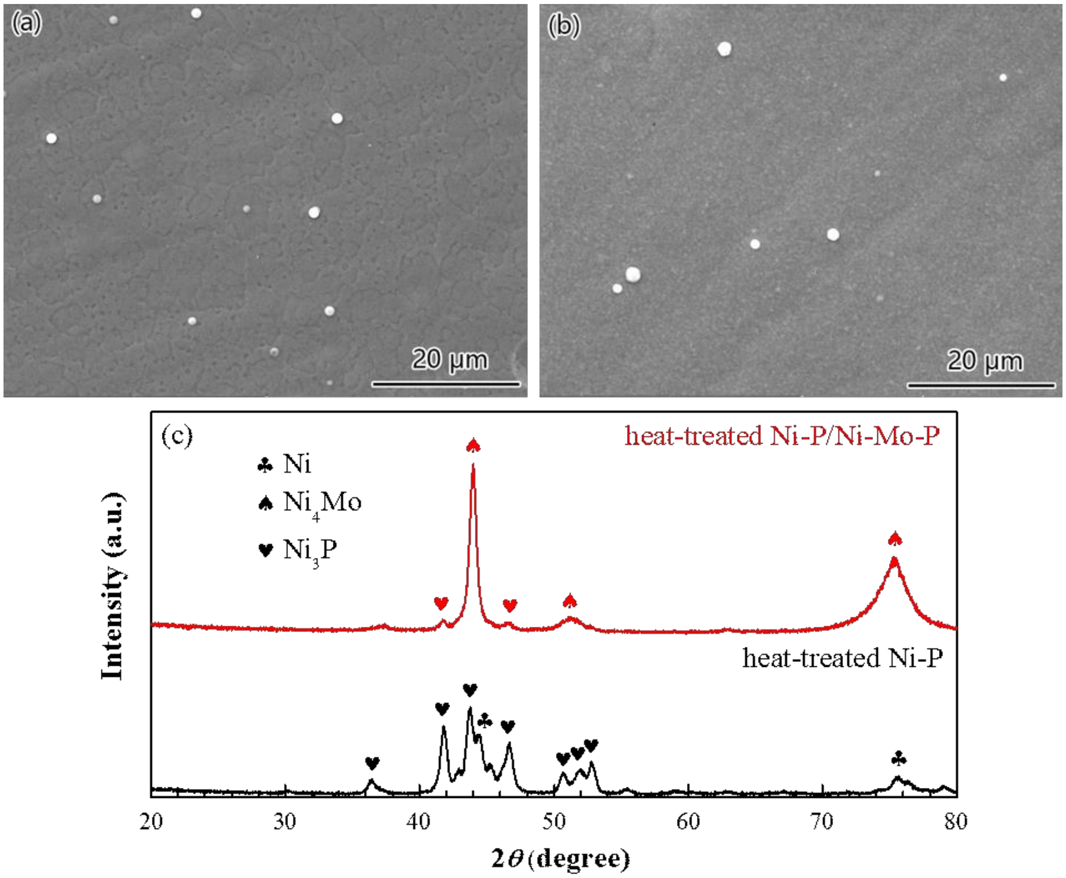

Figure 6.2 SEM surface morphologies of (a) heat-treated Ni-P coating and (b) heat-treated Ni-Mo-P/Ni-P coating; (c) XRD patterns of Ni-P and Ni-Mo-P/Ni-P coatings after heat treatment at 400 °C for 2 h.

Table 6.2 Elemental compositions (wt.%) of various coatings prior to tests.

Species	Ni	P	Mo	O
As-deposited Ni-P	88.68	11.32	-	-
As-deposited Ni-Mo-P/Ni-P	89.30	2.32	8.39	-
Heat-treated Ni-P	83.46	10.34	-	6.20
Heat-treated Ni-Mo-P/Ni-P	82.64	1.94	7.52	7.91

Generally, NiO is the predominant compound formed on the heat-treated Ni-P coating according to previous findings [40]. Therefore, to further clarify the chemical composition of the oxide film on Ni-Mo-P/Ni-P coating, XPS tests were employed and the results are shown in Figure 6.3. The Ni 2p spectrum shows two main peaks at the binding energies of 856.2 eV and 873.9 eV, corresponding to Ni^{2+} $2p_{3/2}$ and Ni^{2+} $2p_{1/2}$, with their satellite peaks at 861.5 eV and 880.0 eV, respectively [41,42], suggesting the presence of NiO. The Mo 3d spectrum can be fitted with two species: the doublet peaks at 231.2 eV and 233.8 eV associated with Mo^{5+} $3d_{5/2}$ and Mo^{5+} $3d_{3/2}$ peaks with a 2.6 eV spin-orbit splitting, and a 2.8 eV spin-orbit splitting between 232.6 eV and 235.4 eV are ascribed to Mo^{6+} $3d_{5/2}$ and Mo^{6+} $3d_{3/2}$ peaks [43–45]. It indicates that Mo(0) is oxidized to Mo(VI) and Mo(V) during the heat treatment but Mo(IV) no longer exists, which is in consistence with the findings of Laszczyńska et al. that Mo(IV) oxide is only present when heated at lower temperatures (200 °C) and transforms to a higher valence at higher temperatures (400 °C) [46]. Furthermore, P peak is not identified from the spectrum, implying the absence of P element in the oxide film.

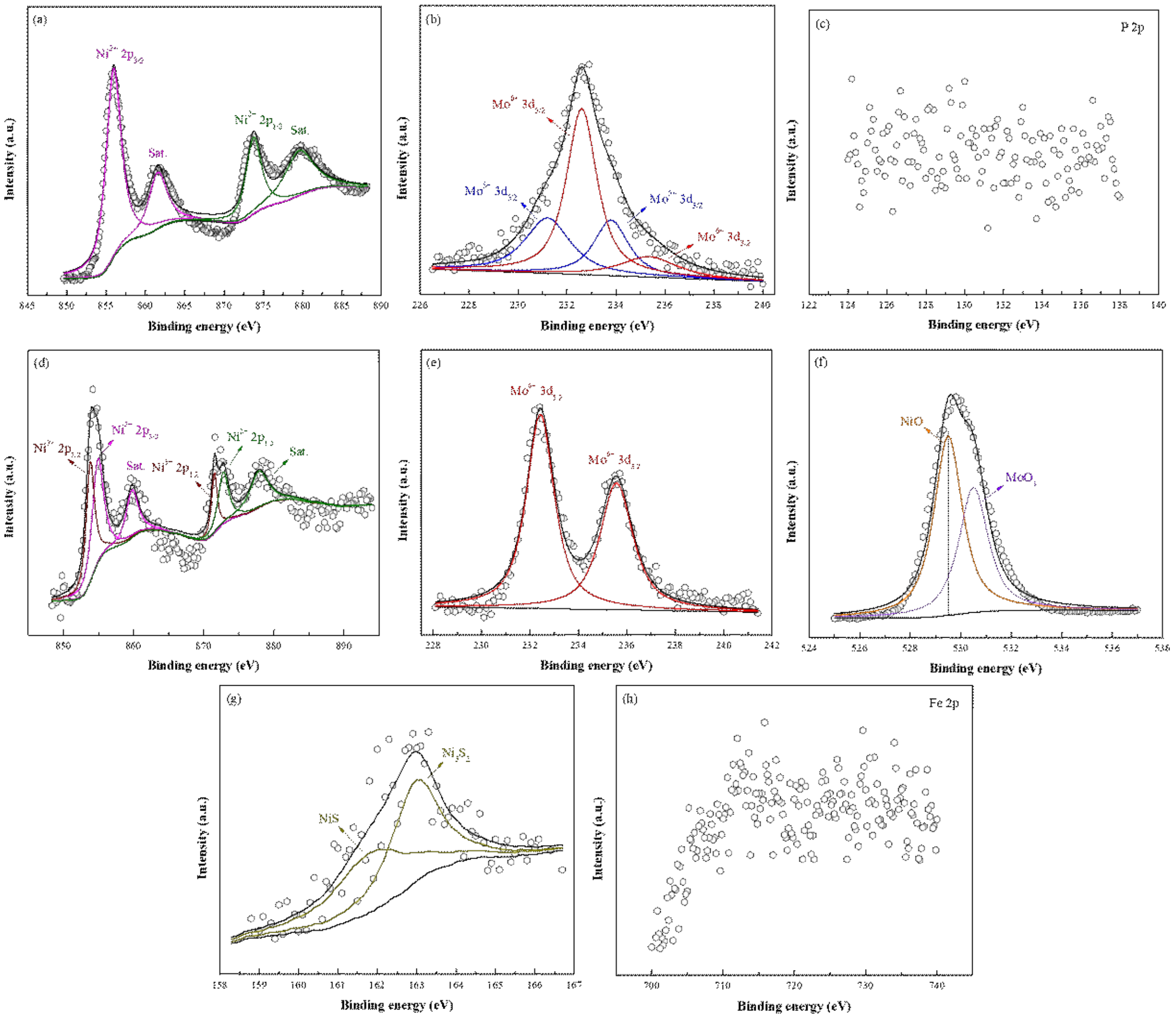

Figure 6.3 XPS spectra of oxide film on heat-treated Ni-Mo-P/Ni-P coating before corrosion tests: (a) Ni 2p; (b) Mo 3d; (c) P 2p; XPS spectra of corrosion product on heat-treated Ni-Mo-P/Ni-P coating after immersion test for 7 d: (d) Ni 2p; (e) Mo 3d; (f) O 1s; (g) S 2p; (h) Fe 2p.

6.3.2 Effect of Mo addition on the corrosion resistance of as-deposited Ni-P composite coatings

The potentiodynamic polarization curves of all the coatings in $CO_2/H_2S/Cl^-$ brine are depicted in Figure 6.4, and the corresponding calculated corrosion potentials (E_{corr}) and corrosion current densities (i_{corr}) by Tafel extrapolation method are listed in Table 6.3, reflecting the overall corrosion tendency quantitatively. For as-deposited coatings, the E_{corr}

value of Ni-Mo-P/Ni-P coating (-387.5 mV) is more negative than that of Ni-P coating (-268.8 mV), suggesting that the coating degradation becomes easier with the Mo addition. The incorporation of Mo results in an increased i_{corr} (3.35 μA·cm^{-2}), which is nearly three times higher than that of Ni-P coating (1.27 μA·cm^{-2}), revealing a higher corrosion rate. Furthermore, the corrosion kinetics information of coatings corresponding to the electrochemical processes can be found from the anodic branches. A current plateau (from -0.1 V_{SCE} to 0 V_{SCE}) is observed for as-deposited Ni-P coating, which is attributed to the high affinity of S species to Ni [47], along with the formation of a thin protective P-rich layer on the surface [48]. Similar phenomenon of the current recession is also seen for as-deposited Ni-Mo-P/Ni-P coating in the same potential range.

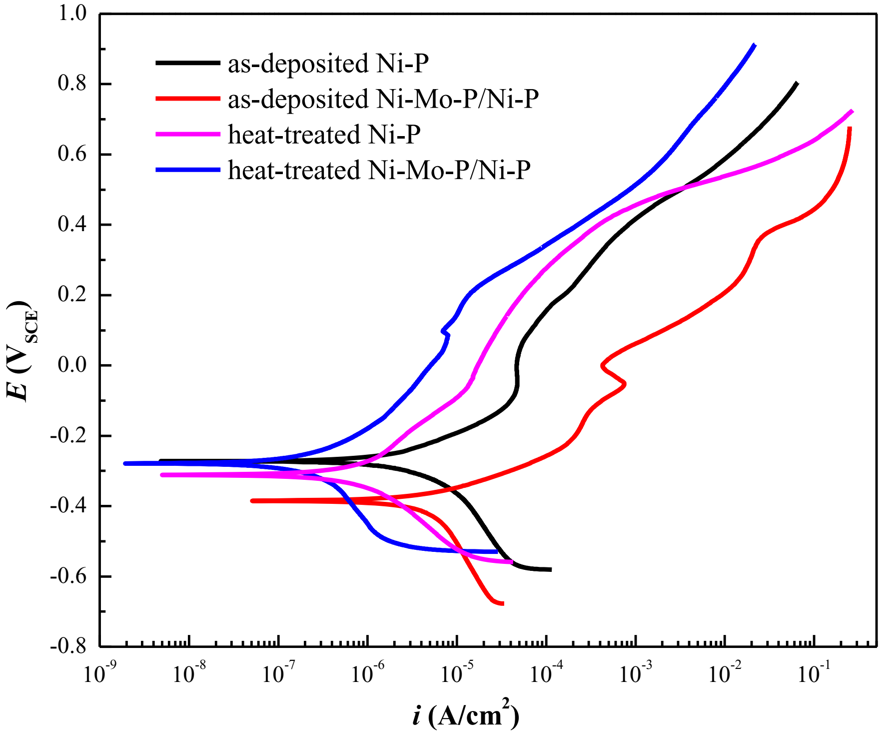

Figure 6.4 Potentiodynamic polarization curves of various coatings in 3.5 wt.% NaCl solution saturated with CO_2 and H_2S.

Table 6.3 Electrochemical parameters of different coatings obtained from the potentiodynamic polarization curves.

Species	E_{corr} (mV vs. SCE)	i_{corr} (μA·cm^{-2})	η (%)
As-deposited Ni-P	-268.8 ± 8.2	1.27 ± 0.17	-
As-deposited Ni-Mo-P/Ni-P	-387.5 ± 12.2	3.35 ± 0.21	-
Heat-treated Ni-P	-312.9 ± 10.5	0.50 ± 0.06	60.6
Heat-treated Ni-Mo-P/Ni-P	-276.3 ± 5.8	0.13 ± 0.02	96.1

EIS tests were then employed to study the changes of electrochemical process caused by the Mo incorporation. The Nyquist plots of as-deposited coatings (Figure 6.5a) show a capacitive semi-arc at high-medium frequencies related to the coating, and another incomplete capacitive semi-arc at low frequencies signifying the charge transfer process at the electric double layer. The radius of the semicircle decreases with the incorporation of Mo, indicating a lowered polarization resistance. The appropriate equivalent electrical circuit (EEC) adopted for EIS data fitting is shown in Figure 6.5c [49], and the fitted parameters are listed in Table 6.4. It consists of solution resistance R_s connected in series with two time constants $Q_c(R_c(Q_{dl}R_{ct}))$: Q_c and R_c are the capacitance and resistance of the coating, respectively; Q_{dl} and R_{ct} are the capacitance of the electric double layer and the charge transfer resistance, respectively, which are adopted to describe the electrochemical process at the coating defects (e.g., micropores for amorphous coating; grain boundaries and crystal defects for crystalline coating). The constant phase element (CPE) (designated as Q_c and Q_{dl}) is introduced to replace pure capacitance for a better fitting, the admittance of which is given as below [50]:

$$Y(Q) = Y_0(Q)(j\omega)^n \quad \text{(Eq. 6.4)}$$

where $Y_0(Q)$ is the admittance constant of CPE; j is the imaginary number; ω is the angular frequency; n is the empirical exponent. The addition of Mo results in higher $Y_0(Q_c)$ and accordingly lower R_c, indicating more defects serving as corrosion pathways in the Ni-Mo-P/Ni-P coating, which is consistent with its crystalline microstructure with more active sites to facilitate the penetration of corrosive medium, as compared to the amorphous Ni-P coating. Likewise, the R_{ct} value declines from 4.00×10^3 $\Omega \cdot cm^2$ to 1.00×10^4 $\Omega \cdot cm^2$, along with the increase of $Y_0(Q_{dl})$, demonstrating that the electrolyte penetration promotes the coating corrosion and consequently results in an elevated corrosion rate at active corrosion sites.

With the help of the electrochemical results as stated above, the Mo addition into as-deposited Ni-P coating poses a detrimental impact on the corrosion performance, which is closely related to its chemical composition and microstructure. As noted in Section 3.1, the P content significantly drops after Mo incorporation, which contributes to the degradation of corrosion resistance. The high-P coating displays better anti-corrosion performance than low-P coating, especially in acidic environments, while low-P coating possesses high mechanical performance due to the crystalline microstructure [3]. However, this type of microstructure owns more active sites for corrosion to take place preferentially. Moreover, Ni and Mo exist in their metallic states independently in the as-deposited coating, as confirmed from XRD results, therefore galvanic corrosion is likely to occur because of the different chemical affinity of Ni and Mo to sulfur species and the reactivity difference of two metals. Rodriguez et al. [51] reported that metallic Ni greatly enhanced the interaction of Mo and S, facilitating the sulfidation of Mo. More importantly, the absence of oxide film on the coating surface profoundly favors the penetration of corrosion electrolyte through corrosion pathways and promotes corrosion.

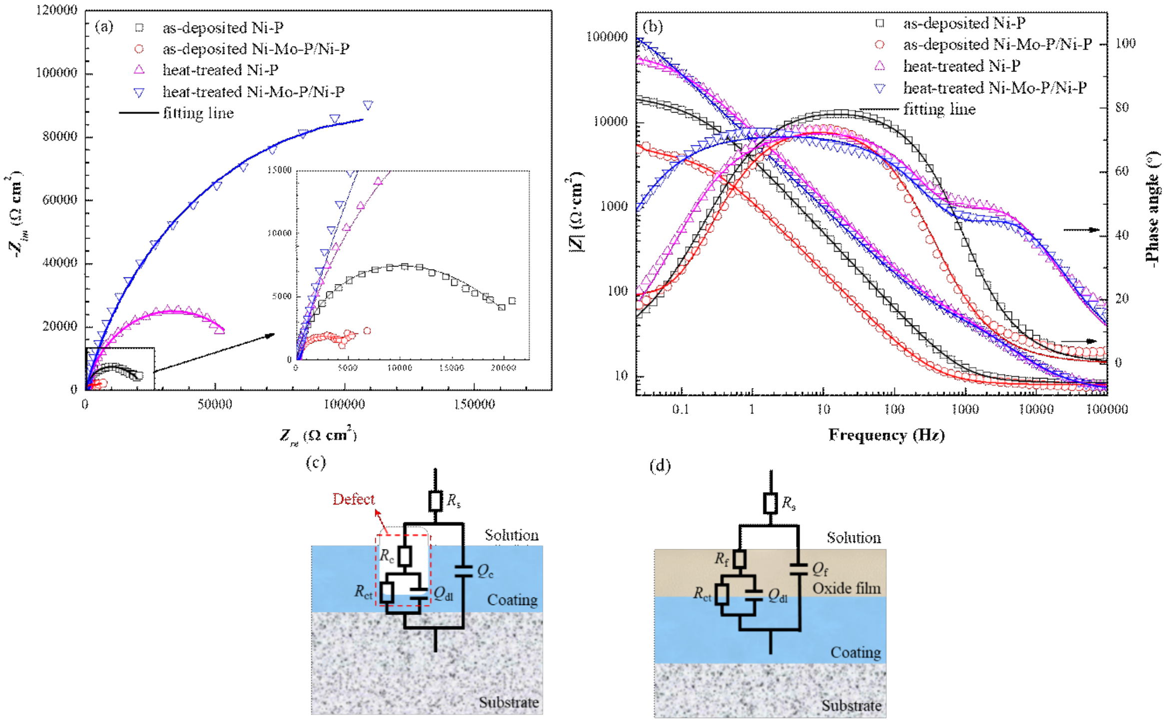

Figure 6.5 (a) Nyquist plots and (b) Bode plots of as-deposited and heat-treated coatings in 3.5 wt.% NaCl solution saturated with CO_2 and H_2S; Equivalent electric circuits used for EIS fitting: (c) as-deposited coatings; (d) heat-treated coatings.

Table 6.4 Fitted and calculated parameters for the impedance spectra in Figure 6.5.

Species	R_s (Ω·cm^2)	$Y_0(Q_c)$ (Ω^{-1}·cm^{-2}·s^n)	R_c (Ω·cm^2)	$Y_0(Q_{dl})$ (Ω^{-1}·cm^{-2}·s^n)	R_{ct} (Ω·cm^2)	Quality of fit
As-deposited Ni-P	6.50	4.80×10^{-5}	1.30×10^{4}	1.50×10^{-4}	1.00×10^{4}	2.96×10^{-4}
As-deposited Ni-Mo-P/Ni-P	7.00	1.67×10^{-4}	4.59×10^{3}	3.05×10^{-2}	4.00×10^{3}	2.55×10^{-3}
	R_s (Ω·cm^2)	$Y_0(Q_f)$ (Ω^{-1}·cm^{-2}·s^n)	R_f (Ω·cm^2)	$Y_0(Q_{dl})$ (Ω^{-1}·cm^{-2}·s^n)	R_{ct} (Ω·cm^2)	Quality of fit
Heat-treated Ni-P	6.87	1.96×10^{-5}	125.1	8.16×10^{-5}	6.66×10^{4}	2.21×10^{-3}

Heat-treated Ni-Mo-P/Ni-P	6.67	1.64×10^{-5}	173.9	2.24×10^{-5}	2.15×10^{5}	1.17×10^{-3}

6.3.3 Effect of heat treatment on the corrosion resistance and oxide film characteristics of Ni-P composite coatings

Since Mo incorporation into as-deposited Ni-P coating leads to a more severe degradation, the effect of heat treatment on the corrosion protection enhancement is further evaluated. As shown from the potentiodynamic curves in Figure 6.4, heat-treated coatings exhibit lower corrosion activity, as evidenced from the curves shifting to the left direction (indicating smaller current densities) as compared to as-deposited coatings. Furthermore, the “pseudo-passivation” behavior is not observed because of the presence of oxide film blocking the contact of the coating and H_2S-containing electrolyte.

To quantitatively characterize the additional anti-corrosion capability contributed by the heat treatment, the corrosion inhibition efficiency (η) is introduced and defined as:

$$\eta = \frac{i_{corr}^{as-deposited} - i_{corr}^{heat-treated}}{i_{corr}^{as-deposited}} \times 100\% \qquad \text{(Eq. 6.5)}$$

As seen in Table 6.3, heat treatment does not remarkably shift E_{corr} to the positive direction. Nonetheless, heat-treated coatings display much lower i_{corr} than as-deposited coatings, and an exceptional corrosion inhibition efficiency (η=96.1%) is obtained for heat-treated Ni-Mo-P/Ni-P coating, signifying the notable corrosion resistance enhancement by the heat treatment. This superb η value significantly outcompetes the recently published result (η=47.9%) brought by the ZrO_2 nanoparticle addition into Ni-W-P/Ni-P coating in sweat/sour brine containing Cl^- [18], which highlights the applicability of Mo addition and heat treatment in improving the anti-H_2S corrosion performance.

The EIS results provide more reliable information on the mass transport of corrosive electrolyte and the corrosion process of the coating. As presented in the Nyquist plots in Figure 6.5a, the shape of semicircles for heat-treated coatings differs from those of as-deposited coatings, indicating the change of corrosion mechanism. The Nyquist plots exhibit a capacitive semi-arc at high frequencies corresponding to the formed oxide film, and another capacitive semi-arc at medium-low frequencies representing the electric double layer, as confirmed clearly from the Bode plots in Figure 6.5b. Therefore, the EEC for heat-treated coatings can be expressed by $R_s(Q_f(R_f(Q_{dl}R_{ct})))$ in Figure 6.5d, which is extensively used in stainless steel systems [52]. Besides ($Q_{dl}R_{ct}$), (Q_fR_f) stands for the formed oxide film due to the heat treatment, where Q_f and R_f are the capacitance and resistance of the oxide film, respectively. Heat-treated Ni-Mo-P/Ni-P coating displays larger R_f and smaller $Y_0(Q_f)$, an implication of better isolation properties of the oxide film than that on heat-treated Ni-P coating. The presence of oxide film causes a notable increase of R_{ct} with respect to as-deposited coatings, with heat-treated Ni-Mo-P/Ni-P coating exhibiting the highest R_{ct}, which signifies the robust corrosion resistance of heat-treated coatings and the co-contribution of Mo addition and heat treatment to the corrosion performance enhancement.

EN measurements were performed to further investigate the corrosion behavior and the oxide film characteristics of heat-treated coatings. Figure 6.6 depicts the typical raw EPN and ECN data of two heat-treated coatings in the $CO_2/H_2S/Cl^-$ brine after immersion for 12 h. The potential noise data show trace fluctuations with the variations in mV scale, suggesting the passive state of the surface. The current-time record exhibits very low amplitude (in nA scale) and high repetition rates, with background noise characteristics clearly observed, indicating that the electrochemical process is greatly eliminated on the surface, except for the irregular fluctuations for heat-treated Ni-P coating, which can presumably be attributed to the occurrence of localized corrosion attack. Similar oscillations appear randomly on heat-treated Ni-P coating as immersion further proceeds, but they are not detected for heat-treated Ni-Mo-P/Ni-P coating in the entire immersion period, implying better anti-corrosion performance of the Mo-containing oxide film.

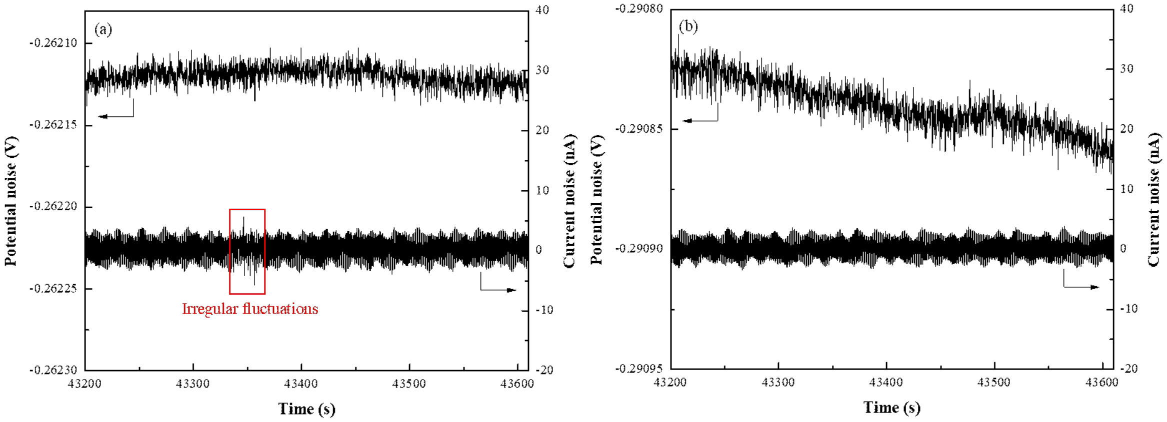

Figure 6.6 Typical raw EPN and ECN data of (a) heat-treated Ni-P coating and (b) heat-treated Ni-Mo-P/Ni-P coating recorded after immersion in CO_2/H_2S-saturated 3.5 wt.% NaCl solution for 12 h.

Generally, the noise data can be analyzed in time and frequency domains. Noise resistance (R_n), commonly used as an indicator of corrosion resistance, is calculated by analyzing the noise data in time domain with the definition given as below:

$$R_n = \frac{\sigma_V}{\sigma_i} \qquad \text{(Eq. 6.6)}$$

where σ_V and σ_i are the standard deviations of potential and current noise data, respectively. The variation of R_n as a function of time is presented in Figure 6.7. It is seen that both coatings undergo a decline of R_n value in the early stage (first 4 h), a possible indication that the oxide film has reached the equilibrium state. Afterwards, R_n values of heat-treated Ni-P coating maintain in the range of 5×10^4 to 8×10^4 $\Omega\cdot cm^2$, while that of heat-treated Ni-Mo-P/Ni-P coating increases with fluctuations after 12 h of immersion and keeps stable at *ac.* 1.3×10^5 $\Omega\cdot cm^2$. The difference of R_n variations for two heat-treated coatings further proves the corrosion protection enhancement owing to Mo addition, which is in good agreement with EIS results.

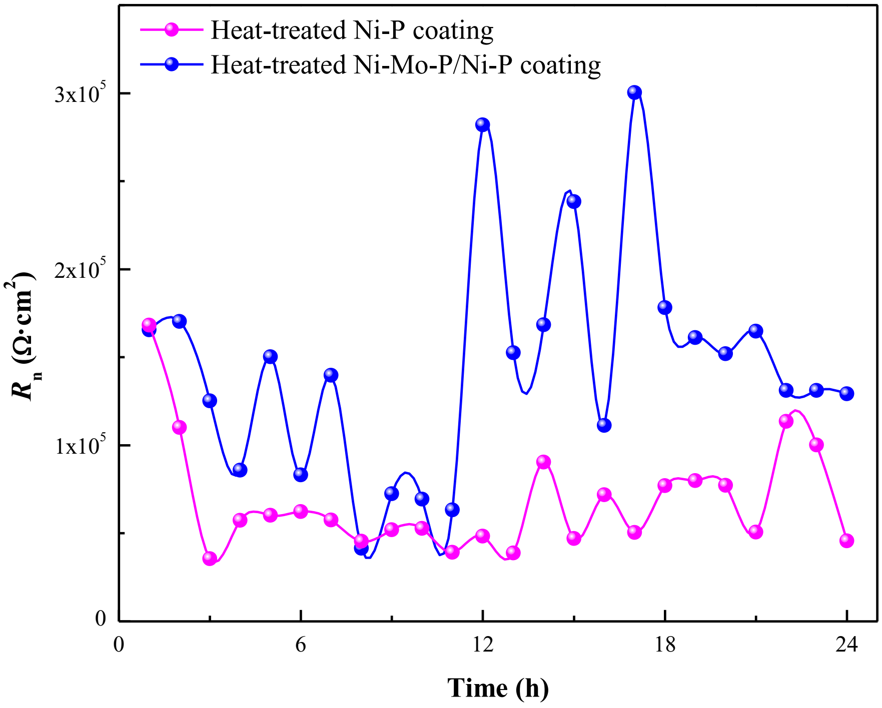

Figure 6.7 R_n as a function of time for heat-treated coatings immersed in CO_2/H_2S-saturated 3.5 wt.% NaCl solution.

To strengthen the analysis of noise data, PSD data were obtained in frequency domain by FFT, and the calculation of noise PSD is based on the equation given as below [53]:

$$\log PSD = A + S \log f \qquad \text{(Eq. 6.7)}$$

where A is the noise intensity, and S is the slope of the linear region of PSD plots, also known as the roll-off slope. The potential PSD plots and the corresponding calculated parameters of two heat-treated coatings after exposed to $CO_2/H_2S/Cl^-$ brine are shown in Figure 6.8. The PSD decreases with the increase of the frequency and exhibits a linear relationship at high-medium frequencies with the slope of S_V, which has been widely adopted to indicate the corrosion type by many investigators [53,54]. The S_V value of heat-treated Ni-Mo-P/Ni-P coating shifts positively from -0.95 after 1 h of immersion to -0.32 and -0.52 after 12 h and 24 h respectively, suggesting that the formed oxide film ensures the passivation on the coating surface. Girija et al. [55] substantiated a low roll-off slope of -0.3 for 304L stainless steel in 0.1% NaOH solution, which was attributed to the passive state of the surface. Similar observations of close to zero S_V has been reported by Fukuda et al. [56], who examined the current transients for pure iron and stainless steels and credited the low S_V to the presence of white noise due to the passive state. In contrast, heat-treated Ni-P coating displays more negative S_V values (close to -2 after 1 h), showing weaker passivation and higher likelihood of localized corrosion. Cheng et al. [53] reported that the roll-off slope approached -2 with the pitting initiation of inhibited A516-70 carbon steel in chloride solution, and a low roll-off slope of -0.5 appeared indicating passivation state, which was caused by the growth of passive film with the addition of 0.05 M CrO_4^{2-}. Therefore, based on the electrochemical noise analysis, the Mo-containing oxide film endows heat-treated Ni-Mo-P/Ni-P coating with better passivation properties and greater anti-corrosion performance than the heat-treated Ni-P coating.

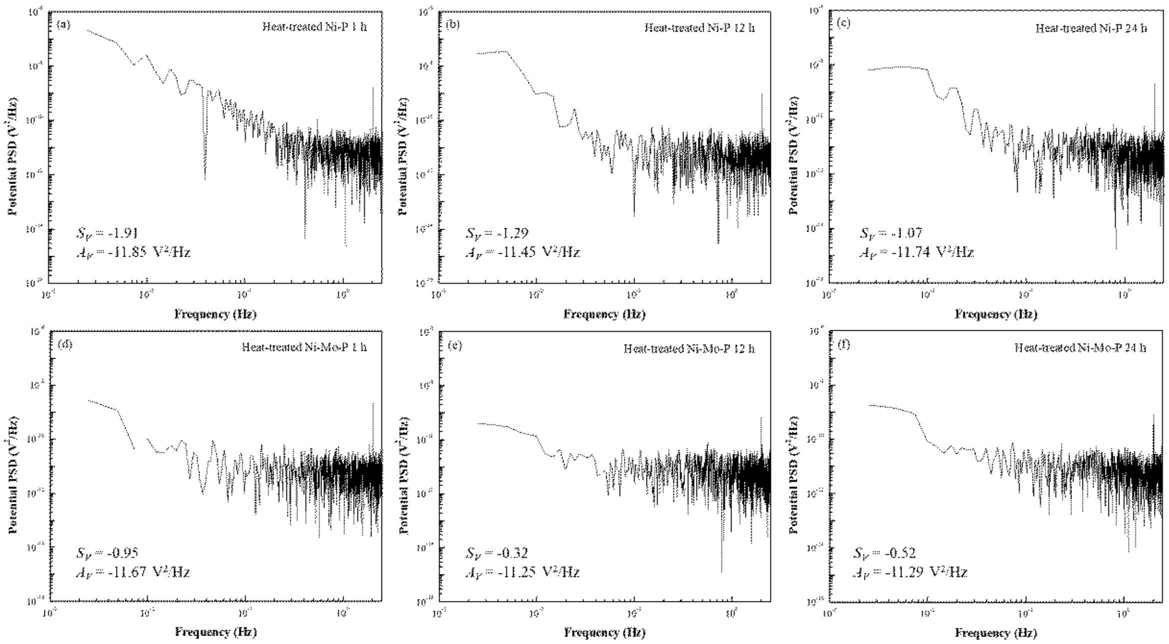

Figure 6.8 The potential PSD plots of heat-treated coatings: (a) Ni-P coating and (b) Ni-Mo-P/Ni-P coating immersed in CO_2/H_2S-saturated 3.5 wt.% NaCl solution at different times.

6.3.4 Anti-corrosion stability of heat-treated Ni-Mo-P/Ni-P coating

To further evaluate the corrosion performance of heat-treated Ni-Mo-P/Ni-P coating for a longer period, 7-day immersion tests were performed in the 3.5 wt.% NaCl solution saturated with CO_2 and H_2S, and the SEM surface and cross-sectional morphologies after immersion are shown in Figure 6.9. As depicted in Figure 6.9a, interlaced corrosion products with clustered needle-like and clay-like structures are observed with the absence of noticeable corrosion pits on the surface, thereby constituting a compact corrosion product layer. The inspection of the coating cross-section shows that the electrolyte penetration does not reach the coating/coating or coating/substrate interface after 1 week of immersion, revealing the satisfactory corrosion resistance of heat-treated Ni-Mo-P/Ni-P coating.

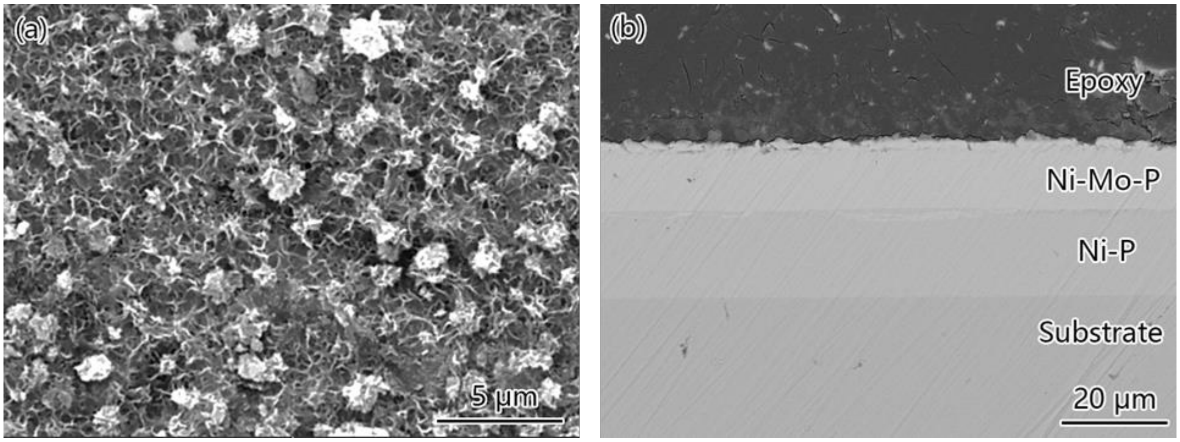

Figure 6.9 SEM (a) surface and (b) cross-sectional morphologies of heat-treated Ni-Mo-P/Ni-P coating after 7 d of immersion in CO_2/H_2S-saturated 3.5 wt.% NaCl solution.

XPS analysis was then employed after immersion tests to examine the chemical composition of corrosion product and investigate the anti-corrosion mechanism, as presented in Figure 6.3. Besides the Ni^{2+} peaks and their corresponding satellite peaks depicted in Figure 6.3a, the Ni 2p spectrum exhibits two additional Ni^{3+} peaks at the binding energies of 855.2 eV and 872.8 eV [57,58], which is in accordance with our previous research of Ni-P coating in H_2S-containing corrosive environments [8,9]. $3p_{5/2}$ and $3p_{3/2}$ doublets at 232.5 eV and 235.5 eV are identified for the Mo 3d spectrum, indicating the sole presence of Mo^{6+}, which predominantly exists in the form of MoO_3 as observed from the O 1s spectrum [59]. The Mo^{5+} peaks are no longer detected after immersion, implicative of the transformation from Mo(V) to Mo(VI) during the corrosion process, which requires further experimental verification. Besides, the other peak at the binding energy of 529.5 eV is assigned to NiO [60]. The S 2p spectrum contains two peaks at 161.9 eV and 163.0 eV belonging to NiS and Ni_3S_2, respectively [61,62]. It is worthwhile noting that Fe peak is not found from the spectrum, highlighting no electrolyte penetration through the coating to the steel substrate after immersion for 7 d, which is in good agreement with the cross-sectional SEM image.

The outstanding anti-corrosion property of heat-treated Ni-Mo-P/Ni-P coating in the H_2S-containing brine is not only derived from the desirable corrosion protection of nickel-based corrosion products (NiO, NiS and Ni_3S_2), but more attributed to the formed MoO_3. As reported [63,64], Mo^{6+} is the primary oxidized species of Mo in the passive film of stainless steels alloyed with Mo and plays a critical role in retarding the corrosion process. Pardo et al. [22] discovered the beneficial effect of Mo^{6+} in the passive film of austenitic stainless steels against the film breakdown by Cl^- attack and accredited it to the formation of Mo insoluble compounds (MoO_3 and $FeMoO_4$) which favored the repassivation. Specifically, MoO_3 demonstrates phenomenal resistance to corrosion induced by H_2S. The sulfidation of MoO_3 by H_2S in aqueous environments mainly follows the reaction below [65]:

$$MoO_3 + 2HS^- \rightarrow MoS_2 + 2OH^- + \frac{1}{2}O_2 \qquad \text{(Eq. 6.8)}$$

The Gibbs free energy (ΔG) of this reaction at room temperature and atmospheric pressure is larger than zero showcasing immunity to sulfidation attack, and this is also validated by the low corrosion rate of molybdenum in corrosive environments containing H_2S [65]. The immunity further coincides with the absence of Mo^{4+} in MoS_2 from the XPS results in this study. Ultimately, the Mo addition and heat treatment concurrently endow the coating with superior corrosion resistance in sweat/sour brine, which is predominantly originated from the compact nickel-based corrosion product layer and the formation of MoO_3 showing immunity to H_2S.

6.4 Conclusions

In summary, the corrosion behavior of electroless Mo-incorporated Ni-P coating was investigated in $CO_2/H_2S/Cl^-$ brine, and the effect of heat treatment on the corrosion resistance improvement was further revealed. The results show that Mo addition adversely affects the corrosion resistance of as-deposited Ni-P coating, while heat treatment profoundly advances the anti-corrosion performance of Ni-Mo-P/Ni-P composite coating.

The Mo incorporation into the as-deposited Ni-P coating results in the change of microstructure from amorphous to crystalline due to the declined P content. Heat treatment of Ni-Mo-P/Ni-P coating at 400 °C for 2 h facilitates the formation of Ni_4Mo phase and trace amount of Ni_3P phase. Furthermore, heat treatment gives rise to the formation of oxide film on the coating surface, with the primary chemical composition of NiO, Mo(V) and Mo(VI) oxides. Heat-heated Ni-Mo-P/Ni-P coating displays the best corrosion resistance, followed by heat-treated Ni-P coating, as-deposited Ni-P coating and as-deposited Ni-Mo-P/Ni-P coating. A superb corrosion inhibition efficiency (η=96.1%) is achieved for the heat-treated Ni-Mo-P/Ni-P coating, and the roll-off slopes approach -0.5, suggesting better passivation properties of the Mo-containing oxide film. The absence of oxide film, together with the formed crystalline microstructure with more active sites for corrosion initiation, contributes to the decreased corrosion resistance of as-deposited Ni-Mo-P/Ni-P coating. Meanwhile, the exceptional corrosion resistance of heat-treated Ni-Mo-P/Ni-P coating is predominantly originated from the compact corrosion product layer composed by nickel oxides and sulfides and the formation of the H_2S-immuned MoO_3.

6.5 References

[1] H. Ashassi-Sorkhabi, M. Es'haghi, Corrosion resistance enhancement of electroless Ni–P coating by incorporation of ultrasonically dispersed diamond nanoparticles, Corros. Sci. 77 (2013) 185–193.

[2] Y. Wang, X. Shu, S. Wei, C. Liu, W. Gao, R.A. Shakoor, R. Kahraman, Duplex Ni–P–ZrO_2/Ni–P electroless coating on stainless steel, J. Alloys Compd. 630 (2015) 189–194.

[3] H. Luo, M. Leitch, Y. Behnamian, Y. Ma, H. Zeng, J.L. Luo, Development of electroless Ni–P/nano-WC composite coatings and investigation on its properties, Surf. Coat. Technol. 277 (2015) 99–106.

[4] M. Gholizadeh-Gheshlaghi, D. Seifzadeh, P. Shoghi, A. Habibi-Yangjeh, Electroless Ni-P/nano-WO_3 coating and its mechanical and corrosion protection properties, J. Alloys Compd. 769 (2018) 149–160.

[5] C. Sun, S. Liu, J. Li, H. Zeng, J.L. Luo, Insights into the interfacial process in electroless Ni–P coating on supercritical CO_2 transport pipeline as relevant to carbon capture and storage, ACS Appl. Mater. Interfaces, 11 (2019) 16243–16251.

[6] L.L. Wang, H.J. Chen, L. Hao, A. Lin, F.X. Gan, Electrochemical corrosion behavior of electroless Ni–P coating in NaCl and H_2SO_4 solutions, Mater. Corros. 62 (2011) 1003–1007.

[7] I.V. Petukhov, N.A. Medvedeva, I.R. Subakova, V.I. Kichigin, Corrosion-electrochemical behavior of Ni-P coatings in deaerated acidic sulfate solutions, Prot. Met. Phys. Chem. Surf. 50 (2014) 875–882.

[8] C. Sun, H. Zeng, J.L. Luo, Unraveling the effects of CO_2 and H_2S on the corrosion behavior of electroless Ni-P coating in $CO_2/H_2S/Cl^-$ environments at high temperature and high pressure, Corros. Sci. 148 (2019) 317–330.

[9] J. Li, C. Sun, H. Zeng, J.L. Luo, Insights into the electrochemical corrosion behavior and mechanism of electroless Ni-P coating in the $CO_2/H_2S/Cl^-$ environment, Corrosion 76 (2020) 578–590.

[10] S. Ranganatha, T.V. Venkatesha, K. Vathsala, Development of electroless Ni–Zn–P/nano-TiO_2 composite coatings and their properties, Appl. Surf. Sci. 256 (2010) 7377–7383.

[11] J.N. Balaraju, K.S. Rajam, Electroless deposition of Ni–Cu–P, Ni–W–P and Ni–W–Cu–P alloys, Surf. Coat. Technol. 195 (2005) 154–161.

[12] W.X. Zhang, Z.H. Jiang, G.Y. Li, Q. Jiang, J.S. Lian, Electroless Ni–Sn–P coating on AZ91D magnesium alloy and its corrosion resistance, Surf. Coat. Technol. 202 (2008) 2570–2576.

[13] L. Zhang, Y. Jin, B. Peng, Y. Zhang, X. Wang, Q. Yang, J. Yu, Effects of annealing temperature on the crystal structure and properties of electroless deposited Ni–W–Cr–P alloy coatings, Appl. Surf. Sci. 255 (2008) 1686–1691.

[14] M. Alishahi, S.M. Monirvaghefi, A. Saatchi, S.M. Hosseini, The effect of carbon nanotubes on the corrosion and tribological behavior of electroless Ni–P–CNT composite coating, Appl. Surf. Sci. 258 (2012) 2439–2446.

[15] J.N. Balaraju, K.S. Rajam, Influence of particle size on the microstructure, hardness and corrosion resistance of electroless Ni–P–Al_2O_3 composite coatings, Surf. Coat. Technol. 200 (2006) 3933–3941.

[16] H. Luo, X. Wang, S. Gao, C. Dong, X. Li, Synthesis of a duplex Ni-P-YSZ/Ni-P nanocomposite coating and investigation of its performance, Surf. Coat. Technol. 311 (2017) 70–79.

[17] S. Afroukhteh, C. Dehghanian, M. Emamy, Preparation of the Ni–P composite coating co-deposited by nano TiC particles and evaluation of it's corrosion property, Appl. Surf. Sci. 258 (2012) 2597–2601.

[18] H. Luo, M. Leitch, H. Zeng, J.L. Luo, Characterization of microstructure and properties of electroless duplex Ni-W-P/Ni-P nano-ZrO_2 composite coating, Mater. Today Phys. 4 (2018) 36–42.

[19] A. Tomio, M. Sagara, T. Doi, H. Amaya, N. Otsuka, T. Kudo, Role of alloyed molybdenum on corrosion resistance of austenitic Ni–Cr–Mo–Fe alloys in H_2S–Cl^- environments, Corros. Sci. 98 (2015) 391–398.

[20] Q.Y. Wang, X.Z. Wang, H. Luo, J.L. Luo, A study on corrosion behaviors of Ni–Cr–Mo laser coating, 316 stainless steel and X70 steel in simulated solutions with H_2S and CO_2, Surf. Coat. Technol. 291 (2016) 250–257.

[21] G. Genchev, C. Bosch, E. Wanzenberg, A. Erbe, Role of molybdenum in corrosion of iron-based alloys in contact with hydrogen sulfide containing solution, Mater. Corros. 68 (2017) 595–603.

[22] A. Pardo, M.C. Merino, A.E. Coy, F. Viejo, R. Arrabal, E. Matykina, Effect of Mo and Mn additions on the corrosion behaviour of AISI 304 and 316 stainless steels in H_2SO_4, Corros. Sci. 50 (2008) 780–794.

[23] G.O. Ilevbare, G.T. Burstein, The role of alloyed molybdenum in the inhibition of pitting corrosion in stainless steels, Corros. Sci. 43 (2001) 485–513.

[24] K. Sugimoto, Y. Sawada, The role of molybdenum additions to austenitic stainless steels in the inhibition of pitting in acid chloride solutions, Corros. Sci. 17 (1977) 425–445.

[25] K. Denpo, H. Ogawa, Passivity of corrosion-resistant alloys in environments containing chloride and hydrogen sulfide, Corrosion 53 (1997) 718–723.

[26] C.R. Clayton, Y.C. Lu, A bipolar model of the passivity of stainless steel: the role of Mo addition, J. Electrochem. Soc. 133 (1986) 2465–2473.

[27] H. Liu, Z. Liu, Evaluation of microstructures and properties of laser-annealed electroless Ni–P/Ni–Mo–P duplex coatings, Surf. Coat. Technol. 330 (2017) 270–276.

[28] G.S. Song, S. Sun, Z.C. Wang, C.Z. Luo, C.X. Pan, Synthesis and characterization of electroless Ni–P/Ni–Mo–P duplex coating with different thickness combinations, Acta Metall. Sin. (Engl. Lett.) 30 (2017) 1008–1016.

[29] A.E. Fetohi, R.A. Hameed, K.M. El-Khatib, Ni–P and Ni–Mo–P modified aluminium alloy 6061 as bipolar plate material for proton exchange membrane fuel cells, J. Power Sources 240 (2013) 589–597.

[30] H. Ashassi-Sorkhabi, S.H. Rafizadeh, Effect of coating time and heat treatment on structures and corrosion characteristics of electroless Ni–P alloy deposits, Surf. Coat. Technol. 176 (2004) 318–326.

[31] J. Wojewoda-Budka, A. Wierzbicka-Miernik, L. Litynska-Dobrzynska, M.J. Szczerba, G. Mordarski, M. Mosiałek, Z. Huber, P. Zieba, Microstructure characteristics and phase transformations of the Ni-P and Ni-P-Re electroless deposited coatings after heat treatment, Electrochim. Acta 209 (2016) 183–191.

[32] M. Czagány, P. Baumli, G. Kaptay, The influence of the phosphorous content and heat treatment on the nano-micro-structure, thickness and micro-hardness of electroless Ni-P coatings on steel, Appl. Surf. Sci. 423 (2017) 160–169.

[33] T. Rabizadeh, S.R. Allahkaram, A. Zarebidaki, An investigation on effects of heat treatment on corrosion properties of Ni–P electroless nano-coatings, Mater. Des. 31 (2010) 3174–3179.

[34] M. Sribalaji, P. Arunkumar, K.S. Babu, A.K. Keshri, Crystallization mechanism and corrosion property of electroless nickel phosphorus coating during intermediate temperature oxidation, Appl. Surf. Sci. 355 (2015) 112–120.

[35] M.A. Shoeib, M.M. Kamel, S.M. Rashwan, O.M. Hafez, Corrosion behavior of electroless Ni–P/TiO_2 nanocomposite coatings, Surf. Interface Anal. 47 (2015) 672–680.

[36] F. Mansfeld, Z. Sun, C.H. Hsu, A. Nagiub, Concerning trend removal in electrochemical noise measurements, Corros. Sci. 43 (2001) 341–352.

[37] F.B. Mainier, M.P.C. Fonseca, S.S. Tavares, J.M. Pardal, Quality of electroless Ni-P (nickel-phosphorus) coatings applied in oil production equipment with salinity, J. Mater. Sci. Chem. Eng. 1 (2013) 1–8.

[38] S. Ranganatha, T.V. Venkatesha, K. Vathsala, Electroless Ni–W–P coating and its nano-WS_2 composite: preparation and properties, Ind. Eng. Chem. Res. 51 (2012) 7932–7940.

[39] R. N. Duncan, The metallurgical structure of electroless nickel deposits: effect on coating properties, Plating Surf. Finish. 83 (1996) 65–69.

[40] D. Dong, X.H. Chen, W.T. Xiao, G.B. Yang, P.Y. Zhang, Preparation and properties of electroless Ni–P–SiO_2 composite coatings, Appl. Surf. Sci. 255 (2009) 7051–7055.

[41] Z. Yan, C. Guo, F. Yang, C. Zhang, Y. Mao, S. Cui, Y. Wei, L. Hou, L. Xu, Cliff-like NiO/Ni_3S_2 directly grown on Ni foam for battery-type electrode with high area capacity and long cycle stability, Electrochim. Acta 251 (2017) 235–243.

[42] M. Xiao, R. Cheng, M. Hao, M. Zhou, Y. Miao, Onsite substitution synthesis of ultrathin Ni nanofilms loading ultrafine Pt nanoparticles for hydrogen evolution, ACS Appl. Mater. Interfaces 7 (2015) 26101–26107.

[43] N. Zeng, D.G. Hopkinson, B.F. Spencer, S.G. McAdams, A.A. Tedstone, S.J. Haigh, D.J. Lewis, Direct synthesis of MoS_2 or MoO_3 via thermolysis of a dialkyl dithiocarbamato molybdenum (iv) complex, Chem. Commun. 55 (2019) 99–102.

[44] H. Li, M. Li, Y. Chu, F. Liu, H. Nie, Effect of different preparation methods of MoO_3/Al_2O_3 catalysts on the existing states of Mo species and hydrodesulfurization activity, Fuel 116 (2014), pp.168–174.

[45] P. Qin, G. Fang, W. Ke, F. Cheng, Q. Zheng, J. Wan, H. Lei, X. Zhao, In situ growth of double-layer MoO_3/MoS_2 film from MoS_2 for hole-transport layers in organic solar cell, J. Mater. Chem. A 2 (2014) 2742–2756.

[46] A. Laszczyńska, W. Tylus, B. Szczygieł, I. Szczygieł, Influence of post−deposition heat treatment on the properties of electrodeposited Ni−Mo alloy coatings, Appl. Surf. Sci. 462 (2018) 432–443.

[47] J.M. Hernandez, D.H. Lim, H.V.P. Nguyen, S.P. Yoon, J. Han, S.W. Nam, C.W. Yoon, S.K. Kim, H.C. Ham, Decomposition of hydrogen sulfide (H_2S) on Ni (100) and Ni_3Al (100) surfaces from first-principles, Int. J. Hydrog. Energy 39 (2014) 12251–12258.

[48] A. Królikowski, P. Butkiewicz, Anodic behavior of Ni P alloys studied by impedance spectroscopy, Electrochim. Acta 38 (1993) 1979–1983.

[49] C. Sun, J. Li, S. Shuang, H. Zeng, J.L. Luo, Effect of defect on corrosion behavior of electroless Ni-P coating in CO_2-saturated NaCl solution, Corros. Sci. 134 (2018) 23–37.

[50] C.N. Cao, J.Q. Zhang, An introduction to electrochemical impedance spectroscopy, Science, Beijing, 2002.

[51] J.A. Rodriguez, S.Y. Li, J. Hrbek, H.H. Huang, G.Q. Xu, The interaction of Ni and Fe with sulfur and molybdenum-sulfide surfaces: a TDS, XPS and hydrogen-chemisorption study, Surf. Sci. 370 (1997) 85–95.

[52] H. Luo, C.F. Dong, X.G. Li, K. Xiao, The electrochemical behaviour of 2205 duplex stainless steel in alkaline solutions with different pH in the presence of chloride, Electrochim. Acta 64 (2012) 211–220.

[53] L. Liu, Y. Li, F. Wang, Pitting mechanism on an austenite stainless steel nanocrystalline coating investigated by electrochemical noise and in-situ AFM analysis, Electrochim. Acta 54 (2008) 768–780.

[54] Y.F. Cheng, B.R. Rairdan, J.L. Luo, Features of electrochemical noise generated during pitting of inhibited A516-70 carbon steel in chloride solutions, J. Appl. Electrochem. 28 (1998) 1371–1375.

[55] S. Girija, U.K. Mudali, V.R. Raju, R.K. Dayal, H.S. Khatak, B. Raj, Determination of corrosion types for AISI type 304L stainless steel using electrochemical noise method, Mater. Sci. Eng. A 407 (2005) 188–195.

[56] T. Fukuda, T. Mizuno, The evaluation of pitting corrosion from the spectrum slope of noise fluctuation on iron and 304 stainless steel electrodes, Corros. Sci. 38 (1996) 1085–1091.

[57] S. Doubaji, B. Philippe, I. Saadoune, M. Gorgoi, T. Gustafsson, A. Solhy, M. Valvo, H. Rensmo, K. Edström, Passivation layer and cathodic redox reactions in sodium-ion batteries probed by HAXPES, ChemSusChem 9 (2016) 97–108.

[58] Y. Hou, L.J. Tang, H.W. Qiao, Z.R. Zhou, Y.L. Zhong, L.R. Zheng, M.J. Chen, S. Yang, H.G. Yang, Ni–Co–O hole transport materials: gap state assisted hole extraction with superior electrical conductivity, J. Mater. Chem. A 7 (2019) 20905–20910.

[59] B.M. Reddy, B. Chowdhury, P.G. Smirniotis, An XPS study of the dispersion of MoO_3 on TiO_2–ZrO_2, TiO_2–SiO_2, TiO_2–Al_2O_3, SiO_2–ZrO_2, and SiO_2–TiO_2–ZrO_2 mixed oxides, Appl. Catal., A 211 (2001) 19–30.

[60] W.L. Dai, M.H. Qiao, J.F. Deng, XPS studies on a novel amorphous Ni–Co–W–B alloy powder, Appl. Surf. Sci. 120 (1997) 119–124.

[61] J. Li, S. Wang, T. Xiao, X. Tan, P. Xiang, L. Jiang, C. Deng, W. Li, M. Li, Controllable preparation of nanoporous Ni_3S_2 films by sulfuration of nickel foam as promising asymmetric supercapacitor electrodes, Appl. Surf. Sci. 420 (2017) 919–926.

[62] J. Yang, C. Yu, X. Fan, S. Liang, S. Li, H. Huang, Z. Ling, C. Hao, J. Qiu, Electroactive edge site-enriched nickel–cobalt sulfide into graphene frameworks for high-performance asymmetric supercapacitors, Energy Environ. Sci. 9 (2016) 1299–1307.

[63] H. Luo, C. Dong, K. Xiao, X. Li, Passive film properties and electrochemical behavior of Co-Cr-Mo stainless steel in chloride solution, J. Mater. Eng. Perform. 26 (2017) 2237–2243.

[64] T.J. Mesquita, E. Chauveau, M. Mantel, R.P. Nogueira, A XPS study of the Mo effect on passivation behaviors for highly controlled stainless steels in neutral and alkaline conditions, Appl. Surf. Sci. 270 (2013) 90–97.

[65] P.M. Natishan, J. Jones-Meehan, G.I. Loeb, B.J. Little, R. Ray, M. Beard, Corrosion behavior of some transition metals and 4340 steel metals exposed to sulfate-reducing bacteria, Corrosion 55 (1999) 1062–1068.

7 Probing the corrosion resistance of a smart electroless Ni-P composite coating embedded with pH-responsive corrosion inhibitor-loaded nanocapsules

ABSTRACT: A smart electroless Ni-P composite coating incorporated with pH-responsive benzotriazole (BTA)-loaded nanocapsules was successfully fabricated and applied on N80 carbon steel, and the improved corrosion resistance was evaluated by electrochemical measurements and surface characterization techniques. The coating incorporated with the functionalized nanocapsules exhibits excellent anti-corrosion performance in the CO_2-saturated brine. This is originated from the filling of the nanocapsules into intrinsic micropores of the coating, which impairs the electrolyte penetration at the beginning stage of immersion, and the release of BTA when triggered by the local acidification of the micropores due to penetration of aggressive medium as immersion further proceeds. Furthermore, the incorporated nanocapsules endow the smart coating with a good anti-corrosion stability, showing a maximum inhibition efficiency of over 80%. The well-protected coating surface shows much less corrosion pits and the absence of lateral coating disbondment at the coating/substrate interface according to the surface characterization results.

7.1 Introduction

The record-breaking level of energy consumption has driven the rapid development of oil and gas industries. However, the corrosion of metal structures in oil-related environments due to the presence of acidic gases (e.g., CO_2 and H_2S) leads to severe material degradation and serious safety concerns [1–3]. Recently, an electroless Ni-P metallic coating has received rising attentions due to its excellent corrosion resistance and good mechanical properties [4–7]. Specifically, the high-phosphorus Ni-P coating (P content > 9 wt.%) with an amorphous microstructure displays an outstanding corrosion resistance in acidic media [8,9], thereby outperforming other candidates in oil-related applications.

Nevertheless, the anti-corrosion performance of the coating fades after long-term service because of the gradual penetration of corrosive electrolyte through the micropores formed due to the hydrogen evolution reaction during the coating deposition process. Such imperfection can be mitigated to some extent by the addition of nanoparticles, such as WC, ZrO_2, TiO_2, etc. [5,8,10–13], which fill in the micropores and consequently block the electrolyte penetration. Alternatively, corrosion can be retarded by the application of corrosion inhibitors. From this perspective, nano-scale containers loaded with corrosion inhibitors are considered as an encouraging supplementary material that can be incorporated into Ni-P coating to achieve an outstanding anti-corrosion performance for longer lifespans.

The method of nanoencapsulation refers to a series of techniques that allows the entrapment of active species (core materials) inside the nanocapsules (shell materials). In recent years, it has attracted widespread interests in many fields, such as food industry, agriculture industry and pharmaceuticals [14–16], due to its advantage of isolating core materials from the surroundings and the controllable release upon meeting certain triggering criteria. Growing attention has also been paid to the utilization of nanocapsules in anti-corrosion coatings [17–25]. The encapsulation of corrosion inhibitors avoids the constant leaching and the direct exposure to the coating matrix, which enables effective utilization of the inhibitors and eliminates the possible coating degradation caused by the continuous interaction between coating and corrosion inhibitors. Furthermore, it also enables the autonomous self-healing by releasing corrosion inhibitors when triggered by external stimuli, e.g., pH value [18–20], temperature [21,22], mechanical damage [23], ion concentration [24,25], etc.

As compared to various reported nanocapsule systems, mesoporous silica nanoparticles (MSN) has drawn extensive attentions due to their advantages of (1) adjustable particle size and large area-to-volume ratio assuring high loading content of inhibitors and the controllable release, (2) good chemical compatibility with multiple coatings and corrosion inhibitors and (3) high mechanical stability [26–28]. As for the core materials in MSN systems, benzotriazole (BTA) is a well-known green and compatible corrosion inhibitor applied in carbon steels, stainless steels, copper and nickel [24,29–32], and the anti-corrosion performance can be achieved by the chemisorption of BTA on metal surfaces to form complex films characterized as $[Fe^{II}(BTA^{-})_2]_n$, $[Cu^{I}BTA^{-}]_n$ and [Ni-BTA], respectively [32]. Borisova et al. [29] synthesized nanocontainers loaded with BTA embedded in hybrid SiOx/ZrOx sol-gel coating for the corrosion protection of aluminum alloy, which demonstrated good pH-dependent release of BTA and improved the corrosion resistance in chloride-containing solutions. Zheng et al. [24] reported a pH/sulfide ion-responsive system based on MSNs loaded with BTA and antibacterial agent to achieve anti-corrosion and anti-fouling performance for copper, and the release system opened when pH value was lower than 5 or $[S^{2-}]$ was higher than 0.02 mM. However, the vast majority of research is focused on the incorporation of nanocapsules with thick organic coatings by physical mixing, while limited findings have been reported for metallic coatings, especially thin electroless Ni-P coating. Therefore, it is desirable to evaluate the feasibility of embedding nanocapsules in Ni-P coating and assess its anti-corrosion performance in oil-related corrosive environments.

Herein, we developed a smart electroless Ni-P coating embedded with pH-responsive BTA-loaded nanocapsules based on MSNs for the first time. A simplified nanocapsule fabrication method was employed in this work to simultaneously prepare MSNs and load inhibitors, with tetraethoxysilane (TEOS) as the silica source and cetyltrimethylammonium bromide (CTAB) as the template, to avoid the use of poisonous organic solvents [33]. Subsequently, the corrosion behavior and anti-corrosion stability of the smart composite coating were evaluated in a sweat brine via various electrochemical measurements and surface characterization techniques. This study is anticipated to point to a promising direction towards developing smart electroless Ni-P coatings with nanoscale functional additives.

7.2 Experimental

7.2.1 Materials and preparation

N80 tubing steel samples with the size of 1 cm × 1 cm × 1 cm were adopted as the substrate for electroless Ni-P coating, and the chemical composition of the samples is (wt.%): C 0.29, Mn 1.38, Si 0.25, Cr 0.037, Cu 0.009, Ni 0.002, P 0.002, S 0.002 and balance Fe. The substrates were sequentially polished to 1200 grit with SiC sandpapers, cleaned with deionized water and alcohol, and then dried in flowing air. The chemical compositions of the electroless coating bath are as follows: 25 g/L of nickel sulfate hexahydrate ($NiSO_4 \cdot 6H_2O$), 30 g/L of sodium hypophosphite monohydrate ($NaH_2PO_2 \cdot H_2O$), 20 g/L of citric acid ($C_6H_8O_7$), 14 g/L of succinic acid ($C_4H_6O_4$), 20 mL/L of lactic acid ($C_3H_6O_3$), 0.06 g/L of sodium saccharin dihydrate ($C_7H_4NNaO_3S{\cdot}2H_2O$), 0.03 g/L of sodium dodecyl sulfate ($C_{12}H_{25}SO_4Na$) and 1 mg/L of lead nitrate [$Pb(NO_3)_2$]. The pH value of the coating bath was adjusted to 6 by adding sodium hydroxide (NaOH). The reagents used for nanocapsule fabrication are TEOS [$Si(OC_2H_5)_4$], CTAB [$(C_{16}H_{33})N(CH_3)_3Br$] and 1H-BTA ($C_6H_5N_3$).

7.2.2 Nanocapsule fabrication

The corrosion inhibitor-loaded nanocapsules were fabricated according to the one-step synthesis method reported by Xu et al. [33] First, 0.2 g of CTAB was added slowly into 200 mL of 0.5 g/L NaOH solution at 80 °C under vigorous magnetic stirring, followed by the addition of 0.3 g of BTA. Then, 2 mL of TEOS was added dropwise to the mixed solution. The reaction was maintained at 80 °C under vigorous stirring for 2 h. The mixture was centrifuged, washed twice with deionized water, and dried in furnace at 90 °C for 6 h. The product was then ground to fine powder for the subsequent coating procedure. As a comparison, as-fabricated nanocapsules without BTA were also prepared, and the fabrication procedure was kept the same as described above except that BTA was not loaded.

7.2.3 Deposition of nanocapsule-embedded Ni-P coating

Prior to coating deposition, the steel substrates were first cleaned with alcohol in an ultrasonic bath for 5 min, degreased with 3 wt.% sodium carbonate (Na_2CO_3) + 3 wt.% NaOH solution at 60 °C for 20 min, and pickled in 10 wt.% hydrochloric acid (HCl) for 50 s for surface activation. Then the substrates were dipped in the plating bath at (85±1) °C at a stirring rate of 200 rpm. Meanwhile, the prepared nanocapsule powder was ultrasonically mixed with a small amount of plating bath solution (approximately 30 mL) for 1 min to avoid the agglomeration, and then the mixed solution was transferred into the heated plating bath, in which the concentration of BTA-loaded nanocapsules was fixed at 0.1 g/L. The coating (denoted as “Ni-P-NC coating”) was obtained after 2 h of electroless plating. For comparison, pure as-deposited Ni-P coating was also prepared following the same procedure except that no nanocapsules were added (denoted as “Ni-P coating”). All the coated samples were cleaned with alcohol by ultrasonic dispersion for 5 min and dried in flowing air for corrosion tests.

7.2.4 Corrosion tests

The corrosion tests in this study include electrochemical measurements and immersion tests. The test solution for both tests is 3.5 wt.% sodium chloride (NaCl) solution saturated with CO_2, and the solution pH is 4.1. The samples were sealed with epoxy, leaving an area of 1 cm^2 for electrochemical tests. Figure 7.1 shows the schematic illustration of corrosion test setup. The electrochemical measurements were performed in a three-electrode system through a Gamry Interface 1000E Electrochemical Workstation, with a carbon rod as counter electrode (CE), the epoxy-sealed sample as working electrode (WE), and a saturated calomel electrode (SCE) as reference electrode (RE). Prior to tests, nitrogen gas was purged in the test solution for 2 h to deoxygenate, and then CO_2 was introduced to reach the saturation. The saturation status was maintained by continuously supplementing CO_2 in the solution during the tests. The open circuit potential (OCP) was first recorded for 1 h to achieve the equilibrium state. Then the electrochemical impedance spectroscopy (EIS) was measured with an alternating current (AC) amplitude of 10 mV applied in the frequency range from 100 kHz to 10 mHz at OCP. The EIS data were fitted with a proper equivalent electrical circuit (EEC) by using ZSimpWin software. The potentiodynamic polarization measurements were performed from -0.3 V to 1.2 V with respect to OCP at a scanning rate of 0.167 mV/s. The immersion tests were conducted in a 1 L vessel and followed the same deoxygenating and purging procedure. The total immersion time was 14 d. The tested samples were taken out after immersion, gently cleaned with deionized water and alcohol, and dried in air for morphological observations.

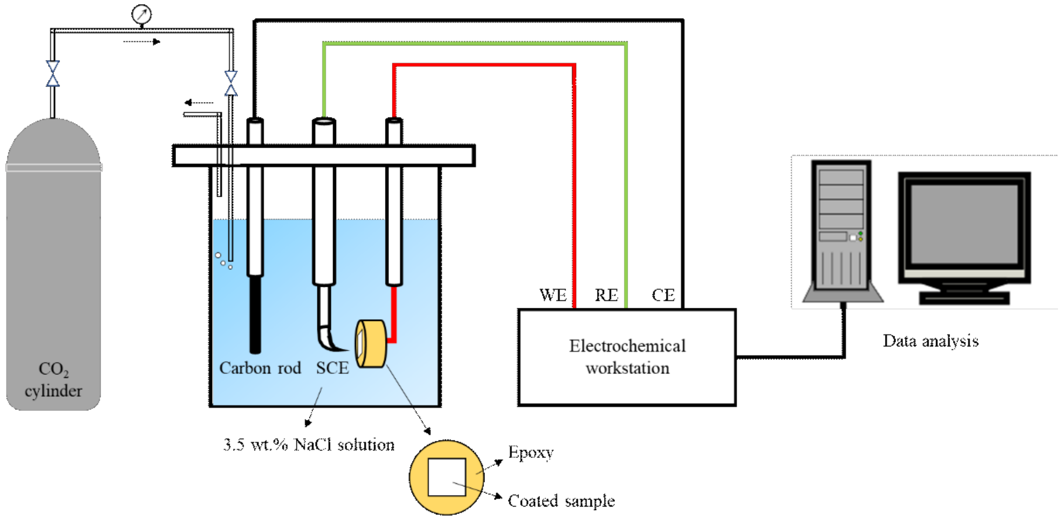

Figure 7.1 Schematic illustration of corrosion setup.

7.2.5 Surface observations and characterizations

The morphologies and chemical compositions of nanocapsules were observed by scanning electron microscopy (SEM, Zeiss Sigma 300 VP), transmission electron microscopy (TEM, JEOL JEM-ARM200CF) equipped with energy-dispersive X-ray spectroscopy (EDS), and the surface and cross-sectional morphologies of the coating were examined by SEM (Tescan Vega-3). X-ray photoelectron spectroscopy (XPS, Kratos AXIS Ultra) was employed to identify the chemical valence. XPS analysis was performed with monochromatized Al Kα ($h\upsilon$ = 1486.71 eV) at 5×10^{-10} Torr, and the C 1s peak at the binding energy of 284.6 eV was used to calibrate the shifted XPS data. XPSPEAK 41 software was then used for XPS data fitting with a Shirley background subtraction and a Gaussian-Lorentzian combination function.

In order to verify the release of BTA from the loaded nanocapsules, the ^{1}H nuclear magnetic resonance (NMR) spectra was obtained by using an Agilent Inova 400 MHz spectrometer. The total volume of each NMR sample was 700 μL. Pure BTA was first dissolved in deuterium oxide (D_2O) solvent as a control group. For the tested samples, the test solution (3.5 wt.% NaCl saturated with CO_2) was diluted 10 times because of the limited allowance of salt concentration of the NMR spectrometer, and CO_2 saturation was still maintained to match the pH value of the test solution. The tested sample consisted of 500 μL of diluted test solution and 200 μL (D_2O) solvent.

7.3 Results and discussion

7.3.1 Characterizations of nanocapsules and nanocapsule-embedded Ni-P coating

The surface morphologies and chemical compositions of BTA-loaded and as-fabricated nanocapsules are presented in Figure 7.2. As seen in Figure 7.2a, BTA-loaded nanocapsules display a near-spherical shape with agglomerated distributions, while a more regular and spherical morphology is observed from as-fabricated nanocapsules (Figure 7.2c). The sizes of both nanocapsules are around 100 nm, and BTA-loaded nanocapsules are slightly larger than as-fabricated ones. The TEM/EDS analysis provides more information about the structural and elemental evolution of nanocapsules due to the loading of BTA. Highly-ordered hexagonal mesopores are formed in the as-fabricated nanocapsules (Figure 7.2d), whereas a less-ordered worm-like structure is exhibited due to the loading of corrosion inhibitor in MSNs as shown in Fig. 2b. Both types of nanocapsules consist of C, Si, O, N and Br elements, and the relatively stronger signal of N element reveals the successful loading of BTA (Figure 7.2e). To summarize, BTA is proved to be loaded into as-fabricated MSNs, which leads to a significant change of nanocapsule morphology, structure and elemental distributions.

Figure 7.3 depicts the surface characterization results of Ni-P coatings with and without nanocapsule incorporation. The as-deposited Ni-P coating exhibits a nodular structure with some micropores on the coating surface due to the hydrogen evolution reaction during the electroless plating process. The morphology of the coating is not changed by introducing the nanocapsules, but the number density of micropores notably declines, as shown in Fig. 3b, signifying the filling effect of nanocapsules. Besides, the doublet peaks at 102.2 eV and 103.1 eV reveal the presence of Si from the XPS spectra (Figure 7.3d) [34], suggesting the successful embedding of nanocapsules in the coating. The cross-sectional images of Ni-P coating and Ni-P-NC coating (Figure 7.3c) indicate that the incorporation of nanocapsules does alter the uniform deposition and good adhesion between coating and substrate. The thicknesses of both coatings are maintained at approximately 20 μm.

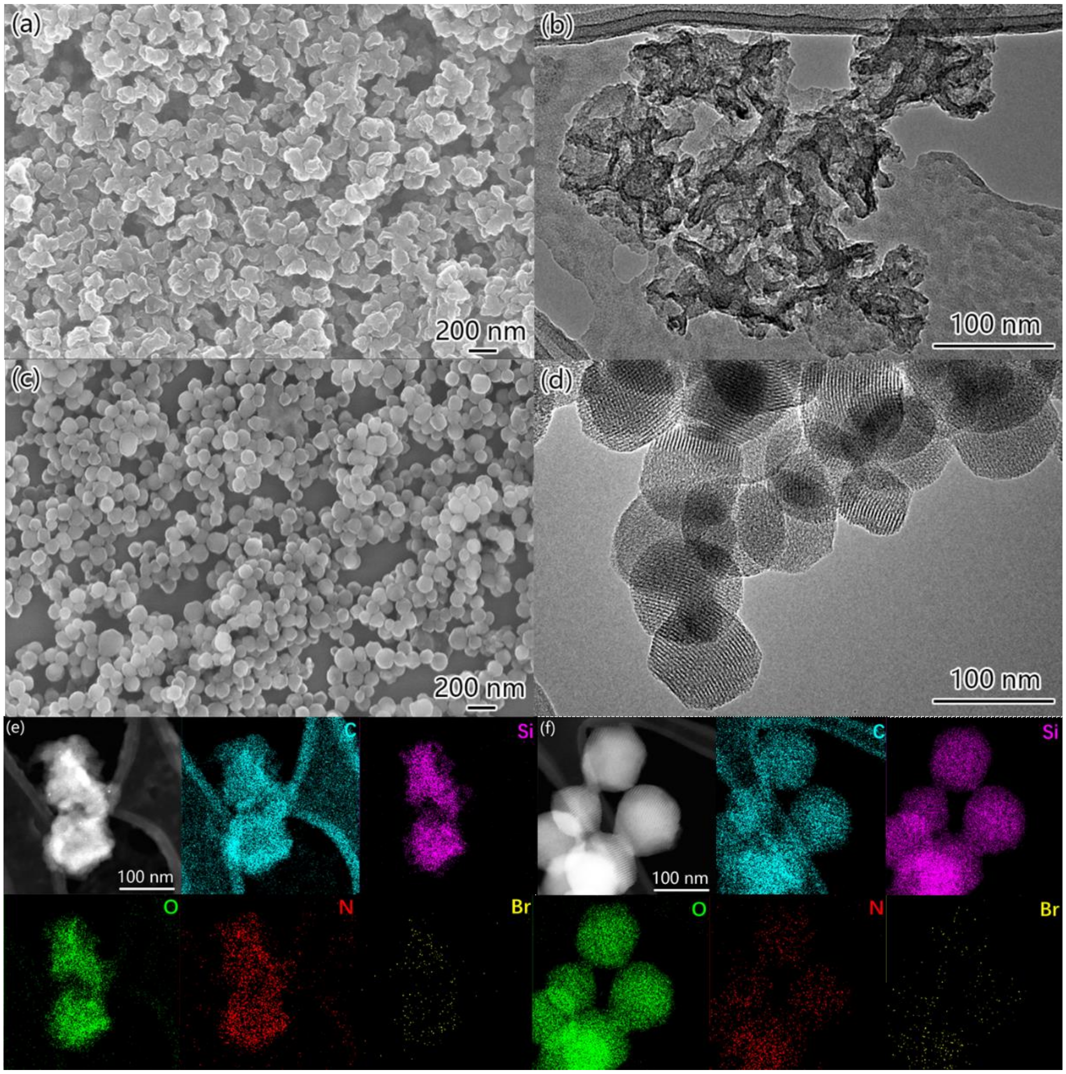

Figure 7.2 (a) SEM and (b) TEM image of inhibitor-loaded nanocapsules.

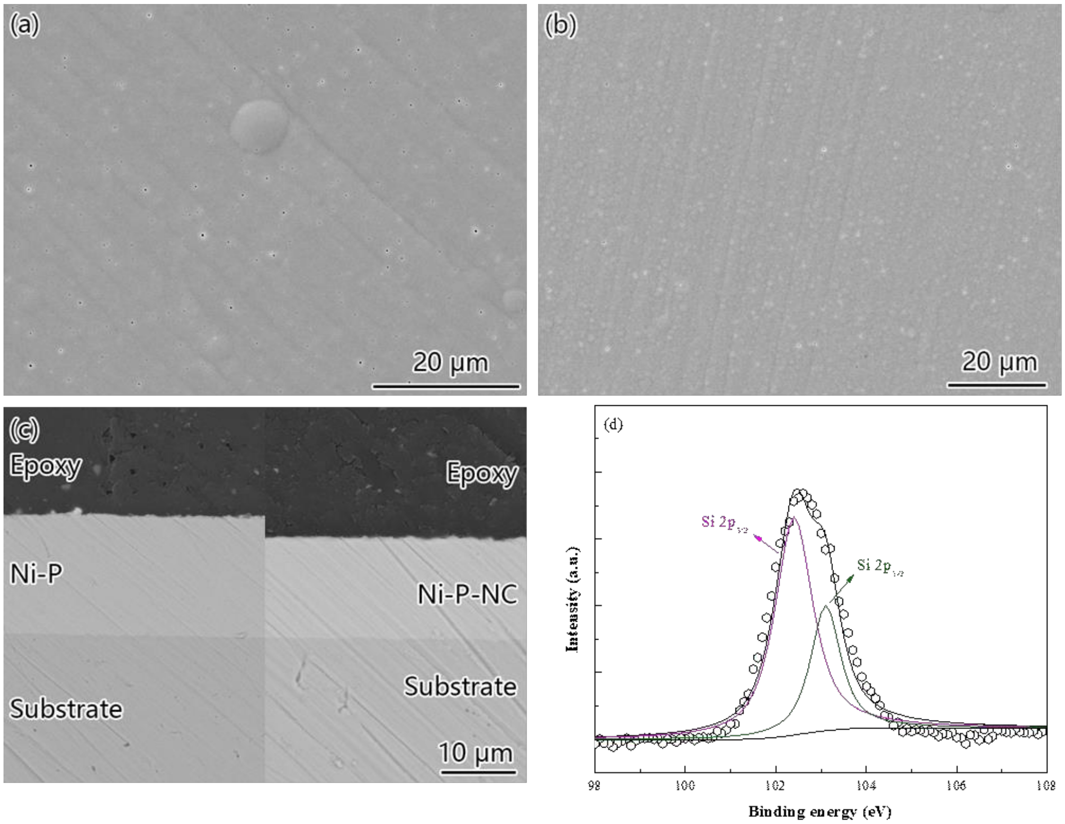

Figure 7.3 SEM surface morphologies of (a) Ni-P coating and (b) Ni-P-NC coating; (c) SEM cross-sectional image of Ni-P and Ni-P-NC coating; (d) Si 2p spectrum obtained from XPS analysis of Ni-P-NC coating.

7.3.2 Effect of embedded nanocapsules on the corrosion resistance of Ni-P composite coating

7.3.2.1 Effect of filling in the micropores of the coating

First, potentiodynamic polarization measurements were carried out to elucidate the anti-corrosion effect of BTA-loaded nanocapsules on Ni-P coating quantitatively. The polarization curves and the corresponding calculated parameters are shown in Figure 7.4. The corrosion potentials (E_{corr}) of fresh Ni-P coating and Ni-P-NC coating are -0.39 V and -0.25 V, respectively, denoting the lowered corrosion tendency in the presence of nanocapsules. As corrosion proceeds, E_{corr} of Ni-P coating shifts positively to -0.30 V after

24 h of immersion, while that of Ni-P-NC coating almost maintains the same (-0.23 V). The corrosion current density (i_{corr}) corresponds to the corrosion rate and thus better reflects the anti-corrosion performance. The i_{corr} of Ni-P coating declines from 0.74 $\mu A \cdot cm^{-2}$ to 0.40 $\mu A \cdot cm^{-2}$ after immersion for 24 h, suggesting the additional protection accredited to the formed corrosion film composed by NiO and $Ni(OH)_2$ serving as a physical barrier [4,35]. Intriguingly, fresh Ni-P-NC coating exhibits the i_{corr} of 0.46 $\mu A \cdot cm^{-2}$ which is lower as compared to fresh Ni-P coating, and it further drops to 0.11 $\mu A \cdot cm^{-2}$ after exposure for 24 h, highlighting the robust corrosion resistance brought by nanocapsule incorporation. It is worthwhile noting that the decrement of i_{corr} for both coatings after the first 24 h of immersion is comparable (0.34 $\mu A \cdot cm^{-2}$ for Ni-P coating vs. 0.35 $\mu A \cdot cm^{-2}$ for Ni-P-NC coating).

The degradation of a metallic coating is primarily governed by the penetration of corrosive electrolyte through the coating and the subsequent consumption of coating material by the electrochemical reaction with the aggressive medium. In electroless Ni-P coatings, the penetration preferentially takes place at the defect sites (mostly intrinsic micropores). As stated above, our previous findings [4,35] revealed that a compact $NiO/Ni(OH)_2$ corrosion film was formed on Ni-P coating surface in acidic solutions, which acted as a barrier layer and mitigated corrosion by hindering the electrolyte penetration. However, this protective film only offered temporary corrosion resistance, which reached its maximum after 24 h and then gradually declined. For Ni-P-NC coating in this study, the limited penetration of corrosion medium, due to the presence of the $NiO/Ni(OH)_2$ film, cannot trigger a great number of nanocapsules to release BTA in the first 24 h of immersion. Therefore, the decrease of corrosion rate is mainly accredited to the co-contribution of the protective corrosion film and the reduced porosity because of the nanocapsules filling in the micropores. This can be verified from the i_{corr} variations of both coatings after 1 d of immersion. For fresh coatings, the corrosion rate is directly related to the coating porosity because the electrolyte penetration and corrosion film formation have not started yet, therefore the lower i_{corr} of Ni-P-NC coating indicates the less porosity due to the micropore filling. As immersion prolongs to 24 h, the additional protection from the corrosion film gradually takes effect and results in the i_{corr} drop for both coatings.

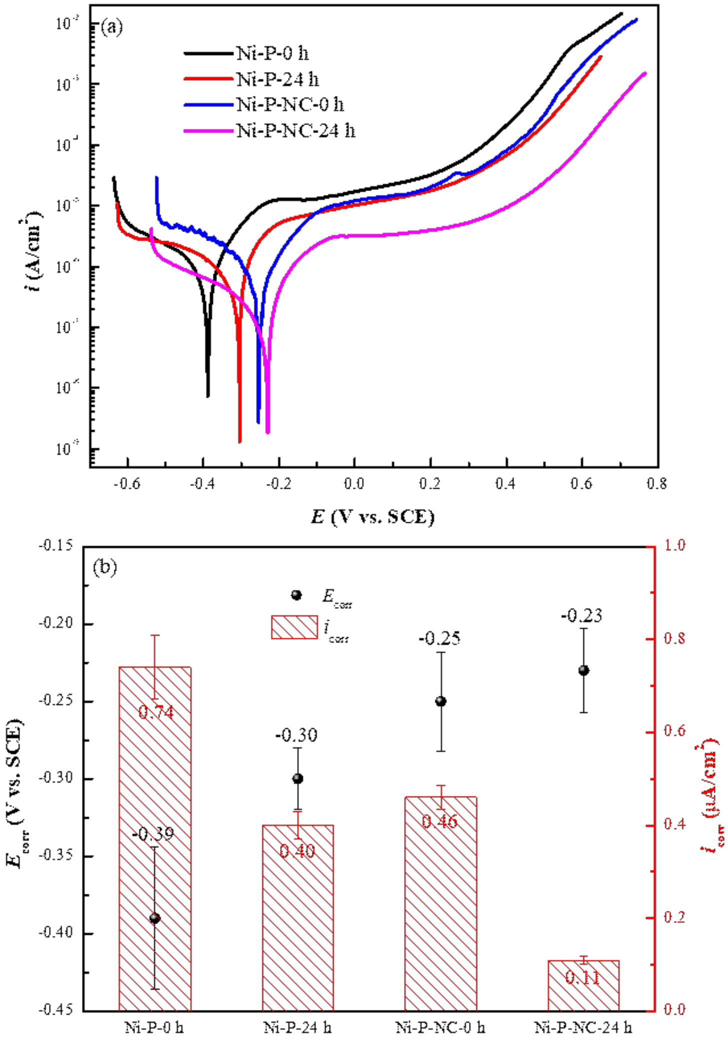

Figure 7.4 (a) Potentiodynamic polarization curves and (b) calculated E_{corr} and i_{corr} values of Ni-P coating and Ni-P-NC coating after exposed to CO_2-saturated 3.5 wt.% NaCl solution for different times.

7.3.2.2 Effect of the release of corrosion inhibitor from nanocapsules

Based on the abovementioned electrochemical results, the effect of micropore filling by nanocapsules on the improvement of corrosion resistance of Ni-P composite coating in the beginning stage of corrosion has been confirmed. Next, time-dependent EIS analysis was carried out to demonstrate the effect of BTA release as electrolyte penetration further proceeds. Figures 7.5 and 7.6 present the EIS plots of Ni-P coating and Ni-P-NC coating, respectively, after immersion for different time periods. Only one time constant (TC) is observed for Ni-P coating, however, Ni-P-NC coating exhibits two TCs as confirmed from the overlapped capacitance loops in the Nyquist plots. This suggests the change of corrosion mechanism with the embedding of BTA-loaded nanocapsules. The shape of semicircles does not vary with time for both coatings, indicating that the corrosion mechanism remains unchanged during the immersion period.

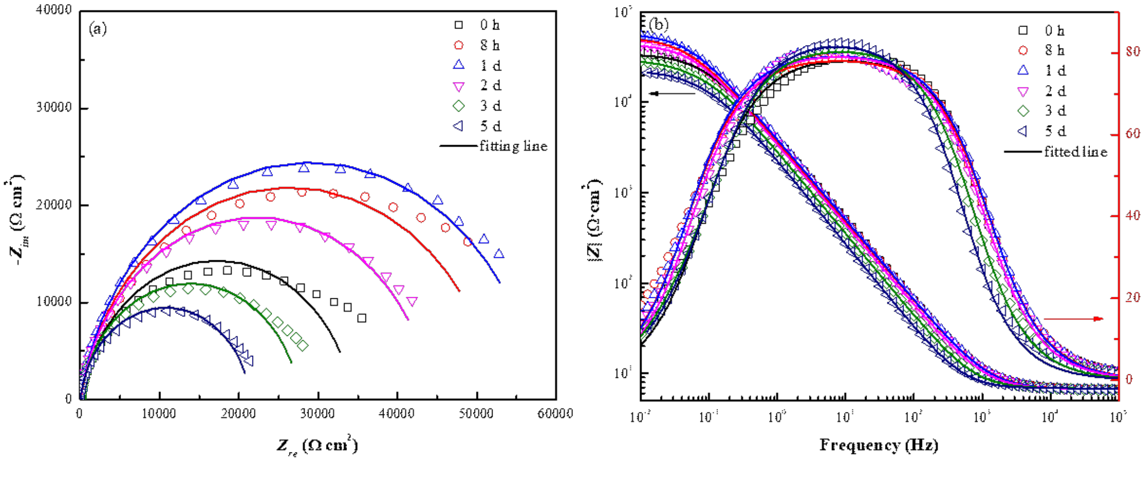

Figure 7.5 (a) Nyquist and (b) Bode plots of Ni-P coating exposed to CO_2-saturated 3.5 wt.% NaCl solution for different times.

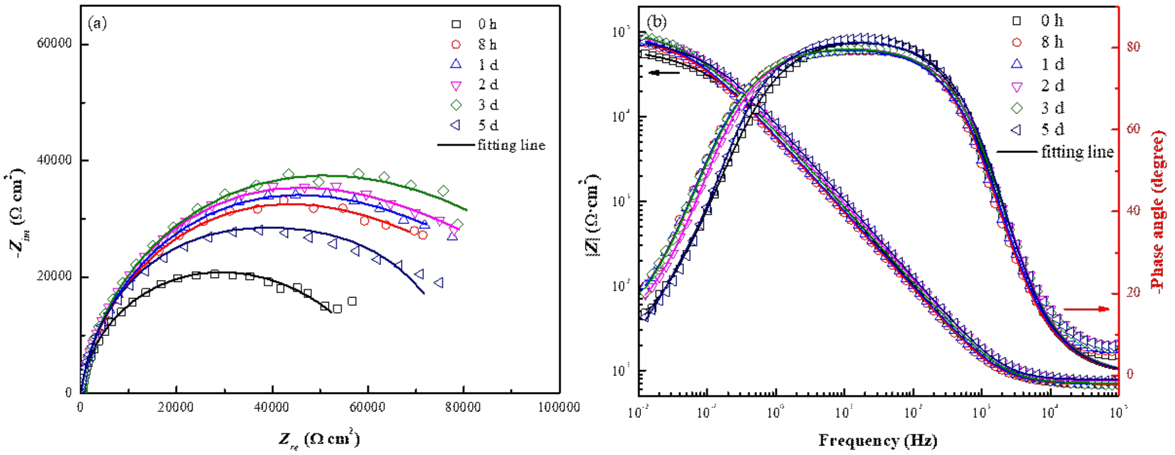

Figure 7.6 (a) Nyquist and (b) Bode plots of Ni-P-NC coating exposed to CO_2-saturated 3.5 wt.% NaCl solution for different times.

To further analyze the corrosion processes of both coatings, the EIS data were fitted using appropriate EECs as shown in Figure 7.7. For Ni-P coating (Figure 7.7a), it is composed by solution resistance R_s connected in series with one time constant ($Q_{dl}R_{ct}$), where Q_{dl} and R_{ct} are the capacitance of the electric double layer and the charge transfer resistance, respectively, which are adopted to describe the electrochemical process at the micropores. The EEC of Ni-P-NC coating (Figure 7.7b) can be expressed by $R_s(Q_f(R_f(Q_{dl}R_{ct})))$, where Q_f and R_f are the capacitance and resistance of the chemisorbed protective [Ni-BTA] film by BTA on nickel [32], respectively. In addition, the constant phase element (CPE, designated as Q_f and Q_{dl}), which accounts for the deviation from the ideal dielectric behavior and is related to interfacial heterogeneity and surface roughness [36,37], is adopted to replace the pure capacitance for a better fitting, and its admittance is given by the following equation [38]:

$$Y(Q) = Y_0(Q)(j\omega)^n \qquad \text{(Eq. 7.1)}$$

where $Y_0(Q)$ is the admittance constant of CPE; j is the imaginary number; ω is the angular frequency; and n is the empirical exponent. The fitted parameters for Ni-P coating and Ni-P-NC coating are listed in Tables 7.1 and 7.2, respectively. The χ^2 values of fitted data based on the EEC are no larger than 3×10^{-3}, implying an acceptable quality of fit.

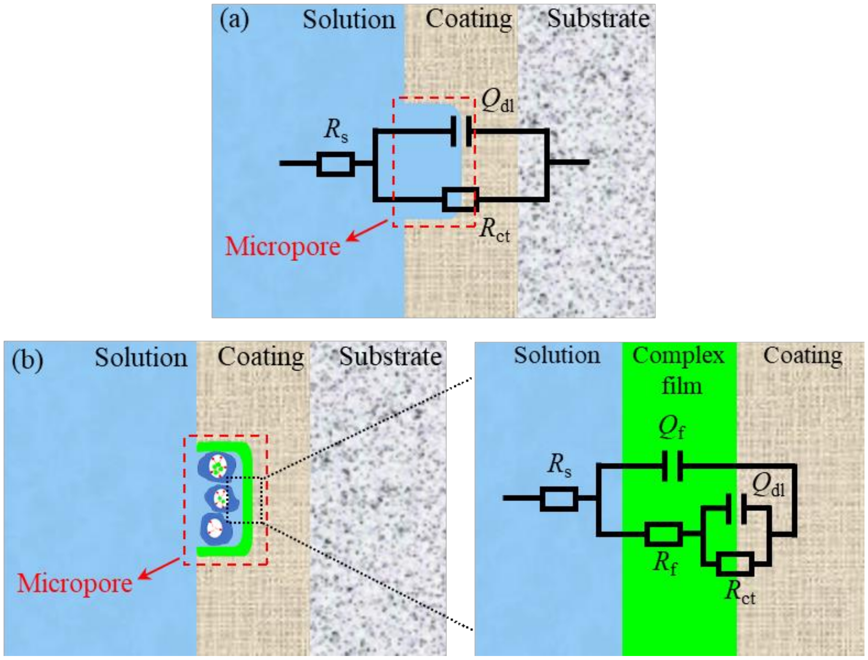

Figure 7.7 Equivalent electric circuit used for EIS data fitting: (a) Ni-P coating; (b) Ni-P-NC coating.

Table 7.1 Main electrochemical parameters fitted from EIS data of Ni-P coating in Figure 7.5.

Immersion time	R_s ($\Omega \cdot cm^2$)	n	$Y_0(Q_{dl})$ ($\Omega^{-1} \cdot cm^{-2} \cdot s^n$)	R_{ct} ($\Omega \cdot cm^2$)	Quality of fit
0 h	6.67	0.884	5.33×10^{-5}	3.44×10^4	2.53×10^{-3}
8 h	6.70	0.881	5.41×10^{-5}	5.28×10^4	1.52×10^{-3}
1 d	6.69	0.892	4.93×10^{-5}	5.79×10^4	9.47×10^{-4}
2 d	6.70	0.893	5.59×10^{-5}	4.45×10^4	1.13×10^{-3}
3 d	6.78	0.907	6.66×10^{-5}	2.77×10^4	1.32×10^{-3}
5 d	6.79	0.922	8.20×10^{-5}	2.15×10^4	1.42×10^{-3}

Table 7.2 Main electrochemical parameters fitted from EIS data of Ni-P-NC coating in Figure 7.6.

Immersion time	R_s ($\Omega\cdot cm^2$)	$Y_0(Q_f)$ ($\Omega^{-1}\cdot cm^{-2}\cdot s^n$)	R_f ($\Omega\cdot cm^2$)	$Y_0(Q_{dl})$ ($\Omega^{-1}\cdot cm^{-2}\cdot s^n$)	R_{ct} ($\Omega\cdot cm^2$)	Quality of fit
0 h	7.00	2.62×10^{-5}	3.35×10^4	7.21×10^{-5}	3.21×10^4	7.15×10^{-4}
8 h	6.86	2.84×10^{-5}	4.34×10^4	4.52×10^{-5}	6.01×10^4	8.17×10^{-4}
1 d	6.94	2.75×10^{-5}	5.38×10^4	4.54×10^{-5}	6.54×10^4	8.75×10^{-4}
2 d	7.09	2.70×10^{-5}	6.29×10^4	3.69×10^{-5}	7.01×10^4	1.61×10^{-3}
3 d	7.04	2.88×10^{-5}	6.93×10^4	3.79×10^{-5}	7.26×10^4	7.18×10^{-4}
5 d	7.76	3.02×10^{-5}	5.97×10^4	5.03×10^{-5}	4.02×10^4	2.02×10^{-3}

According to the fitted data of Ni-P coating, R_{ct} first increases and reaches the maximum at 24 h, denoting the enhanced resistance to mass transport at this stage due to the formed NiO/Ni(OH)$_2$ film. After 24 h, the ratio of less-protective Ni(OH)$_2$ gradually increases due to the water adsorption of NiO, thereby lowering the corrosion resistance [35,39]. As a result, the continuous electrolyte penetration and the lowered resistance of corrosion product notably facilitate the corrosion process, as exhibited in the rapid decrease of R_{ct} and the increase of $Y_0(Q_{dl})$.

As for Ni-P-NC coating, the increase of R_f with immersion time implies the promoted corrosion inhibition of the surface complex film due to the release of BTA. As compared to Ni-P coating, R_{ct} of Ni-P-NC coating does not decrease after 24 h, but keeps augmenting in the first 72 h of immersion, along with a declining tendency of $Y_0(Q_{dl})$, an indication that the corrosion resistance enhancement is not only derived from the micropore filling, but also from the release of BTA as immersion continues. Both R_f and R_{ct} experience a drop at 120 h, which means that all the loaded BTA in the nanocapsules have been released and used up. Obviously, the amount of BTA in Ni-P composite coating can be modified by the concentration of BTA-loaded nanoparticles in the coating bath and the loading content of BTA in the nanocapsules. In this study, the nanocapsule concentration is relatively low (0.1 g/L), therefore the R_{ct} reduction is predictable and acceptable. Also, it should be noted that R_{ct} of Ni-P-NC coating at 120 h is still much larger than that of Ni-P coating at 24 h, indirectly demonstrating the beneficial effect of micropore filling on mitigating corrosion.

Furthermore, additional electrochemical parameters derived from the fitted data are introduced to evaluate the coating properties. Typically, the polarization resistance R_{p} ($R_{\mathrm{p}} = R_{\mathrm{ct}}$ for Ni-P coating and $R_{\mathrm{p}} = R_{\mathrm{f}} + R_{\mathrm{ct}}$ for Ni-P-NC coating) can represent the resistance to corrosion attack and is inversely related to the corrosion rate [40]. Besides, the inhibition efficiency (η) of the nanocapsule-embedded coating can be calculated by the following equation [41]:

$$\eta = {(R_{p,0}{}^{-1} - R_{p,NC}{}^{-1})}\Big/{R_{p,0}{}^{-1}} \times 100\% \qquad \text{(Eq. 7.2)}$$

where $R_{p,NC}$ and $R_{p,0}$ are the polarization resistance of Ni-P coating in the presence and absence of nanocapsules, respectively. The time dependence of R_{p} and η for both coatings after immersion is depicted in Figure 7.8. As seen, R_{p} of fresh Ni-P-NC coating (6.56×10^4 $\Omega\cdot\mathrm{cm}^2$) is not only much higher than that of fresh Ni-P coating (3.44×10^4 $\Omega\cdot\mathrm{cm}^2$), but also outcompetes the maximum R_{p} of Ni-P coating at 24 h (5.28×10^4 $\Omega\cdot\mathrm{cm}^2$), highlighting the effective blocking effect of nanocapsules filled in the micropores prior to the domination of BTA release. As immersion continues, the release of corrosion inhibitor gives rise to the surge of R_{p} for Ni-P-NC coating and higher η values accordingly. The maximum η of 80.5% is achieved at 72 h, followed by 78.5% at 120 h, demonstrating that the BTA encapsulated Ni-P coating offers an outstanding protection to prevent the coating degradation.

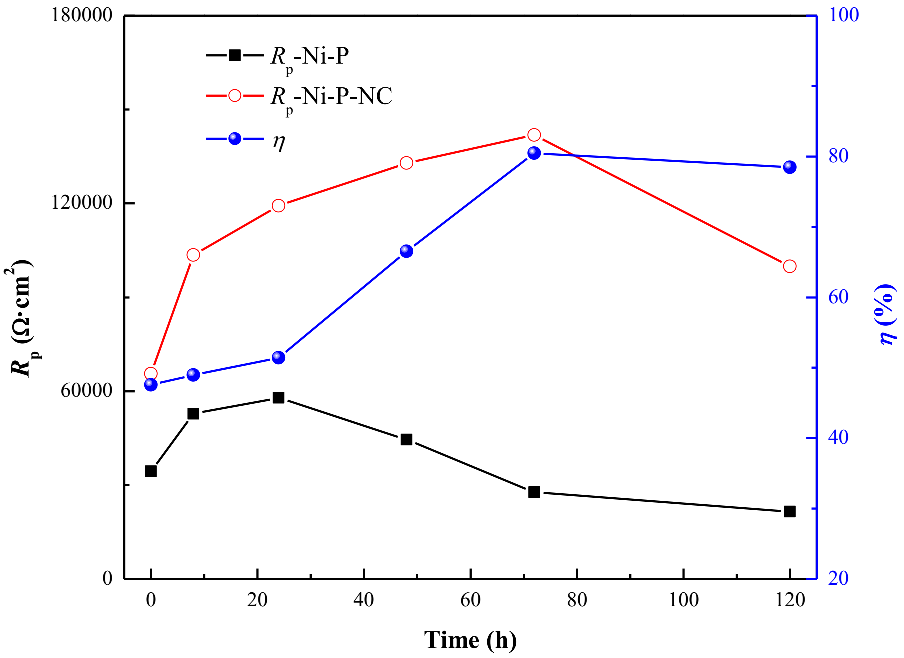

Figure 7.8 R_p and η as a function of immersion time for Ni-P coating and Ni-P-NC coating in CO_2-saturated 3.5 wt.% NaCl solution.

As immersion time prolongs, the formed NiO/Ni(OH)$_2$ film gradually loses its protection, thereby allowing aggressive medium to further penetrate inwards. Such penetration tends to cause the local acidification inside the micropores because of the accumulation of Cl^- ions and the hydrolysis of Ni salts which are formed as a result of anodic dissolution of Ni [42], and thus increases the corrosivity of electrolyte and facilitates corrosion. Besides the effective hindering of the electrolyte penetration by the micropore filling, the decrease of local pH trigger the CTAB desorption due to the weakened electrostatic interaction between CTA^+ and silica matrix, caused by the protonation of silanol groups in acidic environments [43–45]. This consequently leads to the consequent release of BTA, which greatly slows down the electrochemical process and implements the function of pH-responsive corrosion protection. The simplified schematic of BTA release from the nanocapsules is illustrated in Figure 7.9. Even after the corrosion inhibitor is released, the MSN frameworks are still present in the micropores and impede the penetration of corrosion medium. This can be substantiated by the much larger R_p value of Ni-P-NC coating in comparison with that of Ni-P coating after 120 h of immersion

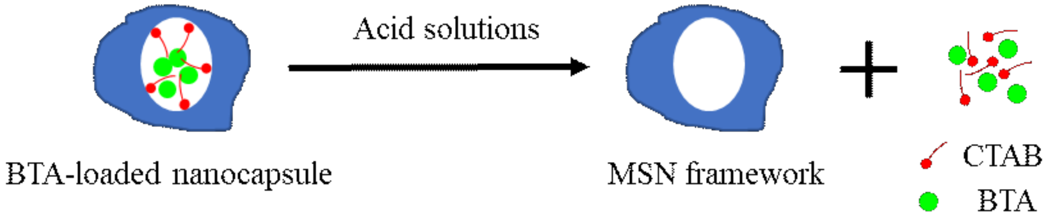

Figure 7.9 Schematic illustration of BTA release from the nanocapsules.

To further confirm the release of BTA from the nanocapsules, ^{1}H NMR analysis was employed and the spectra are shown in Figure 7.10. The chemical shift at 4.7 ppm appears in each sample and corresponds to H_2O/D_2O solvent. Two quartets are identified at the chemical shifts of 7.5 ppm and 7.9 ppm, which are ascribed to BTA [46] in the control group in Figure 7.10a. Only H_2O/D_2O peak is observed for the diluted test solution without nanocapsules (Figure 7.10b), while the one with BTA-loaded nanocapsules displays two quartets with the same chemical shifts (Figure 7.10c), verifying the release of BTA from the loaded nanocapsules in the acidic solutions.

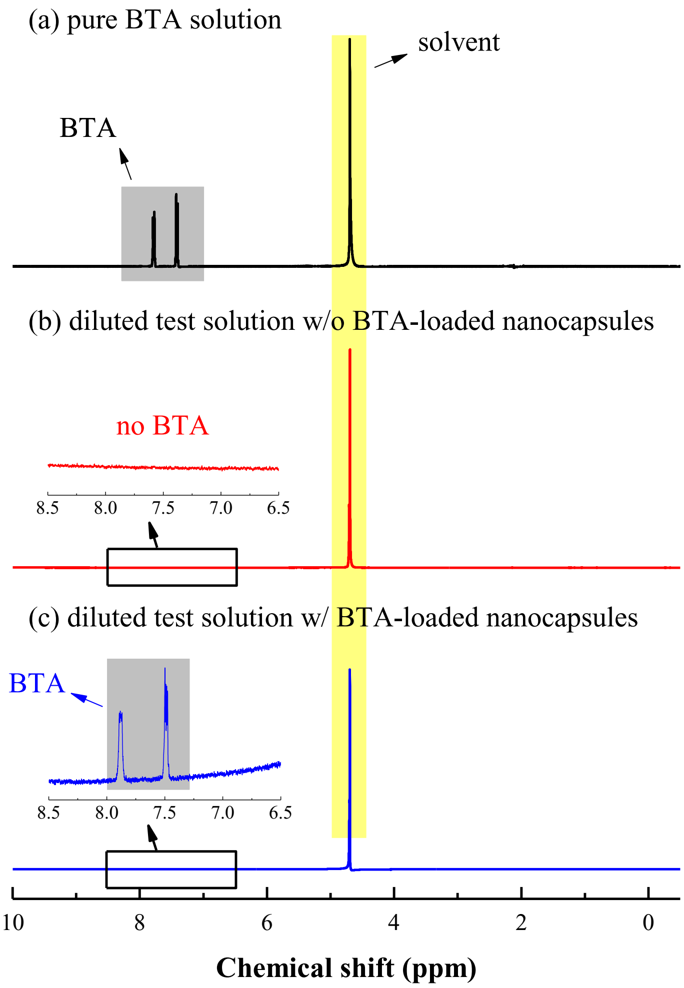

Figure 7.10 ^{1}H NMR spectra of (a) pure BTA solution; (b) diluted test solution without BTA-loaded nanocapsules and (c) diluted test solution with BTA-loaded nanocapsules.

7.3.3 Anti-corrosion stability of nanocapsule-embedded Ni-P coating

After exploring the co-effect of micropore filling and inhibitor release on the corrosion resistance enhancement of the smart Ni-P composite coating, it is desirable to investigate its anti-corrosion stability in acidic environments saturated with CO_2. Figure 7.11 shows the SEM morphologies of Ni-P coating and Ni-P-NC coating after 14 d of immersion in the CO_2/Cl^--containing environment. Apparent corrosion product is observed on the surface of Ni-P coating with the presence of a large number of corrosion pits generated at the sites of micropores, indicating a severe coating degradation facilitated by the gradual penetration of corrosive medium during the immersion. Moreover, the cross-sectional inspection of Ni-P coating (Figure 7.11c) shows the corrosion pathways formed throughout the coating, leading to the lateral coating disbondment at the coating/substrate interface. However, Ni-P-NC coating undergoes quite slight corrosion without noticeable corrosion product after immersion for 14 d, and the number density of corrosion pits is much lower than that of Ni-P coating, signifying the considerably hindered corrosion process. Besides, obvious corrosion pathways are not detected in the coating, nor is the coating disbondment found at the coating/substrate interface. This is because a large portion of micropores has been filled by the embedded nanocapsules, which impedes the penetration of corrosive medium, and the released BTA triggered by the acidic environment offers the additional corrosion resistance, thereby remarkably mitigating the coating degradation and the corrosion of underneath substrate even for an extended experimental period.

In summary, the anti-corrosion mechanism of the functionalized nanocapsules is illustrated by a schematic model in Figure 7.12. In the beginning stage of immersion (up to 24 h) (Figure 7.12a), the electrolyte penetration is notably limited because of the protective Ni-based corrosion product film, so the nanocapsules cannot be triggered to release BTA, and therefore serve as normal nanoparticles that can only reduce the coating porosity. As immersion continues, the temporary Ni-based film gradually loses the protection, allowing more penetration of aggressive medium, which causes the local pH decrease inside the micropores and triggers BTA release. In acidic environments, the release of BTA does not affect the outer MSN shell structure, so even after the inhibitor is completely released and consumed, the MSN frameworks are still left in the micropore and retard the further penetration and corrosion efficiently.

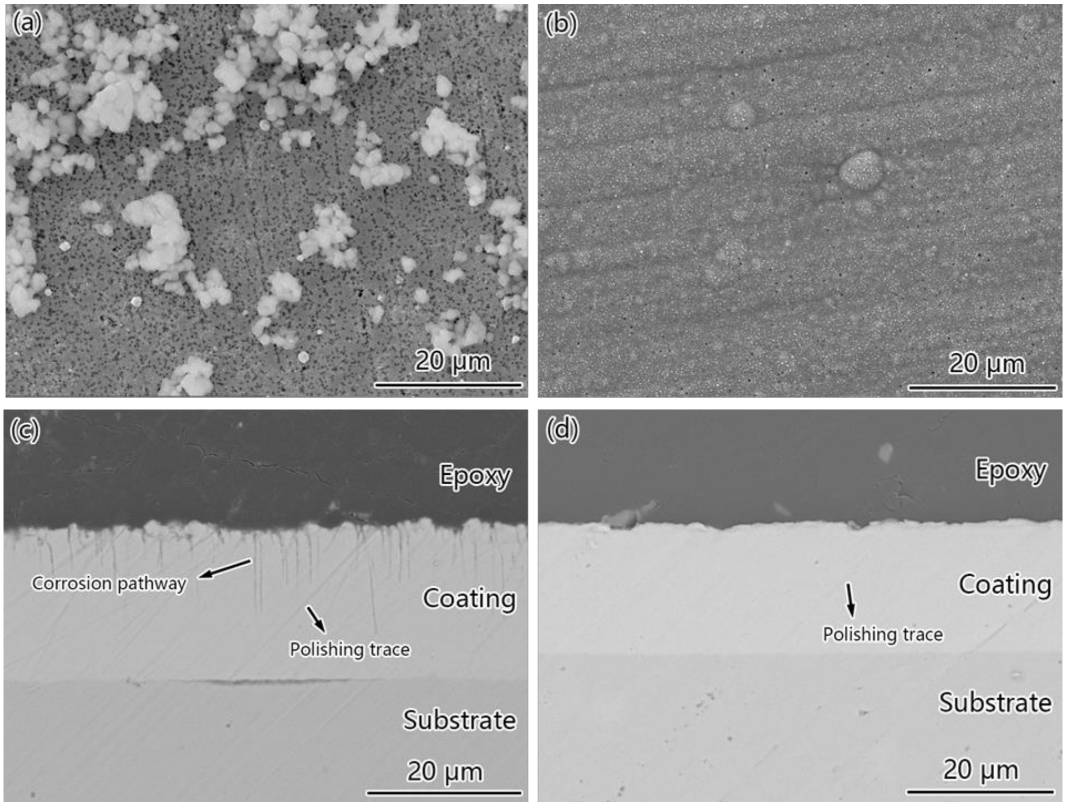

Figure 7.11 SEM (a,b) surface and (c,d) cross-sectional morphologies of Ni-P coating and Ni-P-NC coating, respectively.

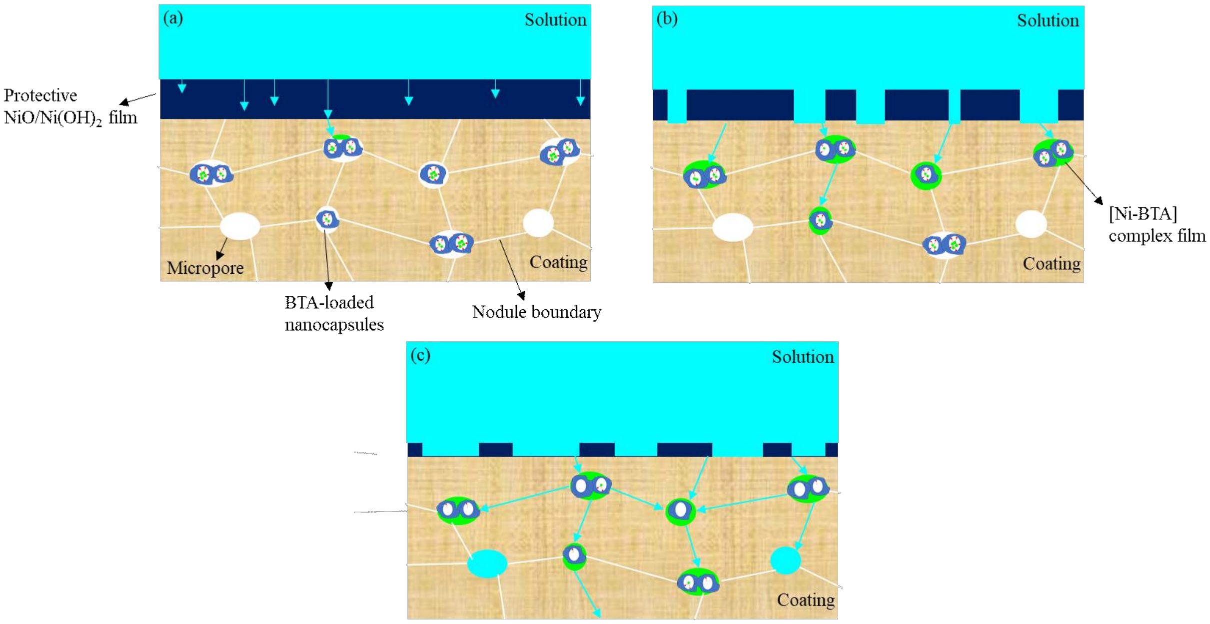

Figure 7.12 Schematic diagram of anti-corrosion mechanism of Ni-P-NC coating.

7.4 Conclusions

In summary, we described the application of a smart electroless Ni-P composite coating embedded with pH-responsive BTA-loaded nanocapsules based on MSNs for the first time, and it exhibits enhanced corrosion protection for N80 carbon steel in aqueous CO_2/Cl^- environment. BTA was successfully encapsulated by a simplified method free of organic solvents, yielding an average particle size of about 100 nm. The loading of BTA notably alters the morphology, structure and elemental distributions of nanocapsules. The functionalized nanocapsules were subsequently incorporated into Ni-P coating, showing good compatibility and less porosity without changing the coating microstructure or the adhesion between coating and substrate.

The incorporation of BTA-loaded nanocapsules mitigates the degradation of Ni-P coating in two aspects: filling in the micropores of the coating and releasing BTA as penetration occurs. In the early stage of corrosion, micropore filling dominates the corrosion protection, together with the formed $NiO/Ni(OH)_2$ protective film, because of the limited electrolyte penetration. As immersion continues, intensified penetration of corrosion medium results in the local acidification in the micropores and hence, triggers the release of BTA from nanocapsules, which greatly impairs the corrosion process. More importantly, Ni-P-NC coating exhibits satisfactory anti-corrosion stability, reflected by a maximum η of over 80%. In addition, the successful pH-responsive BTA release is evidenced by NMR analysis. Surface characterization results demonstrate that much less corrosion pits and corrosion products are observed on the Ni-P-NC coating surface, and lateral coating disbondment at the coating/substrate interface is not detected after 14 d of immersion. In contrast, Ni-P coating exhibits severe localized corrosion and apparent corrosion pathways that result in the coating disbondment, signifying the rapid electrolyte penetration and corrosion process in the absence of nanocapsules. This approach opens new opportunities in the exploration of smart electroless Ni-P coatings with improved corrosion resistance in oil-related acidic environments.

7.5 References

[1] Choi, Y.S., Nesic, S. and Ling, S., 2011. Effect of H_2S on the CO_2 corrosion of carbon steel in acidic solutions. Electrochimica Acta, 56(4), pp.1752–1760.

[2] J. Li, C. Sun, S. Shuang, M. Roostaei, V. Fattahpour, M. Mahmoudi, H. Zeng, J.L. Luo, 2019. Investigation on the flow-induced corrosion and degradation behavior of underground J55 pipe in a water production well in the Athabasca oil sands reservoir. J. Petrol. Sci. Eng. 182, 106325.

[3] Q.Y. Wang, X.Z. Wang, H. Luo, J.L. Luo, A study on corrosion behaviors of Ni–Cr–Mo laser coating, 316 stainless steel and X70 steel in simulated solutions with H_2S and CO_2, Surf. Coat. Technol. 291 (2016) 250–257.

[4] C. Sun, H. Zeng, J.L. Luo, Unraveling the effects of CO_2 and H_2S on the corrosion behavior of electroless Ni-P coating in $CO_2/H_2S/Cl^-$ environments at high temperature and high pressure, Corros. Sci. 148 (2019) 317–330.

[5] H. Luo, M. Leitch, Y. Behnamian, Y. Ma, H. Zeng, J.L. Luo, Development of electroless Ni–P/nano-WC composite coatings and investigation on its properties, Surf. Coat. Technol. 277 (2015) 99–106.

[6] L.L. Wang, H.J. Chen, L. Hao, A. Lin, F.X. Gan, Electrochemical corrosion behavior of electroless Ni–P coating in NaCl and H_2SO_4 solutions, Mater. Corros. 62 (2011) 1003–1007.

[7] J.N. Balaraju, V.E. Selvi, V.W. Grips, K.S. Rajam, Electrochemical studies on electroless ternary and quaternary Ni–P based alloys, Electrochim. Acta 52 (2006) 1064–1074.

[8] Y. Wang, X. Shu, S. Wei, C. Liu, W. Gao, R.A. Shakoor, R. Kahraman, Duplex Ni–P–ZrO_2/Ni–P electroless coating on stainless steel. J. Alloys Compd. 630 (2015) 189–194.

[9] C. Gu, J. Lian, G. Li, L. Niu, Z. Jiang, High corrosion-resistant Ni–P/Ni/Ni–P multilayer coatings on steel, Surf. Coat. Technol. 197 (2005) 61–67.

[10] H. Ashassi-Sorkhabi, M. Es'haghi, Corrosion resistance enhancement of electroless Ni–P coating by incorporation of ultrasonically dispersed diamond nanoparticles, Corros. Sci. 77 (2013) 185–193.

[11] M. Gholizadeh-Gheshlaghi, D. Seifzadeh, P. Shoghi, A. Habibi-Yangjeh, Electroless Ni-P/nano-WO_3 coating and its mechanical and corrosion protection properties, J. Alloys Compd. 769 (2018) 149–160.

[12] S. Ranganatha, T.V. Venkatesha, K. Vathsala, Development of electroless Ni–Zn–P/nano-TiO_2 composite coatings and their properties, Appl. Surf. Sci. 256 (2010) 7377–7383.

[13] S. Afroukhteh, C. Dehghanian, M. Emamy, Preparation of the Ni–P composite coating co-deposited by nano TiC particles and evaluation of it's corrosion property, Appl. Surf. Sci. 258 (2012) 2597–2601.

[14] F. Paulo, L. Santos, Design of experiments for microencapsulation applications: A review, Mater. Sci. Eng. C 77 (2017) 1327–1340.

[15] S. Chen, M. Yang, C. Ba, S. Yu, Y. Jiang, H. Zou, Y. Zhang, Preparation and characterization of slow–release fertilizer encapsulated by biochar-based waterborne copolymers, Sci. Total Environ. 615 (2018) 431–437.

[16] C. Arpagaus, A. Collenberg, D. Rütti, E. Assadpour, S.M. Jafari, Nano spray drying for encapsulation of pharmaceuticals, Int. J. Pharm. 546 (2018) 94–214.

[17] F. Maia, K.A. Yasakau, J. Carneiro, S. Kallip, J. Tedim, T. Henriques, A. Cabral, J. Venâncio, M.L. Zheludkevich, M.G.S. Ferreira, Corrosion protection of AA2024 by sol–gel coatings modified with MBT-loaded polyurea microcapsules, Chem. Eng. J. 283 (2016) 1108–1117.

[18] Z. Zheng, M. Schenderlein, X. Huang, N.J. Brownbill, F. Blanc, D. Shchukin, Influence of functionalization of nanocontainers on self-healing anticorrosive coatings, ACS Appl. Mater. Interfaces 7 (2015) 22756–22766.

[19] J. Fu, T. Chen, M. Wang, N. Yang, S. Li, Y. Wang, X. Liu, Acid and alkaline dual stimuli-responsive mechanized hollow mesoporous silica nanoparticles as smart nanocontainers for intelligent anticorrosion coatings, ACS Nano 7 (2013) 11397–11408.

[20] C. Ding, Y. Liu, M. Wang, T. Wang, J. Fu, Self-healing, superhydrophobic coating based on mechanized silica nanoparticles for reliable protection of magnesium alloys, J. Mater. Chem. A 4 (2016) 8041–8052.

[21] G.L. Li, Z. Zheng, H. Möhwald, D.G. Shchukin, Silica/polymer double-walled hybrid nanotubes: synthesis and application as stimuli-responsive nanocontainers in self-healing coatings, ACS Nano 7 (2013) 2470–2478.

[22] Y. Su, O.F. Ojo, I.K.M. Tsengam, J. He, G.L. McPherson, V.T. John, J.A. Valla, Thermoresponsive coatings on hollow particles with mesoporous shells serve as stimuli-responsive gates to species encapsulation and release, Langmuir 34 (2018) 14608–14616.

[23] A. Latnikova, D.O. Grigoriev, J. Hartmann, H. Möhwald, D.G. Shchukin, Polyfunctional active coatings with damage-triggered water-repelling effect, Soft Matter 7 (2011) 369–372.

[24] Z. Zheng, X. Huang, M. Schenderlein, D. Borisova, R. Cao, H. Möhwald, D. Shchukin, Self-Healing and antifouling multifunctional coatings based on pH and sulfide ion sensitive nanocontainers, Adv. Funct. Mater. 23 (2013) 3307–3314.

[25] F. Maia, J. Tedim, A.D. Lisenkov, A.N. Salak, M.L. Zheludkevich, M.G. Ferreira, Silica nanocontainers for active corrosion protection, Nanoscale 4 (2012) 1287–1298.

[26] J. Lee, J. Kim, T. Hyeon, Recent progress in the synthesis of porous carbon materials, Adv. Mater. 18 (2006) 2073–2094.

[27] A. Stein, Advances in microporous and mesoporous solids—highlights of recent progress, Adv. Mater. 15 (2003) 763–775.

[28] M.J. Hollamby, D. Fix, I. Dönch, D. Borisova, H. Möhwald, D. Shchukin, Hybrid polyester coating incorporating functionalized mesoporous carriers for the holistic protection of steel surfaces, Adv. Mater. 23 (2011) 1361–1365.

[29] M. Finšgar, J. Jackson, Application of corrosion inhibitors for steels in acidic media for the oil and gas industry: a review, Corros. Sci. 86 (2014) 17–41.

[30] M. Finšgar, I. Milošev, Inhibition of copper corrosion by 1, 2, 3-benzotriazole: a review, Corros. Sci. 52 (2010) 2737–2749.

[31] M.M. Mennucci, E.P. Banczek, P.R.P. Rodrigues, I. Costa, Evaluation of benzotriazole as corrosion inhibitor for carbon steel in simulated pore solution, Cem. Concr. Compos. 31 (2009) 418–424.

[32] P.G. Cao, J.L. Yao, J.W. Zheng, R.A. Gu, Z.Q. Tian, Comparative study of inhibition effects of benzotriazole for metals in neutral solutions as observed with surface-enhanced Raman spectroscopy, Langmuir 18 (2002) 100–104.

[33] J.B. Xu, Y.Q. Cao, L. Fang, J.M. Hu, A one-step preparation of inhibitor-loaded silica nanocontainers for self-healing coatings, Corros. Sci. 140 (2018) 349–362.

[34] D. Tan, Z. Ma, B. Xu, Y. Dai, G. Ma, M. He, Z. Jin, J. Qiu, Surface passivated silicon nanocrystals with stable luminescence synthesized by femtosecond laser ablation in solution, Phys. Chem. Chem. Phys. 13 (2011) 20255–20261.

[35] C. Sun, J. Li, S. Shuang, H. Zeng, J.L. Luo, Effect of defect on corrosion behavior of electroless Ni-P coating in CO_2-saturated NaCl solution, Corros. Sci. 134 (2018) 23–37.

[36] P. Córdoba-Torres, T.J. Mesquita, R.P. Nogueira, Relationship between the origin of constant-phase element behavior in electrochemical impedance spectroscopy and electrode surface structure, J. Phys. Chem. C 119 (2015) 4136–4147.

[37] J.-B. Jorcin, M.E. Orazem, N. Pébère, B. Tribollet, CPE analysis by local electrochemical impedance spectroscopy, Electrochim. Acta 51 (2006) 1473–1479.

[38] C.N. Cao, J.Q. Zhang, An introduction to electrochemical impedance spectroscopy, Science, Beijing, 2002.

[39] Li, J., Sun, C., Roostaei, M., Mahmoudi, M., Fattahpour, V., Zeng, H. and Luo, J.L., 2020. Insights into the Electrochemical Corrosion Behavior and Mechanism of Electroless Ni-P Coating in the $CO_2/H_2S/Cl^-$ Environment. Corrosion, 76(6), pp.578–590.

[40] G.A. Zhang, Y. Zeng, X.P. Guo, F. Jiang, D.Y. Shi, Z.Y. Chen, Electrochemical corrosion behavior of carbon steel under dynamic high pressure H_2S/CO_2 environment, Corros. Sci. 65 (2012) 37–47.

[41] J.O.M. Bockris, and A.K. Reddy, Modern electrochemistry: an introduction to an interdisciplinary area, Springer Science & Business Media, 2012.

[42] N. Sato, The stability of localized corrosion, Corros. Sci. 37 (1995) 1947–1967.

[43] L. Jia, Z. Li, J. Shen, D. Zheng, X. Tian, H. Guo, P. Chang, Multifunctional mesoporous silica nanoparticles mediated co-delivery of paclitaxel and tetrandrine for overcoming multidrug resistance, Int. J. Pharm. 489 (2015) 318–330.

[44] O.V. Dement'eva, I.N. Senchikhin, E.M. Sedykh, I.N. Gromyak, V.A. Ogarev, V.M. Rudoy, Mesostructured SiO_2-based nanocontainers synthesized on a functional template: Capacity and rate of unloading, Colloid J. 78 (2016) 52–64.

[45] N.H.N. Kamarudin, A.A. Jalil, S. Triwahyono, V. Artika, N.F.M. Salleh, A.H. Karim, N.F. Jaafar, M.R. Sazegar, R.R. Mukti, B.H. Hameed, A. Johari, Variation of the crystal growth of mesoporous silica nanoparticles and the evaluation to ibuprofen loading and release, J. Colloid Interface Sci. 421 (2014) 6–13.

[46] N. Jagerovic, M.L. Jimeno, I. Alkorta, J. Elguero, R.M. Claramunt, An experimental (NMR) and theoretical (GIAO) study of the tautomerism of benzotriazole in solution, Tetrahedron 58 (2002) 9089–9094.

8 Summary and future prospects

8.1 Summary

The work presented in this dissertation investigated the corrosion behavior and mechanism of electroless Ni-P coating in SAGD-related environments and developed the coating optimization methods for its broader applications and better performance. The corrosion rate of electroless Ni-P coating in CO_2/H_2S environment is higher than that in CO_2 environment because H_2S enhances CO_2 corrosion by affecting both anodic and cathodic processes. The adsorbed $H_2PO_2^-$ layer only exists in the very early stage of corrosion and hardly contributes to the corrosion resistance of Ni-P coating. The corrosion resistance of Ni-P coating first increases and then decreases under both conditions and reaches the maximum values at around 24 h, and the temporary corrosion resistance improvement is ascribed to the formation of corrosion products (NiO and Ni_3S_2) formed on the coating surface. The presence of H_2S facilitates the electrolyte uptake of the coating, and dramatically reduces the stability of Ni-P coating, resulting in faster coating consumption, faster propagation of corrosion pathways and electrolyte penetration, and more severe localized corrosion and coating disbondment at the coating/steel interface. A corrosion model was proposed to interpret the corrosion and degradation process of the coating. The electrolyte penetration leaves corrosion pathways in the coating and initiates the localized corrosion. As corrosion proceeds, the formed NiO and Ni_3S_2 provide extra corrosion resistance which declines with the transformation to other species. The corrosion process is then governed by the rapid dissolution of the substrate as the corrosive medium penetrates to the coating/substrate interface, and the lateral coating disbondment occurs afterwards.

The corrosion of N80 steel is remarkably promoted with the addition of Ca^{2+} ions, however Ni-P coating exhibits outstanding corrosion resistance. The presence of Ca^{2+} leads to the change of corrosion film microstructure of N80 steel and subsequently affects the corrosion behavior. The incorporation of Ca atoms into $FeCO_3$ lattice results in the smaller crystal sizes with more defects, which consequently enhances the electrolyte diffusion and promotes the corrosion process. The critical Ca^{2+} concentration above which the microstructural transformation takes place is between 2,000 ppm and 2,500 ppm. The addition of Ca^{2+} at concentrations higher than the critical value strengthens the corrosion film by improving its compactness. However, the localized corrosion of the steel is accelerated at higher Ca^{2+} concentration due to non-uniformity of corrosion film where the region of loose corrosion film allows the electrolyte penetration. Meanwhile, the introduction of Ca^{2+} also impacts the water chemistry of the aqueous phase, resulting in the accumulation of H^+ and consequently postpones the precipitation of $FeCO_3$. The protection effectiveness of Ni-P coating is barely impacted by Ca^{2+} concentration. The corrosion film, mainly composed by NiO and $Ni(OH)_2$, offers superior corrosion resistance by isolating the electrolyte from coating underneath, which is evidenced by satisfactory impedance results and the absence of corrosion pathways and coating disbondment. Furthermore, the less tendency of scale formation on the coating surface also mitigates the localized corrosion due to the heterogeneous distribution of corrosion film for carbon steels.

Mo addition adversely affects the corrosion resistance of as-deposited Ni-P coating, while heat treatment profoundly advances the anti-corrosion performance of Ni-Mo-P/Ni-P composite coating. The Mo incorporation into the as-deposited Ni-P coating results in the change of microstructure from amorphous to crystalline due to the declined P content. Heat treatment of Ni-Mo-P/Ni-P coating at 400 °C for 2 h facilitates the formation of Ni_4Mo phase and trace amount of Ni_3P phase. Furthermore, heat treatment gives rise to the formation of oxide film on the coating surface, with the primary chemical composition of NiO, Mo(V) and Mo(VI) oxides. Heat-heated Ni-Mo-P/Ni-P coating displays the best corrosion resistance, followed by heat-treated Ni-P coating, as-deposited Ni-P coating and as-deposited Ni-Mo-P/Ni-P coating. A superb corrosion inhibition efficiency (η=96.1%) is achieved for the heat-treated Ni-Mo-P/Ni-P coating, and the roll-off slopes approach -0.5, suggesting better passivation properties of the Mo-containing oxide film. The absence of oxide film, together with the formed crystalline microstructure with more active sites for corrosion initiation, contributes to the decreased corrosion resistance of as-deposited Ni-Mo-P/Ni-P coating. Meanwhile, the exceptional corrosion resistance of heat-treated Ni-Mo-P/Ni-P coating is predominantly originated from the compact corrosion product layer composed by nickel oxides and sulfides and the formation of the H_2S-immuned MoO_3.

Finally, I developed a smart electroless Ni-P composite coating for the enhanced corrosion protection of carbon steel in aqueous CO_2/Cl^- environment via the embedded pH-responsive BTA-loaded nanocapsules based on MSNs for the first time. BTA was successfully encapsulated by a simplified method free of organic solvents, yielding an average particle size of about 100 nm. The functionalized nanocapsules were subsequently incorporated into Ni-P coating, showing good compatibility without changing the coating microstructure or the adhesion between coating and substrate. Moreover, the incorporation of nanocapsules results in a more hydrophobic coating surface with the reduced formation of micropores. The extra corrosion resistance originated from the embedded nanocapsules is substantiated by the decrement of i_{corr} with immersion time, which occurs when corrosive electrolyte penetrates into micropores and causes the localized acidification that triggers the nanocapsules to release BTA. More importantly, Ni-P-NC coating exhibits satisfactory anti-corrosion stability, which is reflected by a maximum inhibition efficiency of nearly 80%. Surface characterization results demonstrate that much less corrosion pits and corrosion products are observed on the Ni-P-NC coating surface, and lateral coating disbondment at the coating/substrate interface is not detected after 14 d of immersion. In contrast, Ni-P coating exhibits severe localized corrosion and apparent corrosion pathways that result in the coating disbondment, signifying the rapid electrolyte penetration and corrosion process in the absence of nanocapsules.

8.2 Future prospects

The suggestions of future work are briefly listed as below, and hopefully they can serve as guidance and inspirations for researchers who are dedicated to corrosion studies of Ni-P coating:

(1) Further understandings of localized corrosion of Ni-P coating and the electrolyte penetration in the coating.

Although the corrosion mechanism of Ni-P coating was explained in this work, the localized corrosion of Ni-P coating at the micropore has not been clearly investigated. Techniques such as scanning electrochemical microscopy (SECM) can be used to study the localized corrosion behavior. In addition, the electrolyte penetration inside the coating is not well studied, and the effects of penetration rate need further investigation.

(2) Development of smart Ni-P coatings with controllable functionalities.

In this work, the anti-corrosion performance of the smart nanocapsule-embedded Ni-P coating under HTHP conditions containing sweat/sour gases is not studied due to the limited time and needs to be further explored. Besides corrosion inhibitors, other functionalized nanocapsules can also be incorporated into Ni-P coating to improve multiple properties, such as wear resistance, lubrication and self-healing.

Bibliography

[1] E.H. Herron, Heavy Oil: A solution to dwindling domestic oil supplies, Petroleum Equities Reports, 2000.

[2] R.M. Butler, G.S. McNab, H.Y. Lo, Theoretical studies on the gravity drainage of heavy oil during in-situ steam heating, Can. J. Chem. Eng. 59 (1981) 455–460.

[3] Oil sand development by the SAGD method,
https://www.japex.co.jp/english/business/ep_o/canada_oilsands.html

[4] R.A. Marriott, P. Pirzadeh, J.J. Marrugo-Hernandez, S. Raval, Hydrogen sulfide formation in oil and gas, Can. J. Chem. 94 (2016) 406–413.

[5] J.D.M. Belgrave, R.G. Moore, M.G. Ursenbach, Comprehensive kinetic models for the aquathermolysis of heavy oils, J. Can. Petrol. Technol. 36 (1997).

[6] H.F. Thimm, Dependence of some SAGD operations characteristics on steam zone pressure. In SPE/CIM Eighth One-Day Conference on Horizontal Well Technology, Society of Petroleum Engineers, 2001.

[7] J. Sun, C. Sun, G. Zhang, X. Li, W. Zhao, T. Jiang, H. Liu, X. Cheng, Y. Wang, Effect of O_2 and H_2S impurities on the corrosion behavior of X65 steel in water-saturated supercritical CO_2 system, Corros. Sci. 107 (2016) 31–40.

[8] S. Nesic, J. Postlethwaite, S. Olsen, An electrochemical model for prediction of corrosion of mild steel in aqueous carbon dioxide solutions, Corrosion 52 (1996) 280–294.

[9] Y. Zheng, J. Ning, B. Brown, S. Nešić, Electrochemical model of mild steel corrosion in a mixed H_2S/CO_2 aqueous environment in the absence of protective corrosion product layers, Corrosion 71 (2015) 316–325.

[10] S. Nesic, K.L.J. Lee, V. Ruzic, A mechanistic model of iron carbonate film growth and the effect on CO_2 corrosion of mild steel. In CORROSION 2002.

[11] B.F. Pots, S.D. Kapusta, R.C. John, M.J.J. Thomas, I.J. Rippon, T.S. Whitham, M. Girgis, Improvements on de Waard-Milliams corrosion prediction and applications to corrosion management. In CORROSION 2002.

[12] W.H. Goodman, M.R. Godfrey, T.M. Miller, N. Comany, Scale and deposit formation in steam assisted gravity drainage (SAGD) facilities. In International Water Conference 2010.

[13] M.R. Simons, Report of offshore technology conference (OTC) presentation. NACE International Oil and Gas Production, 2008.

[14] A. Brenner, Nickel plating on steel by chemical reduction, J. Res. NBS 37 (1946) 31–34.

[15] W. Riedel, Electroless nickel plating, ASM International, 1991.

[16] F.B. Mainier, M.M. Araujo, On the effect of the electroless nickel-phosphorus coating defects on the performance of this type of coating in oilfield environments, SPE Advanced Technology Series, 2(1994) 63–67.

[17] R.M. Lukes, The mechanism for the autocatalytic reduction of nickel by hypophosphite ion, Plating 51 (1964) 969.

[18] P. Cavallotti, G. Salvago, Studies on chemical reduction of nickel and cobalt by hypophosphite. Pt. 2. Characteristics of the process, Electrochim Metallorum 3 (1968) 239–266.

[19] F.B. Mainier, M.P.C. Fonseca, S.S. Tavares, J.M. Pardal, Quality of electroless Ni-P (nickel-phosphorus) coatings applied in oil production equipment with salinity, J. Mater. Sci. Chem. Eng. 1 (2013) 1–8.

[20] R. N. Duncan, The metallurgical structure of electroless nickel deposits: effect on coating properties, Plating Surf. Finish. 83 (1996) 65–69.

[21] A.A. Wronkowska, In situ and ex situ characterization of passive layers on $Ni_{1-x}P_x$ in alkaline solution, J. Electrochem. Soc. 140 (1993) 995.

[22] H. Ashassi-Sorkhabi, S.H. Rafizadeh, Effect of coating time and heat treatment on structures and corrosion characteristics of electroless Ni–P alloy deposits, Surf. Coat. Technol. 176 (2004) 318–326.

[23] S.Q. Guo, L.F. Hou, C.L. Guo, Y.H. Wei, Characteristics and corrosion behavior of nickel-phosphorus coatings deposited by a simplified bath, Mater. Corros. 68 (2017) 468–475.

[24] T.S. Narayanan, I. Baskaran, K. Krishnaveni, S. Parthiban, Deposition of electroless Ni–P graded coatings and evaluation of their corrosion resistance, Surf. Coat. Technol. 200 (2006) 3438–3445.

[25] J. Balaraju, T.S. Narayanan, S. Seshadri, Evaluation of the corrosion resistance of electroless Ni-P and Ni-P composite coatings by electrochemical impedance spectroscopy, J. Solid State Electrochem. 5 (2001) 334–338.

[26] C. Gu, J. Lian, G. Li, L. Niu, Z. Jiang, High corrosion-resistant Ni–P/Ni/Ni–P multilayer coatings on steel. Surf. Coat. Technol. 197 (2005) 61–67.

[27] H. Luo, X. Wang, S. Gao, C. Dong, X. Li, Synthesis of a duplex Ni-P-YSZ/Ni-P nano composite coating and investigation of its performance, Surf. Coat. Technol. 311 (2017) 70–79.

[28] N. El Mahallawy, A. Bakkar, M. Shoeib, H. Palkowski, V. Neubert, Electroless Ni–P coating of different magnesium alloys, Surf. Coat. Technol. 202 (2008) 5151–5157.

[29] Y.W. Song, D.Y. Shan, E.H. Han, Corrosion behaviors of electroless plating Ni–P coatings deposited on magnesium alloys in artificial sweat solution, Electrochim. Acta 53 (2007) 2009–2015.

[30] R.B. Diegle, N.R. Sorensen, C.R. Clayton, M.A. Helfand, Y.C. Yu, An XPS investigation into the passivity of an amorphous Ni-20P alloy, J. Electrochem. Soc. 135 (1988) 1085.

[31] B. Elsener, M. Crobu, M.A. Scorciapino, A. Rossi, Electroless deposited Ni–P alloys: corrosion resistance mechanism, J. of Appl. Electrochem. 38 (2008) 1053.

[23] M. Crobu, A. Scorciapino, B. Elsener, A. Rossi, The corrosion resistance of electroless deposited nano-crystalline Ni–P alloys, Electrochim. Acta 53 (2008) 3364–3370.

[33] H. Habazaki, S.Q. Ding, A. Kawashima, K. Asami, K. Hashimoto, A. Inoue, T. Masumoto, The anodic behavior of amorphous Ni-19P alloys in different amorphous states, Corros. Sci. 29 (1989) 1319–1328.

[34] R.L. Zeller III, Electrochemical corrosion testing of high phosphorus electroless nickel in 5% NaCl, Corrosion 47 (1991) 692–702.

[35] F.C. Walsh, C.P. de León, C. Kerr, S. Court, B.D. Barker, Electrochemical characterisation of the porosity and corrosion resistance of electrochemically deposited metal coatings, Surf. Coat. Technol. 202 (2008) 5092–5102.

[36] Y. Xu, Y. Zhou, T. Luan, Electrochemical characterization and evaluation of electroless coating porosity, J. Funct. Mater. 44 (2013) 902–910.

[37] A.R. Rahimi, H. Modarres, M. Abdouss, Study on morphology and corrosion resistance of electroless Ni–P coatings, Surf. Eng. 25 (2009) 367–371.

[38] H.G. Ying, M. Yan, T.Y. Ma, J.M. Wu, L.Q. Yu, Effects of NH_4F on the deposition rate and buffering capability of electroless Ni–P plating solution, Surf. Coat. Technol. 202 (2007) 217–221.

[39] Z. Xie, G. Yu, B. Hu, X. Lei, T. Li, J. Zhang, Effects of $(NH_4)_2SO_4$ on the characteristics of the deposits and properties of an electroless Ni–P plating solution, Appl. Surf. Sci. 257 (2011) 5025–5031.

[40] Y. Jin, H. Yu, D. Yang, D. Sun, Effects of complexing agents on acidic electroless nickel deposition, Rare Met. 29 (2010) 401–406.

[41] H. Ashassi-Sorkhabi, M. Es'haghi, Corrosion resistance enhancement of electroless Ni–P coating by incorporation of ultrasonically dispersed diamond nanoparticles, Corros. Sci. 77 (2013) 185–193.

[42] S.R. Allahkaram, M.H. Nazari, S. Mamaghani, A. Zarebidaki, Characterization and corrosion behavior of electroless Ni–P/nano-SiC coating inside the CO_2 containing media in the presence of acetic acid, Mater. Des. 32 (2011) 750–755.

[43] B. Zhou, L. Kong, L. Niu, J. Lian, G. Li, Effects of passivation on the properties of Ni-P alloy coating deposited on CFs reinforced PEEK. Surf. Coat. Technol. 232 (2013) 269–274.

[44] X. Xiu-qing, M. Jian, B. Zhen-quan, F. Yao-rong, M. Qiu-rong, Z. Wen-zhen, The corrosion behavior of electroless Ni–P coating in Cl^{-}/H_2S environment. Appl. Surf. Sci. 258 (2012) 8802–8806.

[45] C. Sun, J. Li, S. Shuang, H. Zeng, J.L. Luo, Effect of defect on corrosion behavior of electroless Ni-P coating in CO_2-saturated NaCl solution, Corros. Sci. 134 (2018) 23–37.

[46] C. Sun, H. Zeng, J.L. Luo, Unraveling the effects of CO_2 and H_2S on the corrosion behavior of electroless Ni-P coating in $CO_2/H_2S/Cl^{-}$ environments at high temperature and high pressure, Corros. Sci. 148 (2019) 317–330.

[47] L.L. Wang, H.L. Chen, L. Hao, A. Lin, F.X. Gan, Electrochemical corrosion behavior of electroless Ni-P coating in NaCl and H_2SO_4 solutions, Mater. Corros. 62 (2011) 1003–1007.

[48] J. Li, C. Sun, H. Zeng, J.L. Luo, Insights into the electrochemical corrosion behavior and mechanism of electroless Ni-P coating in the $CO_2/H_2S/Cl^{-}$ environment, Corrosion 76 (2020) 578–590.

[49] M. Yan, H.G. Ying, T.Y. Ma, Improved microhardness and wear resistance of the as-deposited electroless Ni–P coating, Surf. Coat. Technol. 202 (2008) 5909–5913.

[50] T. Rabizadeh, S.R. Allahkaram, A. Zarebidaki, An investigation on effects of heat treatment on corrosion properties of Ni–P electroless nano-coatings, Mater. Des. 31 (2010) 3174–3179.

[51] M. Sribalaji, P. Arunkumar, K.S. Babu, A.K. Keshri, Crystallization mechanism and corrosion property of electroless nickel phosphorus coating during intermediate temperature oxidation, Appl. Surf. Sci. 355 (2015) 112–120.

[52] M.A. Shoeib, M.M. Kamel, S.M. Rashwan, O.M. Hafez, Corrosion behavior of electroless Ni–P/TiO_2 nanocomposite coatings, Surf. Interface Anal. 47 (2015) 672–680.

[53] Y. Gao, L. Huang, Z.J. Zheng, H. Li, M. Zhu, The influence of cobalt on the corrosion resistance and electromagnetic shielding of electroless Ni–Co–P deposits on Al substrate, Appl. Surf. Sci. 253 (2007) 9470–9475.

[54] H. Liu, Z. Liu, Evaluation of microstructures and properties of laser-annealed electroless Ni–P/Ni–Mo–P duplex coatings, Surf. Coat. Technol. 330 (2017) 270–276.

[55] A.E. Fetohi, R.A. Hameed, K.M. El-Khatib, Ni–P and Ni–Mo–P modified aluminium alloy 6061 as bipolar plate material for proton exchange membrane fuel cells, J. Power Sources 240 (2013) 589–597.

[56] H. Liu, R.-X. Guo, Y. Zong, B.-Q. He, Z. Liu, Comparative study of microstructure and corrosion resistance of electroless Ni-W-P coatings treated by laser and furnace-annealing, Trans. Nonferrous Met. Soc. China 20 (2012) 1024–1031.

[57] J.N. Balaraju, K.S. Rajam, Electroless deposition of Ni–Cu–P, Ni–W–P and Ni–W–Cu–P alloys, Surf. Coat. Technol. 195 (2005) 154–161.

[58] Y. Liu, Q. Zhao, Study of electroless Ni–Cu–P coatings and their anti-corrosion properties, Appl. Surf. Sci. 228 (2004) 57–62.

[59] S. Ranganatha, T.V. Venkatesha, K. Vathsala, Development of electroless Ni–Zn–P/nano-TiO_2 composite coatings and their properties, Appl. Surf. Sci. 256 (2010) 7377–7383.

[60] W.X. Zhang, Z.H. Jiang, G.Y. Li, Q. Jiang, J.S. Lian, Electroless Ni–Sn–P coating on AZ91D magnesium alloy and its corrosion resistance, Surf. Coat. Technol. 202 (2008) 2570–2576.

[61] G. Lu, G. Zangari, Corrosion resistance of ternary Ni–P based alloys in sulfuric acid solutions, Electrochim. Acta 47 (2002) 2969–2979.

[62] G.S. Song, S. Sun, Z.C. Wang, C.Z. Luo, C.X. Pan, Synthesis and characterization of electroless Ni–P/Ni–Mo–P duplex coating with different thickness combinations, Acta Metall. Sin. (Engl. Lett.) 30 (2017) 1008–1016.

[63] G. Liu, L. Yang, L. Wang, S. Wang, L. Chongyang, J. Wang, Corrosion behavior of electroless deposited Ni–Cu–P coating in flue gas condensate, Surf. Coat. Technol. 204 (2010) 3382–3386.

[64] J.N. Balaraju, V.E. Selvi, V.K.W. Grips, K.S. Rajam, Electrochemical studies on electroless ternary and quaternary Ni–P based alloys, Electrochim. Acta 52 (2006) 1064–1074.

[65] M. Momenzadeh, S. Sanjabi, The effect of TiO_2 nanoparticle codeposition on microstructure and corrosion resistance of electroless Ni–P coating, Mater. Corros. 63 (2012) 614–619.

[66] H. Jin, S. Jiang, L. Zhang, Structural characterization and corrosive property of Ni-P/CeO_2 composite coating, J. Rare Earths 27 (2009) 109–113.

[67] H. Luo, M. Leitch, H. Zeng, J.-L. Luo, Characterization of microstructure and properties of electroless duplex Ni-W-P/Ni-P nano-ZrO_2 composite coating, Mater. Today Phys. 4 (2018) 36–42.

[68] H. Luo, M. Leitch, Y. Behnamian, Y. Ma, H. Zeng, J.L. Luo, Development of electroless Ni–P/nano-WC composite coatings and investigation on its properties, Surf. Coat. Technol. 277 (2015) 99–106.

[69] S. Zhang, K. Han, L. Cheng, The effect of SiC particles added in electroless Ni–P plating solution on the properties of composite coatings, Surf. Coat. Technol. 202 (2008) 2807–2812.

[70] S. Ranganatha, T.V. Venkatesha, K. Vathsala, Electroless Ni–W–P coating and its nano-WS_2 composite: preparation and properties, Ind. Eng. Chem. Res. 51 (2012) 7932–7940.

[71] A.A. Zuleta, O.A. Galvis, J.G. Castaño, F.Echeverría, F.J. Bolivar, M.P.Hierro, F.J. Pérez-Trujillo, Preparation and characterization of electroless Ni–P–Fe_3O_4 composite coatings and evaluation of its high temperature oxidation behaviour, Surf. Coat. Technol. 203 (2009) 3569–3578.

[72] J.N. Balaraju, Kalavati, K.S. Rajam, Influence of particle size on the microstructure, hardness and corrosion resistance of electroless Ni–P–Al_2O_3 composite coatings, Surf. Coat. Technol. 200 (2006) 3933–3941.

[73] S. Afroukhteh, C. Dehghanian, M. Emamy, Preparation of the Ni–P composite coating co-deposited by nano TiC particles and evaluation of it's corrosion property, Appl. Surf. Sci. 258 (2012) 2597–2601.

[74] M. Alishahi, S.M. Monirvaghefi, A. Saatchi, S.M. Hosseini, The effect of carbon nanotubes on the corrosion and tribological behavior of electroless Ni–P–CNT composite coating, Appl. Surf. Sci. 258 (2012) 2439–2446.

[75] I.R. Mafi, C. Dehghanian, Comparison of the coating properties and corrosion rates in electroless Ni–P/PTFE composites prepared by different types of surfactants, Appl. Surf. Sci. 257 (2011) 8653–8658.

[76] T.R. Tamilarasan, U. Sanjith, M.S. Shankar, G. Rajagopal, Effect of reduced graphene oxide (rGO) on corrosion and erosion-corrosion behaviour of electroless Ni-P coatings, Wear 390 (2017) 385–391.

[77] F. Maia, K.A. Yasakau, J. Carneiro, S. Kallip, J. Tedim, T. Henriques, A. Cabral, J. Venâncio, M.L. Zheludkevich, M.G.S. Ferreira, Corrosion protection of AA2024 by sol–gel coatings modified with MBT-loaded polyurea microcapsules, Chem. Eng. J. 283 (2016) 1108–1117.

[78] Z. Zheng, M. Schenderlein, X. Huang, N.J. Brownbill, F. Blanc, D. Shchukin, Influence of functionalization of nanocontainers on self-healing anticorrosive coatings, ACS Appl. Mater. Interfaces 7 (2015) 22756–22766.

[79] C. Kim, A.I. Karayan, J. Milla, M. Hassan, H. Castaneda, Smart Coating Embedded with pH-Responsive Nanocapsules Containing a Corrosion Inhibiting Agent, ACS Appl. Mater. Interfaces 12 (2020) 6451–6459.

[80] J. Fu, T. Chen, M. Wang, N. Yang, S. Li, Y. Wang, X.Liu, Acid and alkaline dual stimuli-responsive mechanized hollow mesoporous silica nanoparticles as smart nanocontainers for intelligent anticorrosion coatings, ACS Nano 7 (2013) 11397–11408.

[81] H. Li, Y. Cui, H. Wang, Y. Zhu, B. Wang, Preparation and application of polysulfone microcapsules containing tung oil in self-healing and self-lubricating epoxy coating, Colloids Surf. A Physicochem. Eng. Asp. 518 (2017) 181–187.

[82] A. Stankiewicz, Z. Kefallinou, G. Mordarski, Z. Jagoda, B. Spencer, Surface functionalisation by the introduction of self-healing properties into electroless Ni-P coatings, Electrochim. Acta 297 (2019) 427–434.

[83] Z.H. Xie, D. Li, Z. Skeete, A. Sharma, C.J. Zhong, Nanocontainer-enhanced self-healing for corrosion-resistant Ni coating on Mg alloy, ACS Appl. Mater. Interfaces 9 (2017) 36247–36260.

[84] Z.F. Yin, W.Z. Zhao, W.Y. Lai, X.H. Zhao, Electrochemical behaviour of Ni-base alloys exposed under oil/gas field environments, Corros. Sci. 51 (2009) 1702–1706.

[85] J.M. Hernandez, D.H. Lim, H.V.P. Nguyen, S.P. Yoon, J. Han, S.W. Nam, C.W. Yoon, S.K. Kim, H.C. Ham, Decomposition of hydrogen sulfide (H_2S) on Ni (100) and Ni_3Al (100) surfaces from first-principles, Int. J. Hydrog. Energy 39 (2014) 12251–12258.

[86] F. Mansfeld, Z. Sun, C.H. Hsu, A. Nagiub, Concerning trend removal in electrochemical noise measurements, Corros. Sci. 43 (2001) 341–352.

[87] M. Ueda, 2006 FN Speller Award Lecture: Development of corrosion-resistance alloys for the oil and gas industry—based on spontaneous passivity mechanism, Corrosion 62 (2006) 856–867.

[88] M.F. Montemor, Functional and smart coatings for corrosion protection: a review of recent advances, Surf. Coat. Technol. 258 (2014) 17–37.

[89] M. Finšgar, J. Jackson, Application of corrosion inhibitors for steels in acidic media for the oil and gas industry: a review, Corros. Sci. 86 (2014) 17–41.

[90] M. Fenker, M. Balzer, H. Kappl, Corrosion protection with hard coatings on steel: Past approaches and current research efforts, Surf. Coat. Technol. 257 (2014) 182–205.

[91] M. Czagány, P. Baumli, G. Kaptay, The influence of the phosphorous content and heat treatment on the nano-micro-structure, thickness and micro-hardness of electroless Ni-P coatings on steel, Appl. Surf. Sci. 423 (2017) 160–169.

[92] E. Georgiza, J. Novakovic, P. Vassiliou, Characterization and corrosion resistance of duplex electroless Ni-P composite coatings on magnesium alloy, Surf. Coat. Technol. 232 (2013) 432–439.

[93] A. Akyol, H. Algul, M. Uysal, H. Akbulut, A. Alp, A novel approach for wear and corrosion resistance in the electroless Ni-PW alloy with CNFs co-depositions, Appl. Surf. Sci. 453 (2018) 482–492.

[94] Z. Rajabalizadeh, D. Seifzadeh, Application of electroless Ni-P coating on magnesium alloy via CrO_3/HF free titanate pretreatment, Appl. Surf. Sci. 422 (2017) 696–709.

[95] D.P. Li, L. Zhang, J.W. Yang, M.X. Lu, J.H. Ding, M.L. Liu, Effect of H_2S concentration on the corrosion behavior of pipeline steel under the coexistence of H_2S and CO_2, Int. J. Miner. Metall. Mater. 21 (2014) 388–394.

[96] W. He, O.Ø. Knudsen, S. Diplas, Corrosion of stainless steel 316L in simulated formation water environment with CO_2–H_2S–Cl^-, Corros. Sci. 51 (2009) 2811–2819.

[97] Choi, Y.S., Nesic, S. and Ling, S., 2011. Effect of H_2S on the CO_2 corrosion of carbon steel in acidic solutions. Electrochimica Acta, 56(4), pp.1752–1760.

[98] J. Banaś, U. Lelek-Borkowska, B. Mazurkiewicz, W. Solarski, Effect of CO_2 and H_2S on the composition and stability of passive film on iron alloys in geothermal water, Electrochim. Acta 52 (2007) 5704–5714.

[99] X.H. Zhao, Y. Han, Z.Q. Bai, B. Wei, The experiment research of corrosion behaviour about Ni-based alloys in simulant solution containing H_2S/CO_2, Electrochim. Acta 56 (2011) 7725-7731.

[100] M. Stern, A.L. Geary, Electrochemical polarization: I. A theoretical analysis of the shape of polarization curves, J. Electrochem. Soc. 104 (1957) 56–63.

[101] ASTM G59-97, Standard test method for conducting potentiodynamic polarization resistance measurements, In American Society for Testing and Materials, 2014.

[102] L. Wei, X. Pang, K. Gao, Corrosion of low alloy steel and stainless steel in supercritical CO_2/H_2O/H_2S systems, Corros. Sci. 111 (2016) 637–648.

[103] A. Królikowski, P. Butkiewicz, Anodic behavior of Ni P alloys studied by impedance spectroscopy, Electrochim. Acta 38 (1993) 1979–1983.

[104] R.B. Diegle, N.R. Sorensen, G.C. Nelson, Dissolution of glassy Ni-P alloys in H_2 SO_4 and HCl electrolytes, J. Electrochem. Soc. 133 (1986) 1769.

[105] Q.Y. Wang, Y. Behnamian, H. Luo, X.Z. Wang, M. Leitch, H. Zeng, J.L. Luo, Anticorrosion performance of chromized coating prepared by pack cementation in simulated solution with H_2S and CO_2. Appl. Surf. Sci. 419 (2017) 197–205.

[106] T.A. Ho, C. Bae, H. Nam, E. Kim, S.Y. Lee, J.H. Park, H. Shin, Metallic Ni_3S_2 films grown by atomic layer deposition as an efficient and stable electrocatalyst for overall water splitting, ACS Appl. Mater. Interfaces 10 (2018) 12807–12815.

[107] H.W. Nesbitt, D. Legrand, G.M. Bancroft, Interpretation of Ni2p XPS spectra of Ni conductors and Ni insulators, Phys. Chem. Miner. 27 (2000) 357–366.

[108] M. Hao, M. Xiao, Y. Yan, Y. Miao, Synthesizing amorphous Ni-P micro-/nano-composites with perfect roundness or embryo-like structures, Adv. Powder Technol. 28 (2017) 3095–3103.

[109] A.M. Venezia, R. Bertoncello, G. Deganello, X-ray photoelectron spectroscopy investigation of pumice-supported nickel catalysts, Surf. Interface Anal. 23 (1995) 239–247.

[110] C.-C. Wu, C.-F. Yang, Investigation of the properties of nanostructured Li-doped NiO films using the modified spray pyrolysis method, Nanoscale Res. Lett. 8 (2013) 33.

[111] L.Q. Wu, Y.C. Li, S.Q. Li, Z.Z. Li, G.D. Tang, W.H. Qi, L.C. Xue, X.S. Ge, L.L. Ding, Method for estimating ionicities of oxides using O1s photoelectron spectra, AIP Adv. 5 (2015) 097210.

[112] M. Matoba, S. Anzai, A. Fujimori, Thermal expansion, thermoelectric power, and XPS study of the nonmetal-metal transition in $Ni_{1-x}S_{1-y}Se_y$, J. Phys. Soc. Jpn. 60 (1991) 4230–4244.

[113] X. Wang, Q. Xiang, B. Liu, L. Wang, T. Luo, D. Chen, G. Shen, TiO_2 modified FeS nanostructures with enhanced electrochemical performance for lithium-ion batteries, Sci. Rep. 3 (2013) 1–8.

[114] G.A. Zhang, Y.F. Cheng, Electrochemical characterization and computational fluid dynamics simulation of flow-accelerated corrosion of X65 steel in a CO_2-saturated oilfield formation water, Corros. Sci. 52 (2010) 2716–2724.

[115] E. Abelev, T.A. Ramanarayanan, S.L. Bernasek, Iron corrosion in CO_2/brine at low H_2S concentrations: an electrochemical and surface science study, J. Electrochem. Soc. 156 (2009) C331.

[116] T. Dickinson, A.F. Povey, P.M.A. Sherwood, Dissolution and passivation of nickel. An X-ray photoelectron spectroscopic study, J. Chem. Soc., Faraday Trans. 1 73 (1977) 327–343.

[117] X. Cheng, H. Ma, S. Chen, X. Chen, Z. Yao, Corrosion of nickel in acid solutions with hydrogen sulphide, Corros. Sci. 42 (2000) 299–311.

[118] A. Okuwaki, O. Kanome, T. Okabe, The precipitation of Ni_3S_2 from sulfate solutions, Metall. Trans. B. 15 (1984) 609–615.

[119] T.S. De Gromoboy, L.L. Shreir, The formation of nickel oxides during the passivation of nickel in relation to the potential/pH diagram, Electrochim. Acta 11 (1966) 895–904.

[120] A.N. Buckley, R. Woods, Electrochemical and XPS studies of the surface oxidation of synthetic heazlewoodite (Ni_3S_2), J. Appl. Electrochem. 21 (1991) 575–582.

[121] B.I. Onyeachu, E.E. Oguzie, I.C. Ukaga, D.I. Njoku, X. Peng, Ni corrosion product layer during immersion in a 3.5% NaCl solution: electrochemical and XPS characterization, Port. Electrochim. Acta 35 (2017) 127–136.

[122] H. Mansoori, D. Young, B. Brown, M. Singer, Influence of calcium and magnesium ions on CO_2 corrosion of carbon steel in oil and gas production systems-A review, J. Nat. Gas Sci. Eng. 59 (2018) 287–296.

[123] M.M. Vazirian, T.V. Charpentier, M. de Oliveira Penna, A. Neville, Surface inorganic scale formation in oil and gas industry: As adhesion and deposition processes, J. Petrol. Sci. Eng. 137 (2016) 22–32.

[124] M.S. Kamal, I. Hussein, M. Mahmoud, A.S. Sultan, M.A. Saad, Oilfield scale formation and chemical removal: A review, J. Petrol. Sci. Eng. 171 (2018) 127–139.

[125] J. Li, M. Tang, Z. Ye, L. Chen, Y. Zhou, Scale formation and control in oil and gas fields: A review, J. Disper. Sci. Technol. 38 (2017) 661–670.

[126] A.A. Olajire, A review of oilfield scale management technology for oil and gas production, J. of Petrol. Sci. Eng. 135 (2015) 723–737.

[127] J. Li, C. Sun, S. Shuang, M. Roostaei, V. Fattahpour, M. Mahmoudi, H. Zeng, J.L. Luo, 2019. Investigation on the flow-induced corrosion and degradation behavior of underground J55 pipe in a water production well in the Athabasca oil sands reservoir. J. Petrol. Sci. Eng. 182, 106325.

[128] C. Ding, K.W. Gao, C.F. Chen, Effect of Ca^{2+} on CO_2 corrosion properties of X65 pipeline steel, Int. J. Min. Met. Mater. 16 (2009) 661–666.

[129] S.N. Esmaeely, D. Young, B. Brown, S. Nešić, Effect of incorporation of calcium into iron carbonate protective layers in CO_2 corrosion of mild steel, Corrosion 73 (2017) 238–246.

[130] Y. Hua, A. Shamsa, R. Barker, A. Neville, Protectiveness, morphology and composition of corrosion products formed on carbon steel in the presence of Cl^-, Ca^{2+} and Mg^{2+} in high pressure CO_2 environments, Appl. Surf. Sci. 455 (2018) 667–682.

[131] B. Wang, L. Xu, G. Liu, M. Lu, Corrosion behavior and mechanism of 3Cr steel in CO_2 environment with various Ca^{2+} concentration, Corros. Sci. 136 (2018) 210–220.

[132] A. Shamsa, R. Barker, Y. Hua, E. Barmatov, T.L. Hughes, A. Neville, The role of Ca^{2+} ions on Ca/Fe carbonate products on X65 carbon steel in CO_2 corrosion environments at 80 and 150 °C, Corros. Sci. 156 (2019) 58–70.

[133] K. Gao, F. Yu, X. Pang, G. Zhang, L. Qiao, W. Chu, M. Lu, Mechanical properties of CO_2 corrosion product scales and their relationship to corrosion rates, Corros. Sci. 50 (2008) 2796–2803.

[134] X. Jiang, Y.G. Zheng, D.R. Qu, W. Ke, Effect of calcium ions on pitting corrosion and inhibition performance in CO_2 corrosion of N80 steel, Corros. Sci. 48 (2006) 3091–3108.

[135] P.R. Rhodes, Environment-assisted cracking of corrosion-resistant alloys in oil and gas production environments: a review, Corrosion 57 (2001) 923–966.

[136] H. Zhang, Y.L. Zhao, Z.D. Jiang, Effects of temperature on the corrosion behavior of 13Cr martensitic stainless steel during exposure to CO_2 and Cl^- environment, Mater. Lett. 59 (2005) 3370–3374.

[137] L.T. Popoola, A.S. Grema, G.K. Latinwo, B. Gutti, A.S. Balogun, Corrosion problems during oil and gas production and its mitigation, Int. J. of Ind. Chem. 4 (2013) 35.

[138] N. Ghavidel, S.R. Allahkaram, R. Naderi, M. Barzegar, H. Bakhshandeh, 2020. Corrosion and wear behavior of an electroless Ni-P/nano-SiC coating on AZ31 Mg alloy obtained through environmentally-friendly conversion coating. Surf. Coat. Technol. 382, 125156.

[139] Z. Yan, C. Guo, F. Yang, C. Zhang, Y. Mao, S. Cui, Y. Wei, L. Hou, L. Xu, Cliff-like NiO/Ni_3S_2 directly grown on Ni foam for battery-type electrode with high area capacity and long cycle stability, Electrochim. Acta 251 (2017) 235–243.

[140] J. Li, S. Wang, T. Xiao, X. Tan, P. Xiang, L. Jiang, C. Deng, W. Li, M. Li, Controllable preparation of nanoporous Ni_3S_2 films by sulfuration of nickel foam as promising asymmetric supercapacitor electrodes, Appl. Surf. Sci. 420 (2017) 919–926.

[141] X. Zhao, T. Hu, H. Li, M. Chen, S. Cao, L. Zhang, X. Hou, Electrochemically assisted co-deposition of calcium phosphate/collagen coatings on carbon/carbon composites, Appl. Surf. Sci. 257 (2011) 3612–3619.

[142] K. Jiang, Y. Wang, X. Gao, C. Cai, H. Lin, Facile, quick, and gram-scale synthesis of ultralong-lifetime room-temperature-phosphorescent carbon dots by microwave irradiation, Angew. Chem. Int. Ed. 57 (2018) 6216–6220.

[143] K. Song, Y.N. Jang, W. Kim, M.G. Lee, D. Shin, J.H. Bang, C.W. Jeon, S.C. Chae, Precipitation of calcium carbonate during direct aqueous carbonation of flue gas desulfurization gypsum, Chem. Eng. J. 213 (2012) 251–258.

[144] S.V. Green, A. Kuzmin, J. Purans, C.G. Granqvist, G.A. Niklasson, Structure and composition of sputter-deposited nickel-tungsten oxide films, Thin Solid Films 519 (2011) 2062–2066.

[145] W.J. Lee, K. Prasanna, Y.N. Jo, K.J. Kim, H.S. Kim, C.W. Lee, Depth profile studies on nickel rich cathode material surfaces after cycling with an electrolyte containing vinylene carbonate at elevated temperature, Phys. Chem. Chem. Phys. 16 (2014) 17062–17071.

[146] C.N. Cao, J.Q. Zhang, An introduction to electrochemical impedance spectroscopy, Science, Beijing, 2002.

[147] Nešić, S., 2007. Key issues related to modelling of internal corrosion of oil and gas pipelines–A review, Corrosion science, 49(12), pp.4308–4338.

[148] W. Sun, S. Nešić, R.C. Woollam, The effect of temperature and ionic strength on iron carbonate ($FeCO_3$) solubility limit, Corros. Sci. 51 (2009) 1273–1276.

[149] Y. Zhang, H. Shaw, R. Farquhar, R. Dawe, The kinetics of carbonate scaling—application for the prediction of downhole carbonate scaling, J. Petrol. Sci. Eng. 29 (2001) 85–95.

[150] R. Rizzo, S. Gupta, M. Rogowska, R. Ambat, 2020. Corrosion of carbon steel under CO_2 conditions: Effect of $CaCO_3$ precipitation on the stability of the $FeCO_3$ protective layer. Corros. Sci. 162, 108214.

[151] P. Bénézeth, J.L. Dandurand, J.C. Harrichoury, Solubility product of siderite ($FeCO_3$) as a function of temperature (25–250 C), Chem. Geol. 265 (2009) 3–12.

[152] L.N. Plummer, E. Busenberg, The solubilities of calcite, aragonite and vaterite in CO_2-H_2O solutions between 0 and 90 °C, and an evaluation of the aqueous model for the system $CaCO_3$-CO_2-H_2O, Geochim. Cosmochim. Acta 46 (1982) 1011–1040.

[153] Q. Wang, J.H. Li, J.B. Liu, B.X. Liu, Atomistic design of favored compositions for synthesizing the Al-Ni-Y metallic glasses, Sci. Rep. 5 (2015) 16218.

[154] H.A. Alsaiari, A. Kan, M. Tomson, Effect of calcium and iron (II) ions on the precipitation of calcium carbonate and ferrous carbonate, SPE J. 15 (2010) 294–300.

[155] S. Navabzadeh Esmaeely, Y.S. Choi, D. Young, S. Nešić, Effect of calcium on the formation and protectiveness of iron carbonate layer in CO_2 corrosion, Corrosion 69 (2013) 912–920.

[156] L.M. Tavares, E.M. da Costa, J.J. de Oliveira Andrade, R. Hubler, B. Huet, Effect of calcium carbonate on low carbon steel corrosion behavior in saline CO_2 high pressure environments, Appl. Surf. Sci. 359 (2015) 143–152.

[157] H. Mansoori, R. Mirzaee, F. Esmaeilzadeh, A. Vojood, A.S. Dowrani, Pitting corrosion failure analysis of a wet gas pipeline, Eng. Fail. Anal. 82 (2017) 16–25.

[158] K.G. Keong, W. Sha, S. Malinov, Crystallization and phase transformation behaviour of electroless nickel-phosphorus deposits with low and medium phosphorus contents under continuous heating, J. Mater. Sci. 37 (2002) 4445–4450.

[159] C.A. Melendres, M. Pankuch, On the composition of the passive film on nickel: a surface-enhanced Raman spectroelectrochemical study, J. Electroanal. Chem. 333 (1992) 103–113.

[160] M.D.C. Belo, N.E. Hakiki, M.G.S. Ferreira, Semiconducting properties of passive films formed on nickel–base alloys type Alloy 600: influence of the alloying elements, Electrochim. Acta 44 (1999) 2473–2481.

[161] C. Sun, S. Liu, J. Li, H. Zeng, J.L. Luo, Insights into the interfacial process in electroless Ni–P coating on supercritical CO_2 transport pipeline as relevant to carbon capture and storage, ACS appl. Mater. Inter. 11 (2019) 16243–16251.

[162] T.A. Hoang, Mechanisms of scale formation and inhibition, in: Z. Amjad, K.D. Demadis (Eds.), Mineral Scales and Deposits, Elsevier, 2015, pp. 47–83.

[163] Q. Yang, J. Ding, Z. Shen, Investigation of calcium carbonate scaling on ELP surface, J. Chem. Eng. Japan 33 (2000) 591–596.

[164] J.W. Mullin, Crystallization, Elsevier, 2001.

[165] R.J. Bakker, Package FLUIDS. Part 3: correlations between equations of state, thermodynamics and fluid inclusions, Geofluids 9 (2009) 63–74.

[166] R.J. Bakker, Thermodynamic properties and applications of modified van-der-Waals equations of state, in: Ricardo Morales-Rodriguez (Ed.), Thermodynamics - Fundamentals and Its Application in Science, InTech, 2012, pp. 163–190.

[167] Y. Wang, X. Shu, S. Wei, C. Liu, W. Gao, R.A. Shakoor, R. Kahraman, Duplex Ni–P–ZrO_2/Ni–P electroless coating on stainless steel, J. Alloys Compd. 630 (2015) 189–194.

[168] M. Gholizadeh-Gheshlaghi, D. Seifzadeh, P. Shoghi, A. Habibi-Yangjeh, Electroless Ni-P/nano-WO_3 coating and its mechanical and corrosion protection properties, J. Alloys Compd. 769 (2018) 149–160.

[169] I.V. Petukhov, N.A. Medvedeva, I.R. Subakova, V.I. Kichigin, Corrosion-electrochemical behavior of Ni-P coatings in deaerated acidic sulfate solutions, Prot. Met. Phys. Chem. Surf. 50 (2014) 875–882.

[170] L. Zhang, Y. Jin, B. Peng, Y. Zhang, X. Wang, Q. Yang, J. Yu, Effects of annealing temperature on the crystal structure and properties of electroless deposited Ni–W–Cr–P alloy coatings, Appl. Surf. Sci. 255 (2008) 1686–1691.

[171] A. Tomio, M. Sagara, T. Doi, H. Amaya, N. Otsuka, T. Kudo, Role of alloyed molybdenum on corrosion resistance of austenitic Ni–Cr–Mo–Fe alloys in H_2S–Cl^- environments, Corros. Sci. 98 (2015) 391–398.

[172] Q.Y. Wang, X.Z. Wang, H. Luo, J.L. Luo, A study on corrosion behaviors of Ni–Cr–Mo laser coating, 316 stainless steel and X70 steel in simulated solutions with H_2S and CO_2, Surf. Coat. Technol. 291 (2016) 250–257.

[173] G. Genchev, C. Bosch, E. Wanzenberg, A. Erbe, Role of molybdenum in corrosion of iron-based alloys in contact with hydrogen sulfide containing solution, Mater. Corros. 68 (2017) 595–603.

[174] A. Pardo, M.C. Merino, A.E. Coy, F. Viejo, R. Arrabal, E. Matykina, Effect of Mo and Mn additions on the corrosion behaviour of AISI 304 and 316 stainless steels in H_2SO_4, Corros. Sci. 50 (2008) 780–794.

[175] G.O. Ilevbare, G.T. Burstein, The role of alloyed molybdenum in the inhibition of pitting corrosion in stainless steels, Corros. Sci. 43 (2001) 485–513.

[176] K. Sugimoto, Y. Sawada, The role of molybdenum additions to austenitic stainless steels in the inhibition of pitting in acid chloride solutions, Corros. Sci. 17 (1977) 425–445.

[177] K. Denpo, H. Ogawa, Passivity of corrosion-resistant alloys in environments containing chloride and hydrogen sulfide, Corrosion 53 (1997) 718–723.

[178] C.R. Clayton, Y.C. Lu, A bipolar model of the passivity of stainless steel: the role of Mo addition, J. Electrochem. Soc. 133 (1986) 2465–2473.

[179] J. Wojewoda-Budka, A. Wierzbicka-Miernik, L. Litynska-Dobrzynska, M.J. Szczerba, G. Mordarski, M. Mosiałek, Z. Huber, P. Zieba, Microstructure characteristics and phase transformations of the Ni-P and Ni-P-Re electroless deposited coatings after heat treatment, Electrochim. Acta 209 (2016) 183–191.

[180] D. Dong, X.H. Chen, W.T. Xiao, G.B. Yang, P.Y. Zhang, Preparation and properties of electroless Ni–P–SiO_2 composite coatings, Appl. Surf. Sci. 255 (2009) 7051–7055.

[181] M. Xiao, R. Cheng, M. Hao, M. Zhou, Y. Miao, Onsite substitution synthesis of ultrathin Ni nanofilms loading ultrafine Pt nanoparticles for hydrogen evolution, ACS Appl. Mater. Interfaces 7 (2015) 26101–26107.

[182] N. Zeng, D.G. Hopkinson, B.F. Spencer, S.G. McAdams, A.A. Tedstone, S.J. Haigh, D.J. Lewis, Direct synthesis of MoS_2 or MoO_3 via thermolysis of a dialkyl dithiocarbamato molybdenum (iv) complex, Chem. Commun. 55 (2019) 99–102.

[183] H. Li, M. Li, Y. Chu, F. Liu, H. Nie, Effect of different preparation methods of MoO_3/Al_2O_3 catalysts on the existing states of Mo species and hydrodesulfurization activity, Fuel 116 (2014), pp.168–174.

[184] P. Qin, G. Fang, W. Ke, F. Cheng, Q. Zheng, J. Wan, H. Lei, X. Zhao, In situ growth of double-layer MoO_3/MoS_2 film from MoS_2 for hole-transport layers in organic solar cell, J. Mater. Chem. A 2 (2014) 2742–2756.

[185] A. Laszczyńska, W. Tylus, B. Szczygieł, I. Szczygieł, Influence of post−deposition heat treatment on the properties of electrodeposited Ni−Mo alloy coatings, Appl. Surf. Sci. 462 (2018) 432–443.

[186] J.A. Rodriguez, S.Y. Li, J. Hrbek, H.H. Huang, G.Q. Xu, The interaction of Ni and Fe with sulfur and molybdenum-sulfide surfaces: a TDS, XPS and hydrogen-chemisorption study, Surf. Sci. 370 (1997) 85–95.

[187] H. Luo, C.F. Dong, X.G. Li, K. Xiao, The electrochemical behaviour of 2205 duplex stainless steel in alkaline solutions with different pH in the presence of chloride, Electrochim. Acta 64 (2012) 211–220.

[188] L. Liu, Y. Li, F. Wang, Pitting mechanism on an austenite stainless steel nanocrystalline coating investigated by electrochemical noise and in-situ AFM analysis, Electrochim. Acta 54 (2008) 768–780.

[189] Y.F. Cheng, B.R. Rairdan, J.L. Luo, Features of electrochemical noise generated during pitting of inhibited A516-70 carbon steel in chloride solutions, J. Appl. Electrochem. 28 (1998) 1371–1375.

[190] S. Girija, U.K. Mudali, V.R. Raju, R.K. Dayal, H.S. Khatak, B. Raj, Determination of corrosion types for AISI type 304L stainless steel using electrochemical noise method, Mater. Sci. Eng. A 407 (2005) 188–195.

[191] T. Fukuda, T. Mizuno, The evaluation of pitting corrosion from the spectrum slope of noise fluctuation on iron and 304 stainless steel electrodes, Corros. Sci. 38 (1996) 1085–1091.

[192] S. Doubaji, B. Philippe, I. Saadoune, M. Gorgoi, T. Gustafsson, A. Solhy, M. Valvo, H. Rensmo, K. Edström, Passivation layer and cathodic redox reactions in sodium-ion batteries probed by HAXPES, ChemSusChem 9 (2016) 97–108.

[193] Y. Hou, L.J. Tang, H.W. Qiao, Z.R. Zhou, Y.L. Zhong, L.R. Zheng, M.J. Chen, S. Yang, H.G. Yang, Ni–Co–O hole transport materials: gap state assisted hole extraction with superior electrical conductivity, J. Mater. Chem. A 7 (2019) 20905–20910.

[194] B.M. Reddy, B. Chowdhury, P.G. Smirniotis, An XPS study of the dispersion of MoO_3 on TiO_2–ZrO_2, TiO_2–SiO_2, TiO_2–Al_2O_3, SiO_2–ZrO_2, and SiO_2–TiO_2–ZrO_2 mixed oxides, Appl. Catal., A 211 (2001) 19–30.

[195] W.L. Dai, M.H. Qiao, J.F. Deng, XPS studies on a novel amorphous Ni–Co–W–B alloy powder, Appl. Surf. Sci. 120 (1997) 119–124.

[196] J. Yang, C. Yu, X. Fan, S. Liang, S. Li, H. Huang, Z. Ling, C. Hao, J. Qiu, Electroactive edge site-enriched nickel–cobalt sulfide into graphene frameworks for high-performance asymmetric supercapacitors, Energy Environ. Sci. 9 (2016) 1299–1307.

[197] H. Luo, C. Dong, K. Xiao, X. Li, Passive film properties and electrochemical behavior of Co-Cr-Mo stainless steel in chloride solution, J. Mater. Eng. Perform. 26 (2017) 2237–2243.

[198] T.J. Mesquita, E. Chauveau, M. Mantel, R.P. Nogueira, A XPS study of the Mo effect on passivation behaviors for highly controlled stainless steels in neutral and alkaline conditions, Appl. Surf. Sci. 270 (2013) 90–97.

[199] P.M. Natishan, J. Jones-Meehan, G.I. Loeb, B.J. Little, R. Ray, M. Beard, Corrosion behavior of some transition metals and 4340 steel metals exposed to sulfate-reducing bacteria, Corrosion 55 (1999) 1062–1068.

[200] F. Paulo, L. Santos, Design of experiments for microencapsulation applications: A review, Mater. Sci. Eng. C 77 (2017) 1327–1340.

[201] S. Chen, M. Yang, C. Ba, S. Yu, Y. Jiang, H. Zou, Y. Zhang, Preparation and characterization of slow–release fertilizer encapsulated by biochar-based waterborne copolymers, Sci. Total Environ. 615 (2018) 431–437.

[202] C. Arpagaus, A. Collenberg, D. Rütti, E. Assadpour, S.M. Jafari, Nano spray drying for encapsulation of pharmaceuticals, Int. J. Pharm. 546 (2018) 94–214.

[203] C. Ding, Y. Liu, M. Wang, T. Wang, J. Fu, Self-healing, superhydrophobic coating based on mechanized silica nanoparticles for reliable protection of magnesium alloys, J. Mater. Chem. A 4 (2016) 8041–8052.

[204] G.L. Li, Z. Zheng, H. Möhwald, D.G. Shchukin, Silica/polymer double-walled hybrid nanotubes: synthesis and application as stimuli-responsive nanocontainers in self-healing coatings, ACS Nano 7 (2013) 2470–2478.

[205] Y. Su, O.F. Ojo, I.K.M. Tsengam, J. He, G.L. McPherson, V.T. John, J.A. Valla, Thermoresponsive coatings on hollow particles with mesoporous shells serve as stimuli-responsive gates to species encapsulation and release, Langmuir 34 (2018) 14608–14616.

[206] A. Latnikova, D.O. Grigoriev, J. Hartmann, H. Möhwald, D.G. Shchukin, Polyfunctional active coatings with damage-triggered water-repelling effect, Soft Matter 7 (2011) 369–372.

[207] Z. Zheng, X. Huang, M. Schenderlein, D. Borisova, R. Cao, H. Möhwald, D. Shchukin, Self-Healing and antifouling multifunctional coatings based on pH and sulfide ion sensitive nanocontainers, Adv. Funct. Mater. 23 (2013) 3307–3314.

[208] F. Maia, J. Tedim, A.D. Lisenkov, A.N. Salak, M.L. Zheludkevich, M.G. Ferreira, Silica nanocontainers for active corrosion protection, Nanoscale 4 (2012) 1287–1298.

[209] J. Lee, J. Kim, T. Hyeon, Recent progress in the synthesis of porous carbon materials, Adv. Mater. 18 (2006) 2073–2094.

[210] A. Stein, Advances in microporous and mesoporous solids—highlights of recent progress, Adv. Mater. 15 (2003) 763–775.

[211] M.J. Hollamby, D. Fix, I. Dönch, D. Borisova, H. Möhwald, D. Shchukin, Hybrid polyester coating incorporating functionalized mesoporous carriers for the holistic protection of steel surfaces, Adv. Mater. 23 (2011) 1361–1365.

[212] M. Finšgar, I. Milošev, Inhibition of copper corrosion by 1, 2, 3-benzotriazole: a review, Corros. Sci. 52 (2010) 2737–2749.

[213] M.M. Mennucci, E.P. Banczek, P.R.P. Rodrigues, I. Costa, Evaluation of benzotriazole as corrosion inhibitor for carbon steel in simulated pore solution, Cem. Concr. Compos. 31 (2009) 418–424.

[214] P.G. Cao, J.L. Yao, J.W. Zheng, R.A. Gu, Z.Q. Tian, Comparative study of inhibition effects of benzotriazole for metals in neutral solutions as observed with surface-enhanced Raman spectroscopy, Langmuir 18 (2002) 100–104.

[215] J.B. Xu, Y.Q. Cao, L. Fang, J.M. Hu, A one-step preparation of inhibitor-loaded silica nanocontainers for self-healing coatings, Corros. Sci. 140 (2018) 349–362.

[216] D. Tan, Z. Ma, B. Xu, Y. Dai, G. Ma, M. He, Z. Jin, J. Qiu, Surface passivated silicon nanocrystals with stable luminescence synthesized by femtosecond laser ablation in solution, Phys. Chem. Chem. Phys. 13 (2011) 20255–20261.

[217] P. Córdoba-Torres, T.J. Mesquita, R.P. Nogueira, Relationship between the origin of constant-phase element behavior in electrochemical impedance spectroscopy and electrode surface structure, J. Phys. Chem. C 119 (2015) 4136–4147.

[218] J.-B. Jorcin, M.E. Orazem, N. Pébère, B. Tribollet, CPE analysis by local electrochemical impedance spectroscopy, Electrochim. Acta 51 (2006) 1473–1479.

[219] G.A. Zhang, Y. Zeng, X.P. Guo, F. Jiang, D.Y. Shi, Z.Y. Chen, Electrochemical corrosion behavior of carbon steel under dynamic high pressure H_2S/CO_2 environment, Corros. Sci. 65 (2012) 37–47.

[220] J.O.M. Bockris, and A.K. Reddy, Modern electrochemistry: an introduction to an interdisciplinary area, Springer Science & Business Media, 2012.

[221] N. Sato, The stability of localized corrosion, Corros. Sci. 37 (1995) 1947–1967.

[222] L. Jia, Z. Li, J. Shen, D. Zheng, X. Tian, H. Guo, P. Chang, Multifunctional mesoporous silica nanoparticles mediated co-delivery of paclitaxel and tetrandrine for overcoming multidrug resistance, Int. J. Pharm. 489 (2015) 318–330.

[223] O.V. Dement'eva, I.N. Senchikhin, E.M. Sedykh, I.N. Gromyak, V.A. Ogarev, V.M. Rudoy, Mesostructured SiO_2-based nanocontainers synthesized on a functional template: Capacity and rate of unloading, Colloid J. 78 (2016) 52–64.

[224] N.H.N. Kamarudin, A.A. Jalil, S. Triwahyono, V. Artika, N.F.M. Salleh, A.H. Karim, N.F. Jaafar, M.R. Sazegar, R.R. Mukti, B.H. Hameed, A. Johari, Variation of the crystal growth of mesoporous silica nanoparticles and the evaluation to ibuprofen loading and release, J. Colloid Interface Sci. 421 (2014) 6–13.

[225] N. Jagerovic, M.L. Jimeno, I. Alkorta, J. Elguero, R.M. Claramunt, An experimental (NMR) and theoretical (GIAO) study of the tautomerism of benzotriazole in solution, Tetrahedron 58 (2002) 9089–9094.

Appendix: Investigation on the flow-induced corrosion and degradation behavior of underground J55 pipe in a water production well in the Athabasca oil sands reservoir

ABSTRACT: The corrosion behavior of J55 carbon steel pipe was investigated in a water production well environment in the Athabasca oil sands reservoir. The corrosion morphologies and the chemical compositions of corrosion products were examined by surface analysis techniques. The protection performance of the formed corrosion scales was evaluated using electrochemical measurements. The results show that severe erosion corrosion occurs on the inner wall of the pipe and causes a significant thinning, which is the dominant reason for the pipe failure. Likewise, the failure of the thread zone is originated from the severe corrosion of inner wall as well. Localized corrosion of carbon steel occurs in the welding zone because of the galvanic effect between stainless steel and carbon steel. Furthermore, the distributions of corrosion products on the inner wall are notably affected by the flow. Dense and thick Ca-containing corrosion scales act as a physical barrier layer and prevent the steel from further corrosion, whereas localized corrosion occurs in the regions with loose and thin corrosion scales.

A.1 Introduction

Carbon steel has been regarded as the most economic and common material for applications in oil and gas industry. However, corrosion of carbon steel pipes is reported to occur frequently because of the harsh environments under the service condition, which causes huge economic losses and serious safety concerns (Liu et al., 2017; Zhong et al., 2018; Elgaddafi et al., 2016). Specifically, a large portion of carbon steel pipes is buried underground, and the corrosion behavior can be affected by different factors, e.g., temperature, pressure, concentrations of corrosive species, flow rate of the fluid around the pipes, etc. Extensive research has been focused on the effects of various factors on the corrosion mechanism of carbon steel pipes in service (Nešić, 2007; Linter and Burstein, 1999; Cole and Marney, 2012; Cui et al., 2006). In the oil sands reservoirs of Alberta, Canada, up to 80 % of oil reserves are located deeper than 70 meters below the ground, which need in-situ recovery methods such as cyclic steam stimulation (CSS) or steam-assisted gravity drainage (SAGD) (Nasr and Ayodele, 2005). These methods generally work in such a way that high-temperature steam is injected into the well to heat up the bitumen in the surrounding area to lower its viscosity, so that the hot bitumen with higher flowability can be easily transported to the ground. Presently, large-scale operations of bitumen recovery have greatly boosted the demand for the construction of water production wells at the locations of reservoirs. In water production wells, high flow rate together with high salinity creates a harsh corrosive environment and potentially leads to severe corrosion even after short-term service.

Despite considerable interest in the research of sweet and sour corrosion in the oil and gas production (Kermani and Morshed, 2003; Song, 2010; Ren et al., 2005; Feng et al., 2016; Sun and Nešic, 2009), limited attention has been paid to the water production wells. In general, the corrosion in the water production wells is a complicated process, which is closely related to physical, chemical and even geological parameters, such as the constantly changing flow rates of water and sand particles and the concentrations of the corrosive species. Apparently, it is considerably difficult to simulate the actual production condition with the lab-scale tests in relatively short test duration, since the corrosion failure of the wells is a slow and long-term process in field condition. In order to fully reflect the true corrosion behavior of carbon steel pipes in the water production wells, it necessitates the need to conduct the corrosion research under the actual service condition.

This study investigated the corrosion behavior and corrosion scales characteristics of the underground carbon steel pipes in the water production well in the Athabasca oil sands reservoir by surface analysis techniques and electrochemical measurements. Typical locations of the pipe were selected to demonstrate the effect of flow on the corrosion process. Furthermore, the corrosion mechanism was fully discussed, and a corrosion model was proposed to illustrate the corrosion and degradation process. This work is to provide a relevant guidance and reference for corrosion prevention in the actual oil and gas productions.

A.2 Experimental

A.2.1 Materials and preparation

API J55 carbon steel pipes with stainless steel wire wrap screens were used in a water production well of a steam-assisted gravity drainage (SAGD) system in the Athabasca oil sands reservoir in Northern Alberta, Canada. The chemical compositions of the underground water and main field test parameters are listed in Table A.1. The pipes were in service in the well for about six months.

Figure A.1 shows the pictures of the pipe after six months of service. The length of one completed interval of pipes is 100 feet, only 80 % of which is open to the water flow, producing 1500–2500 m^3 of water per day. Each interval contains perforated pipe and non-perforated pipe, and stainless steel wire wraps are covered on the perforated pipe to block sand particles by welding the end of wire wraps on the pipe. The thread zone is located at one end of the non-perforated pipe. Both the perforated and non-perforated pipe are open to flow in this case. The original pipe thickness is 0.25 inches (6.35 mm), and the inner diameter is around 4.1 inches (104 mm).

Table A.1 Chemical compositions of the underground water and main field test parameters of the pipes in the Athabasca oil sands reservoir.

Ion concentrations	Ca^{2+}	(32.9–81.5) mg/L
	Mg^{2+}	(11.2–24.5) mg/L
	Na^{+}	(24.2–185.0) mg/L
	HCO_3^{-}	(410–552) mg/L
	Cl^{-}	(16.0–126.0) mg/L
	SO_4^{2-}	(6.08–54.2) mg/L
Main field test parameters	pH	7.5–8.4
	Dissolved oxygen concentration	(0.1–7.1) mg/L
	Temperature	25–45 °C
	Pressure	~200 psi
	Flow rate inside the pipe	2.0–3.4 m/s
	Flow rate outside the pipe	<0.07 m/s
	Total dissolved solid (TDS)	(560–1100) mg/L

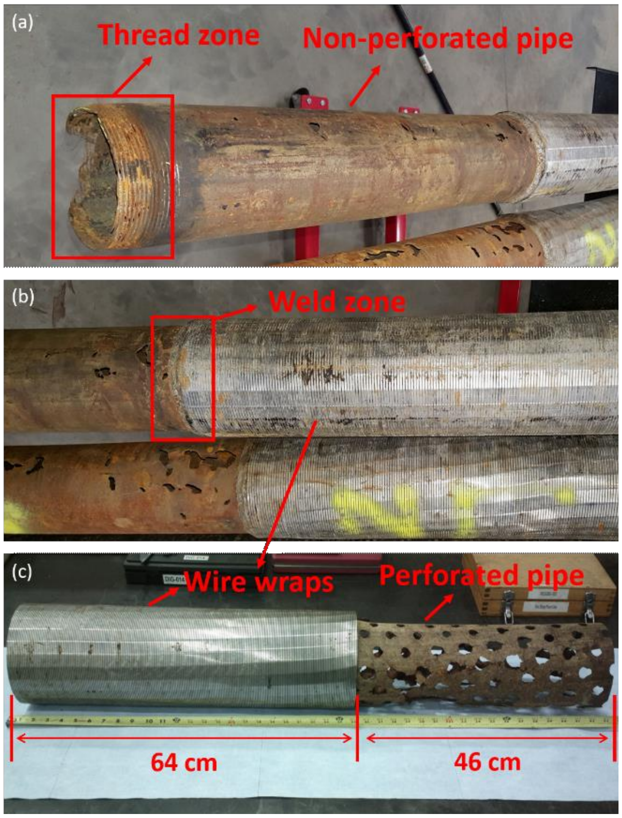

Figure A.1 Schematic of different parts of the pipes after service in the water production well for six months.

Prior to the surface characterizations, the macroscopic corrosion morphologies of the pipes were first observed. The typical locations that reflect the overall corrosion features were then selected and the corresponding samples were cut into smaller pieces for scanning electron microscope (SEM) observation. All the samples were then cleaned with petroleum ether, acetone and alcohol and dried in air. For the cross-sectional observation, the samples were sealed with epoxy and ground with 1200 grit silicon paper to ensure surface flatness. Corrosion products were collected from the pipes, ground to fine powder, cleaned with petroleum ether, acetone and alcohol and dried in air for X-ray diffraction (XRD) analysis.

A.2.2 Surface characterizations

The macroscopic morphologies of the pipes at the selected typical locations were photographed using a digital camera, and the microscopic surface and cross-sectional morphologies were observed using SEM. The elemental compositions and phase structures of the corrosion products were then identified by means of energy dispersive X-ray spectroscopy (EDS) and XRD, respectively. The XRD analysis was carried out with Cu K_α radiation and the patterns were recorded from 10° to 80° at a scanning step of 0.02° and a scanning rate of 4°/min.

A.2.3 Electrochemical measurements

The electrochemical tests were performed to determine the protection performance of corrosion scales by using a Gamry Reference 3000 electrochemical workstation. The steel samples covered with thin and thick corrosion scales were taken from the inner wall of the perforated pipe, and the bare carbon steel was chosen for comparison. The specific areas (including thick and thin corrosion scales) were first selected and cut into 1 cm × 1 cm pieces, then the pieces were welded with wire and the edges of the specimens were sealed with epoxy for electrochemical measurements. For the bare steel, the sample was ground sequentially up to 1200 grit silicon paper. All samples were rinsed with deionized water, degreased with petroleum ether, alcohol and acetone and then dried in air. The electrochemical measurements were conducted in the three-electrode cell system: the steel samples as the working electrode (WE), a carbon rod as the counter electrode (CE), and a saturated calomel electrode (SCE) as the reference electrode (RE). The exposed area of WE was 1 cm^2. The open circuit potential (OCP) was first recorded for 1 hour to obtain the stable state. Electrochemical impedance spectroscopy (EIS) measurements were carried out at OCP with AC amplitude of 10 mV in the frequency range from 100 kHz to 10 mHz. EIS data were then fitted with proper equivalent electrical circuits using ZSimpWin software. The potentiodynamic polarization curves were recorded from -500 mV to 1000 mV (vs. OCP) at a sweep rate of 1 mV/s. All the tests were conducted at room temperature (22 °C) and ambient pressure (0.1 MPa). According to the ionic concentrations of underground water in Table 1, the test solution with compositions (mg/L) of 262.0 $NaHCO_3$, 46.4 Na_2SO_4, 164.0 $CaCl_2$, 70.9 $MgCl_2$ and 14.6 NaCl was prepared. At least three parallel tests were performed to ensure the reproducibility under each test condition and the representative results were reported.

A.3 Results

A.3.1 Macroscopic appearance of corroded carbon steel pipes

The macroscopic corrosion morphologies of the pipes at different locations are shown in Figure A.2. As seen, corrosion occurs at each location in varying degrees, and both localized corrosion and general corrosion are observed. The inner wall of the pipes experiences more severe corrosion as compared to the outer wall. Especially, the corrosion perforation failure is observably derived from the thinning on the inner wall. From Figure A.2a and A.2b, it is obviously seen that the shape of perforations changes from circular to elliptical under the flow impact, indicating that the flow-induced corrosion leads to severe pipe thinning. Besides, several obvious localized corrosion regions are found on the non-perforated pipe. In addition, no significant thinning occurs in the welding zone, but localized corrosion appears near the welds. Some parts of the threads are damaged and fall off due to the corrosion from the inside out in the thread zone.

Figure A.2 Macroscopic images of (a) the outer wall and (b) the inner wall of the perforated pipe; (c) the outer wall and (d) the inner wall of the non-perforated pipe; (e) the outer wall and (f) the inner wall of the weld zone; (g) the outer wall and (h) the inner wall of the thread zone.

A.3.2 Surface analysis of the corrosion scales

The XRD patterns of the corrosion scales on the inner wall are shown in Figure A.3. It mainly consists of iron carbonates as well as small amount of iron hydroxides (γ-FeOOH and α-FeOOH), iron oxides (Fe_2O_3 and Fe_3O_4) and SiO_2. Figure A.3b depicts the comparison of $FeCO_3$ peak locations between the experimental and theoretical results in the 2θ range of 20° to 35°. Some of the $FeCO_3$ peaks shift to the left, implying a lattice structure change. The same shift occurs in the entire range of the spectra. From the EDS results shown hereinafter, Ca element is commonly present in the corrosion product, which suggests the formation of $Fe_xCa_{1-x}CO_3$. It is attributed to the isomorphic substitution effect in CO_2 corrosion process, when Ca ions are present in the medium. After $FeCO_3$ is deposited on the steel surface, a proportion of Fe atoms are replaced by Ca atoms in the $FeCO_3$ lattice, and $Fe_xCa_{1-x}CO_3$ is formed as a double salt by the given equation as below (Sun et al., 2016b):

$$(1-x)Ca^{2+} + FeCO_{3(s)} \leftrightarrow (1-x)Fe^{2+} + Fe_xCa_{1-x}CO_{3(s)} \qquad \text{(Eq. A.1)}$$

Since Ca atoms have a larger size than Fe atoms, the replacement leads to a wider interplanar spacing and a smaller diffraction angle.

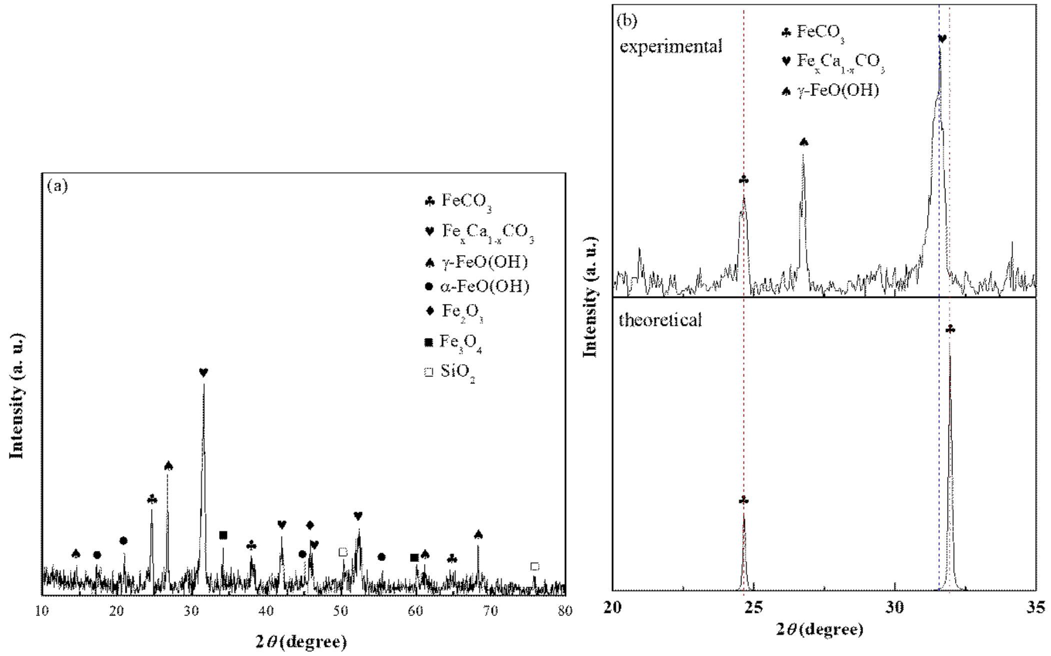

Figure A.3 (a) XRD patterns of the corrosion scales on the inner wall; (b) comparison of $FeCO_3$ peak locations in the 2*θ* range of 20° to 35°.

Comparatively, iron hydroxides (γ-FeOOH and α-FeOOH) are the main components of the corrosion products on the outer wall (Figure A.4). Besides, small amount of iron oxides (Fe_2O_3 and Fe_3O_4) and SiO_2 are detected as well.

Figure A.5 shows the SEM morphologies and EDS analysis of the corrosion product on the inner wall of the perforated pipe, shown in the white box in Figure A.2b. The corrosion scales, composed of Fe, Ca, C and O elements, are compact and less porous. The atomic ratio of (Fe+Ca): C: O is roughly 1: 1: 3 based on the quantitative results, further confirming the formation of $Fe_xCa_{1-x}CO_3$. In addition, small amount of the nodule-like crystalline $FeCO_3$ (Figure A.5b) and fine plate-shaped lepidocrocite (γ-FeOOH) (Figure

A.5c) is also observed. The SEM morphologies of corrosion product on the outer wall of the perforated pipe, shown in the white box in Figure A.2a, are exhibited in Figure A.6. Fe, C and O are the main elements; however Ca element is not detected. The corrosion product on the outer wall mostly displays two typical structures: fine plates (Figure A.6a) and globular structures (Figure A.6b), which correspond to γ-FeOOH and α-FeOOH, respectively (De la Fuente et al., 2011).

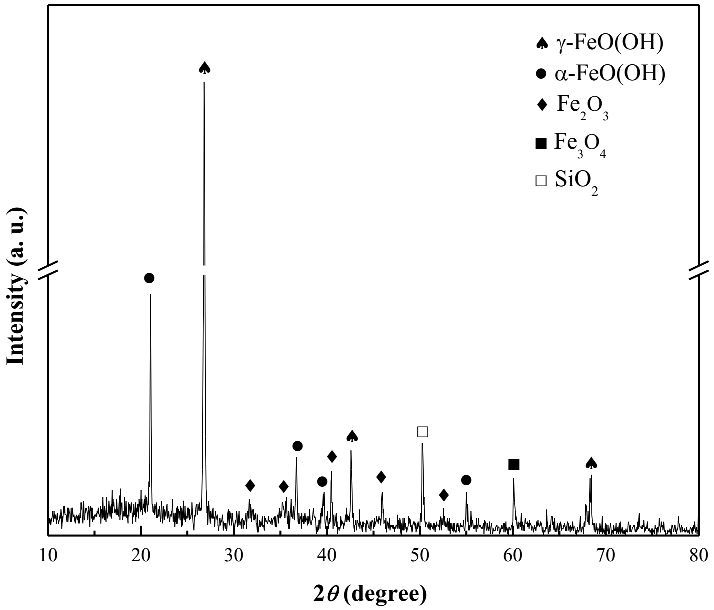

Figure A.4 XRD patterns of the corrosion scales on the outer wall.

Based on the surface analysis results, it is concluded that different corrosion processes take place on the inner and outer wall due to the varying physical and chemical conditions. Moreover, it is seen from Figure A.2 that the pipes exhibit different corrosion behaviors at different locations due to their dissimilar structures. In the next section, some typical locations on the pipes are selected to analyze the corrosion behaviors and the root cause of corrosion.

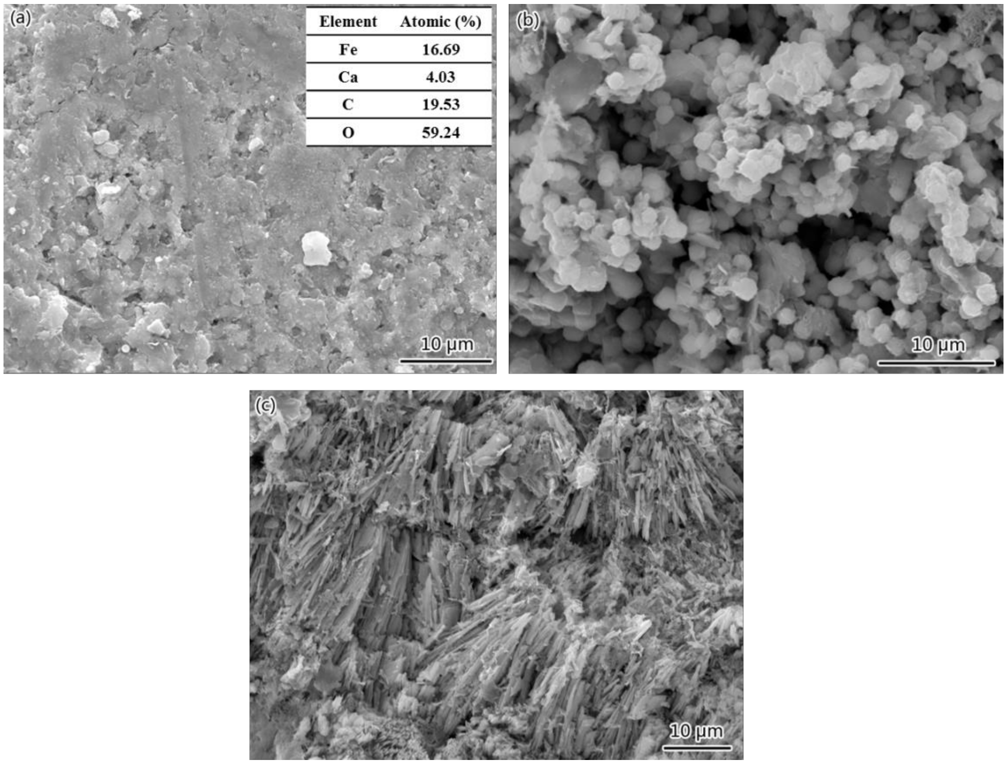

Element	Atomic (%)
Fe	16.69
Ca	4.03
C	19.53
O	59.24

Figure A.5 SEM morphologies of the corrosion product on the inner wall.

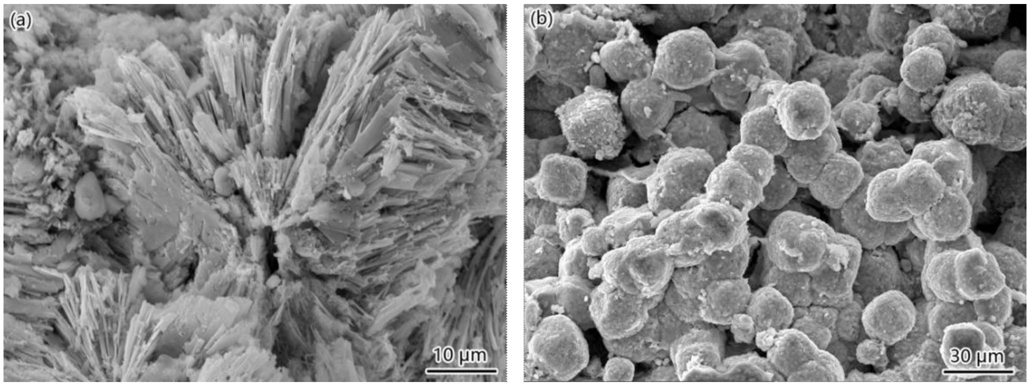

Figure A.6 SEM morphologies of the corrosion product on the outer wall.

A.3.3 Corrosion behavior of the typical locations on the pipe

A.3.3.1 The perforated pipe

Figure A.7 shows the macroscopic images and cross-sectional SEM images of the perforated pipe. It is seen that the corrosion pattern conforms to the flow direction obviously (see the white dashed box in Figure A.7a), and the pipe thickness dramatically decreases in the regions impacted by the flow as shown in Figure A.7b, especially on the right side which is opposite to the flow direction. The thickness here is less than 1 mm including the corrosion scales. Even in the regions along the flow direction on the left side, the pipe thickness drops to around 2.7 mm, only 40 % of the original thickness. Besides, the compactness and thickness of the corrosion scales differ significantly due to the flow distribution shown in Figure A.7d and A.7e. Three typical regions named D, E and F are selected to illustrate the corrosion behaviors, and the flow direction during service is denoted by the blue arrows. At region D, the impact of flow on the pipe along the flow direction is not quite severe despite a high flow rate, and therefore compact corrosion product is formed on the surface. Region E suffers the most direct impact of flow, thus loose corrosion product is formed and flushed away by the flow, which can be verified by the crack between the metal substrate and corrosion scales. Meanwhile, at region F where the flow rate is relatively slow on the outer wall, a thick and compact layer of corrosion product forms on the surface. Fe, C and O elements are detected from all three regions and the element percentage hardly changes as listed in Table A.2.

Table A.2 Chemical compositions (wt.%) of corrosion product in regions D, E and F in Figure A.7d and A.7e.

Region	Fe	C	O
D	63.83	8.71	27.46
E	70.05	7.94	22.01
F	64.88	6.32	28.80

The effect of flow on the corrosion process is further illustrated in Figure A.7c. Three characteristic regions A, B and C are marked, showing different corrosion features. It can be noted that the thickness of the rust layer differs at different regions, which is determined by the non-uniform distribution of physical and chemical factors, such as flow rate and direction, surface conditions of the metal and environmental deposits (Asami and Kikuchi, 2003). At region A, a thick corrosion product layer which has a good adhesion with the metal substrate is deposited on the surface, only with some cracks inside the layer. This type of corrosion scales can block mass transfer and thus retard the corrosion process to some degrees. In contrast, at region B, the high-velocity flow washes away the deposited corrosion product, leaving a thin and less-protective corrosion product layer. An obvious gap is observed between this layer and metal substrate, favoring the corrosion process remarkably and giving rise to severe consumption of the base metal. At region C on the outer wall, slight localized corrosion can be found. The difference of the corrosion scale thickness also corresponds to the perforation location, as seen in Figure A.7a. It is apparent that the thick corrosion scale displaying a band-like shape is located randomly between the perforations, and only thin corrosion product layer covers most of the inner surface. This is due to the non-uniformity of the flow inside the pipe during service.

To further determine the elemental distribution of the corrosion scales, EDS mapping analysis was conducted in the regions in the white box in Figure A.7b, as shown in Figure A.8. The corrosion scales are stratified into two sub-layers. At the inner layer, it mainly contains Fe, C and O elements, together with trace amount of Ca element. High concentration of Ca element is detected at the outer layer, along with Fe and O elements and trace amount of C element, demonstrating that Ca ions in the system are involved in the formation of corrosion product. Limited distributions of Si and O elements are present outside the sub-layers, which is attributed to the physical deposition and adhesion of clay or sand particles. It should be noted that, in some of the Ca-rich regions in Figure A.8e (shown in white), the Fe content is relatively low as indicated in Figure A.8d (shown in white). This phenomenon suggests the presence of carbonates with high Ca content, and therefore it is suspected that $CaCO_3$ forms and precipitates in this environment. As a comparison, the chemical composition of the corrosion scales on the outer wall is shown in Figure A.9. The corrosion product with single-layer structure mainly consists of Fe and O elements, together with small amount of C element only in some localized areas. However, Ca element does not appear in the corrosion scales.

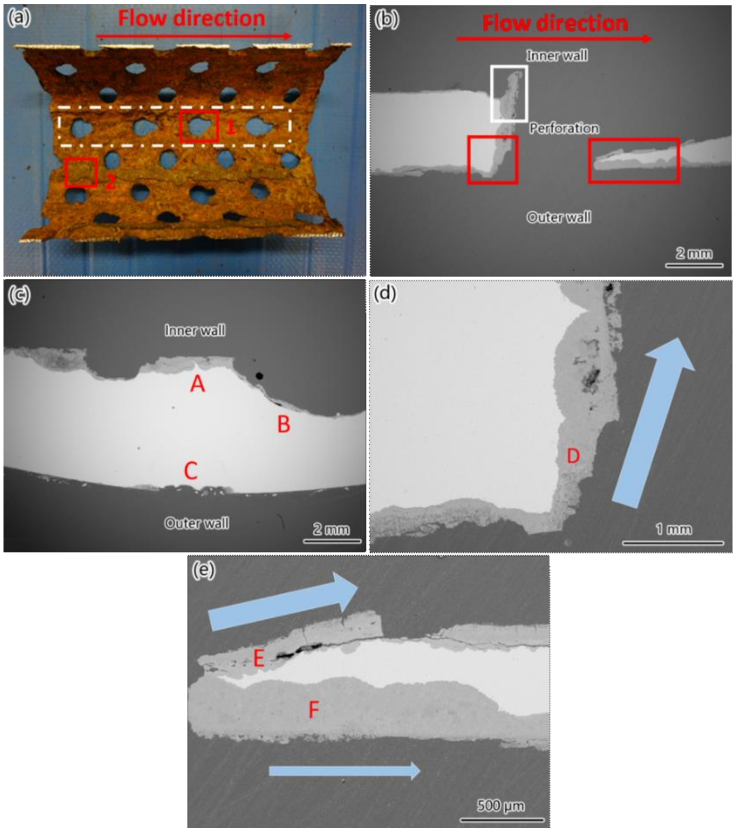

Figure A.7 (a) Macroscopic image of the perforated pipe; (b–c) cross-sectional SEM images of Region 1 and 2, respectively; (d–e) magnified images of regions in the red boxes in (b).

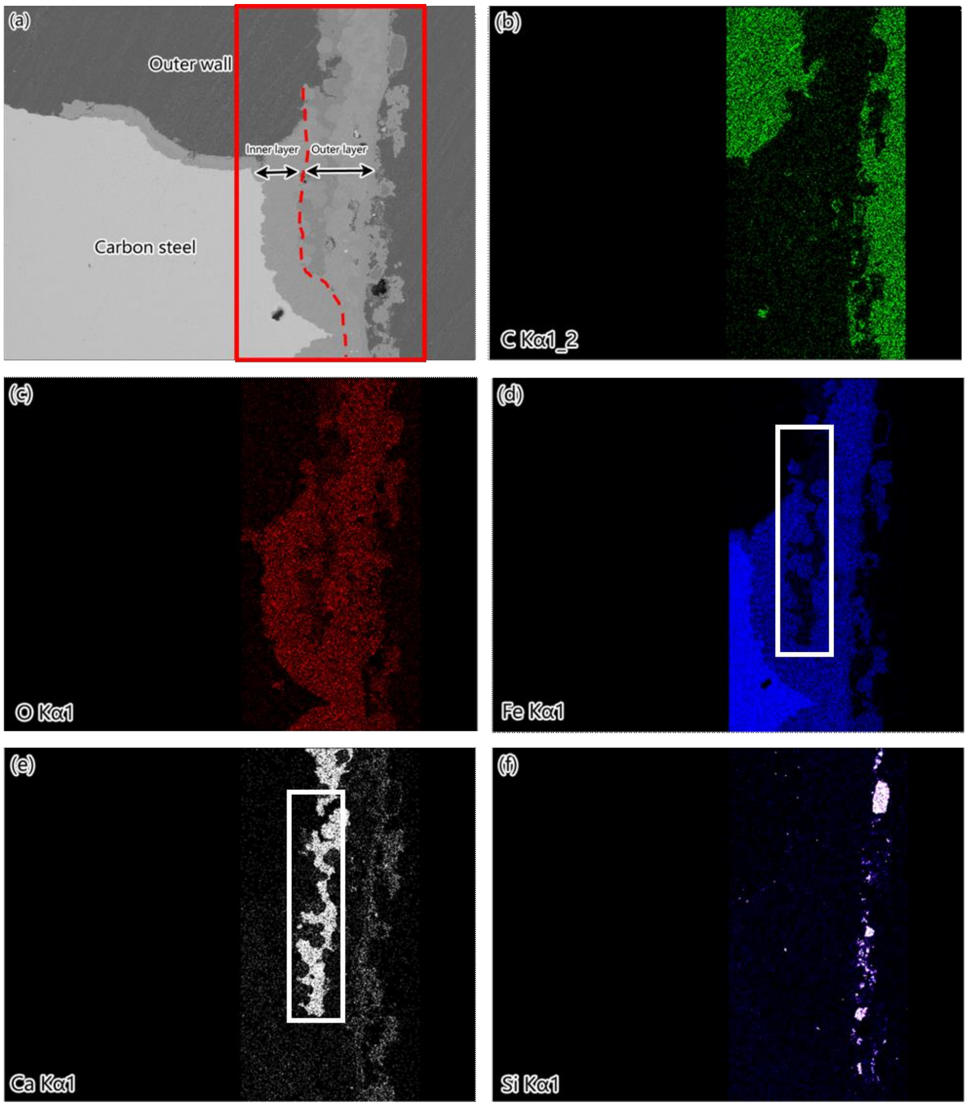

Figure A.8 (a) Cross-sectional image, and (b–f) elemental distributions of the corrosion scales on the inner wall in the selected region inside the white box in Figure A.7b.

A.3.3.2 The thread zone and the weld zone

The SEM cross-sectional images of the thread zone are depicted in Figure A.10. At the location denoted by the red arrow line, corrosion perforation occurs and leads to the complete failure of the threads. It should be noticed that corrosion on the inner wall is much more severe than that on the outer wall, and the thickness of the corrosion scales on the inner wall is larger as well, as seen in Figure A.10b and A.10c corresponding to regions A and B in Figure A.10a.

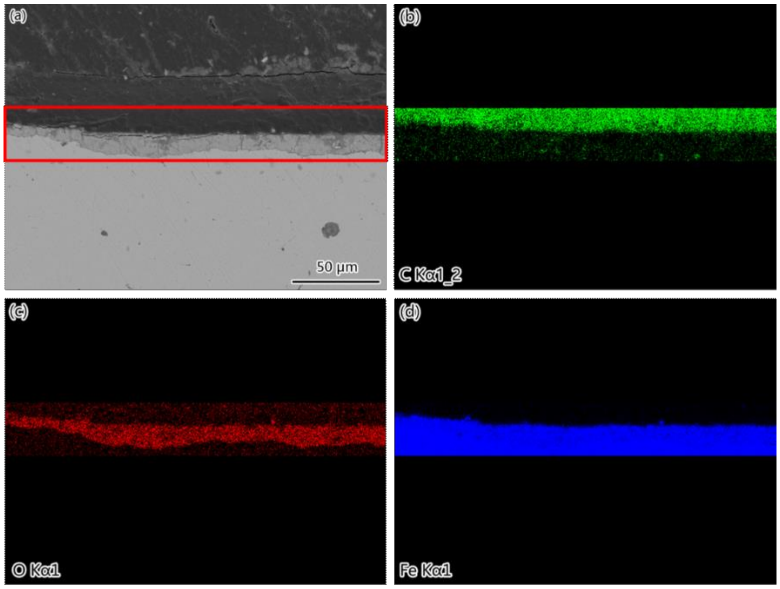

Figure A.9 (a) Cross-sectional image and (b–d) elemental distributions of the corrosion scales on the outer wall.

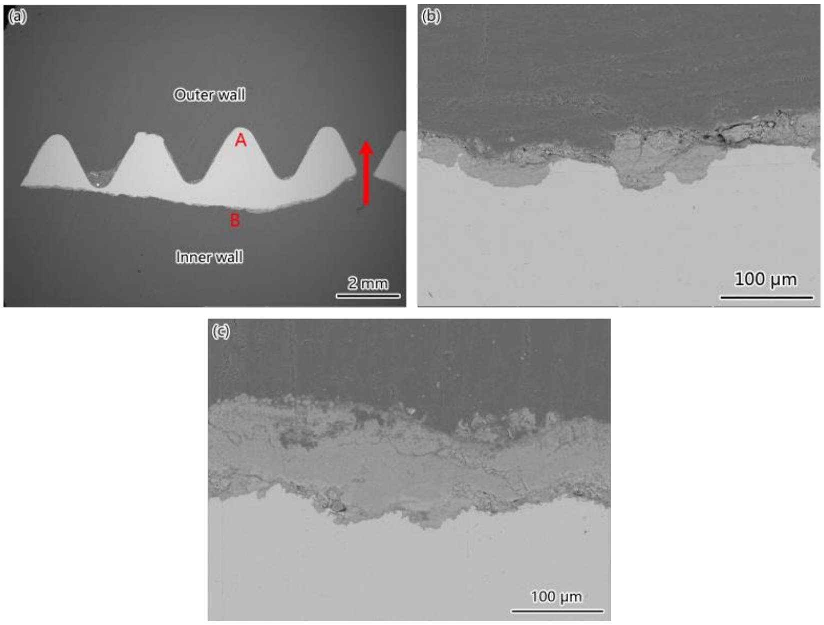

Figure A.10 (a) Cross-sectional SEM images of the thread zone and (b–c) magnified images of regions denoted by A and B in (a).

The macroscopic image, SEM cross-sectional images and corresponding EDS results of the weld zone on the outer wall are shown in Figure A.11. Localized corrosion occurs at the interface between stainless steel and carbon steel due to the galvanic effect, marked by regions A and B. The corrosion of carbon steel is much more severe than that of stainless steel because of its more negative electrode potential. The corrosive electrolyte gradually penetrates along the stainless steel/carbon steel interface, leading to the propagation of localized corrosion between the two materials. Besides, some welding defects are observed inside the weld zone (Figure A.11d), which is confirmed by Si element from the EDS results in Figure A.11e. The welding defect decreases the mechanical strength and serves as potential sites of the localized corrosion. To further investigate the localized corrosion behavior in the weld zone, EDS line scan analysis was performed at the interface of two materials, as seen in Figure A.11g. The significant change of Ca content near the interface also indicates the inward penetration of the corrosion electrolyte. EDS results also reveal that corrosion product mainly consists of Fe and O elements, but the elemental distribution varies along the line scan direction. A decrease of Ca content and an increase of Fe content are observed far from the interface at the carbon steel side, suggesting that the Ca-containing species deposit on the top of the scales and cannot diffuse deeper. This transition in chemical composition of corrosion product is in a good agreement with the two-layer structure mentioned above.

From the above analysis, it is confirmed that the thickness and compactness of corrosion scales vary at different locations, which influences the corrosion severity notably. Therefore, electrochemical tests were conducted to further demonstrate the protectiveness of the corrosion scales.

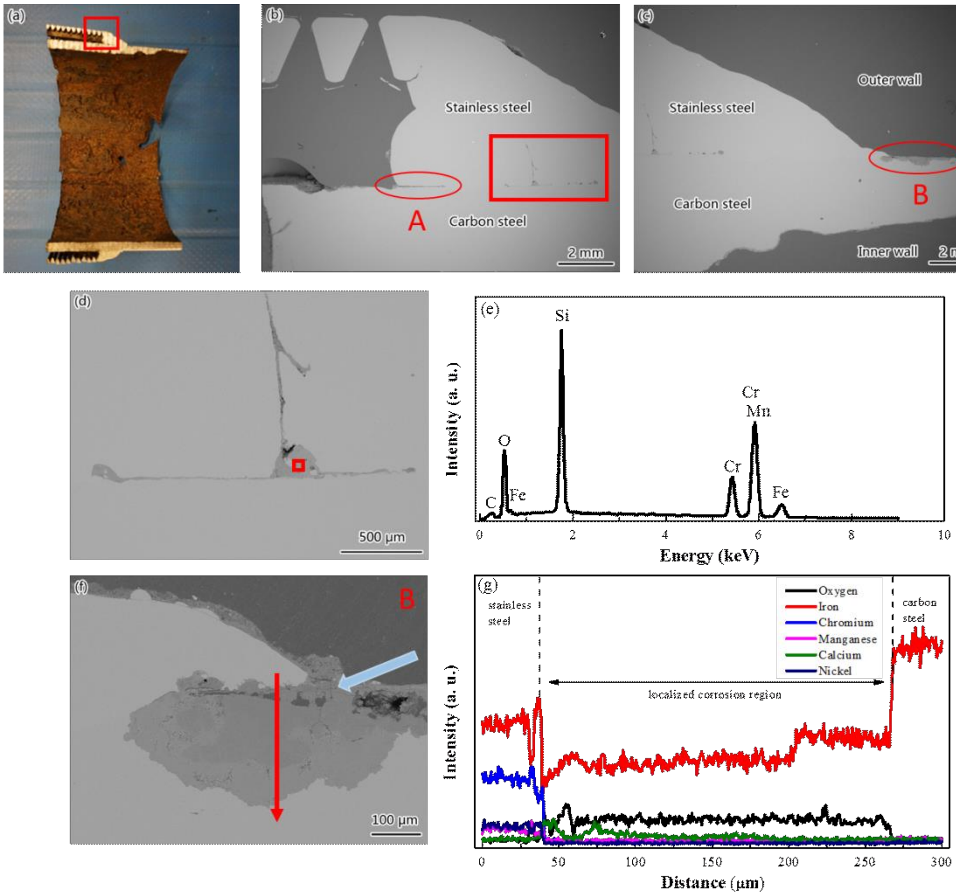

Figure A.11 (a) Macroscopic image and (b) (c) SEM images of the weld zone; (d) (f) magnified images of the welding defect [red box in (b)] and localized corrosion region [region B in (c)]; (e) EDS analysis of the welding defect region and (g) elemental distributions denoted by the red arrow line in (f).

A.3.4 Effect of the formation of corrosion scales on the corrosion of steel

Figure A.12 exhibits the potentiodynamic polarization curves of the steels with corrosion scales and the bare steel. Apparently, the overall anodic branches in the polarization curve of the steel with corrosion scales shift to the region of a lower current density as compared to that of the bare steel, implying that the formed corrosion scales can obviously inhibit the corrosion process. The corrosion potential (E_{corr}) and corrosion current density (i_{corr}) are calculated by the Tafel extrapolation method for each curve, and the corrosion inhibition efficiency (η) of the corrosion scales as compared to the bare steel is obtained by the following equation:

$$\eta = \frac{i_{corr}^{steel} - i_{corr}^{scale}}{i_{corr}^{steel}} \times 100\% \qquad \text{(Eq. A.2)}$$

where i_{corr}^{steel} and i_{corr}^{scale} are corrosion current densities of bare steel and steel with corrosion scales, respectively. All the electrochemical parameters are listed in Table A.3. The steels with corrosion scales display the corrosion potentials between -500 mV and -600 mV, more positive than that of the bare steel (-760 mV), suggesting the tendency less inclined to corrosion. The i_{corr} of thin corrosion scales slightly declines as compared to the bare steel, corresponding to a low η value of 35.3 %. Obviously, the thin scales provide limited protection for steel substrate. However, the η of thick corrosion scales is up to 83%, an indication that the compact and thick corrosion scales can provide a better protection for the steel substrate and thereby retard further corrosion of the steel substrate.

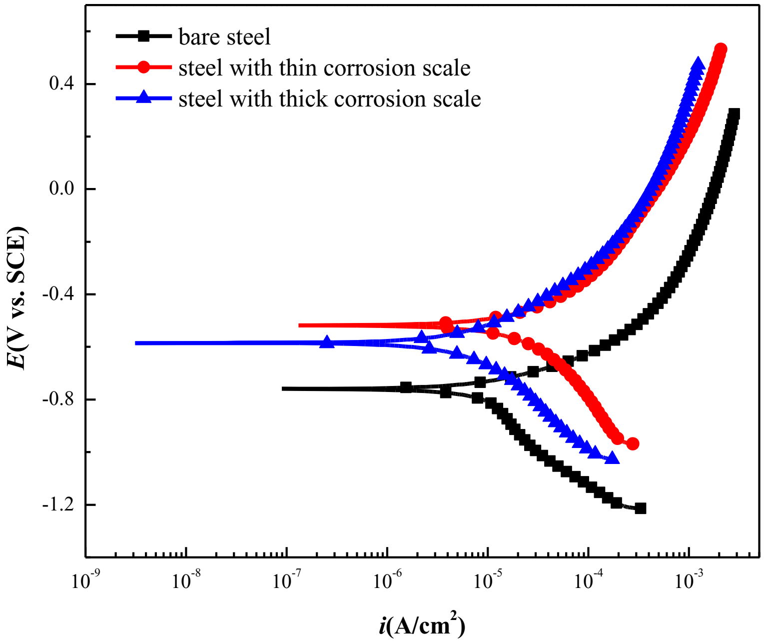

Figure A.12 Potentiodynamic polarization curves of different samples in the simulated solution.

Table A.3 Corrosion potential (E_{corr}), corrosion current density (i_{corr}) and corrosion inhibition efficiency (η) for the bare steel and the steels with corrosion scales.

Sample	E_{corr} (mV vs. SCE)	i_{corr} ($\mu A/cm^2$)	η (%)
Bare steel	-760	24.40	-
Steel with thin corrosion scales	-518	15.70	35.7
Steel with thick corrosion scales	-585	4.16	83.0

Figure A.13 depicts the Nyquist and Bode plots of three samples in the simulated solution. The bare steel displays an inductive loop in the low frequency region due to the non-uniform adsorption of $FeOH^+$ on steel surface (Liu et al., 2014). The Nyquist plots of steels with corrosion scales consist of two semicircles in the high and low frequency region, corresponding to the scale resistance and charge transfer resistance, respectively. In addition, the Warburg impedance appears in the low frequency region for steels with scales, an implication that the presence of scales gives rise to a diffusion-controlled electrochemical process. The steel with thick corrosion scales shows the largest total impedance (Figure A.13b), followed by the steel with thin corrosion scales and the bare steel, implying that the corrosion resistance is improved by the corrosion scales, especially the thick one. The equivalent electrical circuits describing the corrosion system are shown in Figure A.14 (Liu et al., 2014; Zhao et al., 2016). R_s is the solution resistance; Q_{dl} is the capacitance of the double layer, and R_{ct} is the charge transfer resistance; R_L is the inductance resistance, and L is the inductance element; R_{scale} and Q_{scale} is the resistance and capacitance of corrosion scale, respectively; W is the Warburg impedance, which is related to the diffusion process of the electrolyte in the corrosion scales. The pure capacitance (C) in the circuit is replaced by the constant phase element (CPE) (designated by Q) to get a better fitting, which is a complex impedance with the special property that its phase angle is frequency-independent or "constant phase angle" (Brug et al., 1984). CPE accounts for the deviation from the ideal dielectric behavior and is related to interfacial heterogeneity and surface roughness (Córdoba-Torres et al., 2015; Jorcin et al., 2006). The admittance of CPE element [$Y(Q)$] is defined as (Cao and Zhang, 2002):

$$Y(Q) = Y_0(Q)(j\omega)^n \tag{Eq. A.3}$$

where $Y_0(Q)$ and n are the admittance constant and empirical exponent, j is the imaginary number, and ω is the angular frequency. Likewise, the admittance of Warburg impedance [$Y(W)$] can be expressed as (Cao and Zhang, 2002; Qiao and Ou, 2007):

$$Y(W) = Y_0(W)(j\omega)^{1/2} \tag{Eq. A.4}$$

$$Y_0(W) = \frac{nFC_S\sqrt{D}}{\gamma Z_F^0 |I_F|} \tag{Eq. A.5}$$

where n is the number of electrons in the reaction, F is the Faraday constant, C_s is the electrolyte concentration at the surface, D is the diffusion coefficient, γ is the reaction order of the reactant, Z_F^0 is the Faraday impedance without diffusion, and I_F is the faradic current. The fitted data of main electrochemical parameters are listed in Table A.4. It is apparent that the thick corrosion scales exhibit the largest R_{ct} and the smallest $Y_0(Q_{dl})$, followed by the steel with thin corrosion scales and bare steel, revealing that the corrosion scales inhibit the mass transport of the electrolyte and thus slow down the electrochemical reaction rate. Moreover, R_{scale} increases and $Y_0(Q_{scale})$ decreases with the scale thickness, which suggests that the penetration of the corrosive medium is retarded more significantly by the thick corrosion scales, causing the decline of the corrosion rate. Furthermore, the thick scales lead to a much smaller $Y_0(W)$ as compared to the thin scale, demonstrating that the diffusion process is notably hindered.

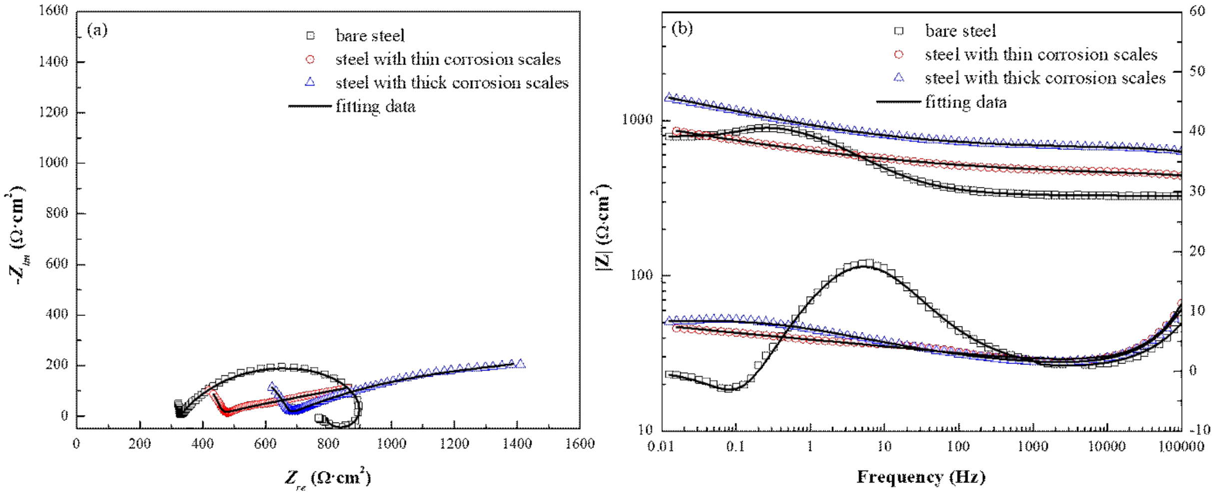

Figure A.13 (a) Nyquist and (b) Bode plots of different samples in the simulated solution.

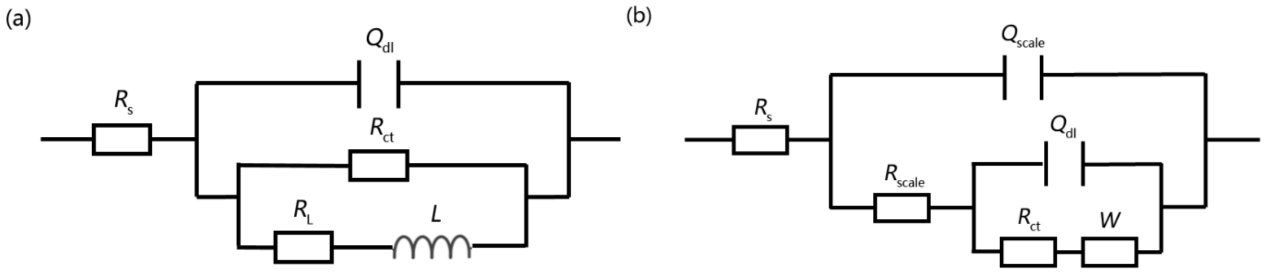

Figure A.14 Equivalent electrical circuits used for EIS data fitting: (a) bare steel; (b) steel with corrosion scales.

Table A.4 Main electrochemical parameters fitted from EIS data.

Sample	$Y_0(Q_{dl})$ ($\Omega^{-1}cm^{-2}s^n$)	R_{ct} (Ω cm^2)	R_L (Ω cm^2)	L (H/cm^2)	$Y_0(Q_{scale})$ ($\Omega^{-1}cm^{-2}s^n$)	R_{scale} (Ω cm^2)	$Y_0(W)$ ($\Omega^{-1}cm^{-2}s^{1/2}$)	Quality of fit
Bare steel	2.66×10^{-4}	470	209	228	-	-	-	1.04×10^{-3}
Thin scales	3.23×10^{-9}	647	-	-	3.24×10^{-3}	414	1.64×10^{4}	6.78×10^{-5}
Thick scales	3.22×10^{-9}	1369	-	-	1.51×10^{-3}	532	31.6	5.85×10^{-6}

A.4 Discussion

A.4.1 Corrosion mechanism of carbon steel pipes under service conditions

For the underground pipes in this study, the inner wall and outer wall undergo different corrosive environments, which results in different corrosion processes. On the inner wall, the high-velocity fluid with corrosive ions flows into the pipe through the perforations. In this process, the presence of HCO_3^- in the aqueous environment leads to the formation of H^+ ions by hydrolysis, and the subsequent corrosion process is mainly controlled by the following reactions (Zhang and Cheng, 2009):

$$HCO_3{}^- \leftrightarrow H^+ + CO_3{}^{2-} \qquad \text{(Eq. A.6)}$$

$$Fe^{2+} + HCO_3{}^- \rightarrow Fe(HCO_3)_2 \qquad \text{(Eq. A.7)}$$

$$Fe(HCO_3)_2 \rightarrow FeCO_3 + CO_2 + H_2O \qquad \text{(Eq. A.8)}$$

$$Fe^{2+} + CO_3{}^{2-} \rightarrow FeCO_3 \qquad \text{(Eq. A.9)}$$

Hence, $FeCO_3$ is formed on the steel surface, which can render protectiveness against corrosion if it covers the surface completely. In the regions covered with corrosion scales, calcium ions in the corrosive medium are readily incorporated into $FeCO_3$ lattice and replace Fe atoms, forming $Fe_xCa_{1-x}CO_3$ on the outer layer of corrosion product. This solid solution is also widely present in some other failure cases of pipelines in the Ca-containing medium (Mansoori et al., 2017). As reported, the corrosion rate of steel is significantly reduced due to the formation of this mixed carbonate at a low concentration of Ca^{2+} ions (less than 100 ppm) (Navabzadeh Esmaeely et al., 2013), and the samples with scales composed by $Fe_xCa_{1-x}CO_3$ exhibited lower current density and corrosion potential compared to that with pure $FeCO_3$. Therefore, the incorporation of Ca into $FeCO_3$ scale enhances the corrosion resistance. Despite that, the presence of calcium leads to porous corrosion scales, leaving corrosion paths inside the scales and allowing corrosive electrolyte to penetrate inwards, which causes further corrosion. However, it should be noted that $CaCO_3$ cannot form in this system, due to the high saturation degree of $CaCO_3$ and relatively low concentrations of Ca^{2+} and CO_3^{2-} (Mansoori et al., 2018).

Comparatively, the outer wall is buried underground and in contact with soil, therefore, the corrosion characteristics follow the features of soil corrosion. When steel is exposed to soil, the main electrochemical reactions are the oxidation of iron and the reduction of oxygen, and the presence of dissolved oxygen retards the formation of $FeCO_3$ and favors the formation of FeOOH (Sun et al., 2016a) The initial corrosion product is $Fe(OH)_2$ which is then further oxidized to $Fe(OH)_3$. However, due to the instability of $Fe(OH)_3$, it easily decomposes to FeOOH by dehydration. γ-FeOOH is first formed and then converted to α-FeOOH as time proceeds (Asami and Kikuchi, 2003). Furthermore, FeOOH can also transform to Fe_2O_3 and Fe_3O_4 under favorable conditions, but the amount of these two types of oxides is quite low. All the related reactions in this process are given as below (Xiao et al., 2008):

$$Fe \rightarrow Fe^{2+} + 2e^{-} \qquad \text{(Eq. A.10)}$$

$$O_2 + 2H_2O + 4e^{-} \rightarrow 4OH^{-} \qquad \text{(Eq. A.11)}$$

$$2Fe + O_2 + 2H_2O \rightarrow 2Fe(OH)_2 \qquad \text{(Eq. A.12)}$$

$$2Fe(OH)_2 + O_2 + 2H_2O \rightarrow 4Fe(OH)_3 \qquad \text{(Eq. A.13)}$$

$$Fe(OH)_3 \rightarrow FeOOH + H_2O \qquad \text{(Eq. A.14)}$$

$$2FeOOH \rightarrow Fe_2O_3 + H_2O \qquad \text{(Eq. A.15)}$$

$$8FeOOH + Fe^{2+} + 2e^{-} \rightarrow 3Fe_3O_4 + 4H_2O \quad \text{(Eq. A.16)}$$

Moreover, the calcium content in the surroundings is much lower than that in the fluid, and Ca ions cannot incorporate into iron oxides/hydroxides, which explain why Ca element was not detected in the corrosion product on the outer wall.

A.4.2 Effect of flow on the corrosion process

Erosion-corrosion generally occurs in the environments having the potential to be both erosive (mechanical component) and corrosive (electrochemical component), with the interaction between corrosive fluid, solid particles and target materials (Islam and Farhat, 2017). In the form of erosion-corrosion, the electrochemical corrosion is accelerated by high mass transfer rate and the removal of protective corrosion scales by solid particles; the mechanical erosion, on the other hand, can be caused by forming loose corrosion product and roughing the metal surface (Hu and Neville, 2009). Therefore, the total material loss from erosion-corrosion is larger than the sum of those from pure corrosion and pure erosion processes, and this interaction between two processes has been reported as the synergistic effect (Tang et al., 2008; Zhou et al., 1996).

In this study, the corrosion features are significantly affected by the flow. Moreover, the different flow conditions which the inner and outer walls are subjected to are also the underlying reasons for having different corrosion processes on both walls and the formation of different corrosion scales. However, the failure of the pipes is mainly derived from the erosion-corrosion of the inner wall. Accordingly, a corrosion model is proposed to interpret the flow-induced corrosion process on the inner wall, as shown in Figure A.15.

On the inner wall, the high flow rate is the most crucial factor affecting the corrosion process, revealing that much more ions, such as Ca^{2+} and HCO_3^-, can participate in the corrosion reactions by the fast mass transfer. In the early stage of corrosion (Figure A.15a), these ions preferentially adsorb onto some regions on the surface where corrosion initiates, giving rise to the gradual formation of the corrosion product. Subsequently, the high-rate flow, accompanied by sand particles, favors the removal of the scales in some areas (named “active sites”). The fresh metal surface can be exposed to the corrosive medium again, leading to the further corrosion of metal substrate. As the corrosion proceeds, the thickness of corrosion scales increases, which protects the carbon steel underneath, while the active sites suffer from continuous erosion-corrosion attack. In addition, micro-galvanic cells can form on the surface with active sites as anodes and corrosion scales as cathodes because steel exhibits more negative potential than corrosion scales (Figure A.15b) (Tan et al., 2011; Zhang et al., 2014). This effect further accelerates the electrochemical reactions and causes severe consumption of carbon steel on the inner wall, and eventually gives rise to the typical erosion-corrosion pattern. Furthermore, the presence of chloride ions in the fluid promotes the flow-induced corrosion (Ilman and Kusmono et al., 2014). The incorporation of Ca into $FeCO_3$ lattices results in the dominance of carbonates with the enrichment of Ca on the outer layer of the scales (Figure A.15c).

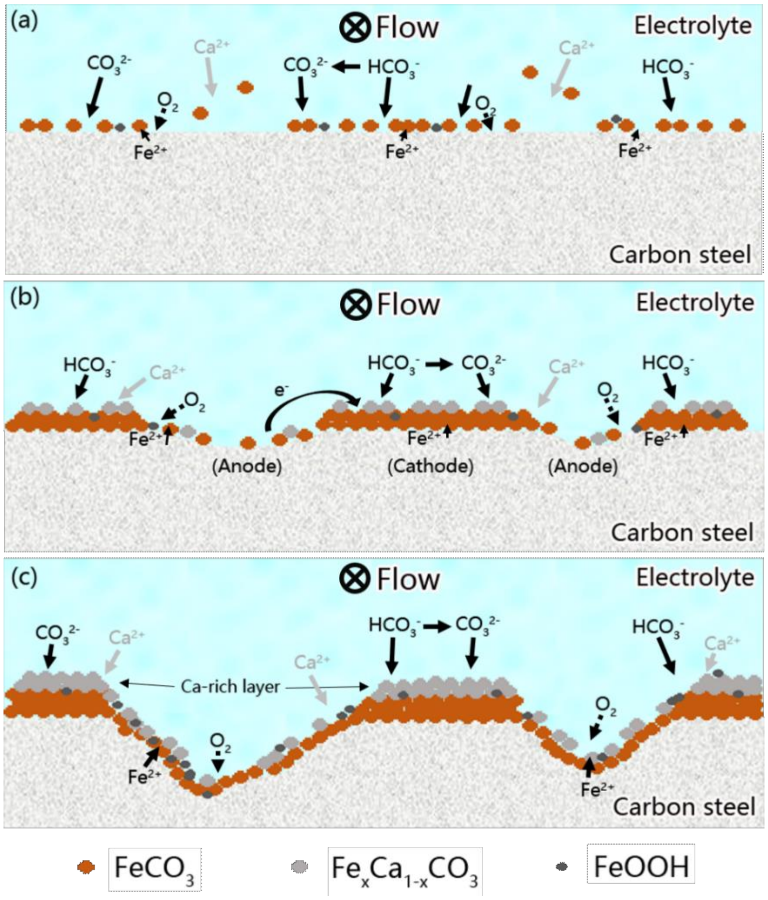

Figure A.15 Schematic model of the corrosion process and failure mechanism of the pipes on the inner wall.

A.5 Conclusions

Severe flow-induced corrosion occurs on the inner wall of J55 carbon steel pipes and contributes to a significant decrease of pipe thickness. The pattern of damaged perforations and the distribution of the corrosion scales inside the pipe correspond to the flow direction obviously. Dense and thick corrosion scales can prevent the steel from further corrosion, and localized corrosion occurs in the regions covered with less corrosion products. The thread zone is severely damaged due to the corrosion originating from the inner wall as well. The carbon steel in the weld zone suffers severe localized corrosion at the interface between stainless steel and carbon steel, which is attributed to the galvanic effect.

Different corrosive environments between the inner and the outer wall result in diverse corrosion rates and corrosion processes. The high corrosion rate on the inner wall is attributed to the fast passing-through flow, and the corrosion products on the inner wall are mainly composed of carbonates. The enrichment of Ca element is found in the outer layer of corrosion scales to form $Fe_xCa_{1-x}CO_3$ double salt, providing extra protection against corrosion. Comparatively, the buried pipes exhibit the features of soil corrosion, and the corrosion is remarkably limited by the slow mass transfer on the outer wall. In this case, a thinner layer of corrosion scales forms, which mainly consists of iron hydroxides (γ-FeOOH and α-FeOOH). Lastly, a corrosion model was established to illustrate the corrosion process and the failure mechanism of the inner wall of the carbon steel pipes.

A.6 References

Asami, K., Kikuchi, M., 2003. In-depth distribution of rusts on a plain carbon steel and weathering steels exposed to coastal-industrial atmosphere for 17 years. Corros. Sci. 45, 2671–2688.

Brug, G. J., Van Den Eeden, A. L. G., Sluyters-Rehbach, M., Sluyters, J. H., 1984. The analysis of electrode impedances complicated by the presence of a constant phase element. J. Electroanal. Chem. 176, 275–295.

Cao, C. N., Zhang, J. Q., 2002. An introduction to electrochemical impedance spectroscopy; Science Press: Beijing, pp: 24–36.

Cole, I. S., Marney, D., 2012. The science of pipe corrosion: A review of the literature on the corrosion of ferrous metals in soils. Corros. Sci. 56, 5–16.

Córdoba-Torres, P., Mesquita, T. J., Nogueira, R. P., 2015. Relationship between the origin of constant-phase element behavior in electrochemical impedance spectroscopy and electrode surface structure. J. Phys. Chem. C, 119, 4136–4147.

Cui, Z. D., Wu, S. L., Zhu, S. L., Yang, X. J., 2006. Study on corrosion properties of pipelines in simulated produced water saturated with supercritical CO_2. Appl. Surf. Sci. 252, 2368–2374.

De la Fuente, D., Díaz, I., Simancas, J., Chico, B., Morcillo, M., 2011. Long-term atmospheric corrosion of mild steel. Corros. Sci. 53, 604–617.

Elgaddafi, R., Ahmed, R., Hassani, S., Shah, S., Osisanya, S.O., 2016. Corrosion of C110 carbon steel in high-pressure aqueous environment with mixed hydrocarbon and CO_2 gas. J. Petrol. Sci. Eng. 146, 777–787.

Feng, X., Lu, X., Zuo, Y., Zhuang, N., Chen, D., 2016. The effect of deformation on metastable pitting of 304 stainless steel in chloride contaminated concrete pore solution. Corros. Sci. 103, 223–229.

Hu, X., Neville, A., 2009. CO_2 erosion–corrosion of pipeline steel (API X65) in oil and gas conditions—A systematic approach. Wear 267, 2027–2032.

Ilman, M. N., Kusmono, 2014. Analysis of internal corrosion in subsea oil pipeline. Case Stud. Eng. Fail. Anal. 2, 1–8.

Islam, M. A., Farhat, Z., 2017. Erosion-corrosion mechanism and comparison of erosion-corrosion performance of API steels. Wear 376, 533–541.

Jorcin, J.-B., Orazem, M. E., Pébère, N., Tribollet, B., 2006. CPE analysis by local electrochemical impedance spectroscopy. Electrochim. Acta 51, 1473–1479.

Kermani, M. B., Morshed, A., 2003. Carbon dioxide corrosion in oil and gas production–a compendium. Corrosion 59, 659–683.

Linter, B. R., Burstein, G. T., 1999. Reactions of pipeline steels in carbon dioxide solutions. Corros. Sci. 41, 117–139.

Liu, T., Chen, L., Bi, H., Che, X., 2014. Effect of Mo on high-temperature fatigue behavior of 15CrNbTi ferritic stainless steel. Acta Metall. Sin. (Engl. Lett.) 27, 452–456.

Liu, Z., Liao, W., Wu, W., Du, C., Li, X., 2017. Failure analysis of leakage caused by perforation in an L415 steel gas pipeline. Case Stud. Eng. Fail. Anal. 9, 63–70.

Mansoori, H., Mirzaee, R., Esmaeilzadeh, F., Vojood, A., Dowrani, A. S., 2017. Pitting corrosion failure analysis of a wet gas pipeline. Eng. Fail. Anal. 82, 16–25.

Mansoori, H., Young, D., Brown, B., Singer, M., 2018. Influence of calcium and magnesium ions on CO_2 corrosion of carbon steel in oil and gas production systems - A review. J. Nat. Gas Sci. Eng. 59, 287–296.

Nasr, T. N., Ayodele, O. R., 2005. Thermal techniques for the recovery of heavy oil and bitumen. In: SPE International Improved Oil Recovery Conference in Asia Pacific, Kuala Lumpur.

Navabzadeh Esmaeely, S., Choi, Y. S., Young, D., Nešić, S., 2013. Effect of calcium on the formation and protectiveness of iron carbonate layer in CO_2 corrosion. Corrosion 69, 912–920.

Nešić, S., 2007. Key issues related to modelling of internal corrosion of oil and gas pipelines–A review. Corros. Sci. 49, 4308–4338.

Qiao, G., Ou, J., 2007. Corrosion monitoring of reinforcing steel in cement mortar by EIS and ENA. Electrochim. Acta 52, 8008–8019.

Ren, C., Liu, D., Bai, Z., Li, T., 2005. Corrosion behavior of oil tube steel in simulant solution with hydrogen sulfide and carbon dioxide. Mater. Chem. Phys. 93, 305–309.

Song, F. M., 2010. A comprehensive model for predicting CO_2 corrosion rate in oil and gas production and transportation systems. Electrochim. Acta 55, 689–700.

Sun, J., Sun, C., Zhang, G., Li, X., Zhao, W., Jiang, T., Liu, H., Cheng, X., Wang, Y., 2016a. Effect of O_2 and H_2S impurities on the corrosion behavior of X65 steel in water-saturated supercritical CO_2 system. Corros. Sci. 107, 31–40.

Sun, J., Sun, C., Zhang, G., Zhao, W., Wang, Y., 2016b. Effect of water cut on the localized corrosion behavior of P110 tube steel in supercritical CO_2/Oil/water environment. Corrosion 72, 1470–1482.

Sun, W., Nešic, S., 2009. A mechanistic model of uniform hydrogen sulfide/carbon dioxide corrosion of mild steel. Corrosion 65, 291–307.

Tan, Y. J., Fwu, Y., Bhardwaj, K., 2011. Electrochemical evaluation of under-deposit corrosion and its inhibition using the wire beam electrode method. Corros. Sci. 53, 1254–1261.

Tang, X., Xu, L. Y., Cheng, Y. F., 2008. Electrochemical corrosion behavior of X-65 steel in the simulated oil–sand slurry. II: Synergism of erosion and corrosion. Corros. Sci. 50, 1469–1474.

Xiao K., Dong, C. F., Li, X. G., Wang, F. M., 2008. Corrosion products and formation mechanism during initial stage of atmospheric corrosion of carbon steel. J. Iron Steel Res. Int. 15, 42.

Zhang, G. A., Cheng, Y. F., 2009. Corrosion of X65 steel in CO_2-saturated oilfield formation water in the absence and presence of acetic acid. Corros. Sci. 51, 1589.

Zhang, G. A., Yu, N.; Yang, L. Y., Guo, X. P., 2014. Galvanic corrosion behavior of deposit-covered and uncovered. Corros. Sci. 86, 202–212.

Zhang, X., Yang, S., Zhang, W., Guo, H., He, X., 2014. Influence of outer rust layers on corrosion of carbon steel and weathering steel during wet–dry cycles. Corros. Sci. 82, 165–172.

Zhao, Q.-H., Liu, W., Li, S.-Z., Zhang, B.-L., Zhu, Y.-C., Lu, M.-X., 2016. Effects of W and Mo additions on wet-dry acid corrosion behavior of low-alloy steels under different O_2 concentrations. Acta Metall. Sin. (Engl. Lett.) 29, 951–962.

Zhong, X., Lu, W., Yang, H., Liu, M., Zhang, Y., Liu, H., Hu, J., Zhang, Z., Zeng, D., 2019. Oxygen corrosion of N80 steel under laboratory conditions simulating high pressure air injection: Analysis of corrosion products. J. Petrol. Sci. Eng. 172, 162–170.

Zhou, S., Stack, M. M., Newman, R. C., 1996. Characterization of synergistic effects between erosion and corrosion in an aqueous environment using electrochemical techniques. Corrosion 52, 934–946.